AFRL-AFOSR-VA-TR-2019-0267

Smart Functional Nanoenergetic Materials

Richard Yetter
PENNSYLVANIA STATE UNIVERSITY

05/21/2019
Final Report

DISTRIBUTION A: Distribution approved for public release.

Air Force Research Laboratory
AF Office Of Scientific Research (AFOSR)/ RTA1
Arlington, Virginia 22203
Air Force Materiel Command

REPORT DOCUMENTATION PAGE	*Form Approved* *OMB No. 0704-0188*

1. REPORT DATE *(DD-MM-YYYY)* 13-April-2019	**2. REPORT TYPE** Final Report	**3. DATES COVERED** *(From - To)* From 11/1/2012-10/31/2018

4. TITLE AND SUBTITLE

Smart Functional Nanoenergetic Materials

5a. CONTRACT NUMBER
FA9550-13-1-0004

5b. GRANT NUMBER

5c. PROGRAM ELEMENT NUMBER

6. AUTHOR(S)

Ilhan A. Aksay,[2] Roberto Car,[2] Bryan Eichhorn,[3] Annabella Selloni,[2] Steven F. Son,[4] Stefan Thynell,[1] Vigor Yang,[5] Richard A. Yetter,[1] and Michael R. Zachariah[3]

5d. PROJECT NUMBER

5e. TASK NUMBER

5f. WORK UNIT NUMBER

7. PERFORMING ORGANIZATION NAME(S) AND ADDRESS(ES)

[1]Department of Mechanical and Nuclear Engineering
The Pennsylvania State University
University Park, PA 16802

[2]Princeton University, Princeton, NJ
[3]University of Maryland, College Park, MD
[4]Purdue University, West Lafayette, IN
[5]Georgia Institute of Technology
Atlanta, GA

8. PERFORMING ORGANIZATION REPORT NUMBER

9. SPONSORING / MONITORING AGENCY NAME(S) AND ADDRESS(ES)

Air Force Office of Scientific Research
Attn: Dr. Mitat Birkan
875 North Randolph Street
Suite 325, Room 3112
Arlington, VA 22203-1768

10. SPONSOR/MONITOR'S ACRONYM(S)

11. SPONSOR/MONITOR'S REPORT NUMBER(S)

12. DISTRIBUTION / AVAILABILITY STATEMENT

Unlimited Distribution

13. SUPPLEMENTARY NOTES

14. ABSTRACT

The Smart Functional Nanoenergetic Materials MURI program explored new methodologies for development of macroscale (micron-sized or larger) composite energetic materials with nanoscale features that provide improved performance over nanoscale particles and ease of processing and handling, managed energy release, reduced sensitivity, and potential for internal/external control and actuation. The reactivity and thermal decomposition of nanostructured materials (including FGS-tetrazine compounds, encapsulated nanocatalysts in energetic oxidizers, metal alloy particles, mesoscopic aggregates, and aluminum clusters) were analyzed along with their combustion performance in liquid and solid composite propellants. Molecular dynamics simulations were performed to understand the decomposition and reactivity of the nanostructured materials and their heat transfer properties in liquid suspensions and gaseous environments. The development of both model systems and new synthesis processes for functionalized graphene sheets (FGS)-tetrazine compounds, Al and Pt nanoparticles on FGS, metallic Al clusters and mesoscopic aggregates, nanoscale inclusion materials, and encapsulated nanocatalysts in energetic oxidizers were accomplished. Assembling nanoparticles into a microparticle with an embedded gas generator was demonstrated to lead to enhanced combustion, a more consistent burn from particle–to-particle, and mesoparticles that burn like independent Al nanoparticles. Nanoconfinement was found responsible for accelerating the decomposition of tetrazines linked to multilayers of FGSs upon rapid heating. The replacement of Al with Al-Li alloy in composite propellants was found to drastically reduce formation of HCl in the products and theoretically increase specific impulse. Theoretical models for the effective thermal conductivity of energetic nanomaterials and the thermal decomposition of hydroxylammonium nitrate and ammonia borane were developed.

15. SUBJECT TERMS

Nanoenergetic Materials, Propulsion

16. SECURITY CLASSIFICATION OF: **Unclassified**			**17. LIMITATION OF ABSTRACT**	**18. NUMBER OF PAGES**	**19a. NAME OF RESPONSIBLE PERSON** Richard A. Yetter
a. REPORT	**b. ABSTRACT**	**c. THIS PAGE**		147	**19b. TELEPHONE NUMBER** *(include area code)* (814) 863-6375

Standard Form 298 (Rev. 8-98)
Prescribed by ANSI Std. Z39.18

Smart Functional Nanoenergetic Materials
FA9550-13-1-0004

Ilhan A. Aksay,[2] Roberto Car,[2] Bryan Eichhorn,[3] Annabella Selloni,[2] Steven F. Son,[4] Stefan Thynell,[1] Vigor Yang,[5] Richard A. Yetter,[1] Michael R. Zachariah[3]

[1]The Pennsylvania State University, University Park, PA
[2]Princeton University, Princeton, NJ
[3]University of Maryland, College Park, MD
[4]Purdue University, West Lafayette, IN
[5]Georgia Institute of Technology, Atlanta, GA

ABSTRACT

The Smart Functional Nanoenergetic Materials MURI program explored new methodologies for development of macroscale (micron-sized or larger) composite energetic materials with nanoscale features that provide improved performance over nanoscale particles and ease of processing and handling, managed energy release, reduced sensitivity, and potential for internal/external control and actuation. The reactivity and thermal decomposition of nanostructured materials (including FGS-tetrazine compounds, encapsulated nanocatalysts in energetic oxidizers, metal alloy particles, mesoscopic aggregates, and aluminum clusters) were analyzed along with their combustion performance in liquid and solid composite propellants. Molecular dynamics simulations were performed to understand the decomposition and reactivity of the nanostructured materials and their heat transfer properties in liquid suspensions and gaseous environments. The development of both model systems and new synthesis processes for functionalized graphene sheets (FGS)-tetrazine compounds, Al and Pt nanoparticles on FGS, metallic Al clusters and mesoscopic aggregates, nanoscale inclusion materials, and encapsulated nanocatalysts in energetic oxidizers were accomplished. Assembling nanoparticles into a microparticle with an embedded gas generator was demonstrated to lead to enhanced combustion, a more consistent burn from particle–to-particle, and mesoparticles that burn like independent Al nanoparticles. Nanoconfinement was found responsible for accelerating the decomposition of tetrazines linked to multilayers of FGSs upon rapid heating. The replacement of Al with Al-Li alloy in composite propellants was found to drastically reduce formation of HCl in the products and theoretically increase specific impulse. Theoretical models for the effective thermal conductivity of energetic nanomaterials and the thermal decomposition of hydroxylammonium nitrate and ammonia borane were developed.

TABLE OF CONTENTS

LIST OF FIGURES

LIST OF TABLES

METRICS

PUBLICATIONS AND MANUSCRIPTS

Published in Peer-Reviewed Journals

1. C. Zangmeister, J. Radney, L.T. Dockery, J.T. Young, X. Ma, R. You and M.R. Zachariah*; The Packing Density of Rigid Aggregates is Independent of Scale*, Proceedings of the National Academy of Sciences, 111, 9037 (2014)
2. H. Wang, G. Jian, J. Delisio and M.R. Zachariah *Assembly and Reactive Properties Al/CuO Nanothermite Microparticles* Combustion and Flame 161, 2203 (2014)
3. J. B. DeLisio, C. Huang, G. Jian and M. R. Zachariah, *Ignition and Reaction Analysis of High Loading Nano-Al/Fluoropolymer Energetic Composite Films*; AIAA-0646 (2014)
4. H. Wang, G. Jian, J. DeLisio, M.R. Zachariah *Microsphere Composites of Nano-Al and Nonothermites: An approach to Better Utilization of Nanomaterials* AIAA-0647 (2014)
5. Christopher M. Sims, Audaldo A. Ponce, Karen J. Gaskell, Bryan W. Eichhorn *Activity Modulation in Graphene-Supported Pt and PtSn Electrocatalysts Dalton Trans.*, 44, 977-987 (2014)
6. F. Yi, J. DeLisio, M. Zachariah, D. LaVan *Nanocalorimetry coupled Time-of-Flight Mass Spectrometry: Identifying evolved species during high rate thermal measurements*, Anal. Chem. 87, 9740, (2015)
7. X. Y. Li, P. Guerieri, W. B. Zhou, M. R. Zachariah, *Direct Deposit Laminate nano-composites with enhanced propellant properties,* ACS Applied Materials and Interfaces, 7, 9103 (2015)
8. G. Young, H. Wang, and M.R Zachariah, *Application of Nano-Aluminum/Nitrocellulose Mesoparticles in Composite Solid Rocket Propellants,* Propellents, Explosive and Pyrotechnics 40, 413 (2015)
9. P. Guerieri, S. DeCarlo, B. Eichhorn, T. Connell, R. Yetter, X. Tang, Z. Hicks, K. Bowen, M.R. Zachariah, *Molecular Aluminum Additive for Burn Enhancement of Hydrocarbon Fuels*, J. Physical Chem. A. *doi/full/10.../acs.jpca.5b08580*
10. G. Young, H. Wang, and M.R Zachariah, *Application of Nano-Aluminum/Nitrocellulose Mesoparticles in Composite Solid Rocket Propellants,* Propellents, Explosive and Pyrotechnics 40, 413 (2015)
11. R. Jacob, B. Wei, M.R. Zachariah, *Quantifying the Enhanced Combustion Characteristice of Electrospray Assembled Aluminum Mesoparticles,* Combustion and Flame 163, 281 (2016)
12. T. Wu, X. Li, H. Hu, J. Delisio, W. Zhou and M.R. Zachariah, *Direct-Deposition to Create High Particle Loadings Propellents with Controlled Architecture: Combustion and Mechanical Properties*, AIAA SciTech 0688 (2016)
13. J. DeLisio, D Mayo, P Guerieri, R Ives, K Bowen, B Eichhorn and M.R. Zachariah, *Oxidation and Decomposition Mechanisms of Air Sensitive Aluminum Clusters at High Heating Rates*, Chem. Phys. Lett. 661, 168 (2016)
14. P. Guerieri, J. DeLisio, and M.R. Zachariah, *Nanoaluminum/Nitrocellulose Microparticle Additive for Burn Enhancement of Liquid Fuels,* Comb. and Flame 176, 220 (2017)
15. R. Jacob, Di. L. Ortiz-Montalvo, K. R. Overdeep, T. P. Weihs and M. R. Zachariah, *Incomplete Reaction in Nanothermite Composites,* Journal of Applied Physics 121, 054307 (2017)
16. J. Delisio, F. Yi, D. LeVan, and M.R. Zachariah, *High Heating Rate Reaction Dynamics of Al/CuO Nanolaminates by Nanocalorimetry-Coupled Time-of-Flight Mass Spectrometry,* Journal of Physical Chemistry C, 121, 2771 (2017)

17. P. Guerieri, R. Jacob, J. DeLisio, M. Rehwoldt and M. R. Zachariah, *Stabilized Microparticle Aggregates of Oxygen-Containing Nanoparticles in Kerosene for Enhanced Droplet Combustion*, Combustion & Flame 187, 77 (2018)
18. M. Alifierakis, K. S. Sallah, I. A. Aksay J. H. Prevost, "Reversible Cluster Aggregation and Growth Model for Graphene Suspensions," *AIChE J.* **2017**, *63*, 5462-5473. DOI: 10.1002/aic.15962
19. B. Uralcan, I. A. Aksay, P. G. Debenedetti, D. T. Limmer, "Concentration Fluctuations and Capacitive Response in Dense Ionic Solutions," *J. Phys. Chem. Lett.* **2016**, *7*, 2333-2338. DOI: 10.1021/acs.jpclett.6b00859
20. C. Zhang, D. M. Dabbs, L.-M. Liu, I. A. Aksay, R. Car, A. Selloni, "Combined Effects of Functional Groups, Lattice Defects, and Edges in the Infrared Spectra of Graphene Oxide," *J. Phys. Chem. C* **2015**, *119*, 18167-18176. DOI: 10.1021/acs.jpcc.5b02727.
21. Y. Li, V. Alain-Rizzo, L. Galmiche, P. Audebert, F. Miomandre, G. Louarn, M. Bozlar, M. A. Pope, D. M. Dabbs, I. A. Aksay, "Functionalization of Graphene Oxide by Tetrazine Derivatives: A Versatile Approach toward Covalent Bridges between Graphene Sheets," *Chem. Mater.* **2015**, *27*, 4298-4310. DOI: 10.1021/acs.chemmater.5b00672.
22. D. J. Bozym, B. Uralcan, D. T. Limmer, M. A. Pope, N. J. Szamreta, P. G. Debenedetti, I. A. Aksay, "Anomalous Capacitance Maximum of the Glassy Carbon–Ionic Liquid Interface through Dilution with Organic Solvents," *J. Phys. Chem. Lett.* **2015**, *6*, 2644-2648. DOI: 10.1021/acs.jpclett.5b00899.
23. H. Belal, C. W. Han, I. E. Gunduza, V. Ortalan, and S. F. Son, "Ignition and combustion behavior of mechanically activated Al–Mg particles in composite solid propellants," Combustion and Flame, 194, pp. 410-418, 2018. https://doi.org/10.1016/j.combustflame.2018.04.010
24. S. Isert S. and S. F. Son., "The Relationship Between Flame Structure and Burning Rate for Ammonium Perchlorate Composite Propellants." Book Chapter in: Shukla M., Boddu V., Steevens J., Damavarapu R., Leszczynski J. (eds) Energetic Materials. Challenges and Advances in Computational Chemistry and Physics, vol 25. Springer, 2017. https://doi.org/10.1007/978-3-319-59208-4_6
25. M. A. Rubio, I. E. Gunduz, L. J. Groven, T. R. Sippel, C. W. Han, R. R. Unocic, V. Ortalan, and S. F Son, "Microexplosions and ignition dynamics in engineered aluminum/polymer fuel particles," *Combustion and Flame*, Vol. 176, pp. 162-171, 2017. https://doi.org/10.1016/j.combustflame.2016.10.008
26. S. Isert, L. Xin, J. Xie, S. F. Son, "The Effect of Decorated Graphene Addition on the Burning Rate of Ammonium Perchlorate Composite Propellants," *Combustion and Flame*, Vol. 183, pp. 322-329, 2017. https://doi.org/10.1016/j.combustflame.2017.05.024
27. D. A. Reese, S. F. Son, and A. H. Yan, "Crystal Encapsulated Nanoparticles Methods and Compositions," US Patent 9,517,361, Dec. 13, 2016. http://www.google.com/patents/US9517361
28. S. F. Son, T. Ombrello, and C. Carter, "Improving Efficiency and Fuel Ignition," Aerospace America, Dec. 2016, p. 58. (Invited overview article in AIAA magazine). https://aerospaceamerica.aiaa.org/year-in-review/improving-efficiency-and-fuel-ignition/
29. B. C. Terry, T. R. Sippel, M. A. Pfeil, I. E. Gunduz, and S. F. Son, "Removing Hydrochloric Acid Exhaust Products from High Performance Solid Rocket Propellant Using Aluminum-Lithium Alloy," *J. Hazardous Materials*, Vol. 317, pp. 259-266, 2016. http://dx.doi.org/10.1016/j.jhazmat.2016.05.067

30. M. A. Pfeil, A. S. Kulkarni, P. V. Ramachandran, S. F. Son, and S. D. Heister, “Solid Amine–Boranes as High-Performance and Hypergolic Hybrid Rocket Fuels,” *J. Propulsion*, Vol. 32(1), 2016. http://dx.doi.org/10.2514/1.B35591
31. S. Isert, C.D. Lane, I.E. Gunduz, and S.F. Son, “Tailored Burning Rates Using Reactive Wires in Composite Solid Rocket Propellants,” *Proceedings of the Combustion Institute*, 36 (2), pp. 2283-2290, 2017. http://dx.doi.org/10.1016/j.proci.2016.06.141
32. B. C. Terry, I. E. Gunduz, M.A. Pfeil, T.R. Sippel, and S.F. Son, “A Mechanism for Shattering Microexplosions and Dispersive Boiling Phenomena in Aluminum–Lithium Alloy Based Solid Propellant,” *Proceedings of the Combustion Institute,* 36 (2), pp. 2309-2316, 2017. http://dx.doi.org/10.1016/j.proci.2016.06.099
33. S. C. Shark, C. R. Zaseck, T. L. Pourpoint, S. F. Son, and S. D. Heister, “Performance and Flame Visualization of Dicyclopentadiene Rocket Propellants with Metal Hydride Additives,” *J. Propulsion*, Vol. 32(4), 2016. http://dx.doi.org/10.2514/1.B35853
34. S. Isert, T. D. Hedman, R. P. Lucht, S. F. Son, “Oxidizer coarse-to-fine ratio effect on microscale flame structure in a bimodal composite propellant,” *Combustion and flame*, Vol. 163, pp. 406-413 (2016). http://dx.doi.org/10.1016/j.combustflame.2015.10.015
35. N. K. Memon, A. W. McBain, S. F. Son, “Graphene Oxide/Ammonium Perchlorate Composite Material for Use in Solid Propellants,” *J. Propulsion*, Vol. 32(1), pp. 1-5 (2016). http://dx.doi.org/10.2514/1.B35815
36. T. D. Hedman, K. Y. Cho, M. A. Pfeil, A. Satija, H. C. Mongia, L. J. Groven, R. P. Lucht, and S. F. Son, “High Speed OH PLIF Applied to Multiphase Combustion (Review),” *Combustion, Explosion, and Shock Waves*, Vol. 52(1), pp. 1-13 (2016). http://dx.doi.org/10.1134/S0010508216010019
37. S. F. Son, B. C. Terry, S. Isert, T. R. Sippel, I. E. Gunduz, and L. J. Groven “Encapsulated Nanoscale Particles and Inclusions in Solid Propellant Ingredients,” p. 323 (Book Chapter) in Energetic Nanomaterials: Synthesis, Characterization, and Application, V. E. Zarko and A. A. Gromov Eds., (2016). ISBN: 978-0-12-802710-3
38. T. R. Sippel, S. F. Son, and L. J. Groven, “Mechanically Activated Metal Fuels for Energetic Material Applications,” US Patent 9,227,883 B2, Jan. 5, 2016. http://www.google.com/patents/US9227883
39. S. Isert, T. D. Hedman, R. P. Lucht, and S. F. Son, “Oxidizer coarse-to-fine ratio effect on microscale flame structure in a bimodal composite propellant,” *Combustion and Flame*, 163, pp. 406-413. (2016) http://dx.doi.org/10.1016/j.combustflame.2015.10.015
40. S. Isert, T. L. Connell, G. A. Risha, T. D. Hedman, R. P. Lucht, R. A. Yetter, and S. F. Son, “Near-surface flame structure characterization of simplified ammonium perchlorate/hydroxyl-terminated polybutadiene compositions,” Combustion and Flame, Vol. 164, p. 201–211, 2016. http://dx.doi.org/10.1016/j.combustflame.2015.11.017
41. M. A. Pfeil, J. D. Dennis, S. F. Son, S. D. Heister, T. L. Pourpoint, and P. V. Ramachandran, “Characterization of Ethylenediamine Bisborane as a Hypergolic Hybrid Rocket Fuel Additive,” *Journal of Propulsion and Power,* Vol. 31(1) pp. 365-372 (2015). dx.doi.org/10.2514/1.B35386
42. S. Isert, L. J. Groven, R. P. Lucht, and S. F. Son, “The Effect of Encapsulated Nanosized Catalysts on the Combustion of Composite Solid Propellants,” *Combustion and Flame*, 162(5), pp. 1821-1828 (2015). doi:10.1016/j.combustflame.2014.11.040

43. B. C. Terry, S. F. Son, L. J. Groven, “Altering Combustion of Silicon/Polytetrafluoroethylene with Two-Step Mechanical Activation,” *Combustion and Flame,* 162(4), pp. 1350-1357 (2015). dx.doi.org/10.1016/j.combustflame.2014.11.005
44. D. A Reese, S. F. Son, and L. J. Groven, "Composite Propellant Based on a New Nitrate Ester," *Propellants, Explosives, Pyrotechnics*, Vol. 39 (5), pp. 684-688 (2014). dx.doi.org/10.1002/prep.201300157
45. T. R. Sippel, S. F. Son, L. J. Groven, S. Zhang, and E. L. Dreizin, “Exploring Mechanisms for Agglomerate Reduction in Composite Solid Propellants with Polyethylene Inclusion Modified Aluminum,” *Combustion and Flame,* 162 (3), 846-854 (2015) dx.doi.org/10.1016/j.combustflame.2014.08.013
46. S. C. Shark, C. R. Zaseck, T. L. Pourpoint, and S. F. Son, “Solid-Fuel Regression Rates and Flame Characteristics in an Opposed Flow Burner,” *Journal of Propulsion and Power* 30 (6), pp. 1675-1682 (2014) dx.doi.org/10.2514/1.B35249
47. B. C. Terry, Y. C. Lin, K. V. Manukyan, A. S. Mukasyan, S. F. Son, and L. J. Groven, “The Effect of Silicon Powder Characteristics on the Combustion of Silicon/Teflon/Viton Nanoenergetics,” *Propellants, Explosives, Pyrotechnics* 39 (3), 337-347 (2014). dx.doi.org/10.1002/prep.201300058
48. T. R. Sippel, S. F. Son, and L. J. Groven, "Aluminum Agglomeration Reduction in a Composite Propellant Using Tailored Al/PTFE Particles," *Combustion and Flame*, Vol. 161(1), pp. 311-321 (2014). dx.doi.org/10.1016/j.combustflame.2013.08.009
49. K. Y. Cho, A. Satija, T. L. Pourpoint, S. F. Son, and R. P. Lucht, "High-Repetition-Rate Three-Dimensional OH Imaging Using Scanned Planar Laser-Induced Fluorescence System for Multiphase Combustion," *Applied Optics*, Vol. 53(3), pp. 316-326 (2014). dx.doi.org/10.1364/AO.53.000316
50. T. R. Sippel, S. F. Son, and L. J. Groven, “Altering Reactivity of Aluminum with Selective Inclusion of Polytetrafluoroethylene through Mechanical Activation,” *Propellants, Explosives, Pyrotechnics*, Vol. 38(2), pp. 286-295 (2013). dx.doi.org/10.1002/prep.201200102
51. S. C. Shark, T. L. Pourpoint, S. F. Son, and S. D. Heister, “Performance of Dicyclopentadiene/H_2O_2-Based Hybrid Rocket Motors with Metal Hydride Additives,” *Journal of Propulsion and Power*, Vol. 29(5), pp. 1122-1129 (2013). dx.doi.org/10.2514/1.B34867
52. T. D. Hedman, L. J. Groven, R. P. Lucht, S. F. Son, “The effect of polymeric binder on composite propellant flame structure investigated with 5 kHz OH PLIF,” Combustion and Flame, Vol. 160(8), pp. 1531–1540 (2013). dx.doi.org/10.1016/j.combustflame.2013.02.020
53. T. R. Sippel, S. F. Son, and L. J. Groven, “Modifying Aluminum Reactivity with Poly (Carbon Monofluoride) via Mechanical Activation,” *Propellants, Explosives, Pyrotechnics*, Vol. 38(3), pp. 321-326 (2013). dx.doi.org/10.1002/prep.201200202
54. T. D. Hedman, K. Y. Cho, L. J. Groven, R. P. Lucht, and S. F. Son, “The Diffusion Flame Structure of an Ammonium Perchlorate Based Composite Propellant at Elevated Pressures,” *Proceedings of the Combustion Institute*, Vol. 34(1), pp. 649–656, (2013). dx.doi.org/10.1016/j.proci.2012.06.171
55. T. D. Hedman, K. Y. Cho, A. Satija, L. J. Groven, R. P. Lucht, and S. F. Son, “Experimental Observation of the Flame Structure of a Bimodal Ammonium Perchlorate Composite Propellant Using 5 kHz PLIF”, *Combust. Flame*, Vol. 159(1), pp. 427-437, 2012. dx.doi.org/10.1016/j.combustflame.2011.07.007
56. T. D. Hedman, D. A. Reese, K. Y. Cho, L. J. Groven, R. P. Lucht, and S. F. Son, “An Experimental Study of the Effect of Catalysts on an Ammonium Perchlorate Based Composite

Propellant," *Combust. Flame*, Vol. 159(4), pp. 1748–1758, 2012. dx.doi.org/10.1016/j.combustflame.2011.11.014

57. M. G. Muraleedharan, A. Rohskopf, V. Yang, and A. Henry. "Phonon optimized interatomic potential for aluminum." AIP Advances 7, no. 12 (2017): 125022. https://doi.org/10.1063/1.5003158
58. M.G. Muraleedharan, D.S. Sundaram, A. Henry, and V. Yang, Thermal conductivity calculation of nano-suspensions using Green–Kubo relations with reduced artificial correlations. Journal of Physics: Condensed Matter, 29(15) (2017), p.155302. https://doi.org/10.1088/1361-648X/aa5f08
59. D. S. Sundaram, V. Yang, and R. A. Yetter. "Metal-based nanoenergetic materials: Synthesis, properties, and applications." Progress in Energy and Combustion Science 61 (2017): 293-365. https://doi.org/10.1016/j.pecs.2017.02.002
60. D.S. Sundaram, P. Puri, and V. Yang, A general theory of ignition and combustion of nano- and micron-sized aluminum particles. Combustion and Flame, 169, pp.94-109 (2016). https://doi.org/10.1016/j.combustflame.2016.04.005
61. D. S. Sundaram, V. Yang, and V. E. Zarko. "Combustion of nano aluminum particles." Combustion, Explosion, and Shock Waves 51, no. 2 (2015): 173-196. https://doi.org/10.1134/S0010508215020045
62. D. S. Sundaram, and V. Yang. "Effect of packing density on flame propagation of nickel-coated aluminum particles." Combustion and Flame 161, no. 11 (2014): 2916-2923. https://doi.org/10.1016/j.combustflame.2014.05.014
63. D. S. Sundaram, and V. Yang. "Combustion of micron-sized aluminum particle, liquid water, and hydrogen peroxide mixtures." Combustion and Flame 161, no. 9 (2014): 2469-2478. https://doi.org/10.1016/j.combustflame.2014.03.002
64. D. S. Sundaram, and V. Yang. "Effects of entrainment and agglomeration of particles on combustion of nano-aluminum and water mixtures." Combustion and Flame 161, no. 8 (2014): 2215-2217. https://doi.org/10.1016/j.combustflame.2014.01.017
65. D. S. Sundaram, P. Puri, and V. Yang. "Thermochemical behavior of nano-sized aluminum-coated nickel particles." Journal of Nanoparticle Research 16, no. 5 (2014): 2392. https://doi.org/10.1007/s11051-014-2392-4
66. G. A. Risha, T. L. Connell Jr., R. A. Yetter, D. S. Sundaram, and V. Yang. "Combustion of Frozen Nanoaluminum and Water Mixtures", Journal of Propulsion and Power, Vol. 30, No. 1 (2014), pp. 133-142. https://doi.org/10.2514/1.B34783
67. D. S. Sundaram, V. Yang, Y. Huang, G. A. Risha, and R. A. Yetter. "Effects of particle size and pressure on combustion of nano-aluminum particles and liquid water." Combustion and Flame 160, no. 10 (2013): 2251-2259. https://doi.org/10.1016/j.combustflame.2013.04.025
68. D. S. Sundaram, P. Puri, and V. Yang. "Pyrophoricity of nascent and passivated aluminum particles at nano-scales." Combustion and Flame 160, no. 9 (2013): 1870-1875. https://doi.org/10.1016/j.combustflame.2013.03.031
69. D. S. Sundaram, P. Puri, and V. Yang. "Thermochemical behavior of nickel-coated nanoaluminum particles." The Journal of Physical Chemistry C 117, no. 15 (2013): 7858-7869. https://doi.org/10.1021/jp312436j
70. D. S. Sundaram, V. Yang, T. L. Connell Jr, G. A. Risha, and R. A. Yetter. "Flame propagation of nano/micron-sized aluminum particles and ice (ALICE) mixtures." Proceedings of the Combustion Institute 34, no. 2 (2013): 2221-2228. https://doi.org/10.1016/j.proci.2012.06.129

71. K. Zhang and S. T. Thynell, “Thermal Decomposition Mechanism of Aqueous Hydroxylammonium Nitrate (HAN): Molecular Simulation and Kinetic Modeling,” The Journal of Physical Chemistry A 2018 122 (41), 8086-8100. DOI: 10.1021/acs.jpca.8b05351
72. K. Zhang and S. T. Thynell, “Examination of the Mechanism of the Yield of N_2O from Nitroxyl (HNO) in the Solution Phase by Theoretical Calculations” The Journal of Physical Chemistry A, 2017, 121 (23), 4505-4516. DOI: 10.1021/acs.jpca.7b01152
73. T. Chatterjee and S. T. Thynell, "Quantum mechanics investigation on initial decomposition of ammonia borane in glyme," International Journal of Chemical Kinetics, 2018, 50:568–581. DOI: 10.1002/kin.21183
74. N. R. Kumbhakarna, K. J. Shah, A. Chowdhury, S.T. Thynell, “Identification of liquid-phase decomposition species and reactions for guanidinium azotetrazolate,” Thermochimica Acta, Vol. 590, 2014, pp. 51-65, DOI: 10.1016/j.tca.2014.06.005.
75. N. Kumbhakarna, S.T. Thynell, “Development of a reaction mechanism for liquid-phase decomposition of guanidinium 5-amino tetrazolate,” Thermochimica Acta, Vol. 582, 2014, pp. 25-34, DOI: 10.1016/j.tca.2014.02.014
76. S.L. Row and L.J. Groven, Smart Energetics: Sensitization of the Aluminum-Fluoropolymer Reactive System, Adv. Eng. Mater. 2018, 20, 1700409. DOI: 10.1002/adem.201700409.

Manuscripts Submitted to or not yet Published by Archival Journals

1. M. G. Muraleedharan, U. Unnikrishnan, A. Henry, and V. Yang, “Flame propagation in nano-aluminum – water (nAl – H_2O) mixtures: the role of thermal interface resistance”, (under review) Combustion and Flame (2018)

Manuscripts in Preparation for Submission to Peer-Reviewed Journals

1. “Experimental and Theoretical Investigation of Enhanced Fuel Decomposition with in the Presence of Colloidal Functionalized Graphene Sheet-Supported Platinum Nanoparticles” H. S. Sim, R. A. Yetter, A. C. T. van Duin, D. M. Dabbs, I. A. Aksay.
2. “Rapid Thermolysis of *s*-Tetrazines Bound to Functionalized Graphene Sheets,” J. B. DeLisio, N. Kumbhakarna, D. M. Dabbs, I. A. Aksay, R. A. Yetter, M. Zachariah, S. T. Thynell.
3. “Unusual Rapid Decomposition Mechanism in *s*-Tetrazines Bound to Functionalized Graphene Sheets,” S. Selcuk, D. M. Dabbs, I. A. Aksay, R. Car, A. Selloni.
4. “Functionalized Graphene Sheet as a Dispersible Fuel Additive for Catalytic Decomposition of Methylcyclohexane” H. S. Sim, R. A. Yetter, A. C.T. van Duin, D. M. Dabbs, I. A. Aksay.
5. “Multifunctional Graphene-Based Additives for Enhanced Combustion of Cracked Hydrocarbon Fuels Under Supercritical Conditions” H. S. Sim, R. A. Yetter, T. L. Connell, D. M. Dabbs, I. A. Aksay.
6. “Electrical and Mechanical Properties of Poly(dimethylsiloxane) Composites Reinforced with Functionalized Graphene and Carbon Black Particles.” M. Bozlar, K. Sallah, C. Punckt, S. Korkut, M. Alifierakis, I. A. Aksay.
7. “Hydrosilylation Cross-linking in Poly(dimethylsiloxane) with Carbonaceous Fillers.” K. Sallah, I. A. Aksay.
8. G. A. Diez, T. D. Manship, B. C. Terry, I. E. Gunduz, and S. F. Son, “Characterization of an Aluminum-Lithium Alloy Based Composite Propellant at Elevated Pressures,” To be submitted to J. Propulsion.

9. M. G. Muraleedharan, K. Gordiz, S. Ju, J. Shiaomi, V. Yang, and A. Henry. “Conductance of the aluminum-aluminum oxide interface: a rigorous comparison of atomistic methods”, (in preparation) Nature Communications (2018)
10. T. Chatterjee and S. T. Thynell, “Development of Gas-Phase Reaction Mechanism for Combustion of Perchloric Acid and Ammonia Using Quantum Mechanics Calculations,” 2nd draft completed.
11. T. Chatterjee and S. T. Thynell, “Development of a Reaction Mechanism for Liquid-phase Decomposition of Ammonia Borane,” 1st draft completed.
12. K. Zhang and S. T. Thynell, “Model Development and Validation of Thermal Decomposition of Concentrated Hydroxylammonium Nitrate,” in preparation.

PRESENTATIONS

1. “Combustion of Solid Fuels and Propellants with Reactive Particles: Functionalized Graphene Sheets for Addressable Energetic Materials,” S. Selcuk, D. M. Dabbs (presenter), A. Selloni, R. Car, I. A. Aksay, M. Rehwoldt, J. B. DeLisio, M.R. Zachariah, Tri-Service Energetic Materials Basic Science Review, 23 August 2017, Arlington, VA.
2. “Propellant Design and Control: MURI12-Smart Functional Nanoenergetic Materials”, R. A. Yetter (presenter), 2017 Space Propulsion and Power Program Review, 25 May 2017, Basic Research Innovation and Collaboration Center, Arlington, VA.
3. “Smart Functional Nanoenergetic Materials: Graphene as a Reactive Material and Carrier of Energetic Materials,” I. A. Aksay, A. Selloni, R. Car, S. Selcuk, D. M. Dabbs (presenter), Tri-Service Energetic Materials Basic Science Review, 17 August 2016, Arlington, VA.
4. “Smart Functional Nanoenergetic Materials,” R. A. Yetter (PI), S. T. Thynell, M. R. Zachariah, B. E. Eichhorn, I. A. Aksay, A. Selloni, R. Car, Steve Son, V. Yang, Space Propulsion and Power Program Review, 1 October 2015, Basic Research Innovation and Collaboration Center, Arlington, VA.
5. “Smart Functional Nanoenergetic Materials,” R. A. Yetter (PI), S. T. Thynell, M. R. Zachariah, B. E. Eichhorn, I. A. Aksay, A. Selloni, R. Car, Steve Son, V. Yang, Space Propulsion and Power Program Review, 18 September 2014, Arlington, VA.
6. “Infrared Spectroscopy of Functionalized Graphene Sheets from First Principle Calculations,” C. Zhang, D.M. Dabbs, I.A. Aksay, R. Car, A. Selloni, APS Meeting Abstracts. Vol. 1. March 2014 (p. 37008).
7. “Smart Functional Nanoenergetic Materials,” R. A. Yetter (PI), S. T. Thynell, M. R. Zachariah, B. E. Eichhorn, I. A. Aksay, A. Selloni, R. Car, Steve Son, V. Yang, Space Propulsion and Power Program Review, 17 December 2013, Arlington, VA.
8. “Graphene Oxide Chemistry,” C. Zhang, A. Selloni, R. Car, D. M. Dabbs, I. A. Aksay, Partner University Fund Review, August 27 and 28, 2013, Princeton, NJ.
9. “Graphene as a Reactive Material and Carrier of Energetic Materials,” I. A. Aksay, A. Selloni, R. Car, C. Zhang, D. M. Dabbs, N. Kumbhakarna, S. T. Thynell, J. B. DeLisio, M. R. Zachariah, AFOSR MURI Review, August 21, 2013, Arlington, VA.
10. “Graphene as a Reactive Material and Carrier of Energetic Materials,” I. A. Aksay, A. Selloni, R. Car, C. Zhang, D. M. Dabbs, N. Kumbhakarna, S. T. Thynell, J. B. DeLisio, M. R. Zachariah, Partner University Fund Review, August 27 and 28, 2013, Princeton, NJ.
11. “Smart Functional Nanoenergetic Materials,” R. A. Yetter (PI), S. T. Thynell, M. R. Zachariah, B. E. Eichhorn, I. A. Aksay, A. Selloni, R. Car, Steve Son, V. Yang, Space Propulsion and Power Program Review, 13 September 2012, Arlington, VA.

12. “Graphene as a Reactive Material and Carrier of Energetic Materials,” I. A. Aksay, A. Selloni, R. Car, D. M. Dabbs, AFOSR MURI Review, August 9, 2012, Arlington, VA.
13. S. F. Son, “Inorganic Nanoenergetic Materials,” Invited presentation at Applied Physics Laboratory, Laurel, Maryland, Dec. 5, 2018.
14. S. F. Son, “Tailored and Multifunctional Propellants and Pyrotechnics,” Invited presentation at Case Western University, Cleveland, Ohio, Nov. 20, 2018.
15. S. F. Son, “Tailored and Multifunctional Propellants and Pyrotechnics,” Invited presentation at the University of Waterloo, Waterloo, Ontario, Canada, Oct. 19, 2018.
16. S. F. Son, “Rising Trends in Experimental Energetic Materials Research,” Gordon Research Conference on Energetic Materials, Discussion Leader Presentation, June 3, 2018, Grand Summit Hotel at Sunday River Newry, Maine.
17. S. F. Son, “Dynamic Measurements in Propellants and Explosives,” Purdue Energetic Materials Summit, West Lafayette, IN, May 22-24, 2017.
18. S. F. Son, “Tailoring the Ignition and Combustion of Aluminum in Propellants, Keynote lecture at Proceedings of Combustion Institute – Canadian Section Spring Technical Meeting, McGill University, Montréal, Canada, May 15-18, 2017.
19. S. F. Son, “Engineered Particles for Improved Propellants and Their Characterization,” Invited presentation at International Pyrotechnic Society, Grand Junction, CO, July 11-13, 2016.
20. S. F. Son, “Tailored Energetic Materials using Modified Aluminum and Alloys,” Invited presentation at Workshop on Pyrotechnic Combustion Mechanisms, Grand Junction, CO, July 9, 2016.
21. S. F. Son, “Overview of Energetic Materials Research at Purdue,” Invited presentation at Energetic Materials Consortium, Texas Tech, Lubbock, Texas, October 13, 2015.
22. S. F. Son, “Tailoring the Combustion of Solid Propellants,” Invited presentation at Brigham Young University, Provo, Utah, September 28, 2015.
23. S. F. Son, “Overview of Energetic Materials Research at Purdue University,” Invited presentation at Orbital-ATK, Promontory, Utah, September 25, 2015.
24. • S. F. Son, “Advanced Solid Propellants,” Invited presentation at University of Utah, Salt Lake City, September 24, 2015.
25. • S. F. Son, “Tailoring the Combustion of Solid Propellants,” Invited presentation at Utah State University, Logan, Utah, September 22, 2015.
26. S. F. Son, "High Energy Density Materials: Nanoscale Energetics,” Invited presentation at the Modern Topics in Energy and Power Technology Meeting at Army Research Lab, Aberdeen, Maryland, July 14-16, 2015.
27. S. F. Son, "Encapsulated Nanoscale Particles and Inclusions in Solid Propellant Ingredients,” Invited Seminar at the American Institute of Aeronautics & Astronautics Delaware Section Lecture Series, Elkton, Maryland, Feb. 4, 2015.
28. C. K. Murphy, B. Terry, and S. F. Son, "Altered Combustion Characteristics of Aluminum Fuels through Low-Level Fluoropolymer Inclusions with and without in situ Nanoaluminum," Purdue University, West Lafayette, Indiana, August 6, 2015. *The Summer Undergraduate Research Fellowship (SURF) Symposium.* Paper 79. http://docs.lib.purdue.edu/surf/2015/presentations/79
29. I. E. Gunduz and S. F. Son, “Flash Ignition of Mechanically Activated Al with Dielectric Inclusions,” 2014 MRS Fall Meeting & Exhibit, November 30 - December 5, 2014 Boston, Massachusetts.

30. B. C. Terry, M. D. Clemenson, L. J. Groven, and S. F. Son, “Characterization of Structural Reactives Involving Aluminum and Aluminum-Silicon Eutectic Alloy with Mechanically Activated Polymer Inclusions,” 2014 MRS Fall Meeting & Exhibit, November 30 - December 5, 2014 Boston, Massachusetts.
31. S. Isert, G. A. Risha, T.L. Connell, Jr., T. D. Hedman, R. P. Lucht, R. A. Lucht, and S. F. Son “Burning Rates and Flame Structures of Ammonium Perchlorate/Hydroxyl-terminated Polybutadiene Compositions at Various Pressures,” Spring Technical Meeting of the Central States Section of the Combustion Institute, Tulsa, Oklahoma, March 16–18, 2014.
32. B. C. Terry, M. A. Rubio, R. Ramachandran, S. F. Son, and L. J. Groven, “Altering Agglomeration in a Composite Propellant with Aluminum-Silicon Eutectic Alloy,” Spring Technical Meeting of the Central States Section of the Combustion Institute, Tulsa, Oklahoma, March 16–18, 2014.
33. S. F. Son, “High-speed OH PLIF and Imaging of Propellant Combustion,” Invited Lecture at University of Texas at El Paso, El Paso, Texas, Jan., 2014.
34. S. F. Son, “High-speed OH PLIF and Imaging of Propellant Combustion,” Invited Lecture at Iowa State University, Ames, IA, Oct., 2013.
35. S. F. Son, “Overview of Energetic Materials Research at Purdue,” Invited lecture at the U.S./France Working Group 1 Meeting at China Lake, California, Sept. 2013.
36. S. F. Son, “Playing With Fire,” Two invited classes lectures to professionals and business leaders at Mickey’s Camp http://www.mickeyscamp.com, Indianapolis, Indiana, Aug. 2013.
37. S. F. Son, “Solid Propellant Combustion Enhancement Using Fluorocarbon Inclusion Modified Aluminum,” Crane Naval Laboratory, Crane, Indiana (Aug. 2013).
38. S. F. Son, “High-speed OH PLIF and Imaging of Propellant Combustion,” Invited Plenary Lecture at the International Pyrotechnic Society Meeting in Valencia, Spain, May, 2013.
39. S. F. Son, “Tailored Energetic Material Particles,” Invited seminar for the Center for Particulates Processes and Products (CP3), Purdue University, Oct. 17, 2012, West Lafayette, Indiana.
40. M.G. Muraleedharan, D.S. Sundaram, and V. Yang, “Heat Transport in Aqueous Suspensions of Alumina Nanoparticles,” AIAA Paper 2016-0509
41. M.G. Muraleedharan, D.S. Sundaram and V. Yang, “Mechanisms of Heat Transport in Nano-Suspensions under Extreme Conditions,” International Conference on Nanoenergetic Materials and Nanoenergetics, 13-15 September 2016
42. D.S. Sundaram and V. Yang, “Heat Transfer between Nano-Aluminum and Ambient Gases,” International Conference on Nanoenergetic Materials and Nanoenergetics, 13-15 September 2016
43. K. Zhang and S. T. Thynell, “Kinetic Modeling of Thermal Decomposition of Aqueous Hydroxylammonium Nitrate (HAN),” 66th JANNAF Propulsion Meeting (JPM), Programmatic and Industrial Base Meeting (PIB), and 49th Combustion (CS), 37th Airbreathing Propulsion (APS), 37th Exhaust Plume and Signatures (EPSS), 31st Propulsion Systems Hazards (PSHS), Joint Subcommittee Meeting, 3–7 June 2019, Dayton, OH.
44. T. Chatterjee and S. T. Thynell, "Development of gas-phase reaction mechanism for ammonium perchlorate using quantum mechanics calculations," Spring Technical Meeting, Eastern States Section of the Combustion Institute, State College, PA, March 4-7, 2018.
45. K. Zhang and S. T. Thynell, "Mechanism Development of Aqueous Hydroxylammonium Nitrate under Thermal Decomposition Conditions," Spring Technical Meeting, Eastern States Section of the Combustion Institute, State College, PA, March 4-7, 2018.

46. K. Zhang and S. T. Thynell, "Ab Initio Investigation of the Nitrosation Reactions of Hydroxylamine in Aqueous Solutions," 10th National Combustion Meeting, College Park, MD, April 25, 2017.
47. S. T. Thynell, "Development of Detailed Models of Chemical Kinetics in the Condensed Phase," JANNAF Combustion Subcommittee Meeting, Newport News, VA, 4-8 December 2017.
48. K. Zhang and S. T. Thynell, "Development of a chemical reaction mechanism of hydroxyl ammonium nitrate," 2016 Spring Technical Meeting Eastern States Sections of the Combustion Institute, Princeton, NJ, March 15, 2016.
49. S. T. Thynell, "Ignition and Combustion Studies of Hydroxylammonium Nitrate," JANNAF Conference on Green Monopropellant Alternatives to Hydrazine, Huntsville, AL, August 2, 2015.
50. S. Thynell, "Experimental and QM Investigation of Decomposition and Early Chemical Kinetics of Ammonia Borane," AFRL sponsored Workshop on Boron Ignition and Combustion, Antelope, CA, January 22, 2015.

HONORS AND AWARDS (list name, award, and year during the last 6 years)

Ilhan A. Aksay, Fellow, National Academy of Inventors, 2014
Ilhan A. Aksay, Fellow, American Association for the Advancement of Science, 2012
Ilhan A. Aksay, Member, Science Academy, Turkey (2012)
S.F. Son, Purdue Bravo Award, 2014
Vigor Yang, Worcester Reed Warner Medal, ASME, 2014
Vigor Yang, Lifetime Achievement Award, JANNAF Interagency Propulsion Committee, 2014
Vigor Yang, David Weaver Best Paper Award, AIAA Thermophysics Technical Committee
Vigor Yang, Member, National Academy of Engineering (NAE), 2015
Richard A. Yetter, Fellow, ASME, 2017
Richard A. Yetter, Fellow, The Combustion Institute, 2018
Michael Zachariah, AIAA Propellants and Combustion Technical Committee Best Paper Award, 2014

PATENTS SUBMITTED

1. I. A. Aksay, K S. Sallah. Conducting elastomers, **2017**, US Patent Application 2017/0243670; August 24, 2017.
2. I. A. Aksay, V. ; Alain-Rizzo, M. Bozlar, D. J. Bozym, D. M. Dabbs, N. Szamreta, C. B. Ustundag, Electrohydrodynamically formed structures of carbonaceous material, International patent application, **2017**, WO 2017165407; March 3, 2017.
3. D. A. Reese, S. F. Son, and A. H. Yan, “Crystal Encapsulated Nanoparticles Methods and Compositions,” US Patent 9,517,361, Dec. 13, 2016. http://www.google.com/patents/US9517361
4. B. C. Terry, S.F. Son, and I. E. Gunduz, “Solid-Rocket Propellants,” Patent number 9850182, 2017.
5. T. R. Sippel, S. F. Son, and L. J. Groven, “Mechanically Activated Metal Fuels for Energetic Material Applications, US Patent 922883 B2, Jan. 5, 2016.

PATENTS AWARDED

1. S. Pan, I. A. Aksay, R. K. Prud'homme, Multifunctional graphene-silicone elastomer nanocomposite, method of making the same, and uses thereof, **2018**, US Patent 9,908,995; March 6, 2018.
2. D. A. Reese, S. F. Son, and A. H. Yan, "Crystal Encapsulated Nanoparticles Methods and Compositions," US Patent 9,517,361, Dec. 13, 2016. http://www.google.com/patents/US9517361
3. B. C. Terry, S.F. Son, and I. E. Gunduz, "Solid-Rocket Propellants," Patent number 9850182 B2, 2017. https://patentimages.storage.gooleapis.com/62/28/49/3c6860883a71ee/US9850182.pdf
4. T. R. Sippel, S. F. Son, and L. J. Groven, "Mechanically Activated Metal Fuels for Energetic Material Applications, US Patent 922883 B2, Jan. 5, 2016. https://patentimages.storage.googleapis.com/f6/5e/14/0f60487778b686/US9227883.pdf

PERSONNEL

Faculty

Bryan Eichhorn, Department of Chemistry, University of Maryland
Michael R. Zachariah, Department of Chemistry, University of Maryland
Ilhan A. Aksay, Professor, Chemical & Biological Engineering, Princeton University
Roberto Car, Professor, Chemistry, Princeton University
Annabella Selloni, Professor, Chemistry, Princeton University
Steven F. Son, Department of Mechanical Engineering, Purdue University
Robert Lucht, Department of Mechanical Engineering, Purdue University
Vigor Yang, Department of Aerospace Engineering, Georgia Institute of Technology
Stefan T. Thynell, Department of Mechanical and Nuclear Engineering, Pennsylvania State University
Richard A. Yetter, Department of Mechanical and Nuclear Engineering, Pennsylvania State University

Postdoctoral Research Associates

H. Wang, Department of Chemistry, University of Maryland
Y. Wang, Department of Chemistry, University of Maryland
Sencer Selcuk, Chemistry, Princeton University
Cui Zhang, Chemistry, Princeton University
L. Groven Department of Mechanical Engineering, Purdue University
I. E. Gunduz Department of Mechanical Engineering, Purdue University
N. Memon Department of Mechanical Engineering, Purdue University
M. Ornek Department of Mechanical Engineering, Purdue University
A. Satija Department of Mechanical Engineering, Purdue University
B. Terry, Department of Mechanical Engineering, Purdue University
Dr. Dilip Srinivas Sundaram (2013-2015), Department of Aerospace Engineering, Georgia Institute of Technology

Graduate Students

J. DeLisio, Department of Chemistry, University of Maryland
P. Guerieri, Department of Chemistry, University of Maryland
R. Jacob, Department of Chemistry, University of Maryland

L. Stevens, Department of Chemistry, University of Maryland
S. DeCarlo, Department of Chemistry, University of Maryland
D. Mayo, Department of Chemistry, University of Maryland
Michail Alifierakis, Chemical & Biological Engineering, Princeton University
Kevin Sallah, Chemical & Biological Engineering, Princeton University
Ameya Sohani, Chemical & Biological Engineering, Princeton University
Betul Uralcan, Chemical & Biological Engineering, Princeton University
G. Diez, AAE
S. Isert, AAE
D. Reese, AAE
M. Ruesch, AAE
T. Sippel, Department of Mechanical Engineering, Purdue University
B. Terry, Department of Mechanical Engineering, Purdue University
K. Y. Cho, Department of Mechanical Engineering, Purdue University
H. Belal, Department of Mechanical Engineering, Purdue University
Murali Gopal Muraleedharan (2013-2018), Department of Aerospace Engineering, Georgia Institute of Technology
N. Kumbhakarna, Mechanical and Nuclear Engineering, Pennsylvania State University
K. Zhang, Mechanical and Nuclear Engineering, Pennsylvania State University
T. Chatterjee, Mechanical and Nuclear Engineering, Pennsylvania State University

Undergraduate Students

Priyanka Goyal (‘16), Chemical & Biological Engineering, Princeton University
Amy Xie (‘17), Chemical & Biological Engineering, Princeton University
Allyson Brown (‘18), Chemical & Biological Engineering, Princeton University
Stephen Wong (‘19), Chemical & Biological Engineering, Princeton University
J. Ruesch, Department of Mechanical Engineering, Purdue University
C. K. Murphy, Department of Mechanical Engineering, Purdue University
C.D. Lane, Department of Mechanical Engineering, Purdue University

Other Personnel

Daniel M. Dabbs, Research Scientist, Chemical & Biological Engineering, Princeton University
Cem Ustundag, Visiting Scientist, Yildiz Technical University, Istanbul, Turkey
T. Manship, Research Engineer, Department of Mechanical Engineering, Purdue University

Collaborators

G. Young, NSWC-IH
J. Hooper – Naval Post-Grad school
K. Bowen JHU
D. Mayo - NSWC-IH
Valerie Alain-Rizzo, Visiting Scientist, Vorbeck Materials
Pierre Audebert, Professor, ENS Cachan, France
Michael Bozlar, Visiting Scientist, Vorbeck Materials
Laurent Galmiche, Scientist, ENS Cachan, France
Yifei M. Liu, Professor, University of California, Berkeley
Fabien Miomandre, Professor, ENS Cachan, France
Michael A. Pope, Professor, University of Waterloo, Ontario, Canada
Jean-Herve Prevost, Civil and Environmental Engineering, Princeton University

Christian Punckt, Associate Director, Institute of Nanotechnology, Karlsruhe Institute of Technology, Germany
Prof. Asegun Henry (Associate Professor, Mechanical Engineering, MIT)

DEGREES AWARDED

J. DeLisio – PhD, 2017, University of Maryland
P. Guerieri – PhD, 2017, University of Maryland
R. Jacob - – PhD, 2018, University of Maryland
S. DeCarlo -- PhD, 2016, University of Maryland
D. Mayo -- PhD, 2014, University of Maryland
L. Stevens -- PhD, 2018, University of Maryland
Michail Alifierakis, Ph.D., Chemical and Biological Engineering, June 2018, Princeton University
Kevin Sallah, Ph.D., Chemical and Biological Engineering, June 2016, Princeton University
David J. Bozym, Ph.D., Chemical and Biological Engineering, June 2015, Princeton University
G. Diez, M.S., May 2018, Purdue University
H. Belal, Ph.D. Aug. 2017, Purdue University
B. C. Terry, Ph.D., Aug. 2015, Purdue University
I. Sert, Ph.D., Dec. 2015, Purdue University
D. Reese, Ph.D., May, 2014, Purdue University
T. Sippel, Ph.D., Aug. 2013, Purdue University
K. Y. Cho, Ph.D., May, 2014, Purdue University
Murali Gopal Muraleedharan, PhD in Aerospace Engineering, December 14, 2018
N. Kumbhakarna, Ph.D. in Mechanical Engineering, May 15, 2014 (now assistant professor of mechanical engineering at IIT Bombay), Pennsylvania State University
K. Zhang, Ph.D. in Mechanical Engineering, May 15, 2019, Pennsylvania State University
T. Chatterjee, Ph.D. in Mechanical Engineering, May 15, 2020, Pennsylvania State University

TECHNOLOGY TRANSFER

"A Method for the Covalent Functionalization and Bridging of Graphene Oxide Sheets" joint disclosure between Ecole Normale Supérieure de Cachan (France) and Princeton University, provisional patent application filed by Princeton University (2016).

Adranos Energetics LLC (start-up company) formed by Dr. Brandon Terry who worked on this project as a Ph.D. and Postdoc. This company aims to develop some of the technology discovered from this project. References: HTTP://ADRANOSENERGETICS.COM, HTTP://NVC.UOREGON.EDU/ADRANOS-ENERGETICS-LLC/, HTTPS://ENGINEERING.PURDUE.EDU/ZUCROW/NEWS/ADRANOS-ENERGETICS-FEATURED-ON-INSIDE-INDIANA-BUSINESS, HTTPS://WWW.YOUTUBE.COM/WATCH?V=QYAQAZSNHQA

Ammonia borane decomposition mechanism provided to AFRL researchers.

INTRODUCTION

Given the constraints on typical bond energies and the commonality of final products produced from combustion of C-H-N-O-Cl-Al based energetic materials, the possibilities for increased stored potential energy and increased thermodynamic performance from these classes of materials are limited. Methods to increase the specific impulse (as well as the density specific impulse) either through the development of new propellants or by reducing the losses of current propellants are significant goals. An increase of several seconds in I_{sp} is considered an important achievement. In the present effort, our goal was to study hierarchically structured nanocomposite energetic materials that could be additives or replacements of fuel particles in current or future propellant formulations. Our interest in nanoenergetic composites arises from previous successes and limitations of adding nanoparticles to propellants as a means of improving performance.

While the introduction of nanosized fuel and oxidizer particles into solid propellants has provided significant benefits in increasing burning rates and reducing agglomeration, there are two major constraints that have limited further investigation, characterization, and implementation of nanomaterials: (i) Their nanometer scale dimensions and the inherently high surface areas reduce their usability, e.g., similar solids loading cannot be achieved, and (ii) Particle-particle interactions dominate making dispersion of such particles nearly impossible. Thus, in order to realize the benefits of nanoparticles in future propellants, new approaches must be undertaken.

The objectives of the *Smart Functional Nanoenergetic Materials* MURI were to:

- Develop new macroscale (micron-sized or larger) energetic materials with nanoscale features that provide improved performance and ease of processing and handling, managed energy release, reduced sensitivity, and potential for internal/external control and actuation.
- Obtain fundamental understanding of the relationship between the integrated multi-length scale design and reactive and mechanical behaviors.

The successful development of multiscale nanoengineered energetic materials may also provide a means to unravel and control the strong correlation that exists between the energy density of a propellant (or explosive) and its sensitivity. In addition to Isp, the addition of nanostructured additives has been shown in the literature to decrease agglomeration/slag and increase combustion efficiency. In some cases, the measured Isp increased by up to 8%, in large part due to the increased combustion efficiency. Because of relatively higher burning rates at lower pressures with nanostructured particles, it was shown that controlling pressure exponents of propellants is possible. In addition to performance gains, integrating other functionality can also be game-changing.

From a materials design perspective much is yet to be gained in the actual performance, multi functionality, and controllability of energetic materials. We recognized that many biological and physical objects derive their unique properties through an integrated multilength scale organization of their constituent nano and microscale structures. A common feature in all these structures is that nanoscale units are all integrated into micron to macro scale structures and are accessible as individual modules for rapid response, usually through the use of porous structures. Such design principles were crucial to the goals of the present work.

The program was divided into four major inter-related areas as outlined in Figure 1: (a) processing of nanoenergetic materials with graphene and metal nanoclusters, (b) multiscale processing to enable the insertion of nanoenergetic matarials into larger units such as graphene sponge, (c) atomistic to mesoscale modeling and design, and (d) experimental analysis and performance characterization for propulsion.

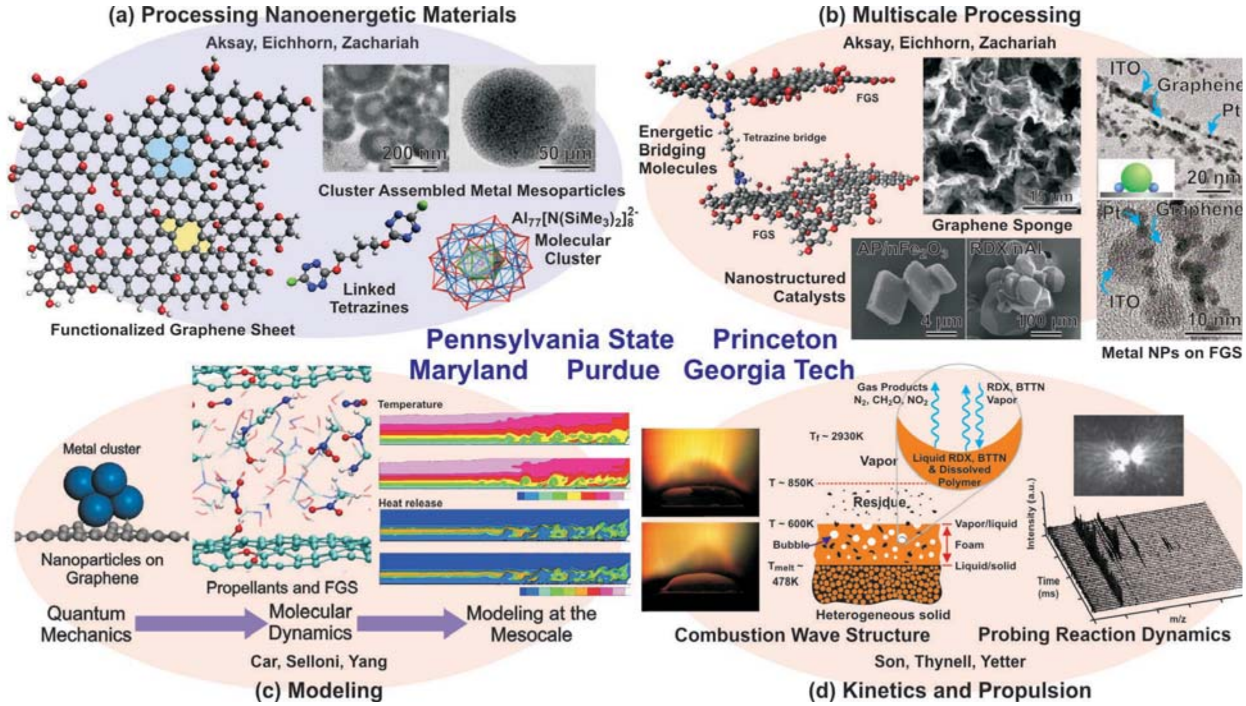

Figure 1: Overview of the proposed research. (a) The energetics of FGSs will be boosted through the addition of nitrogen such as tetrazine-based molecules. Molecular clusters such as the $Al_{77}[N(SiMe_3)_2]_{20}^{2-}$ cluster shown will be used to further boost the energetics of C-H-N-O materials. These can be grouped into cluster assembled metal mesoparticles to further stabilize and desensitize the cluster until needed. (b) Cluster composites and metal nanoparticles will be dispersed on graphene sheets for further stability and to provide a fuel source in proximity to energetic or catalytic particles. The graphene sheets themselves will be linked together to form high surface area matrices; linkages will be energetic molecules of high nitrogen content. (c) The reactions of energetic materials range across length scales, requiring modeling efforts that combine QM and MD simulations to provide information on mechanisms observed at the mesoscale. (d) Characterization techniques will be developed for measurements on the micro- and meso-scales.

SOME OF THE SIGNIFICANT SCIENTIFIC ACCOMPLISHMENTS

Some of the more significant accomplishments from this program include:

1. Compounds of covalently linked tetrazines and functionalized graphene sheets (FGSs) were made (FGS-Tz) using a nucleophilic substitution reaction that permits the synthesis of a wide variety of such materials. Nanoconfinement results from the self-assembly of the tetrazines and FGSs into a multilayered structure of tetrazine molecules held between graphene sheets, a structure imposed by the covalent binding of tetrazines to the FGSs. Molecular dynamic models, combined with characterization of the products of decomposition from the rapid heating of the FGS-Tz, revealed that confining the tetrazines within nanoscale volumes — defined by the spaces between the graphene sheets —plays a principal role in the accelerated and the higher degree of tetrazine decomposition. Reactive, vapor phase products are held in confinement until overpressure separates the graphene

oxide sheets. In contrast, no significant decomposition is observed under slow heating, indicating that tetrazine acts as an unconfined molecule under these conditions. Thus, covalent bonds are necessary but not sufficient to account for both increased rate of decomposition and small molecule production. Under rapid heating rates, >10^5 K/s, both the rate and degree of tetrazine decomposition is significantly increased. Production of molecular nitrogen increases, larger molecular weight compounds suppressed.

2. In addition to molecular tetrazine spacers, carbonaceous nanoparticles have been fabricated and dispersed across FGSs, maintaining the separation between sheets and allowing the incorporation of active molecules for energetic and electrochemical applications.
3. FGSs impart higher electrical conductivity to polymeric resins but result in decreased mechanical flexibility. Tetrazine linking agents may improve both electrical conductivity and flexibility through enhanced connectivity in the FGS network, but this was not tested as of the time of this report.
4. Development of an assembly method to create a new class of nanostructured mesoparticle containing fuel/oxidizer, and gas generating binder. Assembling nanoparticles into a microparticle with an embedded gas generator has been demonstrated unambiguously to lead to enhanced combustion performance, a more consistent burn from particle–to-particle, and mesoparticles that burn like independent aluminum nanoparticles. These benefits result largely from reduced sintering of the nanoparticles within the mesoparticle structure and internal gas generation provided by the interstitial binder. Direct deposition (printing) of mesoparticles was demonstrated to enable solid composites with arbitrary architecture (laminates, fiber reinforcement, etc.).
5. Development of molecular clusters of aluminum. These materials were used as additives in liquid fuels showing enhanced burning rates. These clusters were also mixed with oxidizer in a polymer matrix and combustion properties evaluated.
6. Fabrication and characterization of nanoscale inclusion materials in micron sized aluminum have been developed and characterized. These materials have been sent to many research groups for characterization and study, and significant follow-on research is pursuing our approach to tailor metals for improved ignition and combustion. Single particle laser ignition experiments were performed of composite particles and showed what conditions are necessary for microexplosions.
7. The replacement of aluminum with aluminum-lithium alloy in a composite propellant drastically reduces the formation of HCl in the products. Such alloys burn much like multicomponent liquid fuels with microexplosions. In addition, theoretical performance can be increased by about six seconds and since fewer condensed phase products are formed and much smaller products (including nanoscale particles) are formed due to droplet microexplosions, two phase flow losses are expected to decrease. In addition, a start-up company (Adranos Energetics) is pursuing the development of this technology for significantly improved performance and cleaner exhaust products. Adranos has shown significant improved performance over a baseline aluminumized propellent in small scale motor testing.
8. Metal wires have been used to increase burning rates for decades. To significantly extend the range of achievable burning rates, nanoscale composite wires/foils have been developed to obtain rates never achieved before. Importantly, the wire that we developed breaks up into small product particles in contrast to other wires that form large slag

products. This opens-up the possibility of fully loaded rocket motors (no center perforation), especially if this is coupled with additive manufacturing.

9. Encapsulated catalysts, including decorated graphene oxide, in ammonium perchlorate (AP) crystals have been synthesized and their performance and flame structure in propellants characterized. The characterization used included in situ high speed OH PLIF imaging that was also developed, in part, by this funding.
10. Piezo-reactive materials were developed for potential control of energetic material sensitivity where it was demonstrated that fluoropolymer films with aluminum inclusions store a charge when a force is applied. The piezoelectric polymer/nanoscale aluminum system is highly sensitizable with the application of a DC voltage, lowering the impact energy needed from 63J to 10 J. All solvent soluble fluoropolymer systems investigated with nanoscale aluminum exhibit this ability to be sensitized. Increasing the application voltage is shown to directly correlate to an increase in sensitivity.
11. Experiments and simulations were used to demonstrate that decorating functionalized graphene sheets (FGSs) with platinum nanoparticles (Pt@FGS) stabilized these particles. Addition of these particles to liquid hydrocarbon fuels was observed to enhance decomposition under supercritical conditions. ReaxFF molecular dynamics (MD) simulations supported a mechanism in which synergy between Pt and FGS catalyzed dehydrogenation during n-$C_{12}H_{26}$ pyrolysis. The highest conversion rates and greatest yields of hydrogen and low molecular weight species were observed for fuels containing Pt@FGS particles rather than those containing either FGSs or Pt clusters alone. Analysis of the platinum decorated FGSs post reaction indicated no deterioration of the composite particles.
12. Small quantities (100 ppmw) of graphene with and without the surface decorated with Pt nanoparticles were shown to accelerate the supercritical combustion of dodecane (enhancing the rate by 30%). Enhancement with Pt decorated graphene was shown both experimentally and theoretically to be greater than either Pt nanoparticle or FGS alone due to synergism between the graphene and Pt surface in lowering the H atom desorption activation energy from the surface.
13. A bottom-up approach was followed to obtain a multiscale model of conductive heat transport in an energetic nano-suspension. Equilibrium molecular dynamics (EMD) simulations were performed to investigate the effect of particle volume fraction, particle size, interfacial bonding strength, temperature, and pressure on the thermal conductivity of single and multi-particle nano-suspensions.
14. Non-equilibrium molecular dynamics (NEMD) simulations were employed to study interfaces: behavior of interfacial conductance, and the effect of various parameters on it. Two interfaces were considered: Al_2O_3-H_2O, and Al-Al_2O_3. On the basis of the explored nanoscale physics, a theoretical model for the effective thermal conductivity of energetic nanomaterials was developed.
15. Nanoscale heat transfer effects were studied for the combustion of nAl-H2O suspensions: the role of size-effects on thermal conductivity, thermal interface resistance, Brownian motion and nanolayering on heat conduction was studied.
16. A heat conduction perspective to flame propagation in nanoenergetic materials was provided: the results of which shed light into the design of novel nanoenergetic materials from first principles with advanced burning properties.
17. Initiation of thermal decomposition of ammonium perchlorate has been identified as the formation of the hydroxylammonium cation. That is, migration of oxygen from the

perchlorate anion occurs which results in the early evolution of nitric acid (HNO_3) and nitrogen dioxide (NO_2).

18. The catalytic effects of iron oxide on hydroxylammonium decomposition have been proposed but not validated experimentally.
19. The chemical kinetic details of hydroxylammonium nitrate decomposition and ammonia borane have been represented by reaction mechanisms and validated experimentally.

REPORT ORGANIZATION

The organization of this report is as follows. First, the synthesis and characterization of nanostructured composite particles based on functionalized graphene sheets, followed by composites of aluminum with various interstitial materials, are discussed. Aluminum clusters are included in this discussion. Then a discussion on the fabrication and combustion analysis of solid and liquid fuels and propellants with nanostructured additives is presented. Finally, results on the analysis of energy transfer in nanoparticle laden flows, and on the chemical kinetics of some energetic materials important to the understanding of combustion of these fuels and propellants are described.

FGS-TETRAZINE COMPOUNDS

D. M. Dabbs and I. A. Aksay, Princeton, in collaboration with researchers at the Ecole Normale Supérieure de Cachan, France

We raise the nitrogen content of functionalized graphene sheets (FGSs) via the chemisorption of high-nitrogen content molecules [1]. Such modified FGSs, while less inherently energetic than nitrogen-doped graphene, have the advantage of requiring little or no further processing for use in propellants. We determined that in the decomposition of tetrazines bound to the FGSs, covalent functionalization is insufficient to explain the more rapid and higher degree of tetrazine decomposition in the bound molecules compared to the pure tetrazine, when samples were subjected to very rapid heating (~ 10^5 K/s). We found that the enhanced decomposition of bound tetrazines is caused by the binding of tetrazine-containing molecules to separated graphene sheets leading to the self-assembly of the linked tetrazines and FGSs into a multilayer, stacked compound in which the tetrazines are now confined between the graphene sheets.

For the combustion of liquid hydrocarbon fuels and monopropellants, FGS is known to act as an effective carbocatalyst [2-4] and as a carrier for reactive and catalytic nanoparticles, but a similar benefit for the addition of FGS-Tz compounds to fuels and propellants has not yet been demonstrated. The initial efforts to incorporate FGS-Tz compounds in combustion studies were hindered by the difficulty in dispersing and maintaining the dispersion of the FGS-Tz compounds in liquid fuels (such as dodecane) or solid matrices. Since the micrometer-scale planar dimensions of the FGSs [5] appeared to hinder effective dispersion, focus shifted to the tetrazine functionalization of “nano-graphene oxide” (sheets with maximum lateral dimensions of ~50 nm) [6], which had the desired effect of improving dispersibility and dispersion stability, but the effect on fuels has not been tested at the time of this report.

FGS-Tz compounds are also of interest as components of printable energetic materials to be incorporated into addressable energetic devices, using methods we are developing to synthesize and pattern FGS-based conductive inks. Such inks are used, for example, to print flexible electronic circuits. In the last year of the project, we incorporated FGS-Tz compounds into printable, conductive inks that may eventually be combined with other energetic materials to demonstrate the utility of energetic devices, such as igniters, that do not include metal or metal oxide nanoparticles. For, example, carbonaceous nanoparticle spacers are used to maintain the separation between separate sheets, allowing for the incorporation of active molecules, such as ionic liquids,

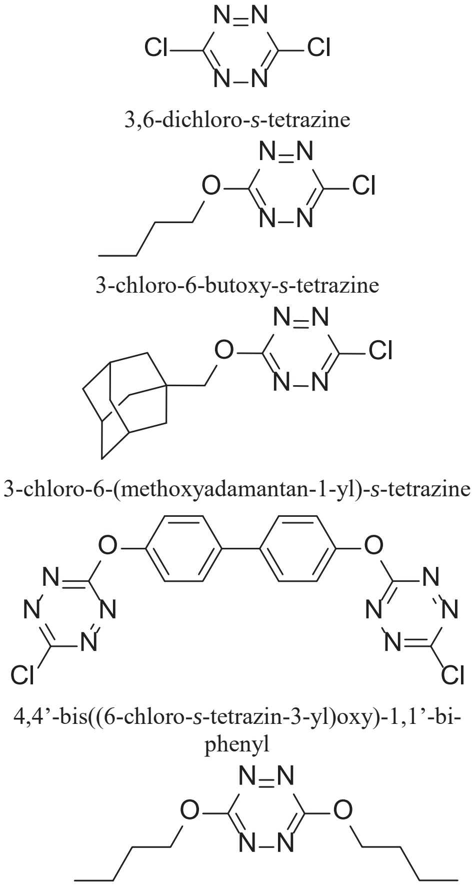

Tz1 3,6-dichloro-*s*-tetrazine

Tz2 3-chloro-6-butoxy-*s*-tetrazine

Tz3 3-chloro-6-(methoxyadamantan-1-yl)-*s*-tetrazine

Tz4 4,4’-bis((6-chloro-*s*-tetrazin-3-yl)oxy)-1,1’-biphenyl

Tz6 3,6-dibutoxy-*s*-tetrazine

Figure 2: Substituted tetrazines synthesized for this study. The disubstituted tetrazine (**Tz6**) was synthesized for comparison but was not expected to react with $\mathbf{FGS_2}$.

Table 1: Phase transitions in pure tetrazines; under streaming nitrogen.

zine	Melting point (°C)	Onset of vaporization (°C)	Onset of decomposition (°C)	Residual mas °C
:1		130 (sublimes)		
:2	44	145	n/a	< 1%
:3	123	226	n/a	< 1%

between graphene sheets. As described below, our studies combined experimental and modeling efforts in the incorporation of modified FGSs into elastomeric matrices similar to compositions that would be used to pattern components, attempting to define those factors that increase the dispersion and dispersion stability of FGS in different matrices, while seeking to improve the structural and electrochemical properties of the resulting composite material.

Tetrazine synthesis

Tetrazines [7] and tetrazoles [8] are classes of high-nitrogen content, aromatic ring molecules (Fig. 1), of interest as energetic materials due to the rapid generation of molecular nitrogen during combustion coupled with very fast burning rates [9]. Our interest lies in using these energetic materials not only to boost the energetics of the proposed nanocomposite but also to serve as processing aids, such as dispersants to aid in the formulation of stable, intermediate suspensions of FGS-Tz compounds, and as energetic bridges between sheets to use as scaffolding for energetic nanocomposites. The use of these inherently energetic materials in conjunction with the high surface area FGS (which may also act as a potential carbocatalyst) provides a method for producing a highly energetic sponge-like material.

Starting with 3,6-dichloro-*s*-tetrazine (**Tz1**), we synthesized 3-chloro-6-butoxy-*s*-tetrazine (**Tz2**), 3-chloro-6-(methoxyadamantan-1-yl)-*s*-tetrazine (**Tz3**) and the linked *bis*-tetrazine compound 4,4’-bis((6-chloro-*s*-tetrazin-3-yl)oxy)-1,1’-biphenyl (**Tz4**) (Fig. 2) [10]. As synthesized, the tetrazines are intrinsically volatile, requiring large substituent groups to stabilize the molecule up to its decomposition temperature (Table 1 and Fig. 3). These tetrazine derivatives are versatile compounds that react by nucleophilic substitution at the hydroxyl groups present on **FGS$_2$** [11].

The general procedures used to first synthesize and then graft the substituted chlorotetrazines onto **FGS$_2$** are shown in Scheme 1. 3,6-dichloro-*s*-tetrazine (**Tz1**) is a versatile precursor for preparing a wide variety of substituted tetrazines through the displacement of a chlorine atom by a nucleophile such as an alcohol, thiol, or amine [7]. Monosubstitution readily proceeds at room temperature, with yields of up to 90% of the theoretical yield based on the stoichiometry of the reaction shown in Scheme 1 [7]. For the *bis*-tetrazine compounds (**Tz4**, Fig. 2), two substitution reactions occur at opposite ends of the molecule. Elemental analysis (Table 2) reveals that the chlorine content of the **FGS-Tz** compounds is much higher than that of the **FGS$_2$** alone; the residual chlorine detected in the unmodified **FGS$_2$** a result of the process used to synthesize **FGS$_2$** from graphite [12-13].

Characterization of FGS2, tetrazines, and FGS-Tz compounds

Covalent links between the electroactive tetrazine and the FGSs were verified using electrochemistry, X-ray photoelectron spectroscopy (XPS), thermal analysis (TA) and Fourier transform infrared (FTIR) spectroscopy. The **FGS$_2$** is readily dispersed in propylene carbonate (PC) [14] which facilitates the reaction between the **FGS$_2$** and monosubstituted tetrazines (Scheme 1). The different **FGS-Tz** compounds remain dispersed in PC and the highly colored tetrazine substituents are revealed by changes in the color and opacity of the suspension. Cyclic voltammetry reveals shifts in the redox potentials of the tetrazine as a result of replacing chlorine atoms with oxygen linkages to the graphene sheets. XPS measurements reveal changes in the ratio of carbon hybridization in the FGS and the presence of an oxygen atom shared between the tetrazine ring and the FGS, as well as providing elemental analysis of the compounds’ composition. TA confirms the amount of tetrazine grafted on the FGS indicated by XPS. FTIR reveals that a close association exists between the tetrazine and the FGS that cannot be removed by washing with solvent.

Cyclic voltammetry

The effect of alkoxy substitution on the electrochemistry of substituted tetrazine derivatives in solution is visible in the cyclic voltammograms (CVs) of tetrazines (**Tz1**, **Tz2**, **Tz4**, and **Tz6**), unmodified **FGS$_2$**, and the grafted **FGS-Tz** compounds (Fig. 4). A gradual and significant shift in the reduction potential to more negative values is clearly observed as each chlorine atom is successively replaced by an alkoxy group, an effect demonstrated using mono- and disubstituted tetrazines (Fig. 4(a)). The sequential shift is a result of the less electron withdrawing effect of the -OR group relative to that of a chlorine atom [10]. In Figure 4(b-d), we display the CVs of suspensions of various **FGS-Tz** compounds after re-dispersing the material in PC-based electrolyte using ultrasonication. For comparison, the CVs of the tetrazine precursors **Tz1**, **Tz2**, **Tz4**, and the unmodified **FGS$_2$** measured under the same experimental conditions are superimposed on that of the related **FGS-Tz** compound. It was found that **FGS-Tz1** compounds could not be synthesized under the conditions shown in Scheme 1 as the more reactive dichloro-compound readily reacted with other constituents of the reaction mixture. The mechanism of this undesirable side-reaction has not been determined. In the other **FGS-Tz** compounds, there was no detectable signal that could be connected to the presence of unreacted tetrazine.

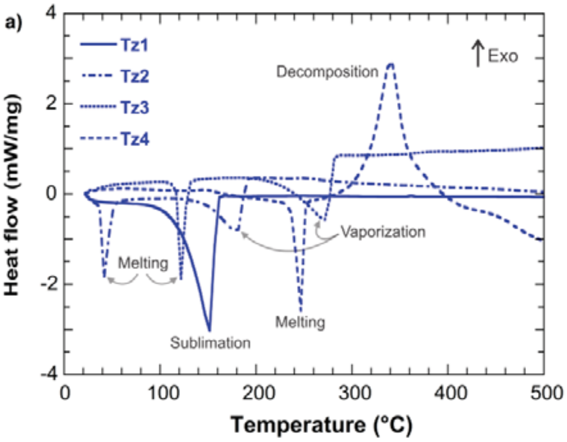

Figure 3: Phase changes in the pure tetrazines as determined by differential scanning calorimetry. Samples were heated at 5 °C/min under a streaming nitrogen atmosphere. The samples were in a loosely-lidded sample holder, which permitted vapor to escape before decomposition. Of the tetrazines tested, only Tz4 had sufficiently high mass to decompose before vaporization.

Scheme 1: General synthetic route leading to the grafting of substituted chlorotetrazines to FGS.

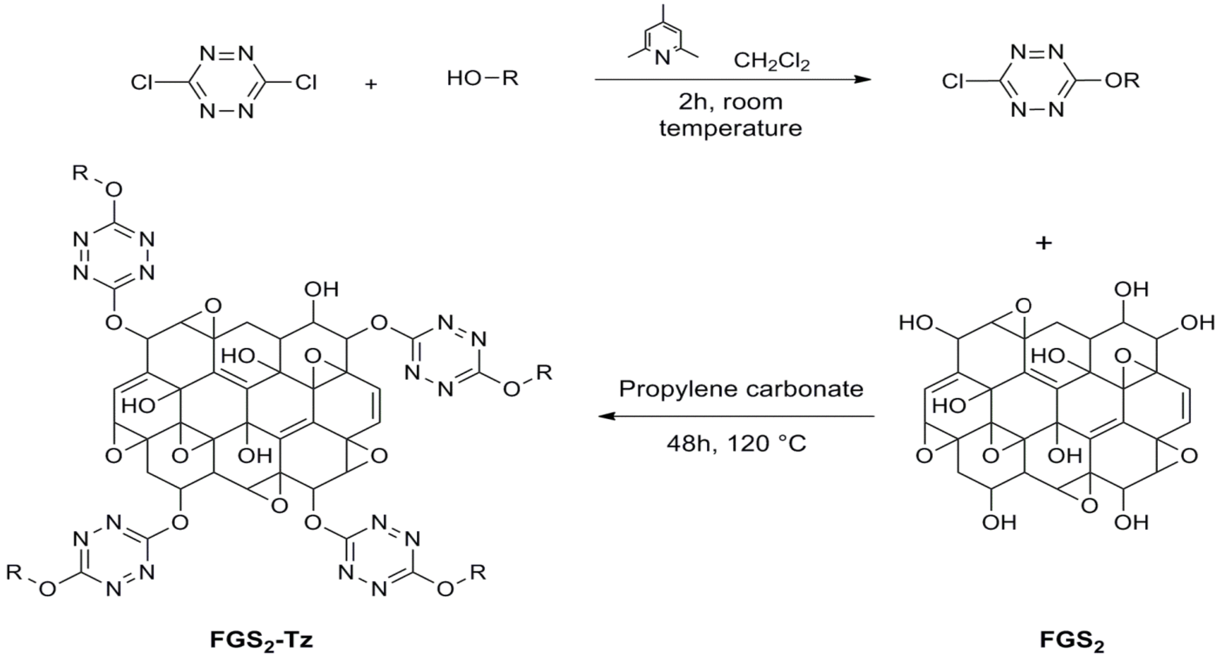

The reduction of the tetrazine core in all **FGS-Tz** compounds is noticeably more difficult (i.e., occurs at lower reduction potentials) than in the precursor tetrazine. This is attributed to the substitution reaction that replaced the electron withdrawing chlorine atom by a more electron donating alkoxy group provided by the hydroxyl groups on the **FGS$_2$**. Moreover, the CVs of the **FGS-Tz** compounds combine the features of the unmodified **FGS$_2$** with the corresponding dialkoxy-tetrazine, as shown in Fig. 4(c) which compares the CVs of the unmodified **FGS$_2$** with that of the disubstituted **Tz6**. From an electrochemical point of view, the electronic environment of the tetrazine core in **Tz6** is similar to the one in **FGS-Tz2** (with two alkoxy groups substituting on the

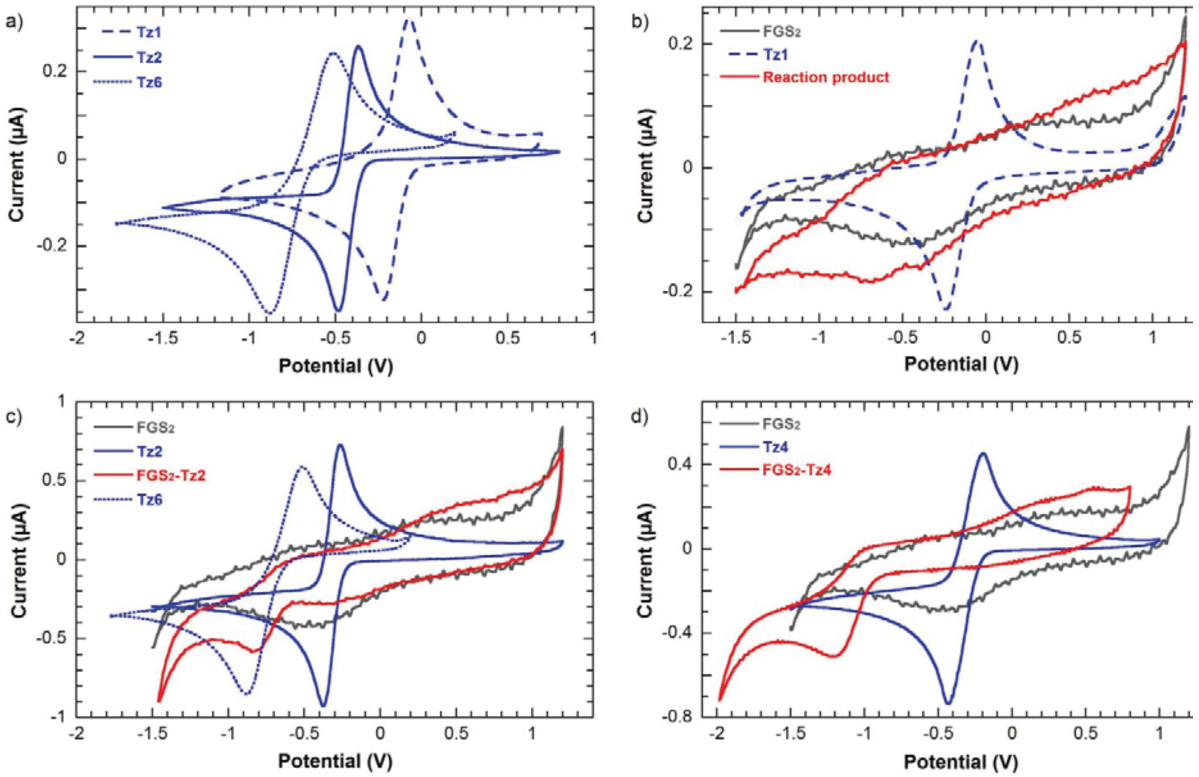

Figure 4: (a) CVs of 3,6-dichloro-*s*-tetrazine (**Tz1**) (blue dashed line), 3-chloro-6-butoxy-*s*-tetrazine (**Tz2**) (blue solid line) and 3,6-dibutoxy-*s*-tetrazine (**Tz6**) (blue dotted line). (b) CVs of **Tz1** (blue dashed line), unmodified **FGS$_2$** (gray) and the solid component of the product from the attempted reaction between **Tz1** and **FGS$_2$** (red). For the latter, there is no evidence that **Tz1** is present, and the resulting CV resembles that of the unmodified **FGS$_2$**. (c) CVs of **Tz2** (solid blue line), unmodified **FGS$_2$** (gray), grafted **FGS$_2$-Tz2** (red) and **Tz6** (blue dashed line). (d) CVs of 4,4'-bis((6-chloro-*s*-tetrazin-3-yl)oxy)-1,1'-biphenyl **Tz4** (solid blue line), unmodified **FGS$_2$** (gray) and grafted **FGS$_2$-Tz4** (red). Each CV was made using suspensions or solutions in propylene carbonate (with 0.1M TBAPF$_6$ as the electrolyte) against a platinum electrode.

tetrazine core) and is very different from the CV for the monosubstituted precursor **Tz2**. The CVs in Fig. 4c exactly reflect the same similarity and difference when the peak positions are compared. Thus, the CVs offer clear evidence that covalent linkage between tetrazine and oxidized graphene through substitution of chlorine by oxygen has been achieved.

X-ray photoelectron spectroscopy

The XPS spectrum of unmodified FGS2 is simple, with strong O(1s) and C(1s) bands and much weaker Cl(2p) (Fig. 5(a)). After grafting by tetrazine derivatives, the most striking feature in the XPS spectra of the **FGS-Tz** compounds is the appearance of a new signal corresponding to N(1s) near 400 eV (Fig. 5(b, c, and d)). Also worth mentioning is the increase in the amount of carbon and the decrease in the oxygen content (Fig. 4, Table 2) associated with the addition of the tetrazine moiety to the FGS. A slightly larger amount of chlorine Cl(2p) (≅ 0.8 ± 0.2%) is visible in **FGS-**

Table 2: Elemental composition of **FGS-Tz** compounds as determined by X-ray photoelectron spectroscopy.

	FGS$_2$	**FGS-Tz2**	**FGS-Tz3**	**FGS-Tz4**
%C	67.5	71.0	79.8	70.2
%N	0.0	12.1	5.8	18.0
%O	31.8	16.4	13.9	10.7
%Cl	0.28	0.50	0.37	0.8

Tz4, possibly indicating that a small amount of the *bis*-tetrazine only reacted at one end, leaving one chlorine on the unbound end of the molecule. These features are consistent with a highly energetic interaction between graphene oxide and tetrazine, in which the chlorine atoms in the tetrazine precursors have been replaced by oxygens in the **FGS$_2$-Tz**

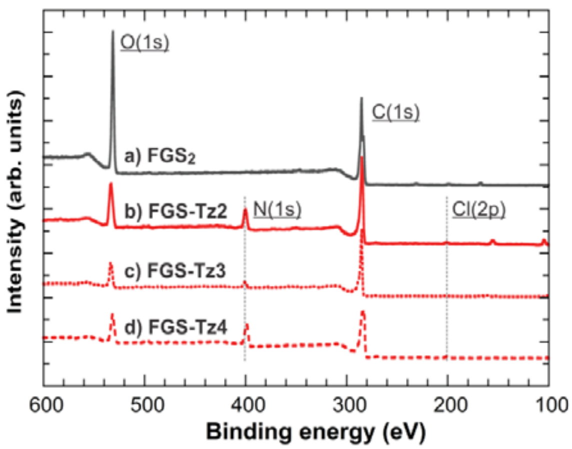

Figure 5: XPS spectra of (a) unmodified **FGS$_2$**, (b) **FGS-Tz2**, (c) **FGS-Tz3**, and (d) **FGS-Tz4**.

When comparing the details of the different elemental signals in the unmodified **FGS$_2$** (Fig. 6(a,b)), and an **FGS-Tz** (Figs 6(c,d,e)) it is first apparent that in the unmodified **FGS$_2$** (i) the C(1s) signal can be decomposed into three main contributions (Fig. 6(a)), underlining the presence of at least 5 types of carbon bonds: sp^2 aromatic and sp^3 carbons (284.5 eV), **C**-O-C epoxy ring and **C**-OH (286.5 eV), **C**=O and O-**C**=O (288.2 eV) while (ii) the O(1s) signal contains a main signal centered at 532.3 eV and divided into two contributions (Fig. 6(b)) [15-17]. After chemical grafting, in the **FGS-Tz**s the C-C (sp^2/sp^3) component in the C(1s) core level spectra becomes dominant by comparison with unmodified **FGS$_2$** (Figs. 6(c)). New contributions appear in the C(1s) spectrum of the **FGS-Tz**, presented here in the spectra for the representative **FGS-Tz2** compound (Fig. 6(c)).

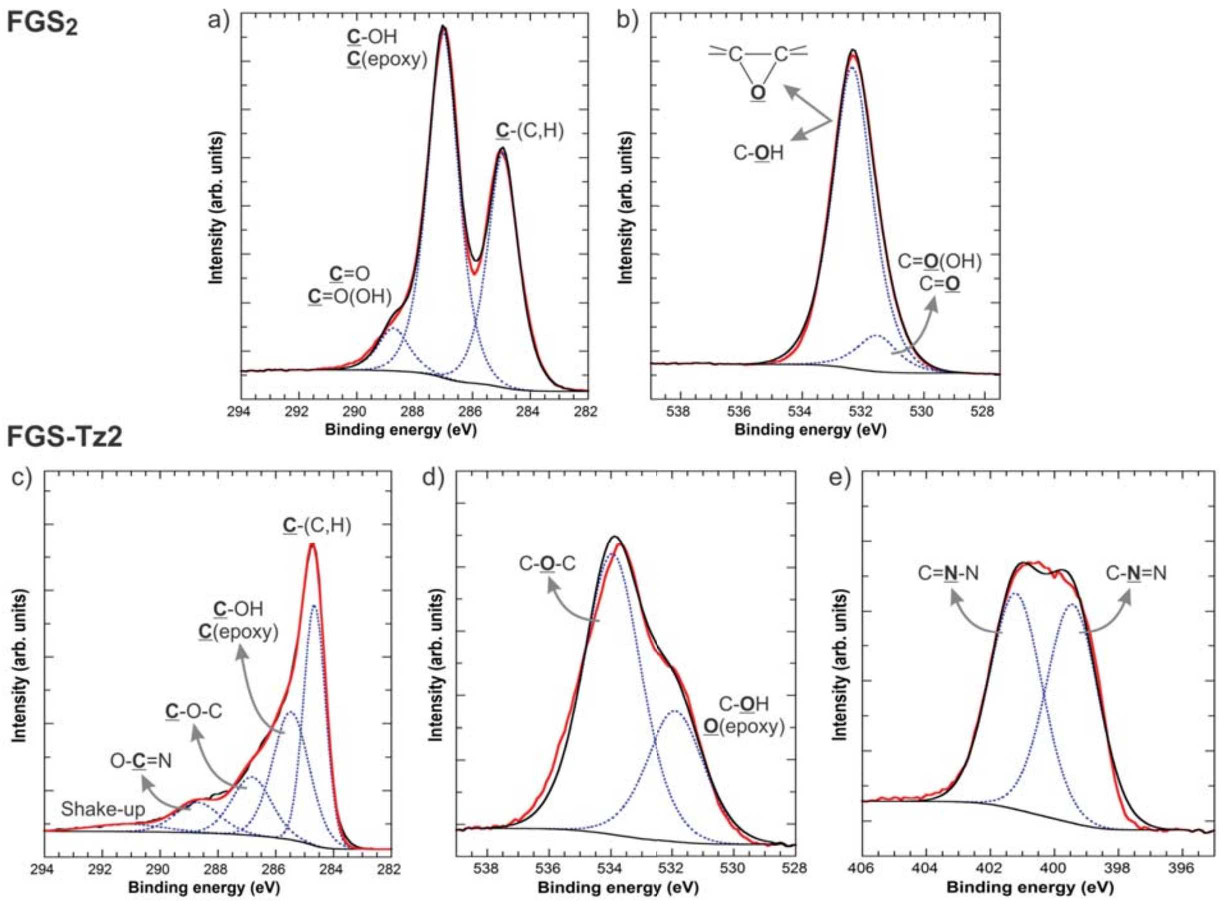

Figure 6: XPS of unmodified **FGS$_2$** (a,b) and **FGS-Tz2** (c,d,e). The core level spectra (C(1s), O(1s), and N(1s)) are shown as red lines, and the curve fitting lines as blue dashed lines (bond assignments) and black solid lines (the sum of the assignment curves).

After functionalization, the two components of the O(1s) spectrum of **FGS$_2$** (Fig. 6(b)) split into three components in the **FGS-Tz2** (Fig. 6(c)). The added component is higher in energy (533.5 eV) which may correspond to the oxygen now linked to the aromatic tetrazine (C-**O**-C=) [15].

In the N(1s) core level signal (Fig. 6(e)), two components of similar intensity and separated by a significant energy difference (1.3 eV) are observed. It is unexpected that the four nitrogen atoms of the tetrazine units are not energetically equivalent in the **FGS-Tz** compound [18]. It was determined that a chemical oxidative post-treatment of the grafted FGS (**FGS-Tz**) did not change the shape of the N(1s) signal, excluding the possibility that partially hydrogenated tetrazine rings might exist in the **FGS-Tz** materials. Thus, the two distinct bands in the N(1s) signals of **FGS-Tz** are specific to the Tz-functionalized material and might be due to specific interactions (like

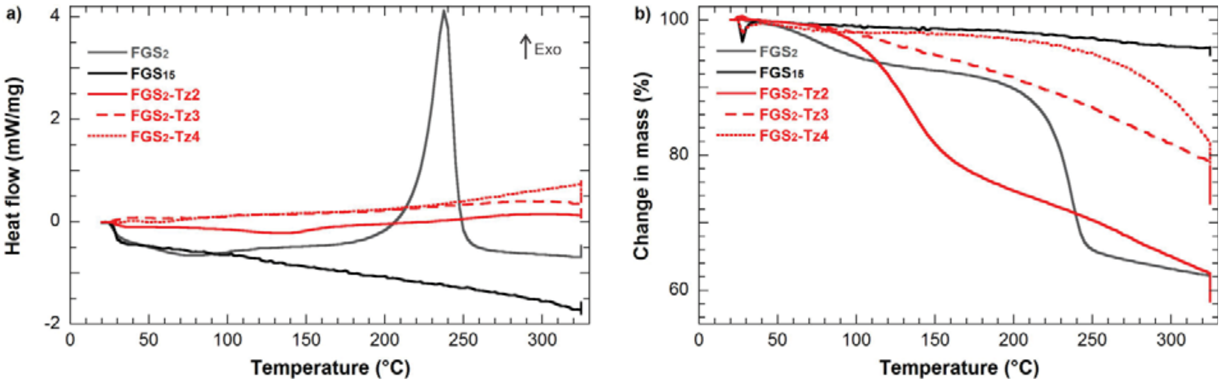

Figure 7: (a) DSC and (b) TG curves for **FGS$_{2}$**, **FGS$_{15}$**, and the **FGS-Tz** compounds. Samples are heated at 5 °C/min under nitrogen to 325 °C and held at that temperature for one hour to release any bound tetrazine. The TG curves for **FGS$_{2}$** and **FGS$_{15}$** are shown for comparison. Residual masses following heat treatment are: **FGS-Tz2**, 58.5% of the original; **FGS-Tz3**, 73.6%; **FGS-Tz4**, 72.7%; **FGS$_{2}$**, 60.2%; and **FGS$_{15}$**, 95.1%.

hydrogen bonding) between the nitrogen atoms of the tetrazine ring that are closer to the graphene sheets and the functionalities thereon (such as carboxylic acids).

Thermal analysis

Thermal analysis of the **FGS-Tz** compounds, unmodified **FGS$_{2}$**, and **FGS$_{15}$**, a thermally reduced **FGS$_{2}$**, by thermogravimetry (TG) and differential scanning calorimetry (DSC) provided additional support for the covalent attachment of tetrazines to **FGS$_{2}$** (Fig. 7). Under the slow (5 °C/min) ramp to 325 °C used in this example, the loss of substituted tetrazine from the **FGS-Tz** compounds appears as a gradual event with no detectable change in the calorimetric properties during heating (Fig. 7(a)), although accompanied by a substantial loss of mass (Fig. 7(b)). A prominent feature of the DSC measurements on unmodified **FGS$_{2}$** is the strong exotherm observed at ~230 °C (Fig. 7a) due to the generation of water vapor and carbon dioxide at the onset of rapid thermal reduction [5]. This exotherm is not present in thermally reduced FGS (for example, in **FGS$_{15}$**) and in the **FGS-Tz** compounds, indicating that the **FGS$_{2}$** used to make the **FGS-Tz** compounds was reduced during the reaction between tetrazine and **FGS$_{2}$**.

Structure and Dispersibility of Nanographene-Tz4 composites

Efforts to disperse FGS or graphene sheets in

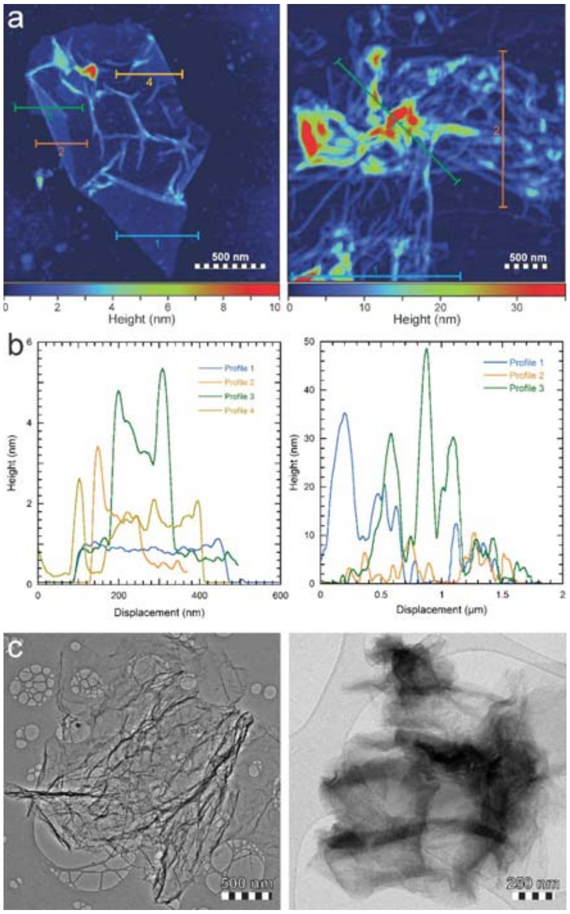

Figure 8: (a) AFM images of nanographene sheet (left) and nanogaphene-Tz4 compound (right). (b) Cross-sectional maps of sheet and compound. The single sheet (left) is wrinkled and folded upon itself. The Tz4-containing compound is a poorly ordered cluster of linked sheets. (c) TEM images of single graphene sheet (left) and graphene-Tz4 compound (right).

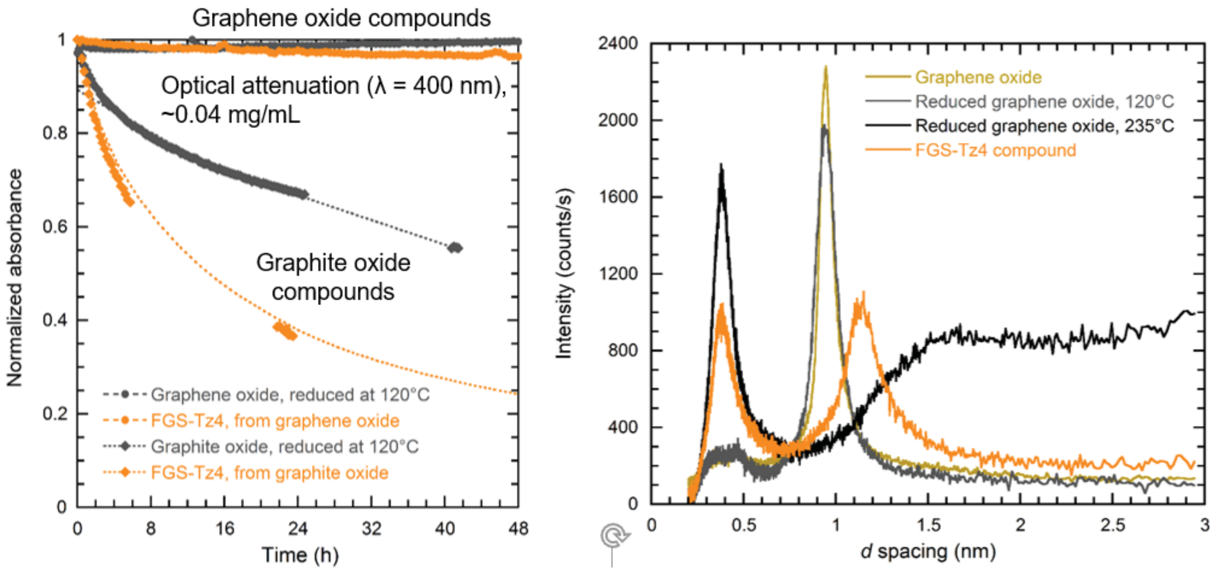

Figure 9: Dispersion stability of graphene and graphene-Tz4 compounds in propylene carbonate (left) and X-ray diffraction patterns of dry sediment from same (right).

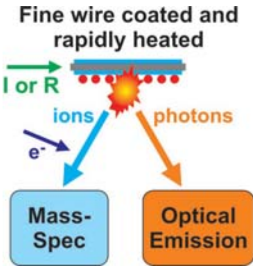

Figure 10: Conceptualization of mass spectrometry and optical emission from T-Jump filament, coated with materials for characterization.

liquid hydrocarbon (LHC) fuels were hampered by the low dispersion stability of the particles in suspension and clogging of fuel lines by large aggregates formed during transit. To address these issues, the procedure for synthesizing the FGS-Tz compound (Scheme 1) was changed, instead using graphene oxide to replace graphite oxide as the starting material in the synthesis. A significant effect on the size and dispersibility of the compounds was immediately observed, as the graphene oxide more readily formed single sheets with lateral sizes on the nanoscale (Fig. 8) with a comparable effect on the structure of the FGS-Tz compounds (Fig. 8). Dispersion stability was significantly improved, with even the compounds remaining in suspension for well over 24 hours (Fig. 9, left). The nature of the stacked aggregate was revealed by X-ray diffraction (Fig. 9, right) wherein the structure of graphene oxide sedimented from suspensions is a well-defined stack with interlayer spacing of less than one nanometer. When heated to 120 °C and held in propylene carbonate for 48 hours (the temperature and duration under which tetrazine molecules were reacted with graphite oxide or graphene oxide – Scheme 1), the interlayer spacing between the graphene oxide sheets was only slightly affected, indicating that 120 °C is too low to thermally reduce the graphene oxide. When heated to 235 °C in propylene carbonate and held for 48 hours, the structure of the resulting sediment was more graphitic, with the interlayer spacing falling below 0.5 nm, indicating the loss of oxygen and hydroxyls during heating—clear evidence that significant thermal reduction occurred [5]. The reaction of tetrazine with graphene oxide at 120 °C for 48 hours resulted in a sediment with two distinct regions: a graphitic region with interlayer spacing below 0.5 nm and an intercalated region with interlayer spacing near 1.2 nm (12 Å). This two-region structure gave rise to the confinement model (described below) used to explain the observed enhanced decomposition of the tetrazine from the compound (as described in the following section).

Unfortunately, the practical effect of improved dispersion stability in LHCs was not addressed during the reporting period.

Decomposition of Tetrazines: Kinetic Analyses

J. Delisio and M. R. Zachariah, University of Maryland

Slow heating of the **FGS-Tz** compounds revealed that the tetrazines slowly desorb from the FGS (Fig. 7) and the tetrazine vapor is lost before decomposition is detected. For insight into the energetic properties of the **FGS-Tz** compounds, temperature-jump time of flight mass spectrometry (T-jump TOFMS; Fig. 10) was performed on **FGS$_2$**, **FGS-Tz**, physical mixtures of **FGS** and pure tetrazine powders, and pure tetrazine samples alone, to analyze the time resolved evolution of gaseous decomposition products at high heating rates (~5 x 10^5 K/s). The T-jump system is comprised of a resistively heated thin platinum wire (0.003” diameter) that receives a current pulse of 3 ms, achieving a maximum temperature of approximately 1200 °C [19]. The time-resolved temperature is determined from the known correlation between resistance and temperature for the platinum wire. Samples were dispersed in either hexane or diethyl ether and then deposited onto the platinum wire as a thin (3-5 μm) coating. Wires are inserted into the TOFMS ionization/extraction region and then heated while pulsing ionization and extraction at 10 kHz resulting in a

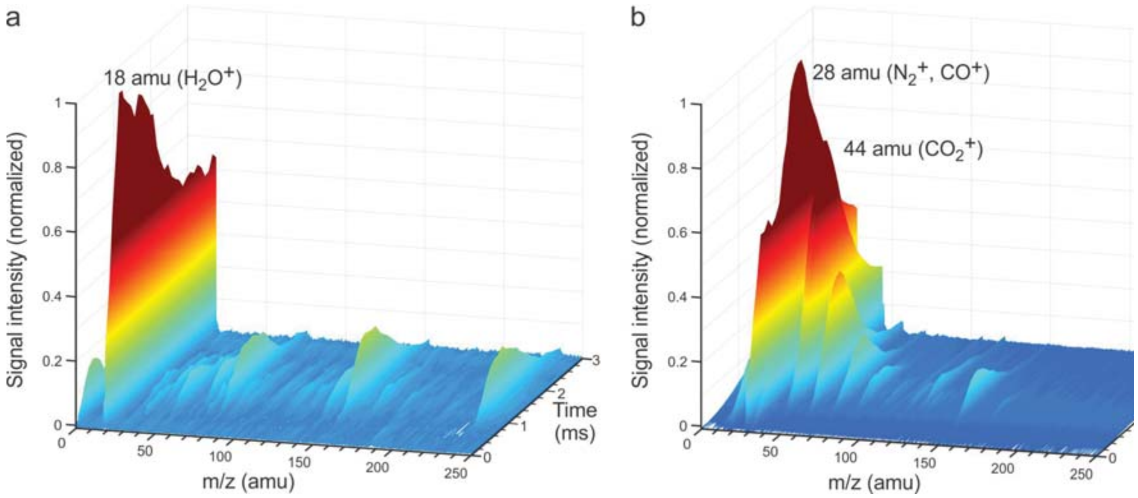

Figure 11: ToF-MS for (a) pure **Tz4** and (b) the **FGS-Tz4** compound. The decomposition of the tetrazine in the pure state is also observed in physical mixtures of unmodified **FGS$_2$** and **Tz4** (e.g., large mass fragments are observed in the decomposition product). (b) The tetrazine decomposition from the **FGS-Tz4** compound is delayed to a higher temperature, but no large mass fragments are observed. This behavior is representative of all **FGS-Tz**s made for this study.

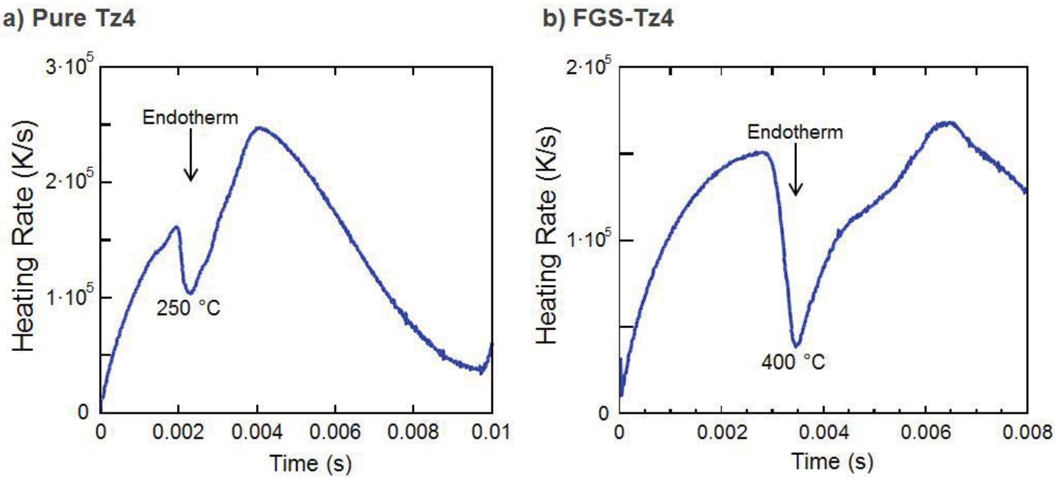

Figure 12: Nanocalorimetric measurements during the rapid heating of (a) **Tz4** and (b) the **FGS-Tz4** compound. The pure tetrazine adsorbs energy and is lost from the sampling Pt wire, subsequently resulting in only partial decomposition (as shown in Figure 8, the decomposition of pure **Tz4** results in large mass fragments). Conversely, the **FGS-Tz4** adsorbs substantially more energy and at higher temperature. The subsequent decomposition is much more complete.

mass spectrum every 0.1 ms.

Pure tetrazines and physical mixtures of tetrazines and **FGS2** had similar products of decomposition for all the **FGS-Tz** compounds made to date. Under rapid heating, the tetrazines vaporize, having adsorbed sufficient energy to sever the link between the tetrazine ring (84 amu) and the primary substituent group. For example, the decomposition of the **FGS-Tz4** compound (Fig. 11) results in the production of methyl adamantane (149 amu), whose mass signature is clearly visible as a product of pure tetrazine decomposition. However, when attached to the FGS, the decomposition of the tetrazine is not only delayed to higher onset temperature, but results in virtually undetectable amounts of large mass fragments with a significant increase in the production of smaller fragments, especially those corresponding to CO_2 (44 amu), N_2 or CO (28 amu), and H_2O (18 amu). The production of these smaller fragments, typically regarded as the final products in the decomposition of a HCNO compound, indicates that the tetrazine more fully decomposes when covalently attached to the FGS.

It should be noted that T-jump TOF-MS measurements on unmodified **FGS2** confirmed the thermal reduction of the **FGS2** through the loss of water and the carbon oxides, but did not show the mixture of fragments observed for the **FGS-Tz** compounds. Also, the generation of **FGS2** reduction products occurred within a very short span. This pulse in the production of water and the carbon oxides was not seen in the **FGS-Tz** compounds, indicating that the **FGS2** was reduced during the reaction with the tetrazine.

Nanocalorimetric measurements (using equipment on loan from the NIST) on **Tz4** and the **FGS-Tz4** compound reveal that bound tetrazines adsorb substantially more energy just prior to decomposition (Fig. 12). Only endotherms due to bond breaking are observed using this characterization technique: the molecule adsorbs energy, breaks apart, and the fragmentation products escape from the sampling Pt wire. In this situation, the exothermic reactions that occur in the vapor phase cannot be observed.

First Principal Molecular Dynamics Simulations of Tetrazine Binding and Decomposition

C. Zhang, S. Selcuk, R. Car, and A. Selloni, Princeton University

We first used density functional theory (DFT) electronic structure calculations to characterize the physical and chemical properties of relevant materials as well as first principles molecular dynamics (FPMD) simulations to gain insights into reaction mechanisms, particularly for the decomposition of tetrazines under rapid heating to high temperatures. In FPMD, the potential energy surface for nuclear motion is generated on the fly from the instantaneous ground state of the electrons within Kohn-Sham DFT [20]. Chemical reactions with low activation energies occur spontaneously in FPMD simulations, making this approach very effective for the study of reactive chemical dynamics in condensed phase. We focused on how the energetics of tetrazine decomposition may be affected by covalently linking tetrazines to graphene sheets. Experimental rapid thermolysis measurements showed that the tetrazine compounds completely decomposed during thermolysis, resulting in small mass fragments (CO, CO_2, H_2O, and N_2) corresponding to complete combustion. This was especially remarkable for the bridging tetrazine designated **Tz4** in our study, 4,4’-bis((6-chloro-s-tetrazin-3-yl)oxy)-1,1’-biphenyl (Fig. 2) [1].

Upon reaction with FGS, the chlorides are replaced with oxygen bridges to the functionalized

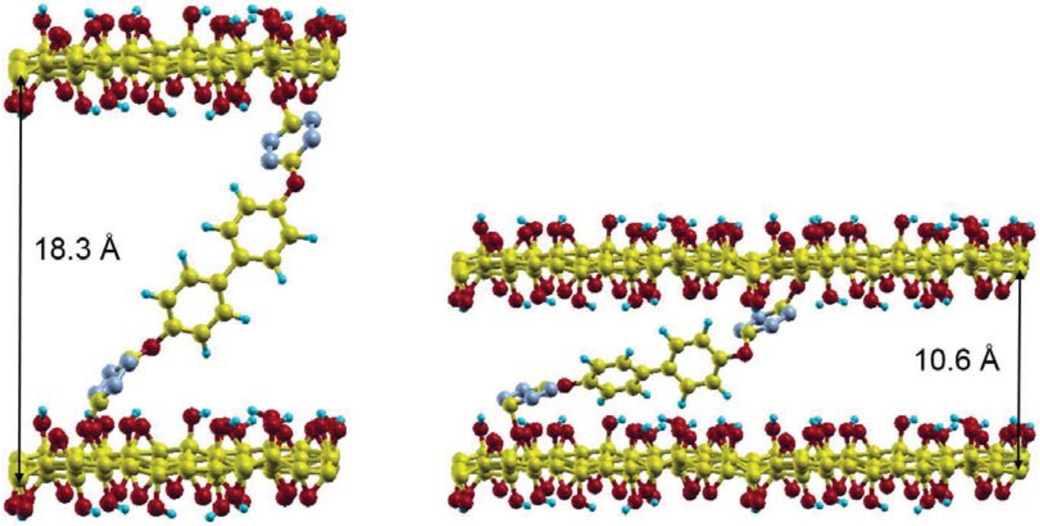

Figure 13: Two neighboring FGSs bridged by a connecting **Tz4** molecule, covalently bound at both ends. The highly expanded model (left) ignores the effect of van der Waals attraction between the sheets. More probably, the sheets are attracted to each other, resulting in a strained conformation of the tetrazine bridge (right).

graphene sheets, with the biphenoxy group acting as the linking agent between the two tetrazine rings (Fig. 13). The surprising observation is that the biphenoxy itself was completely fragmented during rapid thermolysis, demonstrated in the confinement model developed later in the project (see following section).

Our initial efforts to model the decomposition of a tetrazine, as a free molecule and bound to FGS, appeared to corroborate the experimental results observed for rapidly heated materials (as shown in the previous section). In the *ab initio* model, we applied a Nosé-Hoover (NH) thermostat [21] to more accurately reflect the expected thermal oscillations in the FGS [22]. When the NH thermostat is applied, the complete decomposition of the bound tetrazine is no longer observed in the model, and large mass fragments remain a product of decomposition (Fig. 14), contradicting the experimental observations. The revised model confirmed that the first step in the decomposition of the tetrazine molecule is the scission of the oxygen link to the FGS, resulting in an oxygen radical attached to 3-carbon on the tetrazine ring. The scission is quickly followed by the decomposition of the tetrazine rings, releasing the biphenoxy group.

In our previous model we ignored the effect of a constrained volume and internal strains on the energetics of tetrazine decomposition (Fig. 13). By incorporating the van der Waals attraction between neighboring sheets, we observe that the bridging agent (**Tz4**) is constrained and the biphenoxy group forced into a strained conformation, as discussed in the following section.

Confining Energetic Materials at the Nanoscale through Covalent Attachment to FGSs

S. Selcuk, R. Car, and A. Selloni, Princeton University
D. M. Dabbs and I. A. Aksay, Princeton University
J. F. Delisio and M. R. Zachariah, University of Maryland

Molecules confined in nanoscale volumes exhibit phase and energetic behaviors significantly different from those observed for unconfined molecules [23-24]. Experimental studies focus on nano-confinement to control the molecular dynamics and reaction products across a wide range of reactions [25-26], but these largely exclude energetic materials. Investigations of energetic molecules have previously relied on molecular dynamic models that place energetic materials within nano-sized volumes ("nano-reactors"). These predict that confining molecular energetic materials both increases resistance to mechanical shock and raises the temperature for the onset of pyrolysis [27-31], When embedded at the microscale, confinement has shown to modify the energy release rate and decomposition mechanism of energetic crystals embedded in a mesoporous carbonaceous structure [32]. But it is experimentally difficult to reliably insert an energetic molecule into a nano-reactor, leading to a lack of experimental evidence as to the effect of very small volume confinement. We have circumvented this issue by using a linking tetrazine, Tz4 (Fig. 2), to covalently bind to and link separated graphene sheets. The combination of covalent bonding with linked sheets forces the system to *self-assemble* into a multilayer structure in which the tetrazine rings are now confined within the nanovolumes defined by the spacing between the sheets (Fig. 15). The semi-crystalline structure of the FGS-Tz4 is confirmed by X-ray diffraction measurements (Fig. 9).

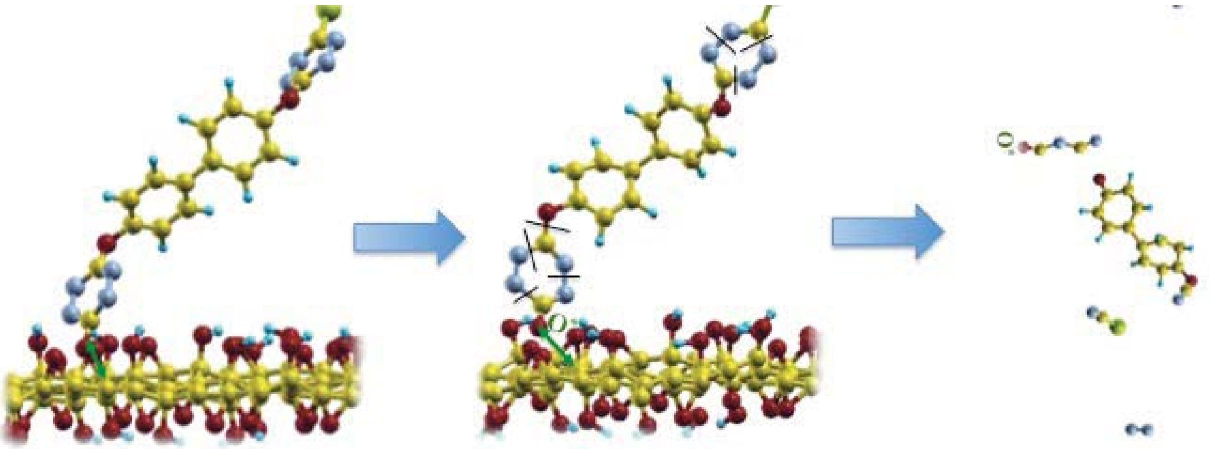

Figure 14: Tetrazine molecules bound to FGS first sever the links to the FGS at sufficiently high temperature without decomposing, creating an oxygen radical. The model indicates that the bound tetrazine contains a large amount of energy, much more than needed to break the link to the FGS, and this adsorbed energy was thought to be sufficient to cause the tetrazine to more fully and rapidly decompose once released from the FGS. This was supplanted by the following confinement model, though the scission of the covalent link is supported by low heating rate thermal analysis.

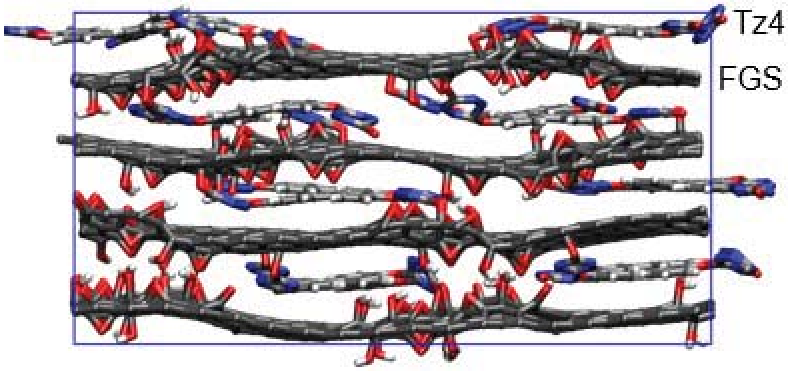

Figure 15: Multilayered stack of FGS sheets separated but linked by intercalated, covalently attached Tz4 molecules (a "confined" configuration).

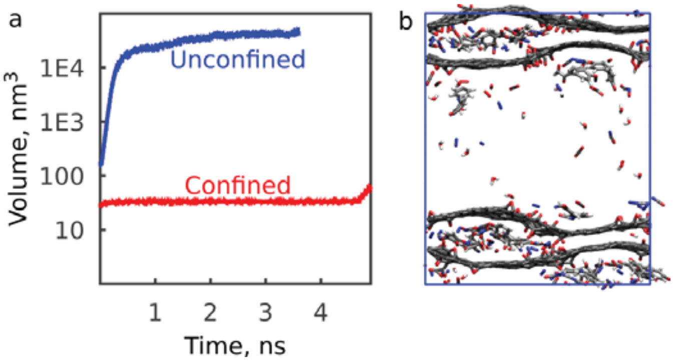

Figure 16: a) Total system volumes for unconfined and confined models during rapid simulated heating. Data were obtained from 1500 K, 1 bar NPT simulations. Note that the y axis is logarithmic. Although the two systems have virtually identical chemical compositions, when unconfined, the FGS-Tz volume expands quickly and reaches a total volume that is three orders of magnitude larger than the confined FGS-Tz, well before any volume expansion occurs in the confined system. (b) After sufficient decomposition, the buildup of more gaseous products in the confined system results in pressure-driven exfoliation of the graphene sheets around 4.8 ns.

Measurements of samples heated at slow rates in thermal analysis [1] confirm our previous models showing that the first step in the decomposition of a bound tetrazine molecule is the scission of the oxygen link between the tetrazine and the FGS, this link being the weakest bond in the FGS-Tz4 compound. When the bond between the FGS and tetrazine breaks in a slowly heated sample, the tetrazine-containing molecules merely diffuse from the FGS aggregate without significant decomposition, acting as an "unconfined" molecule. Rapidly heating crystalline tetrazine, or crystalline tetrazine in a mechanical mixture with FGSs, also vaporizes the tetrazine without significant pyrolytic decomposition. This results in the formation of large mass fragments, detected by mass spectrometry of the product vapors (Fig. 11). In contrast, when in the bound or "confined" state, the tetrazine component of the FGS-Tz compound is held within the spaces between the sheets from which it cannot escape before significant decomposition occurs, resulting in much smaller reaction products (Fig. 11). This contrast between the unconfined and confined state is also indicated by the delayed volume increase during the decomposition of the confined state compared to that of the unconfined state (Fig. 16). Finally, the model shows that the presence of near-neighbor oxygen-containing groups on the FGS (Fig. 15) adds an oxidative (combustive) mechanism that further decomposes the tetrazine (and, to a smaller degree, aids in the decomposition of the biphenyl link in the Tz4 molecule). The more rapid decomposition of the tetrazines due to the higher degree of decomposition results in a faster energy release from the confined system (Fig. 17).

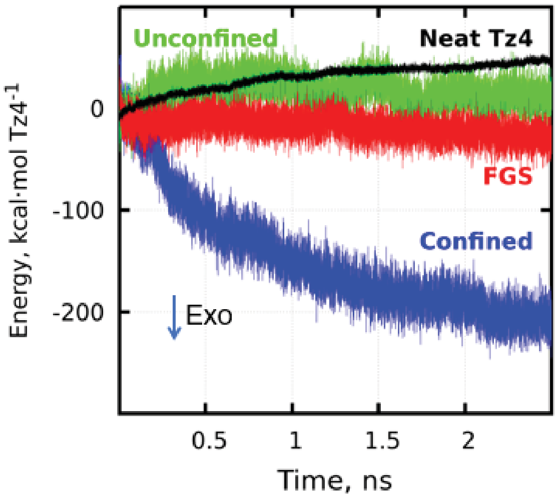

Figure 17: Potential energy profiles for different models with respect to time. All data are normalized by the number of Tz4 molecules in the corresponding systems and the data for the bare FGS model are normalized by the same constant in the confined and unconfined systems. Neat Tz4 decomposition is actually endothermic, partially because it also includes the evaporation of the material from condensed phase. Bare FGS disproportionation is exothermic. The unconfined system lies between the pure tetrazine and FGS, confirming is essentially a non-interacting mixture of Tz4 and FGSs. A significant increase in the released energy is apparent in the simulation of the confined system, corresponding to the production of larger amounts of small molecular weight molecules.

Carbonaceous Nanoparticle Spacers Maintaining Sheet Separation in FGS Aggregates

D. J. Bozym and I. A. Aksay, Princeton University

The addition of dehydrated sucrose nanoparticles increases the gravimetric capacitance of electrochemical double-layer capacitor electrodes produced via the evaporative consolidation of graphene oxide–water–ionic liquid gels by more than two-fold (Fig. 18) [33]. Dehydrated sucrose adsorbs onto graphene oxide and serves as a spacer, preventing the graphene oxide from restacking during solvent evaporation. Despite 61 wt % of the solids being electrochemically inactive dehydrated sucrose nanoparticles, the best electrodes achieved an energy density of ~13.3 Wh/kg, based on the total mass of all electrode components.

Our interest is to use nanoparticles produced via the dehydration of sucrose, a renewable feedstock, as spacers between FGSs, as the density of dehydrated sucrose (DS) is expected to be much lower than that of a metal- or oxide-based nanoparticle of equal size. By this method we thereby minimize the increase in the total weight of a porous material suitable for use in energetic gels and inks, and as a charge carrier for energy storage devices in addressable energetic composites. Using an evaporative consolidation procedure developed by us [13], we combine hydrophilic DS nanoparticles with an aqueous suspension of graphene oxide and a water-soluble ionic liquid (IL), then consolidate the suspension into composites that can be heat treated to reduce the graphene oxide into conductive FGSs.

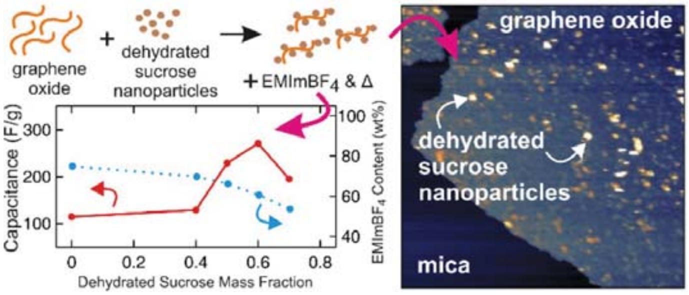

Figure 18: Dehydrated sucrose nanoparticles adhere to FGSs or graphene oxide sheets and act as spacers to maintain sheet separation during evaporative processing. The layering of such decorated FGSs with ionic liquids, such as $EMImBF_4$, yields increased gravimetric capacitance with lower $EMImBF_4$ content as the DS content increases (per gram of heat treated FGS) [33]. (right) The nanosize dehydrated sucrose particles are well-dispersed on graphene oxide or FGS, providing stable separations between adjacent sheets.

Through electrochemical characterization of these composites as electrodes in cyclic voltammetry and electrochemical impedance spectroscopy, we demonstrate that the inclusion of DS effectively prevents the restacking of FGSs while increasing the gravimetric capacitance from 115 to 330 F/g (per gram of FGS) (Fig. 18). Moreover, with this approach, surprisingly high energy densities (up to 13.3 Wh/kg) can be achieved despite the large amounts of DS (as high as 60 wt% solids) used within the electrodes. While this is not the best energy density reported for FGS-based electrodes, it is an impressive value given that the electrodes have not been optimized for other processing parameters and that the DS is expected to be electrochemically inactive. Further improved electrochemical performance is anticipated by making the DS particles conductive and electrochemically active through heat treatments and subsequent optimization of the processing parameters. Also, the stable separation between the sheets will be investigated as a matrix for the integration of crystalline propellants (such as ammonium perchlorate) in which the oxygen content of the FGS is expected to partially offset inhibition by the carbonaceous materials.

FGS-Elastomer Composites for Printable Devices: Structure and Electrical Conductivity of Hybrid Graphene-Carbon Aerogels

K. Sallah, M. Alifierakis, and I. A. Aksay, Princeton University

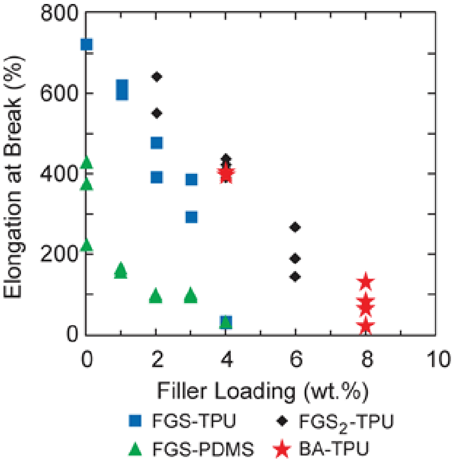

Figure 19: In TPU composites, elongation at break declines roughly linearly with filler loading, with both graphite oxide (FGS$_2$-TPU) and aerogel (BA-TPU) filled composites exhibiting higher elongation than FGS-TPU at similar filler loadings. FGS-PDMS had much lower elongation at break owing to the lower extensibility of the composite, and showed a sharper decline in elongation at break initially and near 4 wt.%, a similar filler loading to where FGS-TPU trended toward zero elongation at break.

Our studies have focused on composite materials composed of FGSs dispersed in elastomeric matrices for incorporation into flexible, conductive, and, eventually, energetic devices. The composites included (i) functionalized graphene sheets formed by the thermal exfoliation of graphite oxide (FGSs), then added to thermoplastic polyurethane (TPU); (ii) FGSs in poly(dimethylsiloxane) (PDMS) elastomer; and (iii) fragmented graphene-carbon hybrid aerogels (Fig. 19) in TPU. The mechanical properties of FGS-TPU composites containing unreduced FGSs formed by the solvent exfoliation of graphite oxide were also considered. Mechanical analysis of these various composites revealed that the elongation at break declines with filler loading across all filler loadings greater than 1 wt.% (Fig. 20).

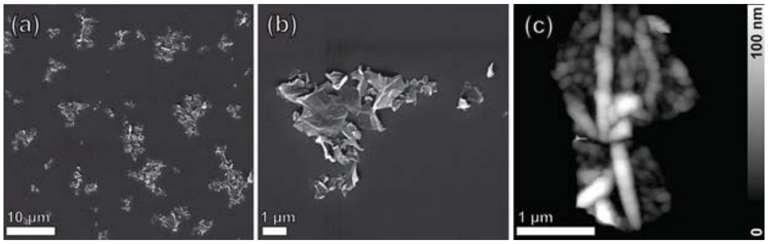

Figure 20: Aerogel fragments deposited from suspension after probe sonication as observed by SEM (a and b) and AFM (c). The aerogel fillers are small aggregates of sheets. With AFM, particle thickness is measured to be tens of nanometers and so particles observed likely consist of aggregates of particles on top of larger sheets.

Elongations reach ~100% or lower at 4 wt.% in FGS composites and 8 wt.% for graphite oxide and aerogel composites (Fig. 19). When filler loading is considered in terms of volume fraction or number of sheets per volume, the improvements in elongation achieved in graphite oxide and aerogel composites are reduced, suggesting that, despite the intrinsic filler differences and dramatic differences in filler distribution, the decline in elongation at break cannot be avoided without significant processing changes. When considering electrical properties as a measure of composite uniformity, both FGS and aerogel composites exhibit conductivity on the order of 10 S/m at 4 wt.%, but it seems that the number

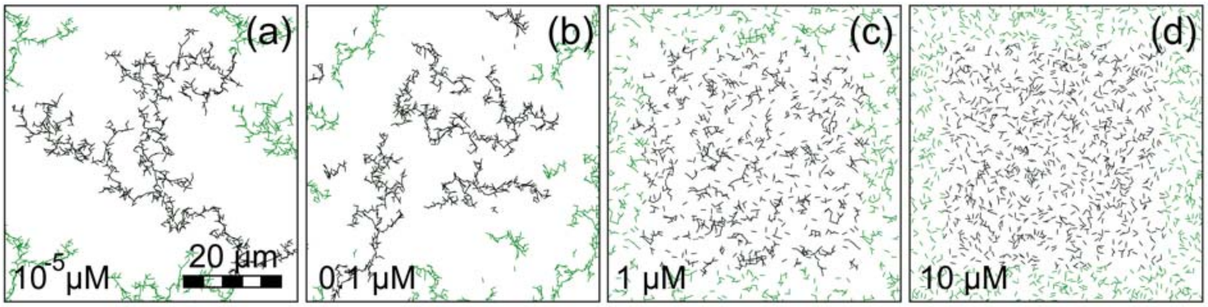

Figure 21: Images from simulations for different surfactant concentrations with constant concentration of particles (~0.49 particles/μm^2, 1,000 particles in a 45 x 45 μm matrix at the step 6×10^6). Particles that are parts of the neighboring simulation domains (the boundary conditions are periodic) appear in green. Particles that belong to clusters that have crossed the boundaries and reappear on the other side appear also in green and their unconnected parts have been moved back to show the complete shape of each cluster and appear in black. All other particles that are part of the main simulation domain appear in black.

of sheets per volume may be lower in the aerogel composites. This hypothesis is strengthened by a much more sensitive conductivity relationship to strain in the aerogel-TPU composites, where conductivity declines about two orders of magnitude over 100% strain, while in FGS-TPU conductivity declines about one order of magnitude over 200% strain. The unique structure of the aerogel particles, composed of linked aggregates of sheets, likely drives the altered performance through its effect on particle dispersion and contact resistances.

Since the decline in elongation at break was shown to be similar for all three types of fillers when filler loading is considered in terms of volume fraction or the number of sheets per volume, it seems that even when large differences in dispersion and filler type exist, similar declines in extensibility may occur. This casts doubt on whether dramatically improving the dispersion of conductive fillers in composites could be a route to achieving improved combinations of conductivity and extensibility. Whether this is true that this decline in extensibility is truly an intrinsic limitation of composites with graphene-based fillers can only be confirmed by further analysis and particularly through the development of models that may show the mechanisms through which failure occurs and through which elongation at failure declines with filler loading.

Cluster Aggregation Models for Graphene Particle Suspensions

M. Alifierakis, K. Sallah, and I. A. Aksay; in collaboration with J.-H. Prevost,
Princeton University

For inks using graphene, graphene oxide, or FGSs, the individual sheets have to be first dispersed in a liquid medium in order to break up the powder aggregates [34]. This is typically achieved through one of two colloidal dispersion methods: (i) decreasing the magnitude of the van der Waals (vdW) attractive forces to the k_BT range (where k_B is the Boltzmann constant and T temperature) by lowering the Hamaker constant through index matching (also useful for exfoliating graphite) [35]; or (ii) counteracting the vdW forces by inducing repulsion between the sheets through electrostatic, steric, or electrosteric interactions [36]. In the application of ink to a substrate, the dispersed suspensions are reconverted to an aggregated state either through the stacking of sheets or with other colloidal particles. In these aggregated structures, a deterministic control of the topological features is of paramount importance to define properties by controlling parameters such as accessible area for chemical reactions, load transfer for mechanical properties, electron and heat transfer for electronic and thermal properties. Heretofore, experiments are used to observe the effects of dispersion quality on the final properties of the products. But, while these experimental studies have been invaluable in many aspects, a connection between the filler's network structure and the properties of the final materials has not been established. In our work, we are attempting to develop a modeling approach to establish the dispersion state of the filler particles, leading to models of graphene-filled materials and thereby providing a theoretical base to understand the important factors that affect the dispersion state of these particles. Currently, we have developed a reversible cluster aggregation (RCA) model for atomically thin macromolecules that qualitatively predicts the experimentally observed macroscopic colloidal aggregated structures.

Our model is, in principle, a reversible aggregation model that exists between diffusion-limited cluster aggregation (DLCA) [37-38] and reaction-limited cluster aggregation (RLCA) [39]. To further reduce the complexity of our models, we represent graphene sheets as 2-dimensional line segments of unit length that move freely (off-lattice simulation) in a square matrix with periodic boundary conditions, then performing translational and rotational steps (Fig. 21). Collisions between sheets and/or clusters occur with a certain probability (which we call the aggregation probability) which lead to cluster formation and growth. Sheets can also be detached from clusters with a certain probability that we call the deaggregation probability.

We have constructed the first reversible aggregation model for non-linear particles to be used to help resolving questions about the aggregation (on a 2D plane or interface) of graphene-like or other atomically thin particle aggregation or needle(rod)-like particles. Comparing experiments and simulations give us similar trends related to the particle cluster size, an indication for the existence of a critical concentration of surfactant at which many dense aggregates are formed, indicating that graphite forms below that concentration with mostly dispersed single particles above it. According to our model, dense clusters form rapidly at the critical surfactant concentration, then plateaus. At low surfactant concentrations aggregation occurs continuously throughout the simulation.

METALLIC CLUSTERS AND MESOSCOPIC AGGREGATES

M.R. Zachariah and B. Eichhorn, University of Maryland

UMD's effort was focused on two directions. 1. Develop techniques that minimize sintering of nanoparticles and maintain the structural integrity of the particles required to enable full enhancement of the energy release. 2) Develop and incorporate into fuel systems that employ novel near zero-valent clusters, in both free and stabilized configurations to assess impact on combustion. We have demonstrated unambiguously that assembling nanoparticles in microparticle with an embedded gas generator leads to enhanced combustion performance, a more consistent burn from particle–to-particle, and that mesoparticles burn like independent aluminum nanoparticles. We have also demonstrated in-house synthesis of a hydrocarbon soluble Al(I) tetrameric cluster, $[AlBrNEt_3]_4$. This material was demonstrated that the addition of very small quantitates of the additive (~ 3 mM) results in a ~ 15% reduction in burn rate.

Molecular Aluminum Additive for Burn Enhancement of Hydrocarbon Fuels

Additives to hydrocarbon fuels are commonly explored to change the combustion dynamics, chemical distribution, and/or product integrity. Here we employ a novel aluminum-based molecular additive (Fig. 22), Al(I) tetrameric cluster $[AlBrNEt_3]_4$ ($Et = C_2H_5$), to a hydrocarbon fuel and evaluate the resultant single-droplet combustion properties. This Al_4 cluster offers a soluble alternative to nanoscale particulate additives that have recently been explored and may mitigate the observed problems of particle aggregation. Results show the $[AlBrNEt_3]_4$ additive to increase the burn rate constant of a toluene-diethyl ether fuel mixture by ~20% in a room temperature oxygen environment with only 39mM of active aluminum additive (0.16 wt % limited by additive solubility) (Table 3). In comparison, a roughly similar addition of nanoaluminum particulate shows no discernable difference in burn properties of the hydrocarbon fuel. High speed video shows the $[AlBrNEt_3]_4$ to induce microexplosive gas release events during the last ~30% of the droplet combustion time. We attribute this to HBr gas release based on results of Temperature-Programmed Reduction (TPR) experiments of the $[AlBrNEt_3]_4$ dosed with O_2 and D_2O. A possible mechanism of burn rate enhancement is presented that is consistent with microexplosion observations and TPR results.

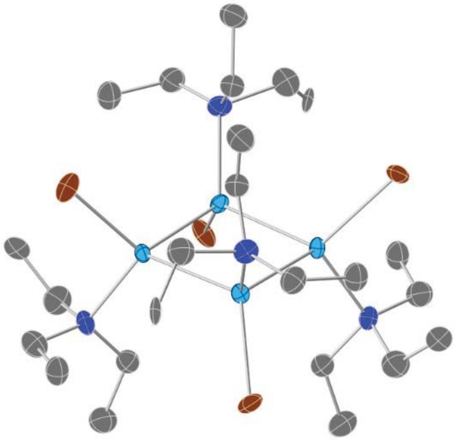

Figure 22: Crystal structure of $[AlBrNEt_3]_4$: Al (light blue) N (dark blue) C (gray) Br (brown), hydrogen atoms omitted for clarity.

Table 3: Experimental samples with measured burning rate constants.

Additive	Active Al Conc.	Percent Increase in Energy Content	Burning Rate Constant Based On:		
			D^2 Trend		Time to Termination
			K (mm^2/s)	R^2 of Fit	K (mm^2/s)
None (Control)	None	None	1.41	0.886	1.47 ± 0.10
Triethylamine	None	None	1.48	0.956	1.52 ± 0.10
0.2 wt% nAl	50 mM	0.14% (42 kJ/L)	1.37	0.987	1.43 ± 0.14
5.2 mM $[AlBrNEt_3]_4$	21 mM	0.06% (18 kJ/L)	(Obscured)	N/A	1.80 ± 0.16
9.7 mM $[AlBrNEt_3]_4$	39 mM	0.11% (33 kJ/L)	(Obscured)	N/A	1.79 ± 0.18

Oxidation and decomposition mechanisms of air sensitive aluminum clusters at high heating rates

Molecular near zero oxidation state clusters of metals are of interest as fuel additives. In this work high heating rate decomposition of the Al(I) tetrameric cluster, $[AlBr(NEt_3)]_4$ (Et = C_2H_5), was studied at heating rates of up to 5×10^5 K/s using temperature-jump time-of-flight mass spectrometry (T-jump TOFMS) (Fig. 23a). Gas phase Al and AlH_x species were rapidly released during decomposition of the cluster, at ~220 °C. The activation energy for decomposition was determined to be ~43 kJ/mol (Fig. 23b). Addition of an oxidizer, KIO_4, increased Al, AlO, and HBr signal intensities, showing direct oxidation of the cluster with gas phase oxygen.

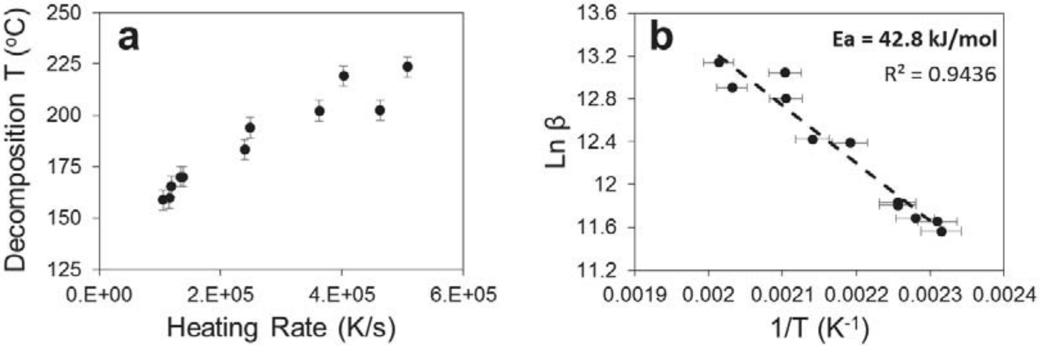

Figure 23: Decomposition temperature (first appearance of m/z = 86) vs heating rate (a) and Arrhenius plot (b) of rapidly heated unoxidized Al(I) tetrameric cluster.

Triisobutylaluminum Additive for Liquid Hydrocarbon Burn Enhancement

Metallizing hydrocarbons has received renewed attention as a potential means to increase energy density and burn rate. Particle agglomeration, however, is a significant concern, impeding both performance as well as practical implementation due to system fouling. Achieving a metallized hydrocarbon without nanoparticles in suspension would avoid particle agglomeration problems. Previous proof-of-concept work with highly reactive organometallic Al-based clusters stabilized by ligands and dissolved in a hydrocarbon showed such a scheme is not only possible, but the decreased size of the cluster molecules relative to nanoparticles substantially increases reactivity and at least an order of magnitude less active aluminum. To increase understanding of how such burning rate effects manifest with dissolved aluminum, a higher valency alkyl aluminum historically used as a hypergol, triisobutylaluminum (IBu_3Al), is dissolved in toluene and isolated droplet combustion is characterized showing up to 60% burning rate increase with 810 mM IBu_3Al relative to that of pure toluene attributed specifically to the aluminum content of the additive molecule (Fig. 24). Flame emission spectroscopy observing AlO emission supports the vital role of gas eruption and droplet disruption to transport additives into the flame (Figs. 25-26).

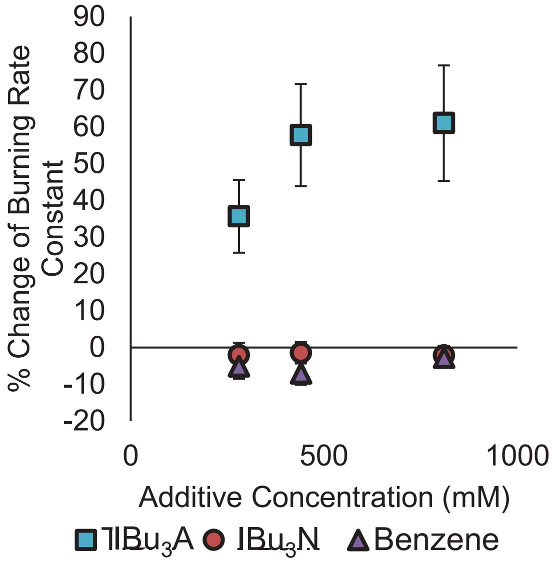

Figure 24: Measured changes of burning rate constant relative to toluene (K = 2.33) with IBu$_3$Al, IBu$_3$N, and benzene additives. Error bars represent one standard deviation in each direction.

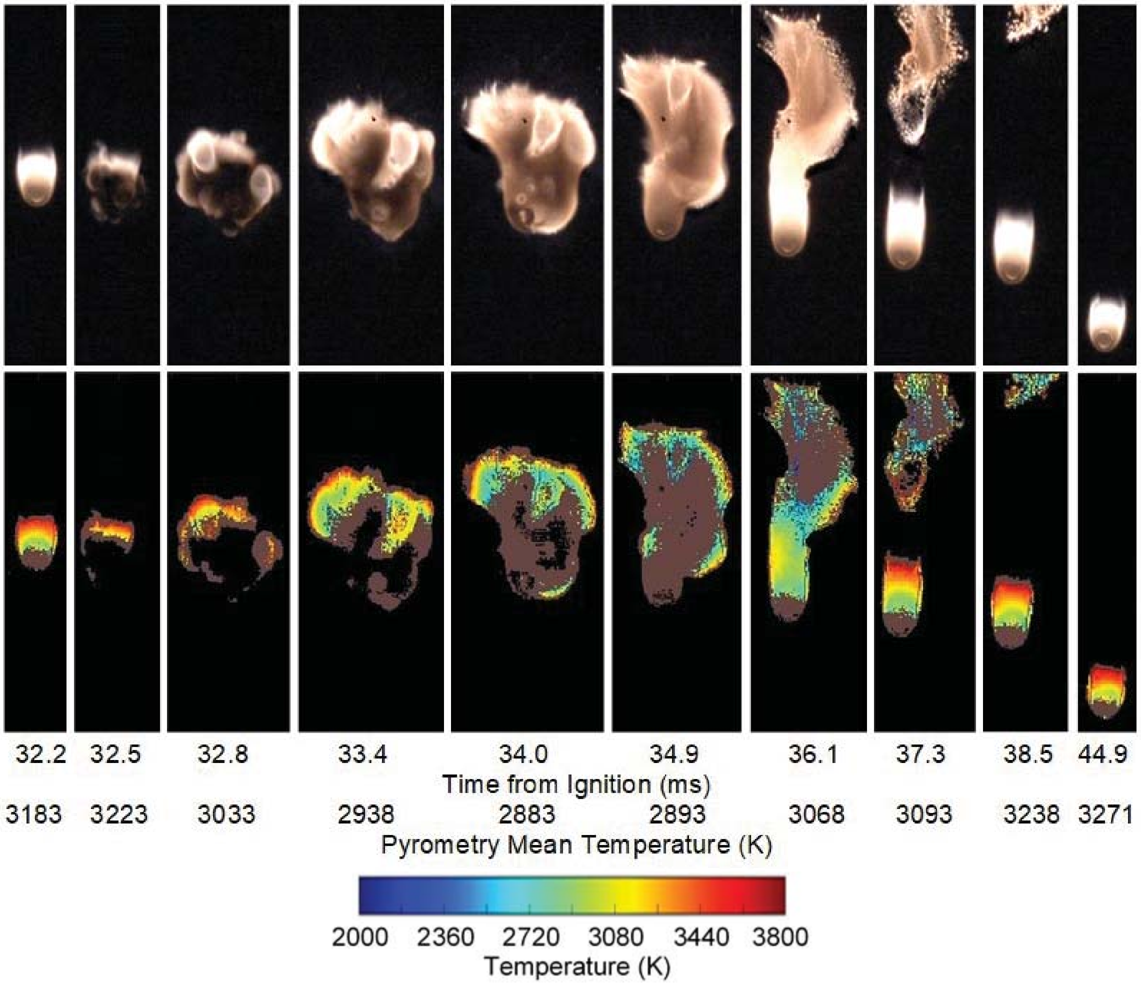

Figure 25: Representative combustion disruption videography and pyrometric temperature estimates of 810 mM IBu$_3$Al in toluene in which the primary droplet survives intact with time from ignition noted per frame.

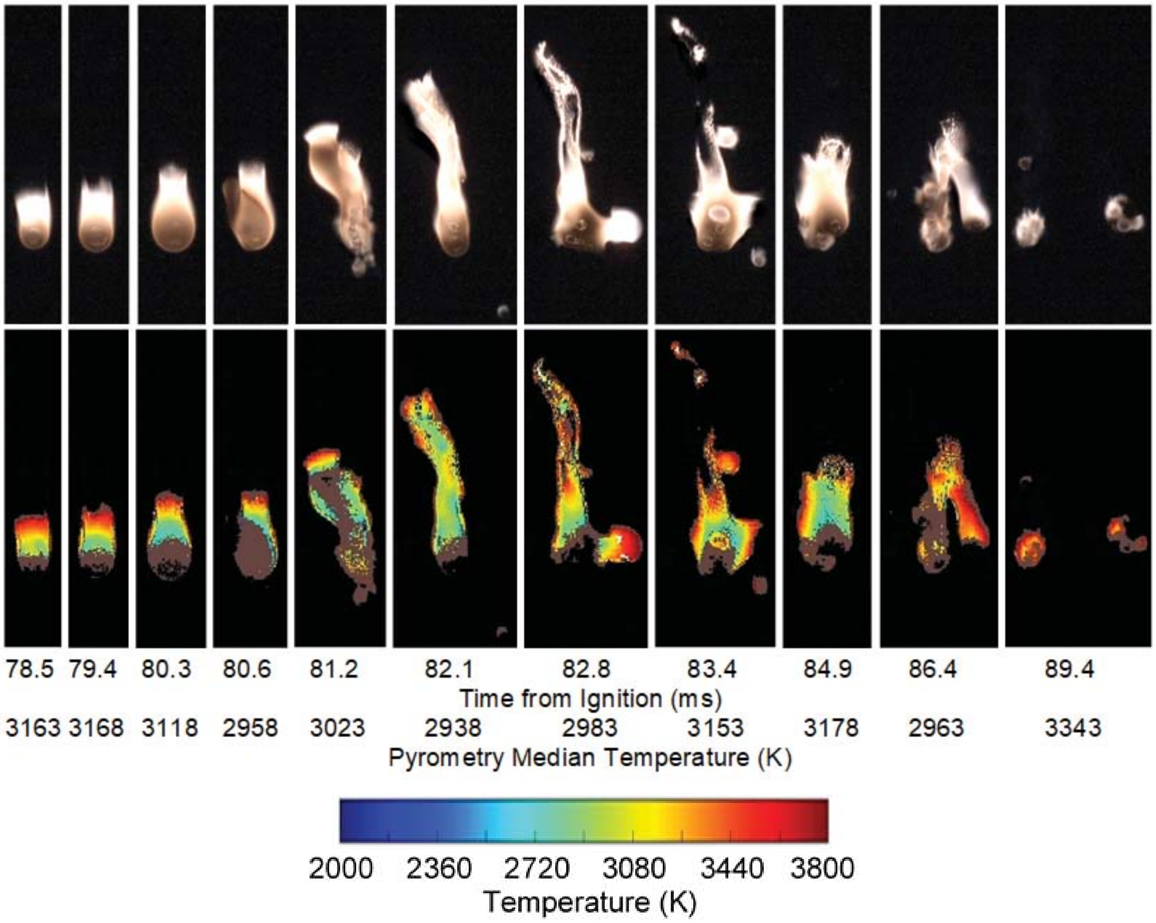

Figure 26: Representative combustion disruption videography and pyrometric temperature estimates of 810 mM IBu_3Al in toluene in which the primary droplet is catastophically disassembled into sub-droplets with time from ignition noted per frame.

Quantifying the Enhanced Combustion Characteristics of Electrospray Assembled Aluminum Mesoparticles

Aluminum particles have been extensively used to enhance the combustion characteristics of propellant, pyrotechnic and explosive formulations. Unfortunately, the relatively high ignition temperatures of aluminum result in severe sintering prior to combustion, leading to early loss of nanostructure and thus a smaller power law exponent for size dependent burning than expected. One such scheme we explore, to defeat sintering, is to create low temperature gas-generation, which helps in breaking up the soft agglomerates before/during combustion. In this work, we characterize the combustion characteristics of electrospray assembled micron scale particles composed of commercial nano-aluminum (ALEX), bound in an energetic polymer matrix composed of nitrocellulose. The nitrocellulose not only acts as a binder for the nanoparticles but also as a dispersant owing to its dissociation at low temperatures (ca. 450K). Combustion characteristics were measured by direct injection of the electrospray assembled particles into the post flame region of a CH_4/O_2 diffusion flame. We find that the composite meso particles show an order of magnitude reduction in average burn times when compared to that of the commercial nano aluminum (ALEX), and are as fast as the smallest nanoparticle burn time (Tables 4 and 5). Scanning electron microscopy of quenched post-combustion particles clearly shows smaller sized products in the combustion of electrospray generated composite particles when compared to ALEX powder (Fig. 27). This latter point should also lead to a more complete reaction and certainly demonstrates that the concept of using a two-stage reacting system: one at low temperatures to generate gas to separate particles followed by the nominal oxidation reaction is at the least a strategy that is worthy of further exploration.

Table 4: Average burn time measurements for commercial nano aluminum powder.

Flame condition ➔	Flame 1 (841 K)	Flame 2 (1040 K)	Flame 3 (1200 K)	Flame 4 (1360 K)
Nano Al Burn time (μs) [*All data points*]	2700 μs	4740 μs	4440 μs	3460 μs
Nano Al Burn time (μs) [*sub 1000 μs data*]	750 μs	663 μs	570 μs	594 μs

Table 5: Average burn time/ standard deviation measurements for aluminum meso particles.

Flame condition ➔	Flame 1 (841 K)	Flame 2 (1040 K)	Flame 3 (1200 K)	Flame 4 (1360 K)
Meso Al Burn time (μs) [10 wt. % NC]	366 μs/ 72 μs	420 μs/ 76 μs	365μs/ 62 μs	326 μs/ 83 μs
Meso Al Burn time (μs) [5 wt. % NC]	302 μs/ 48 μs	286 μs/ 49 μs	357μs/ 153 μs	324 μs/ 88 μs
Meso Al Burn time (μs) [15 wt. % NC]	385 μs/ 63 μs	405 μs/ 63 μs	380μs/ 51 μs	390 μs/ 58 μs

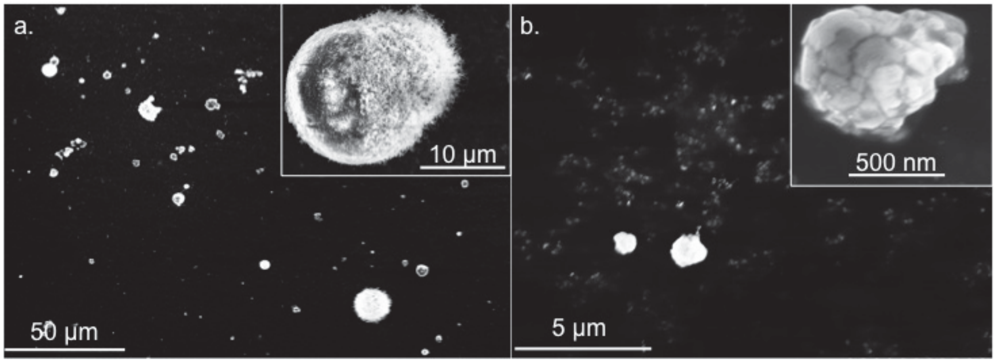

Figure 27: SEM images of the products collected post combustion: a) Commercial nanoaluminum with an inset of an individual particle at high magnification; b) Aluminum meso particles with an inset of an individual particle at high magnification. Meso-particle products particles are smaller indicating less sintering.

Application of Aluminum Mesoparticles in Composite Solid Rocket Propellent

We investigate the potential application of aluminum mesoparticles as an ingredient for solid composite rocket propellants. The basic strategy is to incorporate nanoaluminum in the form of a micron scale particle containing a gas-generator, to enable easier processing, and potential benefits resulting from reduced sintering prior to combustion. The mesoparticles were made by electrospray and comprised aluminum nanoparticles (50 nm) and nitrocellulose to form micrometer scale particles. In this study, 80% solids loaded composite propellants (AP/HTPB based) were made with the addition of micrometer sized (2-3 μm) aluminum (10 wt%), and compared directly to propellants made by directly substituting aluminum mesoparticles for traditional micrometer sized particles. Propellant burning rate was relatively insensitive for mesoparticles containing between 5-15 wt% nitrocellulose. However, direct comparison between a mesoparticle based propellant, to a propellant containing micrometer scale aluminum particles showed burning rates approximately 35% higher while having a nearly identical burning rate exponent (Fig. 28). High speed imaging indicates that propellants using mesoparticles have less agglomeration of particles on the propellant surface

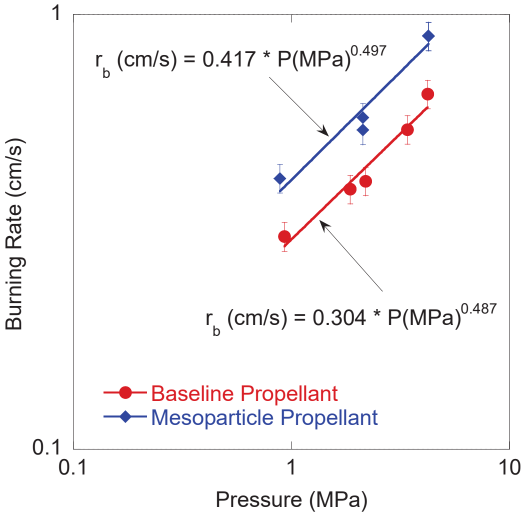

Figure 28: Comparison of burning rates between propellants as a function of pressure.

Assembly and Encapsulation of Aluminum NP's within AP/NC matrix and their Reactive Properties

Aluminum nanoparticles (Al NPs) are commonly employed as fuel supplement to increase the energy density of propellants. However, due to the highly agglomerated state of the NPs and significant pre-combustion sintering, the ignition temperature and ignition delay time of Al NPs are still too high to fulfill the potential of Al NPs as performance additives in propellant burning. In this work, we employed a spray approach to generate near monodisperse microparticles of Al NP's encapsulated within ammonium perchlorate (AP) and a binder (nitrocellulose (NC)) (Fig. 29). The results show that Al/AP/NC composites have an ignition temperature (~700 K), which is significantly lower than Al melting point (~933 K). The reactivity of Al/AP/NC composites was also tested in a confined cell with a constant amount (~25 mg in 13 mL). Although the peak pressure observed for Al/AP/NC is comparable to that of physically mixed Al/CuO nanothermite, the impulse generated is more than two times higher (Fig. 30). The measured flame temperature of Al/AP/NC composites were as high as 2800 K, which is ~500 K higher than Al/AP composites without NC. Furthermore, the potential mechanism for the early ignition of these composites were investigated. It is proposed that gaseous acid released from AP could play an important role in weakening the protective oxide shell on Al nanoparticles which could subsequently lead to the reaction of Al in the high-pressure oxygenated environment at lower temperature.

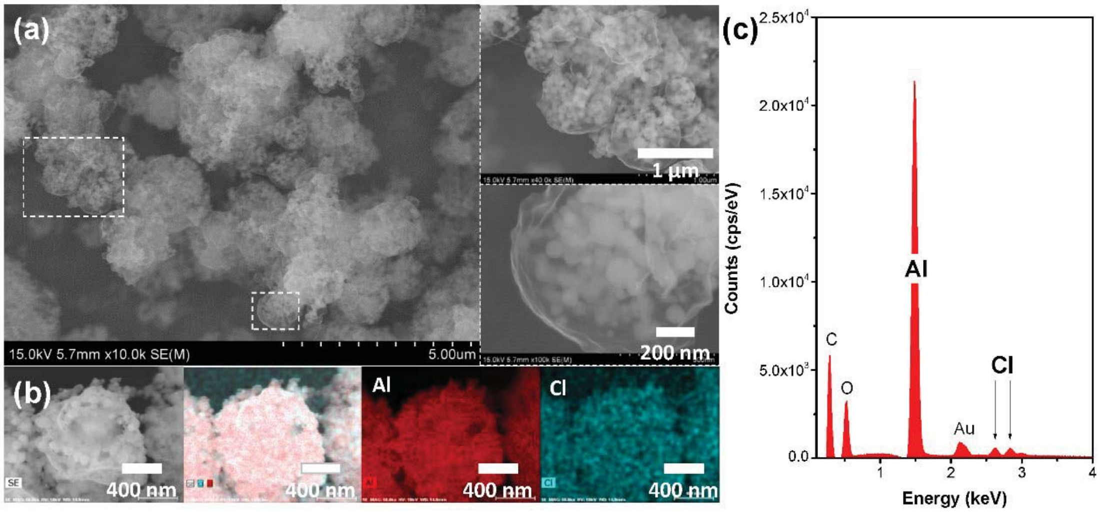

Figure 29: Typical Low (a) and high (inserts of a) resolution SEM images, EDS mapping images of a single particle (b) and elemental result (c), and XRD result (d) of Al/AP/NC composites (14 wt. % NC, Al/AP is in stoichiometric ratio). Note: the Au shows up because of the pre-process of gold coating. Feed rate: 1mL/h.

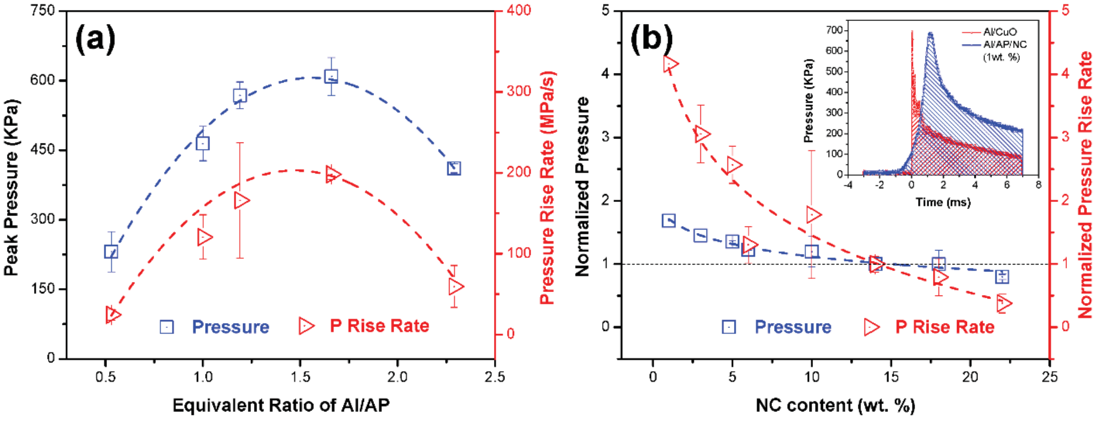

Figure 30: Peak pressure, pressurization rate changes with the equivalent ratio of Al/AP (a, NC is 14 wt. %) and the NC content (b, equivalent ratio: 1.19), respectively. Sample mass was fixed at 25.0 mg and three runs were conducted for each sample.

Nanocalorimetry coupled Time-of-Flight Mass Spectrometry: Identifying evolved species during high rate thermal measurements

We report on measurements integrating a nanocalorimeter sensor into a time-of-flight mass spectrometer (TOFMS) for simultaneous thermal and speciation measurements at high heating rates (Fig. 31). The nanocalorimeter sensor was incorporated into the extraction region of the TOFMS system to provide sample heating and thermal information essentially simultaneously with the evolved species identification. This approach can be used to measure reactions and evolved species for a variety of microstructures such as nanoparticles and thin films. Furthermore, since the calorimetry is conducted within the same proximal volume as ionization and ion-extraction, evolved species detected are in a collision-free environment and thus the possibility exists to interrogate intermediate and radical species. We present measurements showing the decomposition of ammonium perchlorate, copper oxide nanoparticles and sodium azotetrazolate (Fig. 32). The rapid, controlled and quantifiable heating rate capabilities of the nanocalorimeter coupled with the 0.1 ms temporal resolution of the TOFMS provide a new measurement capability and insight into high rate reactions, such as those seen with reactive and energetic materials, and thermal desorption measurements, critical for catalyst characterization and selection.

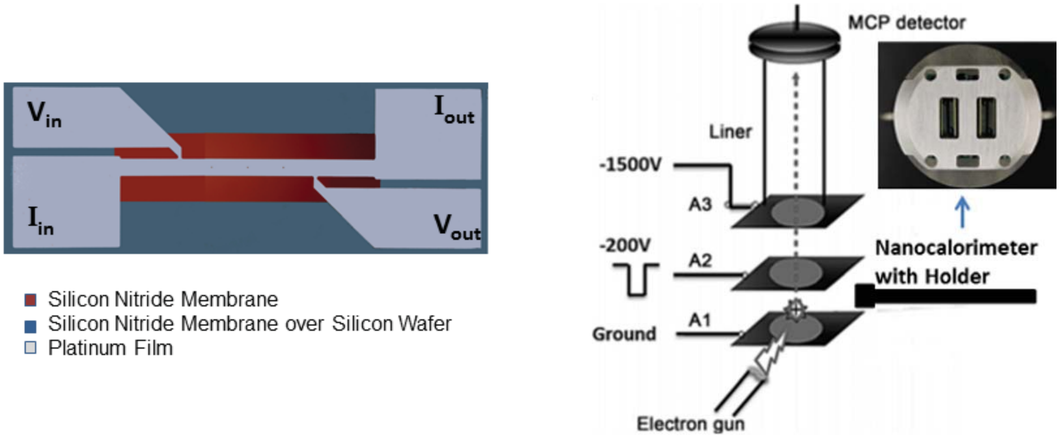

(a) (b)

Figure 31: (a) top review of a typical nanocalorimetry chip, (b) schematic diagram of the nanocalorimeter integrated into the TOF-MS.

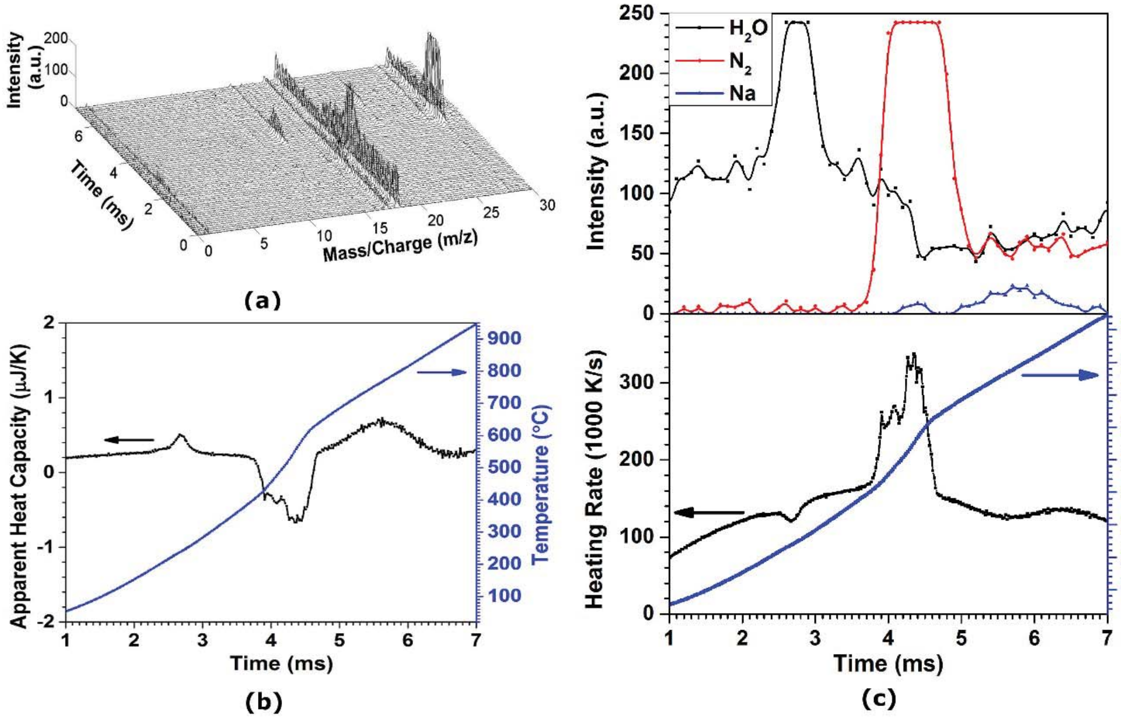

Figure 32: Results for sodium azotetrazolate (Na-TZ). (a) mass spectra, (b) thermal analysis based on nanocalorimetry, (c) synchronized signals of mass spectra and thermal analysis.

In summary UMD's (Eichhorn and Zachariah) has developed new cluster-based materials and reassembled them into microscale components that would enable easier implementation and or enhanced reactive properties.

SOLID FUELS AND COMPOSITE PROPELLANTS WITH NANOSTRUCTURED REACTIVE PARTICLES

S.F. Son, Purdue University, and L. Groven, SDSMT

The objectives of this trust were to fabricate nanoscale-based propellants and characterize their performance. We made significant contributions in several areas including: 1) advanced OH PLIF diagnostics, 2) aluminum fuels with inclusions, 3) encapsulated nanoscale catalysts in ammonium perchlorate, 4) aluminum-lithium based propellants, and reactive nanoscale wires in propellants. The results from these studies are well-documented in the publications listed in this report. Here we will focus on one area, specifically on encapsulated nanoscale particles and inclusions in solid propellant ingredients.

Encapsulated Nanoscale Catalysts

Catalyst efficacy generally scales with surface area [40]. However, the addition of nanoscale particles, such as high surface area catalysts, can result in high processing viscosities, and ultimately brittle composite propellants. This could be alleviated with the use of additional binder; however, performance would be decreased. A possible solution to this dilemma is to encapsulate the catalysts within the crystalline oxidizer particles [41-43]. Since the high surface area components remain within the crystal, rheology and ultimate mechanical properties are unaffected. In addition, the catalyst could be expected to be more effective within an oxidizer crystal than mixed directly into the binder.

Figure 33: Schematic of process to encapsulate nanoscale particles into ammonium perchlorate.

The approach taken by Reese *et al.* [42] and Isert *et al.* [43] to encapsulate nanoscale iron oxide into ammonium perchlorate (AP) is shown schematically in Fig. 33, and the reader is referred to the references for full details. Briefly, a fast-crash solvent-antisolvent approach is used with the nanoscale particles acting as nucleation sites for the crystallization process. Importantly, a fast crystallization process results in preferential nucleation rather than crystal growth, producing catalyst particles that are captured within or physically bonded to crystal surfaces. A slower crystallization process is less effective at capturing particles since crystallization tends to be a purification process. Fortunately, the size produced using this process is appropriate for replacing typical finer AP crystals, which are nominally 25 µm in size.

Reese *et al.* [42] also showed that capture is dependent on antisolvent-to-solvent ratio. Specifically, increased quantities of antisolvent yielded faster nucleation rates, smaller crystals, and improved capture. Sonication of the synthesized materials in a hexane bath also showed that well-captured materials could not be easily displaced from the AP crystals. Inductively coupled plasma emission spectroscopy was used to quantify the level of catalyst captured (up to 92% capture rate was demonstrated). This high level of capture indicates that the nanoscale particles are effective at nucleating crystal growth. Thermogravimetric analysis showed that decomposition was accelerated with encapsulated catalysts over the physical mixtures, as one might expect with more intimate contact.

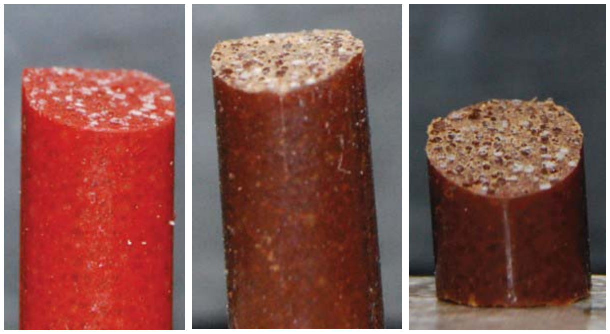

Figure 34: Images of the catalyzed propellant strands (5.8 mm diameter) used by Isert *et al.* [4] [43]. From left to right, 53 µm catalysts mixed in directly, 3 nm catalyst mixed in directly, and 3 nm catalysts encapsulated (inside AP fines only).

Reese *et al.* [42] also showed that capturing the catalysts inside the crystals yielded a significant decrease in particle surface area compared to a physical mix. Again, this would be expected to result in better propellant rheology and final mechanical properties. Initial encapsulation results were also promising for nanoaluminum with ammonium perchlorate and nanoaluminum with cyclotrimethylenetrinitramine (RDX) systems, but more work is needed to optimize and characterize those results. These latter systems may be particularly interesting for explosives applications, but should be carefully explored because sensitivity and compatibility may prove to be unacceptable.

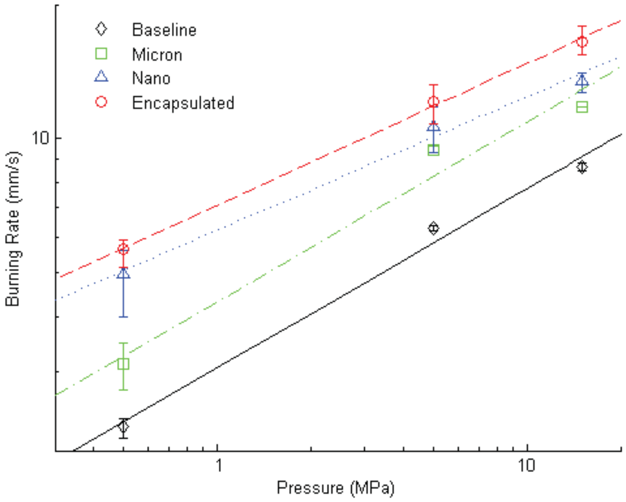

Figure 35: Measured global propellant burning rates. The burning rates for the baseline propellant (Baseline), propellant with micrometer-sized catalyst (Micron), propellant with nano-sized catalyst (Nano), and propellant with the encapsulated catalyst (Encapsulated) are shown. (Modified from [43]).

Isert *et al.* [43] recently explored the effect of the composite particles (fine AP with encapsulated nano-iron oxide catalyst) on the burning rate and flame structure of an AP-based composite propellant. The coarse AP powders used remained the same (with no encapsulated catalyst). The propellant containing the encapsulated catalyst particles was compared to a baseline propellant without a catalyst, a propellant formulated with micrometer-sized catalyst, and a propellant with the same nano-sized catalyst mixed directly. The catalyst loading was held constant. Images of the catalyzed propellants are shown in Fig. 34. The measured burning rates (Fig. 35) showed that the encapsulated fine AP yielded the highest burning rate, followed by nanoscale catalyst mixed in directly.

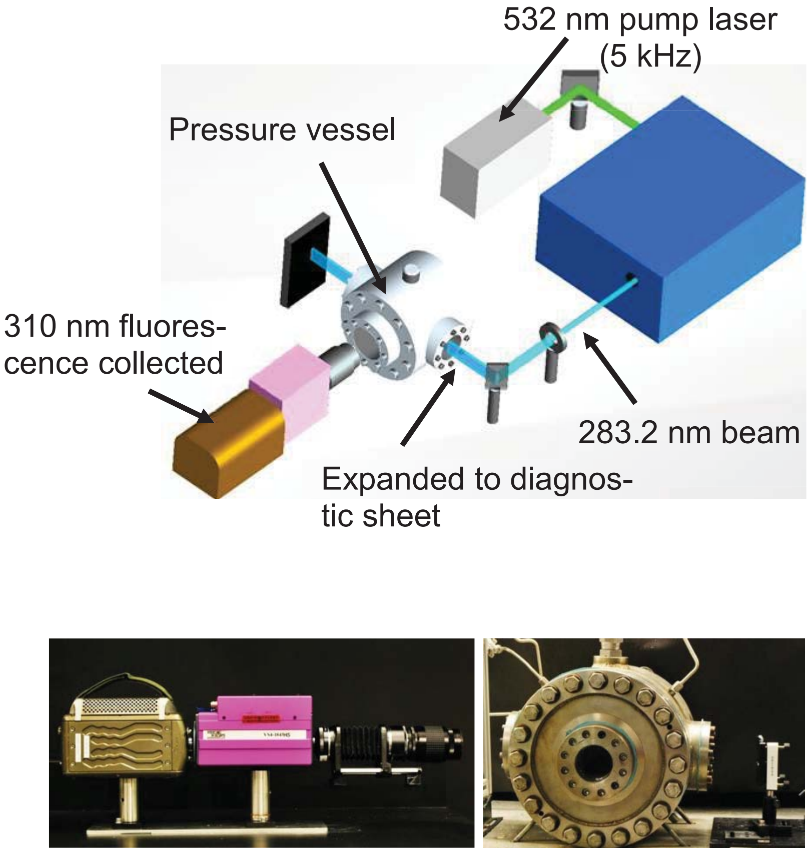

Figure 36: Schematic of the high-speed PLIF system used and images of the camera system and combustion vessel used.

Overall burning rates are useful in evaluating the effectiveness of the encapsulated catalysts in comparison to other formulations, but do not explain why encapsulation dramatically improves burning rate. To understand why this enhancement occurs, direct imaging of the solid propellant flame structure can be done *in situ* using OH planar laser-induced fluorescence (PLIF) [43-47]. Isert *et al.* [43] employed high-speed (5 kHz) OH PLIF to investigate microscale flame structure and single coarse crystal combustion properties (ignition delay and burning time/rate) for the different formulated composite propellants. Since the AP crystals fluoresce in the UV laser sheet, the coarse crystals are visualized clearly. A schematic is shown in Fig. 36, along with images of the camera with intensifier and lens that were used. At higher pressures, adequate signal to noise could not be achieved. Propellants were burned in air at 1 atm, and experiments at pressure were performed in a combustion bomb pressurized with nitrogen at pressures of up to 0.72 MPa.

An example of the kind of imaging obtainable is shown in Fig. 37. The dashed line shows the propellant surface location of the fine AP and binder. For the baseline propellant at elevated pressures, very few coarse particles can be observed protruding above the surrounding fine AP and binder. With the addition of micrometer-sized catalyst, the coarse crystals protrude due to the relatively accelerated burning of the fine AP and binder matrix with respect to the coarse AP. As expected, nanoscale catalysts are more effective, especially if encapsulated, and this is clearly seen by even more protrusion. As the fine AP/binder matrix in the encapsulated catalyst propellant burns away more rapidly, the coarse crystals are exposed to high temperatures sooner, increasing coarse crystal burning rate. In addition, the rapid matrix combustion occurring from encapsulation can cause the coarse crystals to be ejected from the propellant surface [43].

Additionally, dynamic OH PLIF can also be used to quantify the ignition delay of the coarse AP crystals, flame structure, and flame heights [43]. The burning rate enhancement of coarse AP crystals is due in part to the shortening of the coarse AP crystal ignition delay, but this is only significant only at very low pressures. Direct catalyst addition was observed to have some effect on coarse AP burning rate/lifetime. However, comparing the nano-catalyzed and encapsulated catalyst propellants, the differences in global burning rate are not primarily a function of coarse crystal burning rate. The main differences are due to the rate at which the fine AP/binder matrix burns. Interestingly, encapsulated catalyst had no effect on coarse crystal burning rate as compared to nano-catalyzed propellants, as evidenced by no observed statistical difference in the local coarse crystal burning rates [43].

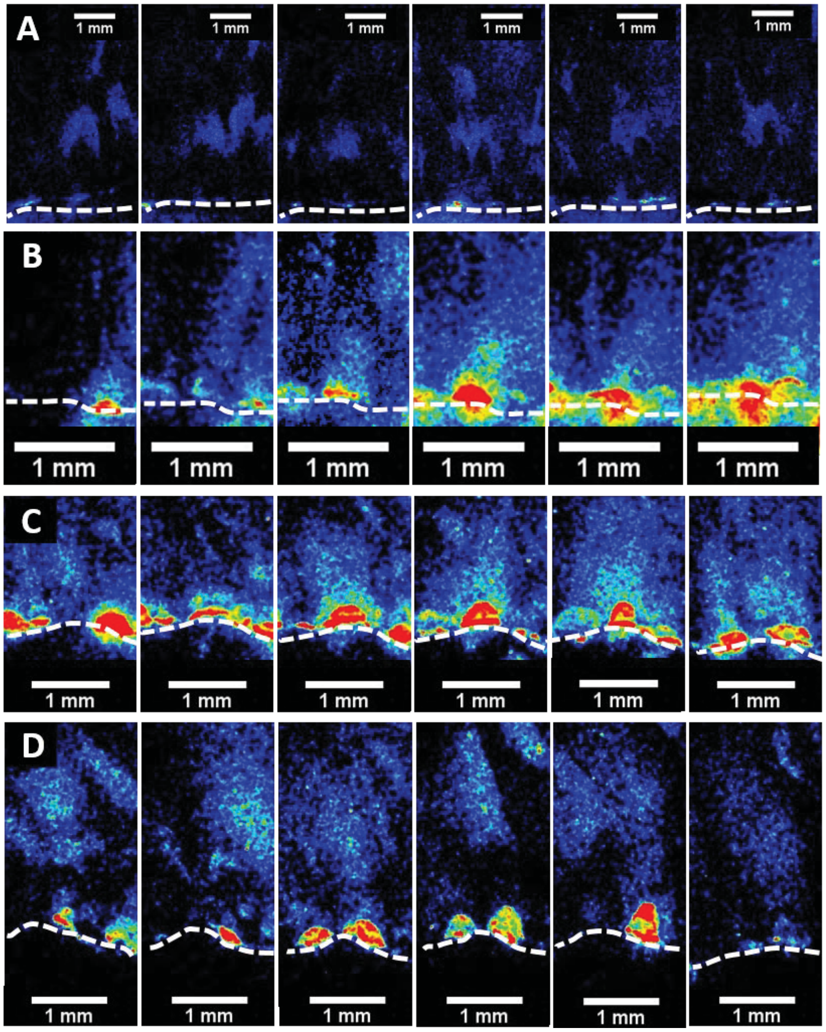

Figure 37: An example of the OH PLIF imaging obtained for baseline propellant (A), propellant with micrometer-sized catalyst (B), propellant with nano-sized catalyst (C), and propellant with the encapsulated catalyst (D). Images were taken at 0.7 MPa and the time intervals are 40 ms, 30.8 ms, 25.3 ms, and 35.4 ms for A, B, C, and D respectively.

Current work is focusing on other higher surface area catalysts, including the encapsulation of decorated graphene-based catalysts. Graphene-based catalysts have ultrahigh surface areas and have been shown to increase low pressure neat nitromethane combustion significantly with only low (< 1 wt.%) addition [48]. Such materials might also be able to be encapsulated within AP. It is also clear that high-speed OH PLIF is proving to be a very useful tool in gaining a more fundamental understanding of how changes in the propellant composition affect the flame structure and surface dynamics. Consequently, we can gain a much more fundamental understanding of what is causing the change in burning rate. This technique could be extended to other species, which may give further insight into the combustion process.

Engineered Metallic Fuels and Alloys

In addition to considering nanoscale catalyst particles, nanoscale metal fuels offer potential advantages, including faster burning rates and more complete combustion. Motivated by this, replacing micrometer scale aluminum in energetic materials with nanoscale aluminum has been studied for more than a decade [49]. However, simply substituting micrometer-scale particles with nanoscale particles in propellants can lead to drawbacks including unfavorable rheology and final mechanical properties. Nanoscale aluminum also has a relatively thick oxide layer that reduces the performance. Indeed, examples of fielded propellants containing nanoscale aluminum are not currently found. A key question is how one can obtain the advantages of nanoscale fuels without the drawbacks. Recently, efforts have focused on micrometer scale aluminum particles with an intraparticle nanoscale structure [50-53]. The ideal solution may be a micrometer sized composite particle that has significantly lower ignition temperature, and when ignited produces much smaller particles/droplets.

In multiphase liquid combustion, microexplosions can occur for some miscible liquids, and also in emulsions [54]. The first observation of this appears to be by Ivanov and Nefedov [55] studying emulsions. A key requirement for this to occur is for one of the constituents to be more volatile than the other. For miscible liquids, a disparity between the liquid-phase mass and thermal diffusion is necessary in establishing droplet dynamics. Mass diffusion in a droplet is one to two orders of magnitude slower than thermal diffusion [54], and this disparity in diffusivities holds for a metal droplet (e.g., a very large Lewis number). As a droplet gasifies, the concentration of the more volatile component in the surface region decreases relative to the core. This is because near the surface, the diffusion scale is small so that the volatile component can diffuse out quickly. However, liquid near the center remains relatively unchanged with a higher concentration of the more volatile, lower-boiling-point component. With continued heating, it is possible that the liquid in the interior can be heated beyond the local boiling temperature and become superheated. If this occurs, the interior liquid can suddenly nucleate and gasify once it exceeds the superheat limit (empirically found to be about 90% of the critical temperature for some liquids by Blander and Katz [56]).

For nucleation, the concentration of the more volatile component must be sufficiently high. Again, this nucleation can result in significant internal pressures and result in fragmentation or breakup of the droplet, as has been observed by many researchers [54]. This has often been termed droplet microexplosion. Importantly, for microexplosion to occur, the volatilities of the components must be sufficiently different. Microexplosion is also more likely with increasing pressure [54], but one could expect that at very high pressures it may become inhibited. With the surface relatively devoid of the more volatile component, vaporization can occur just under this surface region causing “eruptions” and subsequent ejections of smaller droplets. Here we term this phenomenon dispersive boiling. This has been observed in other systems such as gelled fuels [57], although the mechanism there is driven by a surface buildup of the gelling agent rather than the accumulation of a less volatile component. However, the concept is similar.

In contrast to miscible liquids that are a single liquid phase of two or more liquids mixed on the molecular level, emulsions are multiple phase mixtures of liquids that are not mixed molecularly. Water-in-oil emulsions are the most common systems considered in combustion studies, with water droplets dispersed within an oil fuel. A small amount of surfactant is used to stabilize the system. Again, the embedded more volatile component (often water) can be heated to its limit of superheat and violently disperse the droplet. Microexplosion of emulsions are reported to occur more readily, more often, and with more intensity than miscible mixtures [54]. The reason for this is that the more volatile component may not be as inhibited from nucleating by the less-volatile component in emulsions.

Shattering microexplosions and dispersive boiling of metal fuels, such as aluminum in propellants or other energetic material applications, would clearly be beneficial. For example, droplet breakup in a rocket motor could decrease the size of the burning aluminum droplets and therefore improve combustion efficiency and decrease two-phase flow losses that can be up to about 10% [58-60]. In addition, injection of droplets cannot be directly controlled in solid propellants, as with liquid systems with injector design, so shattering microexplosion and dispersive boiling of engineered aluminum droplets is of significant practical interest.

In a clear analogy to liquid fuels, metal alloys are like miscible liquid fuels in that the atoms or molecules are mixed intimately to form a single phase, eutectic, or solid solution. Likewise, inclusions of more volatile materials within a metal fuel (e.g., a polymer in aluminum), are the equivalent to an emulsion where multiple phases are intertwined together but not atomically or molecularly mixed. The intertwining of phases in a metal can be achieved using milling processes, which can result in lower particle ignition temperatures and dispersive dynamics [50-53]. This method is also inexpensive and readily scalable. Another approach to achieve a similar outcome could be the direct bottom-up fabrication of nanoscale fuel particles held together with a more volatile binder [61]. These composite particles also exhibit lower ignition temperatures and dispersive dynamics. To date very little research has been directed toward these modified fuel particles and much more research is needed. In the following we review some recent efforts.

Composites of Nanoscale Aluminum Particles

As discussed above, one approach to obtain a micrometer sized particle with nanoscale features is to assemble a particle composed of nanoscale metal (e.g., aluminum) with a binder. An example of this work, described earlier in this report (Wang *et al.* [61]), considered the fabrication of a composite particle composed of nanoaluminum (oxide passivated) and a nitrocellulose binder using an electrospray technique. In addition to being gas producing, nitrocellulose is an energetic material itself. Additionally, nitrocellulose produces water as it reacts, which can then subsequently react with the aluminum. The microsphere composites showed enhanced combustion behavior when ignited by rapid wire heating compared to micrometer sized aluminum and nanoaluminum alone. As described earlier, the UMD group with Young [62] formulated a solid propellant with these aluminum mesoparticles. In comparison with micrometer scale aluminum particles, the burning rate was 35 wt.% higher and high-speed imaging qualitatively showed less agglomeration.

This bottom-up approach, and others, shows significant promise. However, there may be some drawbacks such as the oxide passivation on the nanoscale aluminum or the presence of voids in the mesoparticles making the theoretical maximum density less than expected.

Micrometer Sized Aluminum Particles with Inclusions

An alternative approach to fabricating macroscale composites composed of nanoscale particles is to engineer composite particles by beginning with micrometer sized aluminum and introducing nanoscale inclusions of another, more volatile material, again analogous to a liquid emulsion. One approach is using mechanical activation (MA), which is the process of milling an inclusion material into a parent material (e.g., a polymer into aluminum). This process with proper choice of milling conditions can result in micrometer scale particles with nanoscale intraparticle features [50-53]. This approach is illustrated conceptually in Fig. 38, along with a scanning electron microscopic (SEM) image of an engineered composite particle. Mechanical activation is a scalable approach and can yield high-density, nanostructured particles with high energy (aluminum) content, as shown by Sippel *et al.* [50]. Due to the lower quantity of oxide present on particles, their combustion enthalpy can be as much as 60% higher than similar mixtures of nanoaluminum and nano-oxidizers. Most importantly, the presence of polymer inclusions with low volatilization temperature can result in microexplosions and enhanced particle breakup, earlier particle ignition, and faster combustion.

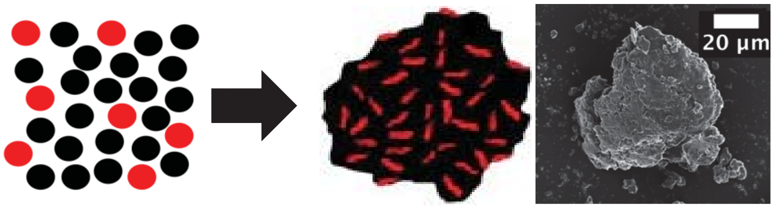

Figure 38: A schematic of the concept of producing a fuel particle with inclusions (left) where initial particles are milled to produce a micrometer scale particle with inclusions. An SEM image of an Al/PTFE particle is shown on the right.

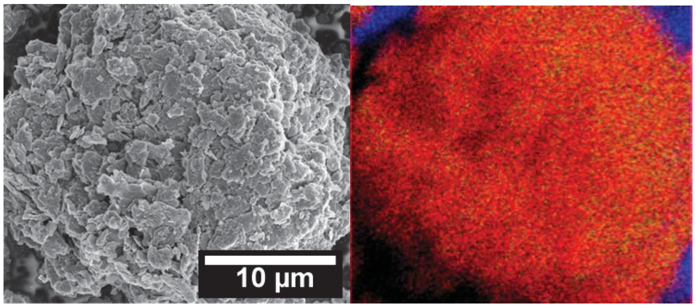

Figure 39: An SEM image of a single Al/PMF particle and EDS compositional map showing presence of atomic aluminum, fluorine, and carbon for 70/30 wt.% Al/PMF milled for 52 h. (modified from [50]). Al= red, C= blue, and F = green.

In addition to inclusion materials that simply have a higher volatility (but are nominally non-interacting with aluminum), some inclusion materials can react directly with aluminum such as oxidizing and fluorinating inclusion materials. Materials that have been considered include poly(carbonmonofluoride) (PMF) and polytetrafluoroethylene (PTFE). PMF is also commonly referred to as graphite fluoride. Due to its graphitic nature, a composite of very finely divided layers of PMF and aluminum results. Figure 39 shows an SEM image of such a composite particle and also the corresponding energy dispersive x-ray spectroscopy (EDS) atomic map. This shows a very uniform distribution of PMF, as indicated by the fluorine (green dots distributed in the image). These composite particles can be fabricated to be very electrostatic discharge sensitive, as well as optically sensitive (camera flash ignition has been demonstrated) [51]. Both of these characteristics are shared with nanoscale aluminum, though Al/PMF particles are nearly 400 times larger in diameter.

Sippel *et al.* [50,52] also considered inclusions of PTFE with aluminum in composite particles. These particles were thoroughly characterized and were used in a composite propellant. Using microscopic imaging, it was observed that the tailored particles promptly ignite at the burning surface and break into smaller particles, which can increase the heat feedback to the burning surface and improve combustion efficiency. Figure 40 shows two images from high speed microscopic imaging of a baseline spherical aluminized AP composite propellant and a similar propellant with aluminum replaced by the same amount of 70/30 wt.% Al/PTFE composite particles. It is clear that although the initial sizes are very nearly the same, particles ignite much more readily, as evidenced by the higher surface luminosity. Additionally, Al/PTFE results in much smaller burning particles that leave the burning surface with higher velocity. This is indicated by many longer luminous streaks observed above the propellant surface. Since aluminum and Al/PTFE particles were sieved to similar sizes prior to use, this also indicates smaller burning fragments are produced from breakup of Al/PTFE particles during combustion.

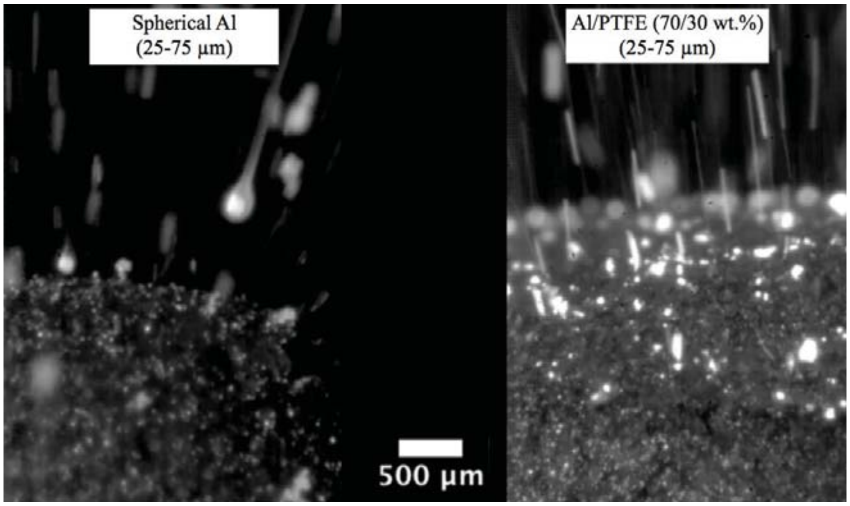

Figure 40: The left image is from a high-speed microscopic video of baseline spherical aluminized AP composite propellant. The right image is for an Al/PTFE 70/30 wt.% based propellant. Images were captured with the same exposure duration.

To quantify the size of the product droplets formed, combustion products were collected using a plume traversing collection plate and were subsequently analyzed microscopically. Figure 40 shows particles collected from both the baseline spherical aluminized and the 70/30 wt.% Al/PTFE containing propellants. The differences are seen to be dramatic. The baseline propellant product sizes are much larger than the 70/30 wt.% Al/PTFE based propellant. From analysis of the captured condensed phase products, it is clear that the propellant with modified aluminum particles results in faster, more complete aluminum combustion. Both Al/PTFE 90/10 and 70/30 wt.% composite particles were observed to reduce the coarse product fraction and diameter. The most significant reduction occurs for the 70/30 wt.% based propellant, where average coarse product diameter is 25 μm, which is smaller than the original Al/PTFE particle size, and is also smaller than the 76 μm average coarse products size collected from baseline spherical aluminized propellant. Some unreacted crystalline aluminum and AP was observed in the x-ray diffraction of the spherical baseline propellant, compared to none for the modified aluminum composite-based propellants. The enhanced aluminum combustion observed with use of modified aluminum also results in a 25% increase in propellant burning rate at 6.89 MPa due to improved heat feedback to the propellant surface as aluminum droplets burn closer to the surface.

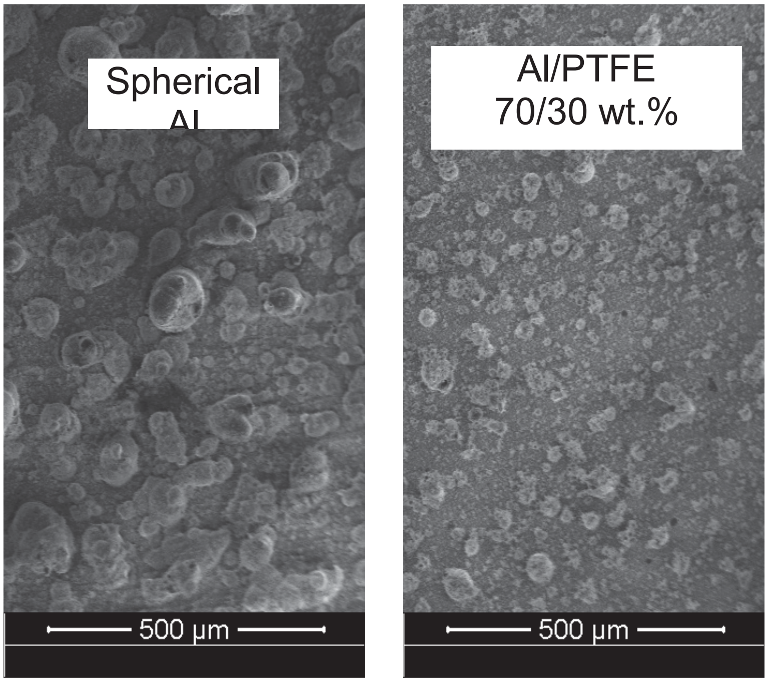

Figure 41: The left image is of particles collected from a baseline spherical aluminized propellant. The right image is for Al/PTFE 70/30 wt.% based propellant.

Though the incorporation of reactive polymer inclusions (e.g. fluoropolymers) within aluminum can significantly enhance combustion, it is unclear whether inclusion-aluminum reactivity is requisite to ignition and combustion enhancement. To investigate this question, aluminum modified with low-density polyethylene (LDPE) inclusions were considered recently in propellants [53]. Unlike fluorocarbons, LDPE is not expected to have significant chemical reactivity with the aluminum. In a solid propellant formulation, the results are qualitatively similar to those found with use of PTFE inclusions, and product size was significantly reduced for the Al/LDPE particles as well. The similar results indicate that the gasification properties are likely the most important in regard to breakup of particles and droplets in propellant configurations. An advantage of LDPE inclusions is that they could be scaled with much less concern for safety, because little reaction can occur between the Al and LDPE directly.

Current work in this area includes laser ignition of single particles to elucidate the dynamics and heating rate thresholds needed for disruptive ignition. For example, if the heating is slow, gas buildup caused by inclusion decomposition within the particles will simply vent and no breakup will be observed. In addition, work is proceeding to consider other inclusion materials and also other metals or alloys.

It is clear with the ubiquitous use of metals, and especially aluminum, in energetic materials that there are likely other applications of these modified particles, such as use in explosives and pyrotechnics. These other applications are currently being explored. The current milling approach is low cost, scalable and results in high density particles that are roughly the same size as frequently used metal particles (could be considered as drop-in replacements). Open questions include: (1) what inclusion materials would be optimal for specific applications, and (2) what determines the particle microexplosion dynamics precisely.

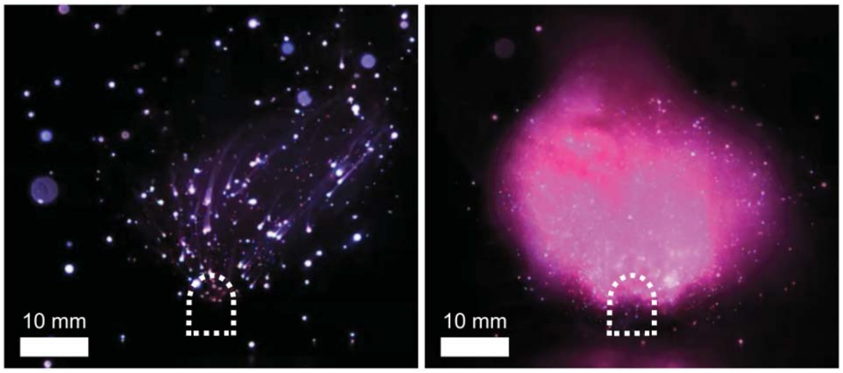

Figure 42: The left image is of a metalized AP propellant burning at 1 atm. The right image is the same propellant, but with aluminum replaced with 80/20 wt.% Al/Li alloy (one-to-one atomic alloy). The dashed line is the propellant strand.

Microexploding Alloy Fuel Particles

We argue here that alloys are the metallic analog of miscible hydrocarbon fuels, and we have begun exploring aluminum-lithium alloys as a replacement for aluminum in propellants, in part because of the possibility for droplet dispersion. As discussed previously, for microexplosive droplet shattering or dispersive boiling to occur, a large difference in constituent volatility is required [54]. The boiling points for aluminum (2519 °C) and lithium (1342 °C) adequately meet the volatility requirement. The results of thermochemical equilibrium calculations show that aluminum-lithium alloys can be formulated in AP composite propellants to have good specific impulse. Also, greatly reduced hydrochloric acid (HCl) is predicted in the products. Significant lithium chloride, LiCl (a gas at these temperatures) forms in the place of HCl because of the halophilic nature of lithium.

Figure 42 shows the combustion of a baseline aluminized AP composite (26.80/61.48/11.72 wt.% Al/AP/HTPB) and a propellant where the aluminum has been replaced with 80/20 wt.% Al/Li intermetallic compound. The magenta color of the flame is due to lithium chloride in the products. Figure 43 shows images from backlit high-speed microscopic videos of the same two propellants. The left image shows the baseline aluminized propellant combustion with large agglomerates forming at the surface. The burning droplets form an alumina cap on the otherwise spherical droplet as they leave the propellant surface, and alumina smoke appears above the droplet surface, forming a long tail. In contrast, the Al/Li alloy propellant surface can be seen to erupt from dispersive boiling, propelling droplets off the surface. Above the surface, larger droplets can also be seen ejecting smaller droplets in a dispersive boiling mode. This is similar to what is observed in gelled droplets (e.g., see [57]). Other droplets (typically smaller droplets) can also be seen to expand quickly and microexplode (shattering the droplet) presumably due to superheated lithium in the droplet core suddenly gasifying and reacting with chlorine. An example of this shattering explosion can clearly be seen in Fig. 43. Alumina smoke above burning droplets and oxide caps on droplet surfaces are rarely observed. Since the flame temperature for the burning droplets is well above the boiling temperature of both lithium and aluminum, homogeneous gas phase reactions are expected to occur in gases away from the surface. The LiCl produced is also gaseous at these temperatures, and the alumina product formed appears to be much smaller than in the baseline propellant. This could reduce two phase flow losses in rocket motors, resulting in further performance improvements.

Figure 44 shows schematically the dynamics of metal combustion. In the top case, a homogeneous metal melts and then burns in a normal fashion. The initial solid particle may or may not be spherical. The middle case shows an alloy system that also melts first, followed by preferential gasification of the more volatile component from the surface, and then dispersive boiling that ejects smaller droplets. The bottom case proceeds similarly, but the core has a higher concentration of the volatile component and the conditions are just right so it can superheat and then suddenly flash to vapor resulting in a shattering microexplosion. Both of these alloy combustion/evaporation modes are observed in the Al/Li based propellant.

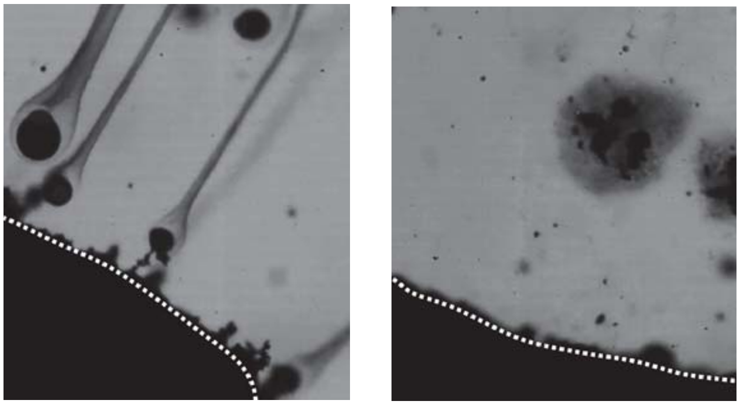

Figure 43: The left image is of a metalized AP propellant burning at 1 atm. The right image is the same propellant, but with aluminum replaced with 80/20 wt.% Al/Li alloy (one-to-one atomic alloy). Note the shattering droplet seen in the right image. The dashed line is the propellant strand. All exposures are 1 μs.

In Figure 45 the temperature and the more volatile species concentration, [V], in an alloy droplet that is evaporating or burning is shown schematically. The surface region lies between diffusion radius (r_d) and the surface radius (r_s), and shows a drop in [V]. Here T_{SH} and $T_{BP,v}$ are the superheating limit temperature and the boiling point of the more volatile component respectively. If the entire core is superheated, then a shattering microexplosion would be expected. However, if only part of the core is superheated, or nucleation is induced near the boiling temperature, then dispersive boiling would be expected that can eject droplets but does not entirely shatter the droplet. A shattering microexplosion would be expected more often for smaller droplets, and this is observed experimentally for this system.

Much work remains to be done with Al/Li based propellants, but initial experiments and calculations appear promising. The Al/Li alloy will react in the presence of water, so stability will need to be addressed and further characterization is needed. Similar to the inclusion materials, other energetic material applications of this alloy are possible and are being explored. Other alloy systems could also be of interest.

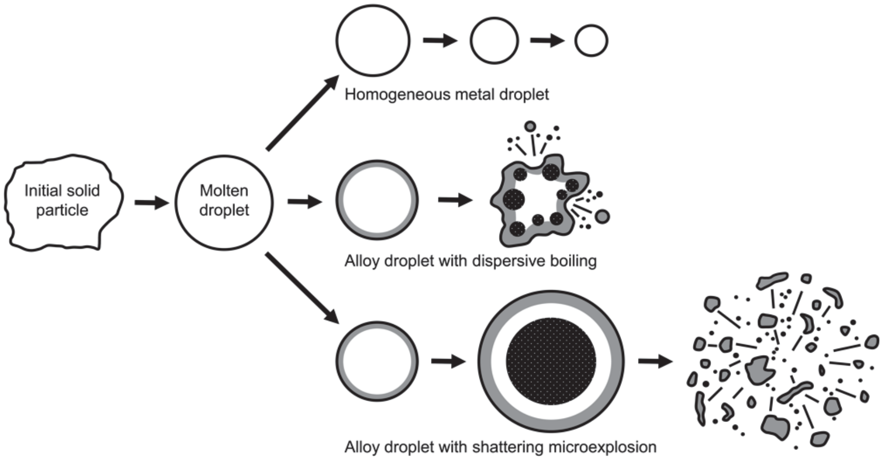

Figure 44: A schematic of homogeneous droplet evaporation, dispersive boiling, and shattering microexplosion due superheating and flashing to vapor. The gray surface regions indicate the presence of a volatile component concentration gradient and the dark regions indicate vapor nucleation.

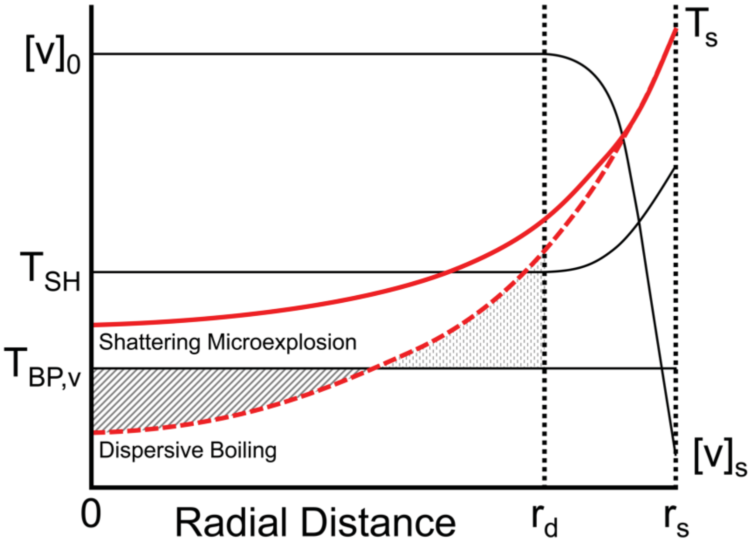

Figure 45: A schematic representation of temperature and more volatile species concentration, [V], in an alloy that is evaporating or burning. Conditions for shattering microexplosions and dispersive boiling are shown schematically.

Conventionally, composite propellant formulators could only change constituents and their size distributions. Nanoscale ingredients have promised to improve performance; however, the high surface area brings unintended consequences such as poor rheology and ultimately unacceptable mechanical properties, making adoption unlikely. In this overview, we reviewed some recent efforts to tailor particles to achieve improved performance.

One approach explored is to encapsulate nanoscale materials into crystalline particles. This can be accomplished by using a fast crash process, for example. Encapsulated nanoscale catalysts have shown improved performance over direct physical mixing into an AP composite propellant. Additionally, since most of the high surface area components are within the crystals and not in direct contact with the binder, higher solid loadings than with conventional nanocatalysts can be potentially considered. Other crystal systems and nanoscale fuels could also be explored.

The other dominant solid component in many composite propellants is aluminum powder. As Bob Geisler [63] said, "When God created aluminum powder he realized rocket scientists would over-use it unless he gave it some undesirable characteristics… He made it agglomerate to droplet sizes of up to several hundred micrometers at the surface of solid propellants as it begins to burn….He also provided condensed phase products which accumulate in motor re-circulation zones as useless unexpended slag weight. These products also give rise to two-phase-flow velocity and thermal lag losses which reduce the delivered performance…" The conventional approach of just replacing micrometer-sized aluminum with nanoscale aluminum has not proven to be a viable approach. An alternative is to engineer or tailor the intraparticle structure of micrometer sized particles to have nanoscale features. The proper choice of inclusion materials can lead to dispersive dynamics that produce smaller droplets for combustion and ultimately smaller condensed phase products.

Milling of inclusion materials into metals, like aluminum, has been shown to be an effective approach and shows promise in overcoming some of the vexing problems of using aluminum in solid propellants. The nanoscale intraparticle features of the composite particle leads to much easier ignition, and smaller products are typically formed since the particles fragment when heated. We argue here that metal particles with inclusion materials are analogous to emulsions (e.g., water and fuel oils) studied in hydrocarbon combustion.

Another analogy to hydrocarbon combustion is miscible fuels and metal alloys. It is well known that miscible fuels with disparate volatility can lead to droplet microexplosions (breakup of the droplet by phase change). An example was presented here of initial results from an aluminum-lithium alloy based solid propellant. The burning surface was observed to eject drops from the surface. Some of these droplets, especially the larger ones, continue to boil in a dispersive manner, launching smaller droplets from the mother droplet (termed dispersive boiling here). In others, much of the droplet core can be superheated up to a limit, and then suddenly vaporize due to intraparticle boiling, causing inflation of the aluminum rich surface layer leading to the dramatic shattering of the drop. Further work is needed to fully characterize the aluminum lithium alloy system (and perhaps others), and other applications should also be explored.

Much work lies before in developing each of these approaches to the level that full implementation can occur, but results appear promising. Eventually, high density/energy particles may be fabricated precisely by high throughput, bottom-up processes, but even today, scalable approaches that yield viable high-density composite particles can be engineered for a variety of applications using milling processes.

Future directions include applying additive techniques to print reactive wires in propellants or include multifunctional components, such as piezoelectric or electrical properties. Much of the developed techniques could readily be applied to explosives or pyrotechnics also. Further, modified aluminum could be applied to energy applications with metals as fuel-carriers.

LIQUID FUELS/PROPELLANTS WITH NANOSTRUCTURED REACTIVE PARTICLES

R.A. Yetter, Penn State University, I. Aksay and D. Dabbs, Princeton University, M. Zachariah and B. Eichhorn, UMD

The objective of this effort was to study the dispersion of various composite particle systems into liquid fuels/propellants, while investigating the multifunctionality of these particles with respect to enhancement of fuel/propellant decomposition, injection, and combustion. Such performance enhancements may include reduced ignition delay and/or permit high combustion efficiency in shorter residence times [64-78]. In this respect, smart functional nano-energetic materials, which can be dispersed in liquid propellants, are promising for advanced propulsion systems including rockets, ramjets, scramjets, and pulse detonation engines. These materials can serve as multifunctional additives providing higher endothermicity, reaction rates, and energy density over the pure fuels/propellants. For example, the nanoparticle composites can enhance thermal decomposition of the fuel by forming more reactive products prior to injection into a combustor. Once injected into the combustor, these materials may be used for hypergolic ignition or to catalyze the low temperature oxidation chemistry, reducing ignition delay by releasing sufficient radicals, and enhancing recovery of energy by recombination kinetics in the dissociated products following combustion.

This research focused on the effects of colloidal nanoparticles, such as functionalized graphene sheets (FGS) with and without platinum nanoparticles, on supercritical hydrocarbon pyrolysis in a flow reactor. Extensive pyrolysis experiments were performed which examined the effects of FGS and platinum-decorated FGS (Pt@FGS) on pyrolysis of methylcyclohexane (MCH) and n-dodecane under supercritical conditions. For combustion and fuel injection experiments, the flow reactor experiment was combined with an optically accessible windowed combustion chamber with a single fuel element injector, also operated under supercritical conditions. This setup permitted the injection of fuels under controlled temperature and pressure environments. A schematic of the combined experimental setup is illustrated in Fig. 46. Further details of the combustor are shown in Fig. 47.

The flow reactor (Fig. 46) was modeled after the work of Stewart [71] as an isothermal, isobaric, system. The mixtures were fed using a high-pressure syringe pump through a coiled capillary tube (2.16 mm i.d., 3.18 mm o.d.) immersed in a heated sand bath. The supercritical pyrolysis experiments were conducted at constant temperature and pressure. The composition of the reacted mixture was analyzed using gas chromatography (GC) to evaluate fuel conversion as a function of temperature and fuel composition for a specific flow rate or reaction time. A high–pressure, 10-position valve (MPV) was used to automatically collect multiple, quenched samples in 5 mL storage loops. Pressure transducers (OMEGA PX309-7.5KG5V, with an error of ±0.25%) were used to measure the pressure at the inlet and outlet of the reactor during each experiment. The pressure drop measured across the reactor was typically less than 0.05 MPa. Three K-type thermocouples were affixed to the reactor coil on its outer surface near the beginning, mid-point, and end of the reactor to measure the temperature in the fluidized bath. A custom National Instrument Data Acquisition (DAQ) system was used to record the temperatures and pressures. The maximum uncertainties of the temperature and pressure measurements were ± 1.25% and ± 2.20%, respectively.

During a supercritical pyrolysis experiment, samples of decomposed fuel were collected using the MPV at the operating pressure. At the conclusion of an experiment, liquid-gas separation was performed on each sample, which had been stored at high pressure (approximately 4.72 MPa) and room temperature. The samples were released from the MPV, one loop at a time, into a specially constructed separation and dilution system. Using this apparatus, gaseous and liquid products were separated and diluted to concentrations that could be analyzed accurately using a gas chromatograph. The samples were stored at near atmospheric pressure in a glass bulb, while a stainless-steel bulb was used when the samples were stored at pressures above 760 mmHg. The gaseous products were analyzed using an Agilent 7890A gas chromatograph (GC) equipped with a flame ionization detector (FID) and an HP-Plot Q column. Hydrogen was identified and quantified using an Agilent 3000A micro GC with a thermal conductivity detector (TCD). Gas chromatographic analysis of the liquid products was performed using a Varian CP-3800 GC/FID and a Shimadzu QP-5000 GC-MS. Further details on the flow reactor and sample separation procedure are provided elsewhere [78].

Supercritical combustion experiments were conducted by coupling a supercritical fuel pyrolysis flow reactor with an optically accessible pressure vessel and three-way diverting valve. The system was located in a reinforced concrete test cell and remotely operated. The pressure vessel had a volume of 66.6 cm3 and layered quartz windows (6.35 mm thick sacrificial window and 31.75 mm thick pressure window) on two sides for back-lighting and visualization during operation. The capillary tube injector had an inner diameter, de, of 254 μm and a corresponding length to diameter ratio (L/d_e) of ~ 400. The entire experiment was remotely controlled using a custom LabVIEW operating program. Oxidizer (air) and inert gas (N_2) mass flow rates were controlled using choked flow orifices. High-speed shadowgraph imaging and schlieren technique served to visualize non-reacting, reacting fuel jets, and turbulent flames. The images of fuel jets and turbulent flames obtained using high-speed cinematography and schlieren images are then analyzed and compared between pure (baseline) fuels and the same fuels containing nanometer-sized inert, catalytic, or reactive materials. Spreading angle, ignition delay, and conversion efficiency are characterized as a function of flow rate, temperature and type of nanoparticles.

For the pyrolysis experiments, the reaction mechanisms and kinetics of pure fuels and mixtures with nanoscale particles were investigated using ReaxFF molecular dynamics (MD) simulations to bridge a gap between experimental findings and theoretical understandings. These calculations were conducted with a collaboration with Professor Adri van Duin at Penn State University. Further details of the ReaxFF method can be found in the review papers [79,80] and papers related to this effort.

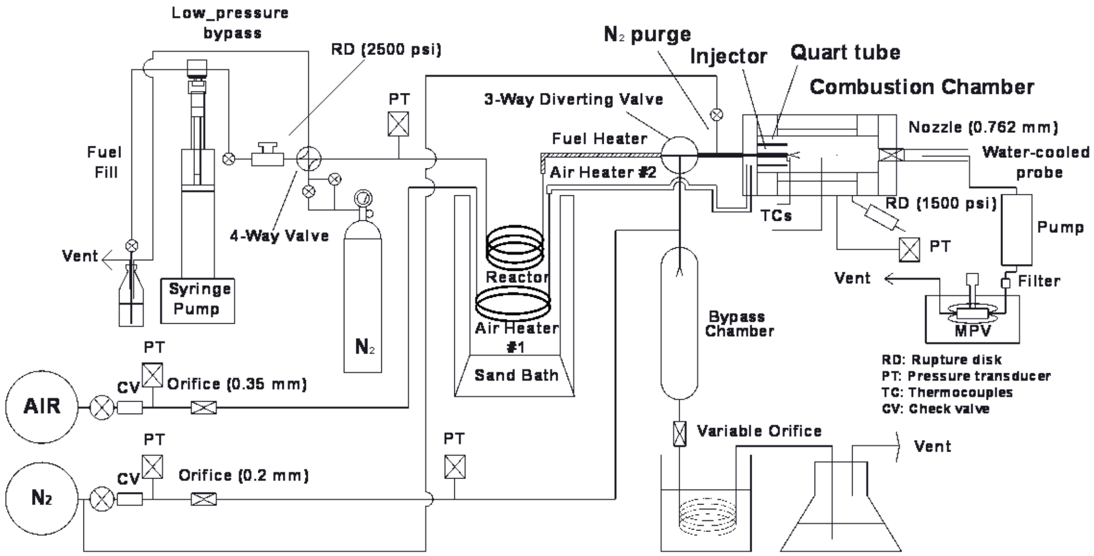

Figure 46: Schematic diagram of the supercritical reactor experiment and optically accessible chamber used for supercritical combustion/injection experiments.

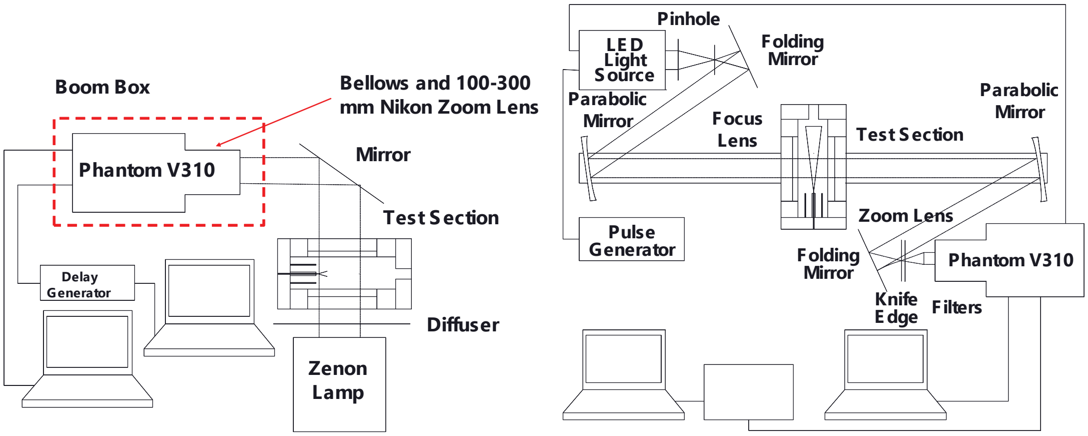

(a) High-speed shadowgraph (b) Schlieren

Figure 47: High speed shadowgraph and schlieren setups.

Supercritical Pyrolysis Experiments of Liquid Propellants with FGS Additives

Figure 48 illustrates the effects of FGS and Pt@FGS additives on n-$C_{12}H_{26}$ conversion under supercritical pyrolysis at three different temperatures (480, 500, and 530 °C), under a constant pressure of 4.75 MPa, and using a constant flow rate of 5.0 mL/min. In the mixtures, the loading concentrations of each suspension were set to 50 ppmw, without regard for the platinum content, or the numbers of defect sites or functional groups. In order to provide a baseline, supercritical thermal decomposition experiments of pure n-$C_{12}H_{26}$ were performed at a similar temperature and pressure under the identical flow rate. Compared to the baseline conversion, FGS-containing n-$C_{12}H_{26}$ at 480 and 500 °C showed minimal, if any, conversion enhancement. On the other hand, the inclusion of 10 ppmw Pt in the n-$C_{12}H_{26}$ (requiring the addition of 50 ppmw Pt@FGS to the n-$C_{12}H_{26}$) clearly showed conversion enhancement over the entire range of tested temperatures.

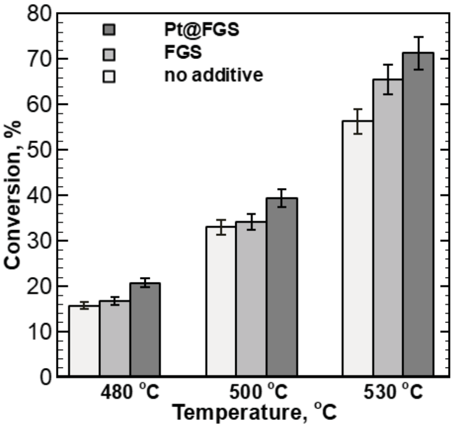

Figure 48: Effect of FGS and Pt@FGS on n-$C_{12}H_{26}$ conversion rate at three different temperatures and at a fixed pressure of 4.75 MPa.

For the supercritical pyrolysis of pure n-$C_{12}H_{26}$ and n-$C_{12}H_{26}$ containing FGS and Pt@FGS 50 ppmw mixtures, the gaseous and liquid products identified and quantified in this study were mainly hydrogen, C_1 to C_{11} n-alkanes, C_2 to C_{12} 1-alkenes, and C_4 to C_{12} 2, 3, 4-alkenes, which is in good agreement with previous studies on the decomposition of pure n-$C_{12}H_{26}$ [81-83]. The product speciation observed from the thermal decomposition of n-$C_{12}H_{26}$ with or without the additives was nearly the same, although significant changes were found in the relative concentrations, particularly hydrogen. With the addition of the particles, the product yields were observed to be higher at different temperatures, particularly for the low molecular weight species. In regards to increases in mole fractions of C_1-C_4 alkanes and C_2-C_4 alkenes with the addition of 50 ppmw Pt@FGS, we found percent increases in the C_1-C_4 alkanes/C_2-C_4 alkenes of 47.1/42.3 % at 480 °C, 23.8/24.8 % at 500 °C, and 30.7/35.2 % at 530 °C, as shown in Fig. 49.

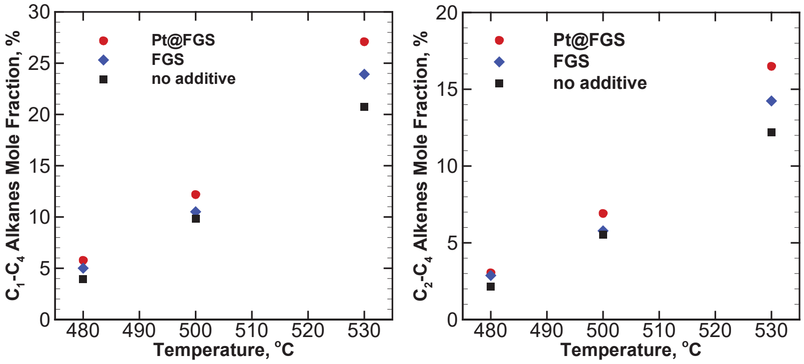

Figure 49: Effect of FGS and Pt@FGS on n-$C_{12}H_{26}$ conversion rate at three different temperatures and at a fixed pressure of 4.75 MPa.

Results presented in Fig. 50 compare the hydrogen selectivity (i.e., the percent yields of products) from supercritical pyrolysis of n-$C_{12}H_{26}$ with and without Pt@FGS. The inclusion of Pt@FGS resulted in higher selectivity for the low molecular weight species such as hydrogen, C_1-C_4 alkanes, and C_2-C_4 alkenes, which because of their molecular size could lead to higher endothermicity during cooling and higher burning rates during combustion [84,85]. Moreover, lower mole fractions were found for the large molecular weight species, such as C_5-C_{11} alkanes and C_5-C_{12} alkenes with increasing temperature. The hydrogen yield was observed to increase from 200 ppm to 2516 ppm (a factor of 12.5) at 480 ºC. Even at 500 and 530 ºC, the selectivity for hydrogen increases by a factor of approximately 2.5. Similar studies have been conducted with methylcyclohexane (MCH) (not reported here) where the presence of Pt@FGS was also observed to enhance dehydrogenation, and increase the yields of hydrogen and toluene, consistent with other studies [86-88] using Pt catalysts to catalyze dehydrogenation of MCH and form increased yields of toluene and hydrogen.

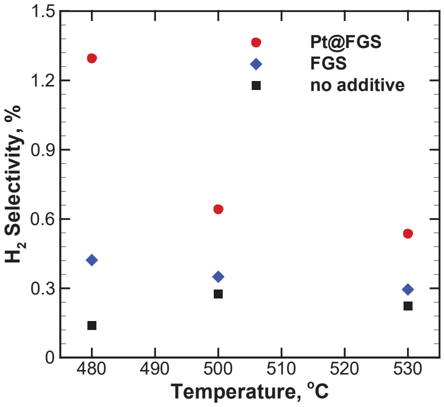

Figure 50: Hydrogen selectivities from n-$C_{12}H_{26}$ pyrolysis with or without FGS and Pt@FGS.

Figure 51 shows a comparison of transmission electron micrograph (TEM) images and particle size distribution on the Pt@FGS before and after supercritical pyrolysis at 530 °C, 4.75 MPa and 5.0 mL/min. The TEM images indicate that the Pt@FGS structure did not change, and in particular, the Pt nanoparticles attached to the FGS remained stable through the course of the reaction. The particle size distribution and average particle size also did not change after the supercritical pyrolysis reaction. Their survival indicates the potential to further use the Pt@FGS in the gas-phase after injection of the fuel into a combustor.

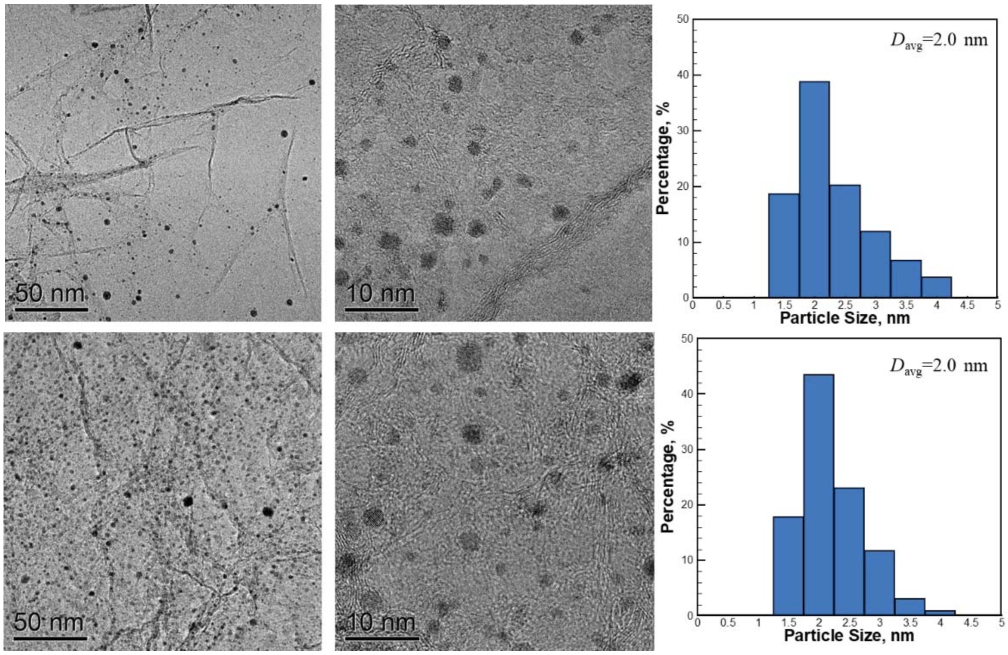

Figure 51: TEM images and Pt particle size distributions of Pt@FGS before (top) and after (bottom) supercritical pyrolysis.

Additional experiments were performed under different flow rates, varying from 2.5 to 8.0 mL/min, corresponding to residence times ranging from 9.1 to 19.6 sec. Over the range of residence times examined, the inclusion of Pt@FGS gave higher conversions than the pure *n*-$C_{12}H_{26}$ baseline, and thus showed the accelerating effect on reaction rates at different extents of reaction. The selectivities for hydrogen and C_2-C_4 alkenes are higher with Pt@FGS at shorter residence times than without Pt@FGS. On the other hand, the selectivities for C_1-C_4 alkanes with and without Pt@FGS increased in a nearly parallel manner with residence time. Increasing temperature and conversion yielded more C_4 to C_{12} branched alkanes, cycloalkanes, and cycloalkenes in *n*-$C_{12}H_{26}$ /Pt@FGS mixtures than in pure *n*-$C_{12}H_{26}$. This result implies that polymerization to form branched or cyclic structures was favored in the presence of Pt@FGS, and thus gave higher selectivities for those structures.

ReaxFF-MD Simulations

In order to support our experimental findings, NVT ReaxFF-MD simulations were performed with system temperatures ranging from 1500 to 1900 K. A previous ReaxFF-MD study [89] suggested that the time step should be approximately 0.1 fs to 0.25 fs to properly conserve energy while describing chemical reactions. Because the system temperatures in this study were as high as 1900 K, a time step of 0.2 fs was chosen to efficiently capture catalytic decomposition during MD simulations. The simulation temperatures considered here are significantly higher, and the residence times are significantly shorter than those found in experimental conditions. However, these MD simulations still provide fundamental insight on the initiation processes altered by the presence of a catalyst in the fuel at a reasonable computational cost.

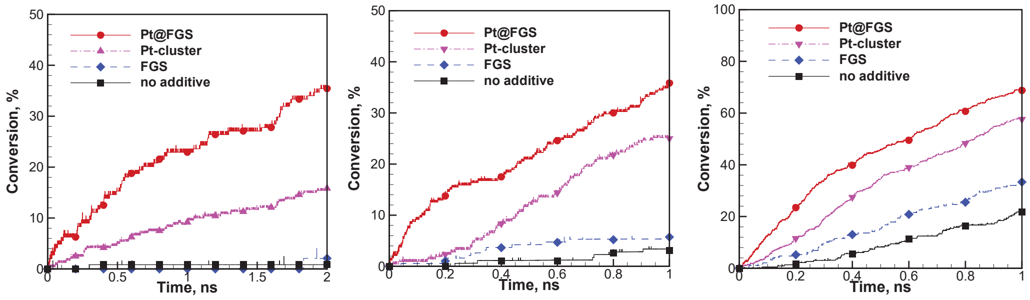

(a) 1500 K (b) 1650 K (c) 1800 K

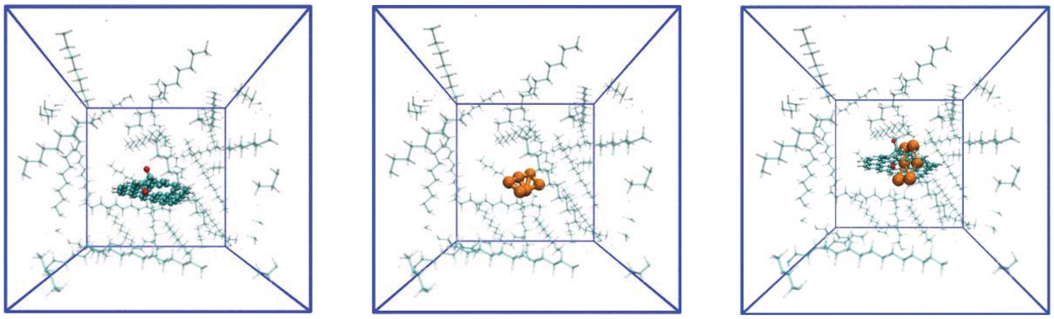

(d) n-$C_{12}H_{26}$ /FGS (e) n-$C_{12}H_{26}$ /Pt-cluster (f) n-$C_{12}H_{26}$ /Pt@FGS

Figure 52: Time evolution of conversion rates for n-$C_{12}H_{26}$ and n-$C_{12}H_{26}$ containing FGS, Pt-cluster, and Pt@FGS at temperatures of 1500 K (d), 1650 K (e), and 1800 K (f) from the NVT ReaxFF-MD simulations. In addition, the initial system configurations of n-$C_{12}H_{26}$ with FGS (d), Pt-cluster (e), and Pt@FGS (f) were shown (cyan: C, white: H, red: O, and orange: Pt).

Figure 52 (a) - (c) shows the time evolution of the conversion rates of n-$C_{12}H_{26}$ containing a FGS, a Pt-cluster, and a Pt@FGS at three different temperatures. The initial system configurations are shown in Fig. 52 (e) – (f). The conversion rates of n-$C_{12}H_{26}$ molecules became significantly faster in the presence of particles. The inclusion of FGS at 1800 K increased the conversion rate by 53 % compared to the pure fuel. When the Pt-cluster and Pt@FGS were present in the fuel, the decomposition rates accelerated even more over the temperature range studied. At 1500 K and 1 ns, the conversion rates in the presence of Pt@FGS (22.9 %) were increased by nearly a factor of 2.5 compared to the Pt-cluster (9.2 %). Pt@FGS was found to exhibit higher catalytic activity at lower temperatures compared to the Pt-cluster case. These results support the pyrolysis experimental observations that the decoration of Pt onto FGS exhibited a further promoting effect on the decomposition of n-$C_{12}H_{26}$.

From the product distribution analysis, the most abundant product was ethylene for all MD simulations, due to the predominant β-scission of the initial fuel radicals such as $C_{12}H_{25}$ and C_nH_{2n-1} ($n \leq 6$). The species found in the simulations were hydrogen, water, C_1 to C_{15} alkanes (C_{12} = fuel), C_2 to C_{12} alkenes, C_4H_6, C_5H_6, C_5H_8, C_6H_8, C_6H_{10}, C_7H_{12}, C_8H_{14}, and some oxygenated compounds such as CH_4O, C_2H_4O, and $C_5H_{12}O$. Major species such as hydrogen, C_1 to C_4 alkanes and C_2 to C_4 alkenes observed in the MD simulations were in good agreement with those from the pyrolysis experiments. Experimental measurements for oxygenates, and in particular CO and CO_2, were made using GC/TCD and GC/FID with methanation catalyst having a minimum detectable limit of approximately 1.0 ppm for CO and CO_2. However, oxygenated species were not detected in any of the experiments. The maximum oxygen content that would be added from the 50 ppmw FGS_{100} addition was estimated to be ~0.5 ppmw. With this level of addition, the oxygenated species would be below the detection limit for GC analysis. The reaction product analysis of MD simulations indicates that mole fraction of the oxygenated species was observed to be relatively low and smaller than that of water molecule. Furthermore, formation of water molecules appeared to be more favored at higher temperatures than at low temperatures.

Figure 53 presents the time evolutions of major products (H_2, C_1-C_4 n-alkanes, and C_2-C_4 alkenes) during MD simulations. Consistent with the experimental observation, the introduction of Pt@FGS showed the highest hydrogen formation over the other additives. Formation of low-carbon-number products was increased by adding Pt@FGS to the fuel compared to the cases with only FGS added to the fuel and the pure fuel. As a minor species, the water molecule was observed to form in the presence of FGS and Pt@FGS due to the participation of the hydroxyl radical (OH) in the fuel decomposition. Some oxygenated compounds such as acetaldehyde (C_2H_4O) were also found for both cases, indicating that the oxygen-functional groups that decorate FGS reacted with the fuel molecules or their derivatives. The observation of minor species including C_4H_6, C_5H_6, C_5H_8, C_6H_8, C_6H_{10}, C_7H_{12}, and C_8H_{14}, support the measurements of branched and cyclic species from the pyrolysis experiments [71]. Unlike the experimental observation, a series of 1-alkenes was a major group of the products in the MD simulations. This clear difference between the experiments and simulations is partially due to the much higher temperatures of the simulations, which lead to β-scission rather than recombination of the small hydrocarbon radicals to form alkanes.

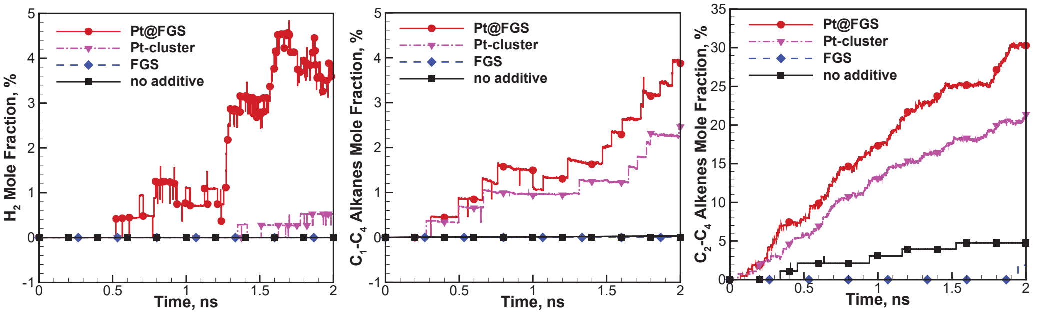

(a) 1500 K

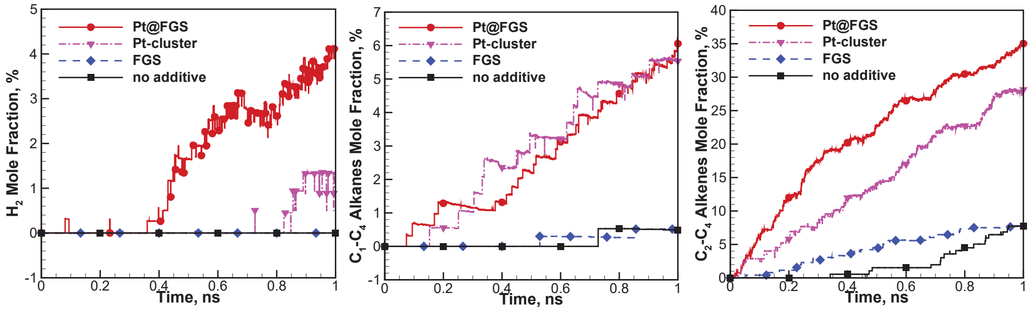

(b) 1650 K

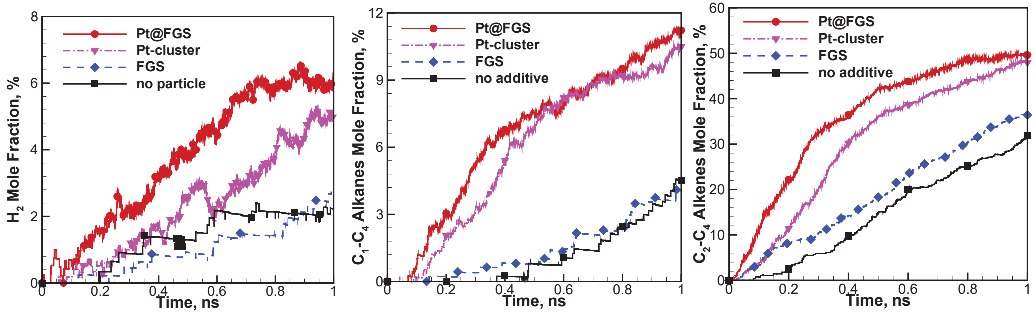

(c) 1800 K

Figure 53: Time evolution of mole fractions of hydrogen, C_1-C_4 alkanes, and C_2-C_4 alkenes for *n*-$C_{12}H_{26}$ and *n*-$C_{12}H_{26}$ containing FGS, Pt-cluster, and Pt@FGS at temperatures of 1500 K (a), 1650 K (b), and 1800 K (c) from the NVT ReaxFF simulations.

A comparison of the kinetic parameters between the experiments and ReaxFF-MD simulations is summarized in Table 6. The global activation energy and pre-exponential factor were calculated using first-order global kinetics. For the pure fuel, the pre-exponential factor and activation energies determined from the ReaxFF-MD simulations qualitatively agreed with the experimental values. Pt@FGS resulted in the largest reduction in activation energy because the Pt cluster was assisted in catalyzing the fuel pyrolysis by the FGS substrate. This reduction in activation energy may provide further enhancement on the conversion rate of the fuel in the presence of Pt@FGS.

Table 6: Kinetic parameters for decomposition of n-$C_{12}H_{26}$ and n-$C_{12}H_{26}$ containing various particles.

Additives	Experiment		MD Simulations	
	E_a	log A	E_a	log A
Pt@FGS	239.8	15.1	135.4	13.0
Pt-cluster	N/A	N/A	173.9	14.0
FGS	266.0	16.2	226.2	15.0
No particle	278.6	17.0	281.0	16.5

Units: **E_a (kJ/mol), log A (1/sec)**

Fuel Decomposition Enhancement Mechanisms

The reaction mechanism for thermal cracking of n-alkanes under supercritical conditions differs significantly from the gas phase reaction mechanism at high temperature and low pressure. For the gas phase reaction, the unimolecular reactions such as carbon-carbon (C-C) or carbon-hydrogen (C-H) bond cleavage are dominant, yielding primary alkyl radicals that undergo successive decomposition by β-scission to produce abundant low molecular weight alkenes such as ethene and propene [71]. This gas phase reaction is, however, in striking contrast to the supercritical phase reaction, which is dominated by secondary bimolecular hydrogen abstraction reactions between alkyl radicals and the fuel [71,81]. The concentration of alkyl radicals is so high at the densities of the supercritical conditions that forming alkanes such as ethane and propane (Fig. 49) is favored unlike the alkenes in the gas phase reaction (Fig. 53). However, even though the reactions responsible for consuming most of the fuel are different between low and high pressures, the reactions that initiate the decomposition are analogous.

The inclusion of Pt@FGS was found to promote both unimolecular and bimolecular reactions, which is supported by the formation of larger amounts of C_1-C_4 alkanes and C_2-C_4 alkenes, compared to the amounts formed by the pyrolysis of pure n-$C_{12}H_{26}$. As discussed previously, Pt@FGS appears to accelerate the overall decomposition during the early stages of reaction via production of a larger radical pool resulting from reactions with lower activation energy (i.e., lower than the barriers associated with C-C and C-H bond scissions or about 335kJ/mol [90]). Bimolecular reactions involving secondary products are promoted due to the higher concentrations of radicals and the higher collision frequency under supercritical conditions. In addition, lower amounts of C_5-C_{11} alkanes and C_5-C_{12} alkenes were found to form in the presence of Pt@FGS with increasing temperature, indicating that the particles likely catalyze the decomposition of high-molecular weight products via secondary reactions [71].

The fuel-consuming reactions observed during the ReaxFF-MD simulations were classified into four categories including C-C bond cleavage, dehydrogenation, hydrogenation, and H-abstraction. Figure 54 shows a comparison of these categories for each particle type at different temperatures. FGS itself served as a catalyst to promote C-C bond cleavage, hydrogenation, or dehydrogenation. Frequent adsorption of fuel molecules onto the FGS surface, observed during the simulations, caused the C-C and C-H bonds of the fuel molecule to often break. In a few cases, dehydrogenation of the fuel molecules was found to occur by losing their hydrogen atoms to the oxygen-functional groups on the FGS. Since the number of these functional groups was limited to only two in the present MD simulations, this process was rarely observed. However, such proton transfer reactions played a major role in previous studies where FGSs were observed to accelerate the flame propagation of liquid nitromethane [95] and the present work on the thermal decomposition of methylcyclohexane (not discussed here).

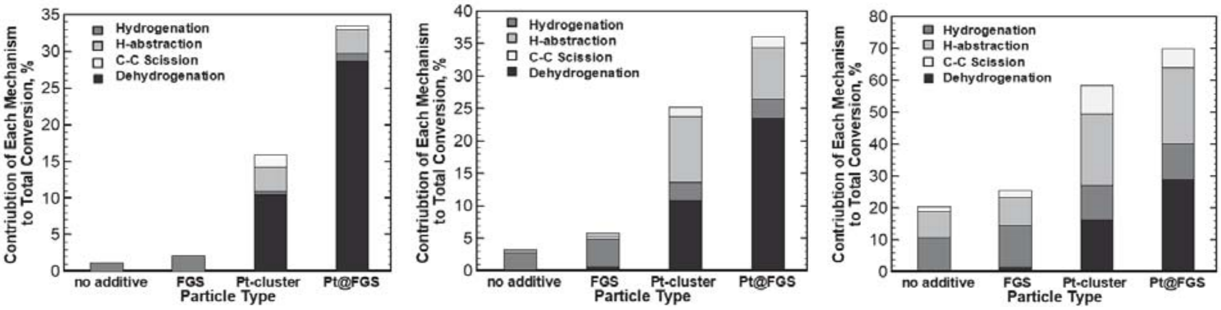

1500 K 1650 K 1800 K

Figure 54: Comparison of reaction mechanisms for pyrolysis of n-$C_{12}H_{26}$ without or with various additives for temperatures ranging from 1500 to 1900 K at a fixed density of 0.31 g/cm^3. (a) 1500 K and t=2.0 ns, (b) 1650 K and t=1.0 ns, and (c) 1800 K and t=1.0 ns.

If a Pt cluster or Pt decorated FGS was present in the mixture, the fuel-consuming reactions were dominated by dehydrogenation via loss of a H atom to the Pt to form n-$C_{12}H_{25}$, particularly at the lower temperatures of 1500 K and 1650 K. The adsorption of the fuel molecule onto a Pt@FGS particle appeared to lower the energy barrier for C-H bond cleavage, even below that of the Pt cluster. The alkyl radical that formed was short-lived and subsequently underwent β-scission, where the products were 1-alkenes and small hydrocarbon radicals. With the hydrogen atom attached to the Pt, a second fuel molecule would quickly adsorb onto the Pt atom, and undergo dehydrogenation. The remaining H atoms attached to the Pt desorbed as molecular hydrogen.

The recovery of a clean Pt surface by desorption of molecular hydrogen was frequently observed during the MD simulations. This observation supports the TEM imaging analysis of Pt@FGS showing that the Pt nanoparticles pinned to the FGS surface were not deformed and contaminated by the high temperature and pressure reactions. As eluded to above, it was found that the Pt@FGS resulted in a higher conversion rate and higher hydrogen yield than did the Pt-cluster, and may result from hydrogen atoms rolling over to the FGS surface, forming molecular hydrogen, which then would separate from the FGS (referred to as hydrogen spillover). However, Psofogiannakis and Froudakis [90,91] recently found that H_2 dissociates quickly from a Pt-cluster, whereas migration of H atoms from the Pt to a graphite surface must overcome a large energy barrier greater than 60 kcal/mol. Because of this high energy barrier, they argued that hydrogen spillover would be difficult to occur. While hydrogen spillover may still be a possibility with the functionalized graphene sheets, such steps were not captured in the post analysis of the modeling results. Other processes were observed that might influence the overall reaction rates, such as the migration of an oxygen atom from the edge of FGS to the Pt surface.

For pure n-$C_{12}H_{26}$ decomposition, or decomposition when particles were present, once radicals formed either by C-C bond rupture in the gas-phase or from dehydrogenation at a particle surface, any large alkyl radical would initially decompose by β-scission. The smaller hydrocarbon radicals that formed, for example C_2H_5 or C_3H_7, would undergo C-H bond cleavage generating free hydrogen atoms. With the build-up of the radical pool, both the small hydrocarbon radicals and the H atoms reacted with the fuel via H-abstraction, making them important fuel consuming steps. Also, the free hydrogen atoms in the gas phase, and to a much lesser extent those attached to surfaces, enabled hydrogenation of the fuel molecule to form carbocations. Thus, hydrogenation became of increased importance with the growth of the hydrogen radical pool at higher temperatures and/or with the presence of Pt.

Gas-phase dissociation of the fuel C-C bonds became more important as the temperature increased because of the high activation energy of these reactions compared to the activation energy for dehydrogenation and hydrogen abstraction steps. In addition to gas-phase dissociation, the fuel molecules were observed to adsorb onto the surface of the particles and to subsequently desorb. However, during desorption, some of the fuel molecules underwent C-C bond cleavage at the weakest bond sites due to the stronger adsorption onto the Pt@FGS thereby leaving small hydrocarbon fragments behind on the particles.

Cracked hydrocarbons that remained bound to the surface are a possible precursor for initiating coke deposition onto the Pt@FGS. While coke deposition can reduce the catalytic activity of Pt@FGS, carbon layers were not observed to form for the conditions of the present study. In some cases, the early breakdown of the Pt catalyst was observed during hydrocarbon interactions at the highest temperatures. In particular, structural distortions and strain in the carbon network of Pt@FGS due to thermal stress were sometimes noticeable at the longest reaction times. The Pt@FGS configurations overall exhibited thermal stability at high temperatures, even while the bonding energies between Pt and FGS are relatively weak.

In summary, the ReaxFF-MD simulations have shed significant light on possible enhancing mechanisms provided by the presence of Pt@FGS on the fuel conversion process. This work investigated theoretically and experimentally the synergetic effects and enhancement mechanisms of colloidal graphene-based additives on supercritical fuel decomposition of normal dodecane. Supercritical pyrolysis experiments showed that the addition of FGS-based particles at a loading concentration of 50 ppmw increased the conversion rates and product yields, preferentially selecting the production of low molecular weight species while diminishing the production of high molecular weight species. Pt@FGS exhibited additional enhancement in the conversion rate of n-$C_{12}H_{26}$ by up to 24.0 % compared to FGS. FGS-based particles appear to alter initiation mechanisms, which result in higher hydrogen formation and low-carbon-number products. Hydrogen selectivity at 480 ºC for n-$C_{12}H_{26}$ decomposition was observed to increase by nearly a factor of 10. The enhancing mechanisms of FGS-based materials on pyrolysis were studied using ReaxFF-MD simulation. The simulation results were in general agreement with the experimental observations, showing enhanced conversion rates and lowered activation energies in the presence of the particles. A combination of Pt and FGS facilitated catalytic dehydrogenation forming a n-$C_{12}H_{25}$ radical. Another catalytic fuel-consuming step is hydrogenation of the fuel molecule resulting in production of a carbocation, as a free hydrogen atom is donated to the fuel molecule. The recovery of the catalyst was observed, resulting from dissociation of H_2 molecule from the surface of the Pt. These results demonstrate that a low mass loading of a high surface area material employed either as an additive or a means of distributing another additive can significantly enhance, and be used to tailor, the conversion of liquid hydrocarbon fuels/propellants under supercritical conditions. Such enhancements benefit practical propulsion systems which require high conversion efficiency in a short residence time. The formation of H_2 and C_2H_4 are particularly useful fuels in the combustion chamber because of their fast reaction rates. The current work further demonstrated that the experimental flow reactor study combined with ReaxFF-MD simulation could provide a guidance to develop the design of novel catalysts as well as understand reaction mechanisms for hydrocarbon fuel decomposition.

Supercritical Combustion of Liquid Propellants with FGS Additives

Supercritical combustion experiments were performed with four different types of particles including inert silica, FGS, 5wt%Pt@FGS, and 20wt%Pt@FGS to investigate the global effects on combustion. Normal dodecane was chosen as a model fuel for a liquid rocket bipropellant fuel. The loading concentrations of the particles were set to 100 ppmw except for inert silica (10^4 ppmw). Two equivalence ratios were tested at 0.19 (fuel flow rate = 2.5 mL/min) and 0.38 (fuel flow rate = 5.0 mL/min).

Figure 55 shows a comparison of the injection, mixing, and ignition sequences of the pure, baseline fuel as well as the same fuel containing 100 ppmw 5wt%Pt@FGS which was heated and cracked under supercritical conditions (shown in Table 7). Measurement of ignition delay time was determined using the known frame rate of the camera and the number of frames captured between the start of injection and ignition kernel formation. The appearance of the fuel jets for the baseline and FGS containing fuels was similar at 3.0 ms, but still developing, whereas the 5wt%Pt@FGS containing fuel jet appeared fully developed. This difference is likely due to the change in fuel composition, catalyzed by 5wt%Pt@FGS. From our pyrolysis experiments, increased low-carbon-number products in the fuel may facilitate jet development in a shorter time. In the presence of 5wt%Pt@FGS, the ignition kernel was observed to form around 3.5 ms, leading to a flame that propagated along the jet. Flame propagation was similar in all cases. The fuel jet development time increased to about 9.0 ms for the no particle case. The captured high-speed images support an autoignition process that occurs by an explosive ignition kernel, which forms downstream of the supercritical jet. The ignition kernel location for pure fuel was observed at about $61.6d_e$, however in the presence of the additives, the kernel formation occurred at approximately $32.8d_e$ downstream of the injector exit. When ignition occurs, many small-scale wrinkles are initially observed about the kernels, whereas once the turbulent flame becomes stabilized, large-scale fluid structures are observed. These flame structures may be related to the turbulent gas-like behavior of supercritical fluids, which is quite different from liquid sprays under subcritical conditions, where break-up of fluid ligaments into droplets is important. This observation is consistent with jet mixing during supercritical combustion of cryogenics [92]. Also, once the diffusion flame is fully developed, fast-moving eddies exist along the flow stream direction, enhancing the local turbulence, mixing, and combustion [93].

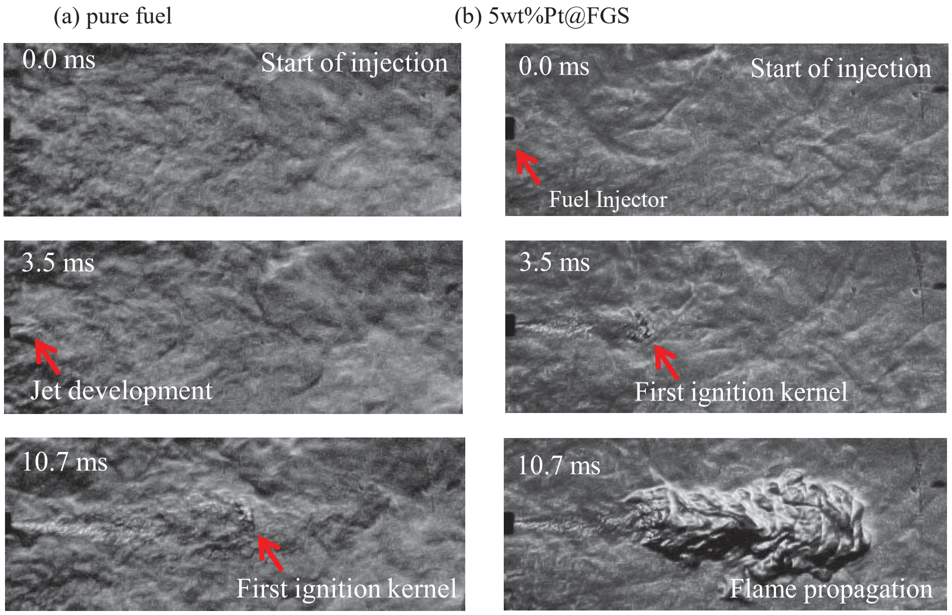
(a) pure fuel (b) 5wt%Pt@FGS

Figure 55: Time sequence of schlieren images starting with injection initiation, penetration, autoignition, and developed-turbulent diffusion flames for (a) pure n-$C_{12}H_{26}$ and (b) n-$C_{12}H_{26}$ containing 100 ppmw 5wt%Pt@FGS at a fuel flow rate of 5.0 mL/min (equivalence ratio of 0.38), Pch,ini=3.49 MPa, Tfuel=832 K, and Tair=777 K.

Table 7: Effect of Particle Additives on Measured Ignition Delay, Flame Lift-off Length, and Percentage Increase in Conversion of n-$C_{12}H_{26}$

Combustion Parameter	Fuel Mixture					
	Pure Fuel	Fuel/silica	Fuel/nAl	Fuel/FGS	Fuel/5% Pt@FGS	Fuel/20% Pt@FGS
Ignition Delay Time (ms)	12.4±1.2	12.1	9.6±1.3	9.4±1.4	4.9±0.5	4.2±0.5
Lift Off Length (mm)	1.7±0.3	N/A	N/A	1.6±0.1	1.2±0.1	0.8±0.1
Increase in Conversion (%)	REF.	-3.0	9.6±2.0	9.0±2.1	24.5±4.8	34.8±3.4

The fuel flow rate was 5.0 mL/min (equivalence ratio of 0.38).
$P_{ch,ini}$=3.49 MPa, T_{fuel}=832 K, and T_{air}=777 K.
The % increase in conversion results are given relative to the pure fuel baseline.

Table 7 shows a comparison of measured ignition delay times for four different particle types including fumed silica, nAl, FGS, and Pt@FGS. For pure fuel, the ignition delay was approximately 12.4 ms. Karwat et al. [94] studied autoignition of n-$C_{12}H_{26}$ using rapid compression experiments, measuring ignition delay times ranging from 44.0 to 56.0 ms over a temperature and pressure range of 710 - 790 K and 0.29 - 0.36 MPa, respectively, for a fixed equivalence ratio of 0.97. Compared to these published lower pressure results, a considerably shorter ignition delay time for cracked n-$C_{12}H_{26}$ under supercritical conditions was measured (12.4 ms). This finding suggests a potential benefit of using a supercritical fuel in an advanced propulsion system. Pt@FGS particle addition reduced the ignition delay time by nearly a factor of 3 compared to the baseline fuel. Specifically, 20wt%Pt@FGS reduced the ignition delay time from 12.4 ms to nearly 4.1 ms. The shorter ignition delay results from the combination effects of Pt@FGS on both the initial fuel pyrolysis and subsequent combustion processes. The graphene-based additives promote production of volatile species (for example, hydrogen and ethylene) during pyrolysis. Because of their faster reaction rates, the presence of these species in the injected fuel aids in reducing the ignition delay time. Although the graphene particles may not necessarily directly be the ignition enhancing mechanism, the defect sites or oxygen-functional groups on the FGS have been shown previously to serve as catalytic sites for enhancing the burning rate of nitromethane, as demonstrated in the liquid strand burning results of Sabourin et al. [95] and the ab initio molecular dynamics studies of Liu et al. [96]. Addition of nAl particles at 1,000 ppmw into the fuel resulted in approximately a 22.8% reduction in ignition delay time. The nAl particles, which are heated nearly to the core melting temperature prior to injection, may facilitate ignition by reacting with available oxidizer. Dreizin [97] revealed that the oxide layer on the aluminum particle changes its phase from amorphous to γ-alumina with increasing temperature up to approximately 900 K. This phase transition of oxide layer may promote the oxidation rate of aluminum particles, which could lead to faster ignition relative to the baseline fuel.

The particle additive effects on the flame lift-off length were studied during steady-state combustion. Time-averaged images of light emission from the diffusion flame were obtained from the high-speed shadowgraphs. The lift-off distance was defined using the steady-state flame structures obtained approximately 1.5 sec after the camera triggered. From the averaged images, the flame front can be determined based on the brightness of the images. The lift-off distance was measured by defining the distance between the injector exit and the flame front, using the known outer diameter of the injector to obtain an appropriate measurement scale. As shown in Table 7, particle addition significantly reduces the lift-off length by up to 53.8% (Pt@FGS). A comparison of measured lift-off distance indicated that the reaction zone stabilized much faster when 20wt%Pt@FGS was added to the fuel. This correlates well with the change in pyrolyzed fuel composition prior to injection, as the increased extent of fuel pyrolysis produces a reduced bulk density, prior to injection, which in turn affects the injection velocities of the fuel into the pressurized chamber.

The particle effect on pressure rise in the combustion chamber was studied and related to the percent conversion of that specific fuel mixture relative to that of the baseline fuel. Calculated percent increases in fuel conversion for the various fuel compositions containing particle additives are presented in Table 7. The percentage increase was calculated based on the averaged pressure rise at the offset time of 3.5 sec for all combustion experiments. Fumed silica seemed to have a negligible effect even at the highest loading of 10^4 ppmw. FGS-based particles including FGS and Pt@FGS all showed an enhancing effect on the percentage increase in conversion. The Pt@FGS at 100 ppmw loading exhibited significant increases of up to 25.0 and 34.9% for 5wt%Pt@FGS and 20wt%Pt@FGS, respectively, relative to the baseline case. From these results, higher loading concentration of Pt onto FGS should be investigated to determine whether even higher conversion can be achieved.

The impact of particle additives on the flame structure, such as flame spreading angle, was investigated using images obtained from high-speed shadowgraphy, captured during steady-state combustion. Flame spreading angles based on the flame boundary for different particle types were analyzed. Figure 56 provides a comparison of 25-frame-averaged images (high speed shadowgraphs) and three different particle types including FGS, 5wt%Pt@FGS20, and 20wt%Pt@FGS20. From these averaged images, flame spreading angles were defined at a downstream length of 26 injector nozzle diameters ($26d_e$) where the spray angles seem to be stabilized. The flame spreading angle was measured from the center line (shown in Fig. 56), to a tangent line drawn along the outer portion of the flame edge at a pre-defined number of jet diameters downstream of the injector. When 20wt%Pt@FGS was present in the fuel, the calculated tangent of the spreading angle was increased by 34.6%. Based on the axisymmetric assumption, increasing the flame spreading angle corresponds to a larger flame area, resulting in greater chemical energy release within the combustor volume and thus an increased chamber pressure.

(a) pure fuel (b) FGS

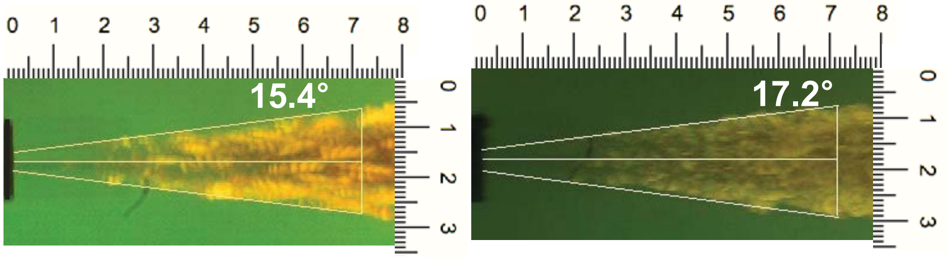

(c) 5wt%Pt@FGS (d) 20wt%Pt@FGS

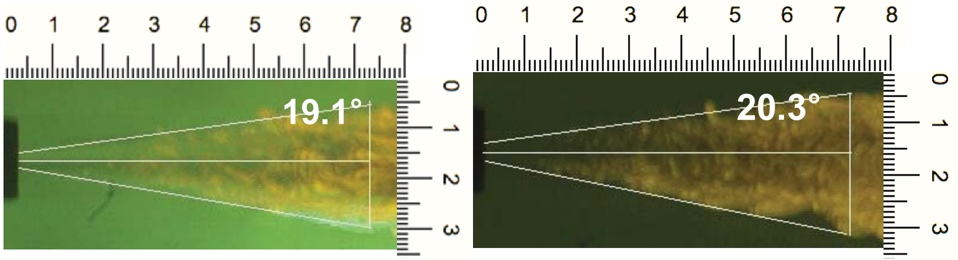

Figure 56: Spreading angles for n-C12H26 as well as n-C12H26 containing 100 ppmw FGS and Pt@FGS at a fuel flow rate of 5.0 mL/min (equivalence ratio of 0.38), Pch,ini=3.49 MPa, Tfuel=832 K, and Tair=777 K (Each graduation is 0.1 mm).

Reduction of the initial chamber pressure to achieve subcritical fuel injection (Pr=0.78, 1.41 MPa) was investigated at a fuel flow rate of 5.0 mL/min, T_{fuel}=832 K, and T_{air}=777 K, with the addition of 100 ppmw 5wt%Pt@FGS. Similar to the high pressure (supercritical) combustion experiments, the presence of Pt@FGS resulted in a higher fuel pressure and greater chamber pressure rise. The fuel pressure for the particle case was roughly 10% higher than the baseline, while the chamber pressure was increased by 18%. A comparison of subcritical and supercritical chamber conditions indicates greater conversion (24.5%) was achieved under supercritical conditions. As the composition of the fuel injected into the chamber is similar between the subcritical and supercritical combustion chamber operation, the higher burning rate associated with supercritical combustion is attributed to the improved mixing and increased collision rates.

Figure 57 shows high speed shadowgraphs captured during the injection and ignition of *n*-$C_{12}H_{26}$ containing 5wt%Pt@FGS at 100 ppmw under subcritical conditions at 5.0 mL/min. High temperature luminous regions were observed, which represent separate ignition points that formed in the presence of FGS-based particles. The distributed nature of these points leads to overall shorter ignition delay times. No distributed luminous regions were observed to occur during the pure fuel baseline experiment.

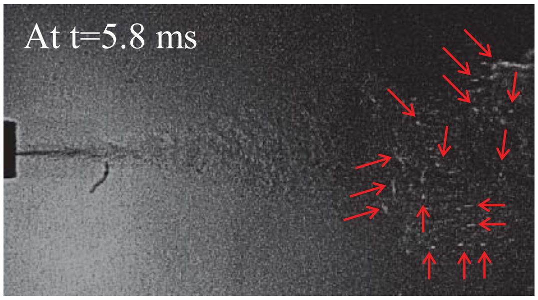

Figure 57: Luminous regions occur for *n*-$C_{12}H_{26}$ containing 100 ppmw Pt@FGS at an initial chamber pressure of 1.41 MPa (Pr=0.78, subcritical), a fuel flow rate of 5.0 mL/min, T_{fuel}=832 K, and T_{air}=777 K (Arrows represent the particle ignition).

The effects of low loadings of particle addition on injection, ignition, and combustion of hydrocarbon fuels under supercritical conditions were experimentally studied using a high pressure and high temperature windowed combustor coupled to a flow reactor and feed system. Images of fuel jets and turbulent flames, captured using high-speed cinematography, were analyzed to provide comparisons between pure (baseline) fuels and the same fuel containing inert, catalytic, or reactive particle additives. In this study, fumed silica, nanometer-sized aluminum, FGS, and FGS decorated with varying amounts of nanometer sized platinum particles (5.0 and 20.0 percent by weight) were considered. Spreading angle, ignition delay, lift-off distance, and percent fuel conversion were characterized. Quantitative as well as qualitative effects of the particle addition on injection, ignition, and combustion process were compared against the pure fuel baseline. Addition of 100 ppmw 20wt%Pt@FGS reduced ignition delay of *n*-$C_{12}H_{26}$ by nearly a factor of 3, increased spreading angles by approximately 35.0%, reduced the flame lift-off length by 50.0%, and yielded an increase in conversion by 35.0% relative to the pure fuel baseline. The enhancement mechanisms result from the combination effects of the Pt@FGS on both the fuel pyrolysis and combustion processes. In particular, the graphene-based additives are observed to yield higher formations of volatile species (for example, hydrogen and ethylene) during pyrolysis. Because of their faster reaction rates, the presence of these species in the injected fuel mixture can aid in reducing ignition delay time and increasing conversion rates for a given residence time. Furthermore, the preserved functionalities on the Pt@FGS after the pyrolysis processes, including the defect sites, oxygen-functional groups, and/or Pt nanoparticles may play a role in catalyzing the ignition and combustion chemistry when the particles are introduced into the combustor environment, as evident from the distributed ignition process. These results demonstrate that a low mass loading of a high surface area material employed either as an additive or a means of distributing another additive (i.e., platinum) can enhance, and be used to tailor, the conversion, ignition, and combustion of liquid hydrocarbon fuels/propellants under supercritical conditions, resulting in reduced ignition delay and improved combustion.

Enhancement of Solid Fuel Combustion Using Amorphous Ti–Al–B Nanopowder Additives

In another approach to the mesoparticles and the metal particles with inclusions discussed previously, we conducted research with Albert Epshteyn and Brian T. Fisher at the Naval Research Laboratory (NRL) who had developed a wet sonochemical synthesis of relatively air-stable reactive mixed-metal nanopowders (RMNPs) [97-101]. Metal containing hydrides and chlorides were reacted in a mostly unreactive organic solvent under continuous sonication to produce mixed metal intermetallic reactive powders (Ti–Al–B compositions). Bomb calorimetry analysis has shown that RMNP samples have up to 19% higher volumetric and 24% higher gravimetric energy densities relative to comparable nanometer-sized aluminum (nAl) particles [98].

We performed a study using the Ti–Al–B RMNPs, which also contain lithium, hydrogen, carbon, and chlorine both from solvent activation and from the original metal hydride precursors, as a potential energetic fuel additive at a 10 wt % loading to hydroxyl-terminated polybutadiene (HTPB) fuel. Combustion studies were conducted using a static-fired sub-scale hybrid motor to investigate the influence of the RMNPs on the regression rate of HTPB using gaseous oxygen as the oxidizer. As a means of comparison, solid fuel samples containing the same loading of nAl particles were investigated as well.

Addition of 10 wt% RMNPs to HTPB solid fuel increased the measured regression rate by approximately 20%, for all oxidizer mass flow rates considered (Fig. 58). The slope of the burning rate curve mimics that of pure HTPB. Regression rates measured for HTPB containing 10 wt.% nAl exhibited an increased slope, ranging from values comparable to pure HTPB under low-flow conditions and reaching the RMNP-loaded regression rate at the highest flow rate. Post-firing observations suggest that under reduced-flow conditions, an increasing fraction of nAl accumulates in the melt layer. Evolution of gaseous species from heating RMNPs may aid in particle ejection and reduction of particle aggregation and sintering. Entrainment and subsequent combustion of the RMNPs contributes to the overall heat release enhancing the regression rate relative to the nAl-loaded fuel under reduced oxidizer flow conditions.

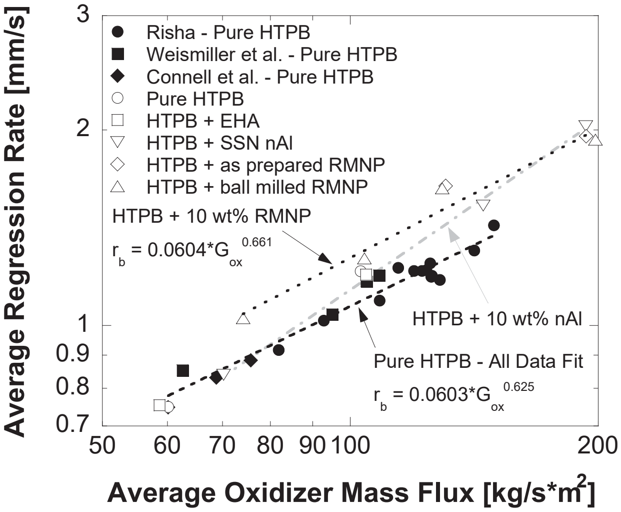

Figure 58: Average solid fuel regression rate data obtained from solid fuel grain analysis over a range of oxidizer mass flow rates at a nominal motor pressure of 221 ± 8 psia. Shown with pure HTPB regression rate data from [103,104].

Enhancement of Liquid Propellant Burning with nAl/NC Composite Mesoparticle Additives

Pressurized strand burner combustion experiments were also conducted for hydroxylammonium nitrate-based propellants containing nitrocellulose and nanometer-sized aluminum particles, as well as UMD nAl/NC composite mesoparticles as energetic additives. Measured HAN269MEO15 (an aqueous HAN-based propellant containing nearly 15 wt% methanol) burning rates were reduced by nearly an order-of-magnitude at 3.8 MPa by introducing 1 wt% NC into the mixture. The slope-break region observed for HAN269MEO15 diminished with NC addition as well. Addition of approximately 16 wt% nAl to the composition nearly recovered the HAN269MEO15 burning rate.

Aging experiments were conducted by combining NC and nAl or mesoparticles with methanol in aqueous HAN solution, sealing the container with a glove finger, and left sitting under ambient conditions to determine whether slow reaction between the nAl and oxidizer occurred. After allowing the samples to stand several days, gas was observed to have evolved from the NC/nAl/HAN269MEO15 mixture, as the glove finger had expanded. No expansion was observed for the sample comprising aqueous HAN, methanol, NC, and mesoparticles, and no reaction has been observed for aqueous HAN/methanol mixtures containing NC.

In addition to increasing energy density and propellant performance (i.e., combustion temperature, specific impulse, and etcetera) nAl addition increases the propagation rate at a given pressure. A reduced burning rate resulting from NC addition may be recovered by introducing aluminum to the composition, thus the burning rate, pressure dependence and subsequently the energy density of the HAN269MEO15 propellant may be tuned by adding NC and nAl in the proper proportions. Figure 33 indicates nearly an order of magnitude reduction in burning rate when 1 wt% NC is introduced to HAN269MEO15. The propagation speed is recovered by adding approximately 16 wt% nAl to the composition. Preliminary results suggest mesoparticle addition in favor of nAl may further enhance the propellant burning rate.

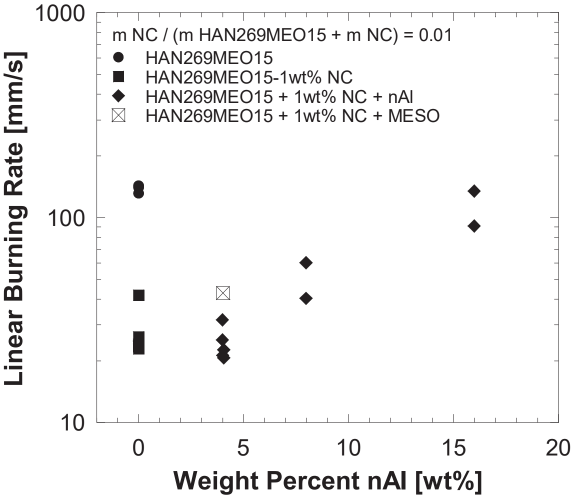

Figure 59: Measured burning rates for HAN269MEO15 compositions containing NC with nAl and mesoparticles.

These results suggest that the energy density may be increased while simultaneously tailoring burning rates of the HAN-based propellant using NC and nAl as additives. Although reaction was observed for direct nAl addition into aqueous HAN, no gas was observed to evolve from a propellant containing NC/nAl mesoparticles suggesting that the NC coating may act as a buffer or inhibitor preventing reaction between the nAl and solution.

DECOMPOSITION BEHAVIOR OF ENERGETIC MATERIALS AND NANOENERGETIC INGREDIENTS

S. Thynell, Penn State University

Decomposition of Ammonium Perchlorate with Embedded Particles

Ammonium perchlorate (AP) is a commonly used oxidizer in solid propellants (Fig. 60). Its mass fraction is usually about 85% with at least two particle sizes, with the remainder being hydroxyl-terminated polybutadiene (HTPB) and aluminum particles. Catalysts are added to modify the burning behavior, in some cases with the objective of reducing the susceptibility to combustion instabilities. However, it is not well understood how the catalytic effects occur. Many different catalysts are used, with iron oxide being one of the cheapest and quite effective. Professor Son provided samples (about 50 mg) of Fe_2O_3 nano-particles embedded within the crystals. One of the goals of this subcontract was to provide a deeper insight into the burning rate enhancement caused by these particles. Our research effort focused on three parts: a) condensed-phase decomposition of AP, b) gas-phase decomposition of ammonia and perchloric acid, and c) condensed-phase decomposition of hydroxylammonium nitrate.

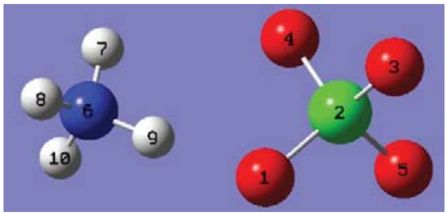

Figure 60: Ammonium cation (left) and perchlorate anion.

Condensed-phase decomposition of AP with and without Fe_2O_3 particles

The condensed-phase decomposition of AP, with and without Fe_2O_3 particles, was investigated using quantum mechanics (QM) calculations, since experimental results are available in the literature. Using density functional theory (B2PLYP) with a standard Pople derived basis set [6-311+g(3df,2p)], the forward and backward free energy barriers are estimated to be 52.8 and 48.1 kcal/mol. The QM calculations also include intrinsic reaction coordinate calculations, which connects the reactants to the products via the identified transition state by following the minimum energy path. Figure 61 shows the transition state, which by inspection involves a great deal of symmetry. Subsequent calculations identified more than 40 species and 250 reactions.

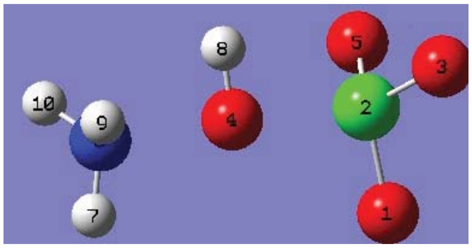

Figure 61: Transition state structure of initiation of AP decomposition in the condensed phase.

There is significant evidence of the catalytic role of iron oxide on hydroxylamine from experimental studies by Cisneros et al. [105]. The addition of 10 ppm of Fe^{3+} or Fe^{2+} to NH_2OH/H_2O (50/50 wt.%) liquid produces initially a brown residue followed by violent reaction/boiling. The brown residue was believed to be rust (iron oxide, Fe_2O_3) or FeO(OH). Addition of 200 ppm of Fe_2O_3 particles to NH_2OH/H_2O (50/50 wt.%) produces much lower rates of pressure and temperature rise until a critical temperature is reached (where NH_2OH undergoes a self-reaction). The enhanced reactivity of Fe^{3+}/Fe^{2+} ions compared to Fe_2O_3 particles is probably due to: 1) iron ions produce smaller particles with a very large surface area, and 2) residual ions also react with the NH_2OH. In order to explore the catalytic role, QM calculations were performed at the B3LYP/6311+**/GD3BJ/SMD/H2O level of theory. Here the first goal is to identify pathways to the formation of iron oxide. We assume each Fe^{3+} ion is coordinated with 6 H_2O molecules in an octahedral shape. The reaction is

$[Fe\bullet 6OH_2]^{3+}+NH_2OH=[FeOH\bullet 5OH_2]^{2+}+NH_3OH^{+}$, $\Delta G_f<2$kcal/mol, $\Delta G_{rxn}=-4$kcal/mol (1)

That is, the reactions are very fast since the forward free energy barrier is <2 kcal/mol and the overall free energy change of the reaction is negative. Subsequent similar reactions may give $Fe(OH)_3$, those reactions are barrierless as no transition states could be identified. Brown residue believed to be rust (iron oxide, Fe_2O_3) or FeO(OH). Caused by reactions among $Fe(OH)_3$. The addition of 200 ppm of Fe_2O_3 to NH_2OH/H_2O (50/50 wt.%) produces much lower rates of pressure and temperature rise until a critical temperature is reached, at which time NH_2OH self-reacts highly exothermically forming N_2 as one of the final products. NH_3, N_2O, H_2O, HNO formations begin with (units in kcal/mol)

$Fe(OH)_3 + NH_2OH = Fe(ONH_2)(OH)_2 + \mathbf{H_2O}$, $\Delta G_f=6.7$, $\Delta G_{rxn}= - 0.7$ (2)
$\mathit{Fe(ONH_2)(OH)_2} + NH_2OH = Fe(NH_2)(OH)_2 + \mathbf{H_2O} + \mathbf{HNO}$, $\Delta G_f=20$, $\Delta G_{rxn}= - 17.8$ (3)
$Fe(NH_2)(OH)_2 + NH_2OH = \mathit{Fe(ONH_2)(OH)_2} + \mathbf{NH_3}$, $\Delta G_f=0$, $\Delta G_{rxn}= - 14$ (4)
$HNO + HNO = \mathbf{N_2O} + \mathbf{H_2O}$, $\Delta G_f=6.7$, $\Delta G_{rxn}= - 0.7$ (5)

Species in blue italics is regenerated. Here reactions (3) and (4) will occur until the hydroxylamine is depleted. N_2 formation, however, begins with reaction within a coordinated complex (units in kcal/mol) and barrier is lower than (3) above. The reactions are few and begin and ends with the presence of $Fe(OH)_3$, which is regenerated:

$Fe(OH)_3\bullet 2NH_2OH\bullet 2H_2O = [Fe(OH)_4]^{-}\bullet NH_2NH_2OH^{+}\bullet 2H_2O$, $\Delta G_f=18.9$,$\Delta G_{rxn}= - 20.4$ (6)
$NH_2NHOH = H_2NN + \mathbf{H_2O}$, $\Delta G_f=7.8$, $\Delta G_{rxn}= - 17.2$ (7)
$\mathit{Fe(OH)_3} + H_2NN = Fe(NNH)(OH)_2 + \mathbf{H_2O}$ $\Delta G_f=1.5$, $\Delta G_{rxn}= - 12.5$ (8)
$Fe(NH_2)(OH)_2 + H_2NN= Fe(NNH)(OH)_2 + \mathbf{NH_3}$ $\Delta G_f=0$, $\Delta G_{rxn}= - 25.8$ (9)
$Fe(NNH)(OH)_2 + NH_2OH = \mathit{Fe(OH)_3} + \mathbf{NH_3} + \mathbf{N_2}$ $\Delta G_f=8.5$, $\Delta G_{rxn}= - 114$ (10)

It is noted that the overall free energy changes of the reactions are all negative and forward free energy barriers are very low. However, many issues remain. The QM calculations should be performed at higher-level methods and ground state geometries (spin state) should be checked. One should also employ other molecular structures as reactive sites, including Fe^{3+} and Fe^{2+}. Furthermore, meso-scale models should also be used to validate reaction mechanism. Additionally, it would be of interest to examine extent of catalytic effects on hydroxylammonium nitrate and AF315 liquid propellants.

Gas-phase reactions of ammonia and perchloric acid

In the gas phase, catalytic effects from Fe_2O_3 are also possible. However, proton transfer has occurred producing ammonia and perchloric acid, which then implies that initiation reactions are different compared to the condensed phase. The identified important initiation reactions between NH_3 and $HOClO_3$ using the compound method G4(MP2) of the Gaussian 09 program package are shown by reactions (11)-(16). Here the rate constant k is computed from $k = AT^{n}\exp(-\Delta H / RT)$

	A	n	$E/\Delta H_f$	
$HOClO_3+M = OH+ClO_3+M$	1.45×10^{17}	0	52.7 (E)	(10)
$NH_3+HOClO_3 = NH_3O+HOClO_2$	3.12E+05	2	46.6	(11)
$NH_3+HOClO_3=H_2O+NH_2OClO_2$	2.74E+05	2	45.5	(12)
$NH_3+HOClO_3=$*trans*-$NH_2OH+HOClO_2$	4.25E+05	2	52.7	(13)
$2HOClO_3=O_3ClOClO_3+H_2O$	1.84E+04	2	49.4	(14)
$2HOClO_3+H_2O=O_3ClOClO_3+2H_2O$	3.45E-02	3	38.5	(15)
$2HOClO_3+NH_3=O_3ClOClO_3+H_2O+NH_3$	4.78E-02	3	35.3	(16)

where ΔH_f is the forward enthalpic barrier. Current reaction mechanisms for the gas phase use reaction (10) as the initiation reaction [106-108] but with a barrier of 39.1 kcal/mol. The actual barrier is, however, much higher by about 13.6 kcal/mol. Many additional reactions in the gas phase have been identified, in addition to those available on the web site of Dr. M.C. Lin [109]. In the gas phase, the Polyrate program of Truhlar [110] is used to compute the kinetic rates based on variational transition state theory and an account of tunneling effects and symmetry. It should be noted that Zhu and Lin [111] have been unable to identify any reactions in a solution phase that were considered by Tanaka and Beckstead [112]. Regarding catalytic effects in the gas phase, the relevant reactions could be quite similar to those in the condensed phase. The ammonia oxide (NH_3O) formed in reaction (11) is readily converted to hydroxylamine. However, reaction (12) is also important compared to reaction (11).

Condensed-phase decomposition of hydroxylammonium nitrate

The objective of this work was to develop a detailed chemical mechanism for thermal decomposition of hydroxylammonium nitrate ($NH_3OH^+\cdot NO_3^-$, or HAN)-water solutions based on quantum mechanical (QM) simulations. The mechanism was examined via kinetic modeling by comparing the simulation predictions with previous experimental results from the flow reactor tests and fast-thermolysis studies.

Reaction Mechanism Development

HAN has been considered as a potential replacement of hydrazine in the next-generation spacecraft thrusters [113-115]. The advantages of HAN-based propellants include low toxicity, high energy density, high specific impulse, and environmentally friendly emissions. The performance of HAN-water solutions has been extensively studied under a wide range of conditions using various experimental techniques. Unique behaviors emerge under thermal decomposition and combustion conditions, such as autocatalytic kinetics [116,117], complicated decomposition products [118,119], and unusual combustion wave structures [114,120,121], all of which reflect a very complex chemical and physical process. A widely cited global reaction is given by:

$$4HAN \rightarrow 3N_2O + 2HNO_3 + 7H_2O \tag{17}$$

Previous understanding of the chemical process of HAN decomposition was limited to several global steps, most of which lack proper kinetic data and have not been theoretically validated.

The approach we adopted to investigate the decomposition process was QM calculations using the Gaussian09 software. All the structures of species and transition states (TSs) were optimized using ωB97X-D density functional theory [122] with the 6-311++G** basis set. The SMD continuum solvation model [123] with water as the solvent was implemented to carry out the solution-phase calculations. Zero-point vibrational energies (ZPVE) were computed using the unscaled vibration frequencies obtained by SMD-ωB97X-D. Gibbs free energy corrections were computed based on the ideal-gas partition functions and the rigid-rotor harmonic oscillator approximation. Intrinsic reaction coordinate (IRC) calculations were conducted to assign the correct reactants and products to the identified TSs.

The mechanism, which consists of over 100 species and 350 elementary steps, describes multiple kinetic processes. Decomposition begins with the nitration (-NO_2) of hydroxylamine, leading to the first formation of HONO. Potential nitration agents in HAN solutions include HNO_3, NO_2^+, N_2O_5 (O_2NO-NO_2), and after HONO formation, N_2O_4 (ONO-NO_2 and O_2N-NO_2) and N_2O_3 (ON-ONO and ON-NO_2). The following reactions are considered potentially important in the initial stage due to the relatively low free energy barriers ($\Delta G_f < 25$ kcal/mol at 300 K):

$$\mathrm{HNO_3 + H^+ \rightleftharpoons NO_2{}^+ + H_2O} \tag{18}$$
$$\mathrm{HNO_3 + HNO_3 \rightleftharpoons O_2NONO_2 + H_2O} \tag{19}$$
$$\mathrm{NH_3OH^+ + O_2NONO_2 \rightleftharpoons NH_3ONO_2{}^+ + HNO_3} \tag{20}$$
$$\mathrm{NH_2OH + NO_2{}^+ \rightleftharpoons NH_2O(H)NO_2{}^+/O_2N\text{-}NH_2OH^+} \tag{21}$$
$$\mathrm{HAN + NO_2{}^+ \rightleftharpoons NH_3ONO_2{}^+ + HNO_3} \tag{22}$$
$$\mathrm{NH_2O(H)NO_2{}^+/O_2N\text{-}NH_2OH^+ \rightleftharpoons HONO + HNO + H^+} \tag{23}$$

Reactions between hydroxylamine and HONO lead to two diverging pathways: HONO scavenging and its regeneration. HONO scavenging is realized via nitrosation reactions, in which hydroxylamine first converts to nitroso- (-NO) species. Potential nitrosation agents include HONO, NO^+, N_2O_4 (ON-ONO_2 and O_2N-NO_2), N_2O_3 (ON-NO_2 and ON-ONO) and N_2O_2 (ON-NO). The free energy barriers of the nitrosation steps (27)-(30) are predicted to be 2-15 kcal/mol lower than corresponding nitration reactions. The results agree with previous experimental observations that the hydroxylamine is oxidized much faster by nitrous acid than by nitric acid [124,125].

$$\mathrm{HONO + H^+ \rightleftharpoons NO^+ + H_2O} \tag{24}$$
$$\mathrm{HNO_3 + HONO \rightleftharpoons ONONO_2 + H_2O} \tag{25}$$
$$\mathrm{NO^+ + NO_3{}^- \rightleftharpoons ONONO_2} \tag{26}$$
$$\mathrm{NH_3OH^+ + ONONO_2 \rightleftharpoons NH_3ONO^+ + HNO_3} \tag{27}$$
$$\mathrm{HAN + NO^+ \rightleftharpoons NH_3ONO^+ + HNO_3} \tag{28}$$
$$\mathrm{NH_2OH + NO^+ \rightleftharpoons NH_2O(H)NO^+/\ ON\text{-}NH_2OH^+} \tag{29}$$
$$\mathrm{NH_3ONO^+/NH_2O(H)NO^+/ON\text{-}NH_2OH^+ \rightleftharpoons ON\text{-}NH_2O + H^+} \tag{30}$$

Once formed, HNO has a strong tendency to dimerize at a very high rate (10^6-10^9 $M^{-1}s^{-1}$ at 300 K) [126,127]. Both the HNO dimers and nitrosation product (ON-NH_2O) are isomers of hyponitrous acid (HONNOH). The isomerization transformations can be realized via intramolecular or H_2O/H_3O^+-assisted hydrogen transfer, or via fast protonation/deprotonation under acidic/basic conditions [128,129].

$$\mathrm{ON(H)N(H)O/ON\text{-}NH_2O \xleftrightarrow{H_2O/H^+/OH^-} HONNOH/HONNO^- \longrightarrow N_2O + H_2O/OH^-} \tag{31}$$

The conversion rate of (31) depends on the starting *cis-*/*trans-* configurations and solution acidity. For *trans-* isomers, N_2O formation is significantly suppressed at mildly acidic conditions (0<pH<4) with the accumulation of *trans*-HONNOH, but largely accelerated in solutions with negative pH due to the acid-catalyzed reaction (32), whereas the decomposition of the *cis-* isomers is about 4-6 orders of magnitude faster than the *trans-* species under all pH conditions of interest [128].

$$(\textit{trans-}\text{ or }\textit{cis-})\text{HONNOH} + H_2O + H_3O^+ \rightarrow N_2O + 2H_2O + H_3O^+ \tag{32}$$

It was observed in previous studies that most hydroxylamine would be oxidized to produce HONO autocatalytically when the solution contains a large excess of HNO_3 [125,130]. Some works attributed the autocatalytic decomposition of HAN solutions to the same kinetic process, even though no direct evidence of HONO generation has been reported [131,132]. Several potential HONO regeneration pathways were investigated. The kinetically feasible pathways are realized via H-abstraction reactions by NO_2 and NH_2O:

$$NO_2 + NH_2OH \rightleftharpoons HONO + NH_2O \tag{33}$$
$$NO_2 + NH_2O \rightleftharpoons HONO + HNO \tag{34}$$
$$NO_2 + HNO \rightleftharpoons HONO + NO \tag{35}$$
$$NH_2O + HNO \rightleftharpoons NH_2OH + NO \tag{36}$$

Figures 62-64 show the free energy surfaces (at 298 K) and TSs' structures of important steps involved in the nitration, nitrosation, and HONO regeneration pathways.

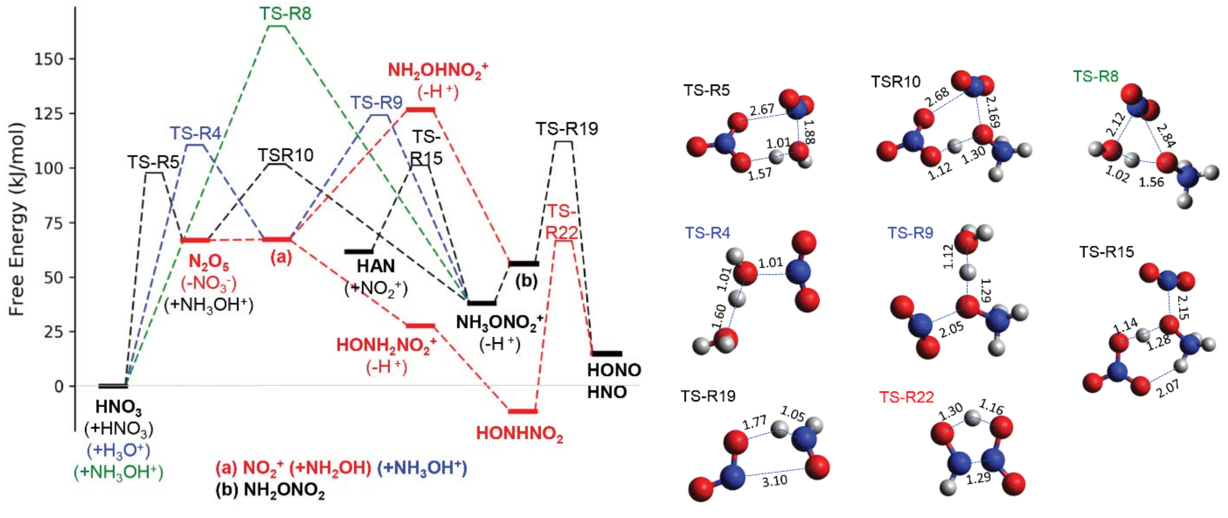

Figure 62: Schematic representation of the free energy surface (298 K) and TSs structures in the nitration pathways.

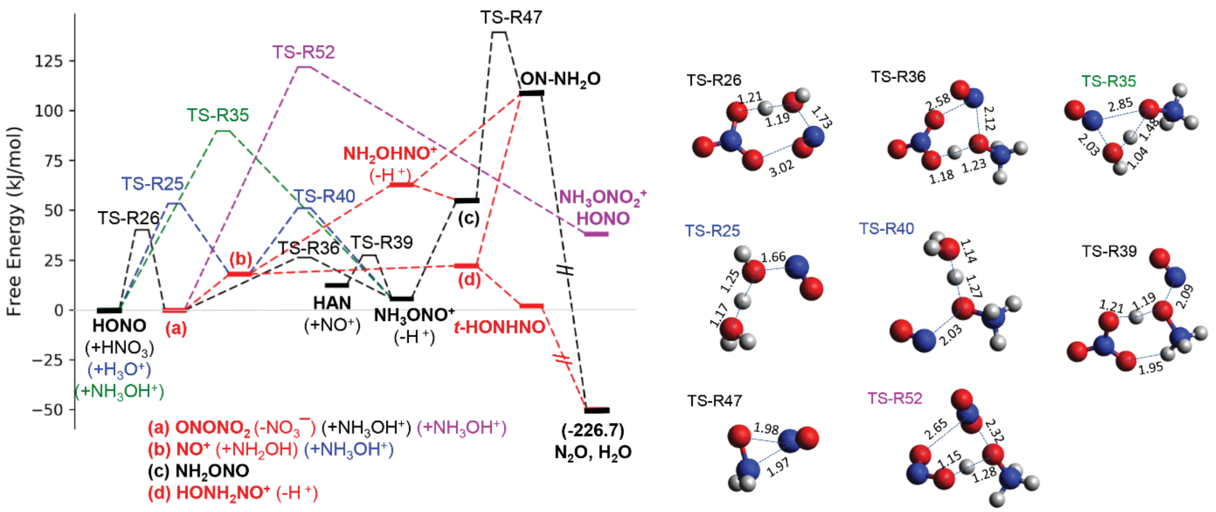

Figure 63: Schematic representation of the free energy surface (298 K) and TSs structures in the nitrosation pathways.

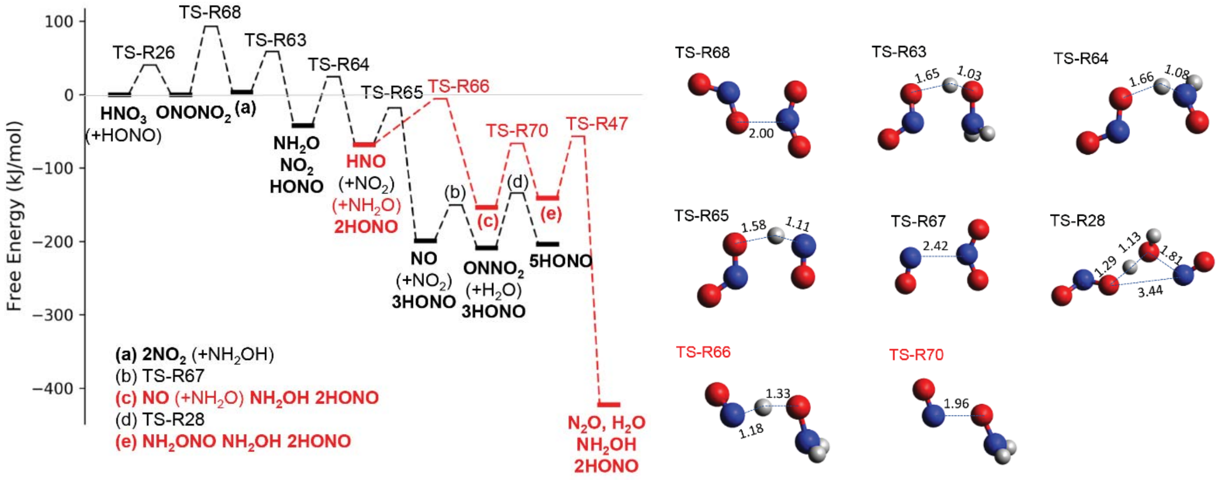

Figure 64: Schematic representation of the free energy surface (298 K) and TSs structures in the HONO-regeneration pathways.

Kinetic Modeling

The goal of this part of the work is to examine the above mechanism via kinetic modeling, and to explain the kinetic features of HAN solutions observed in previous flow reactor tests and fast thermolysis studies. The chemical rate constants of the elementary reactions were calculated using the thermodynamic formulation of the conventional transition state theory (TST) with the consideration of reaction degeneracy (σ) and the tunneling effect (Γ):

$$k_{\mathrm{TST}} = \sigma\Gamma\, k_{\mathrm{B}}T/h \cdot \exp\left(-\Delta G^{\ddagger}/RT\right) \tag{37}$$

The diffusion effect on rate constants was considered by assuming a quasi-steady state (QSSA) to the encounter complexes and estimating the diffusion rate using the Stokes-Einstein equation. The overall rate constants were then fitted into the three-parameter Arrhenius equation (A, n, E_{a}):

$$k = AT^n \exp(-E_\mathrm{a}/RT) \tag{38}$$

The species' ODEs were integrated numerically using the double-precision version of the VODE code:

$$dy_i/dt = \dot{w}_i \tag{39}$$

Figure 65a exhibits the calculated species' evolutions in 0.1 m HAN at 493 K along with the experimental data from Ref. [132]. The evolutions of NH_3OH^+ and N_2O generally capture the trend of experimental data. NO is also predicted to evolve noticably as HAN decomposes. Figure 65b shows the first-order plots regarding the consumption of HAN up to 60% at 463-523 K, in which the concentration of the undecomposed HAN ($[HAN]_u$) is defined based on the stoichiometry of the global reaction (17):

$$[\mathrm{HAN}]_\mathrm{u} = 0.1\ \mathrm{m} - [\mathrm{N_2O}]/0.75 \tag{40}$$

The experimental $\ln([HAN]_u)$-t profiles roughly show a the first-order behavior, whereas the curvature in the predicted results indicates the presence of an autocatalytic process. However, the catalytic effects of HONO and NO_2 are expected to be negligible, considering that both species remain at considerably low concentrations ($<10^{-9}$ m).

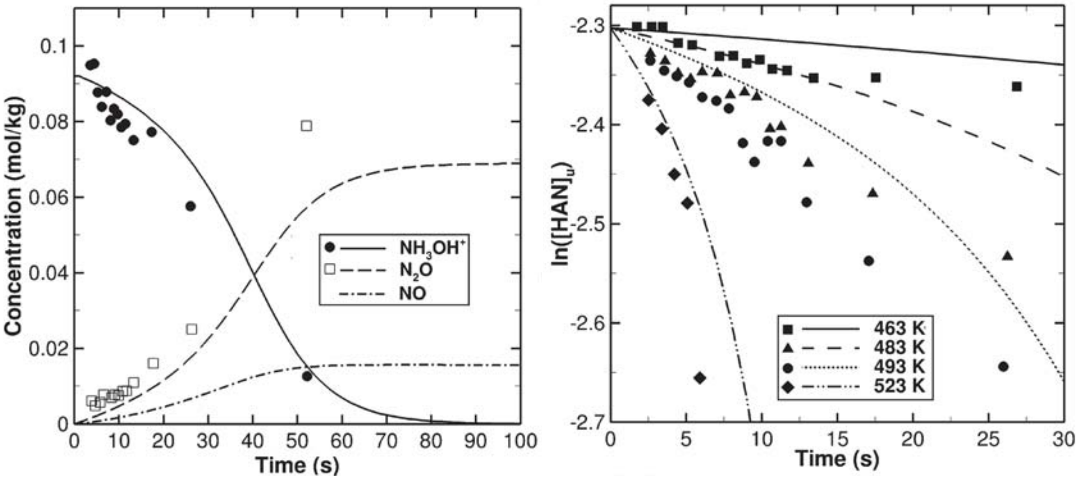

Figure 65: (a) Evolutions of major species in 0.1 m HAN at 493 K. (b) First-order consumption rate of 0.1 M HAN at 463-523 K.

In a similar flow reactor test [131], strong autocatalytic behaviors were observed in 0.82-2.0 m HAN, which was reflected by the abrupt changes in the species' spectra once the flow was heated to a certain temperature. Figure 66 shows the predicted evolutions of major and minor species in 0.82 m HAN at 445 K. Reaction accelerates considerably after 10 s, and over 90% of the initial hydroxylamine is consumed within the next 10 s. The major products in the fast decomposition period include N_2O, NO, and H_3O^+, whereas NO_2 emerges much later when almost all the hydroxylamine has been consumed, along with the reduction of NO and H_3O^+. As for the minor species, NH_2O first accumulates in the early stage of reaction followed by the evolution of

HONNOH and HNO. All three species are consumed in the fast decomposition period. HONO only emerges in the late stage along with NO_2 and N_2O_4.

Sensitivity analysis (SA) was performed to identify the rate-determining processes in HAN decomposition under the conditions discussed above. SA results suggest a nitration-nitrosation pathway in the early to middle stage of reaction:

$$HNO_3 + H^+ \rightleftharpoons NO_2^+ + H_2O \qquad (k_1, k_{-1})$$

$$NH_3OH^+ + NO_2^+ \rightarrow HONO + HNO + 2H^+ \qquad (k_2)$$

$$HONO + H^+ \rightleftharpoons NO^+ + H_2O \qquad (k_3, k_{-3})$$

$$NH_3OH^+ + NO^+ \rightarrow N_2O + H_2O + 2H^+ \qquad (k_4)$$

$$HNO + HNO \rightarrow N_2O + H_2O \qquad (k_5)$$

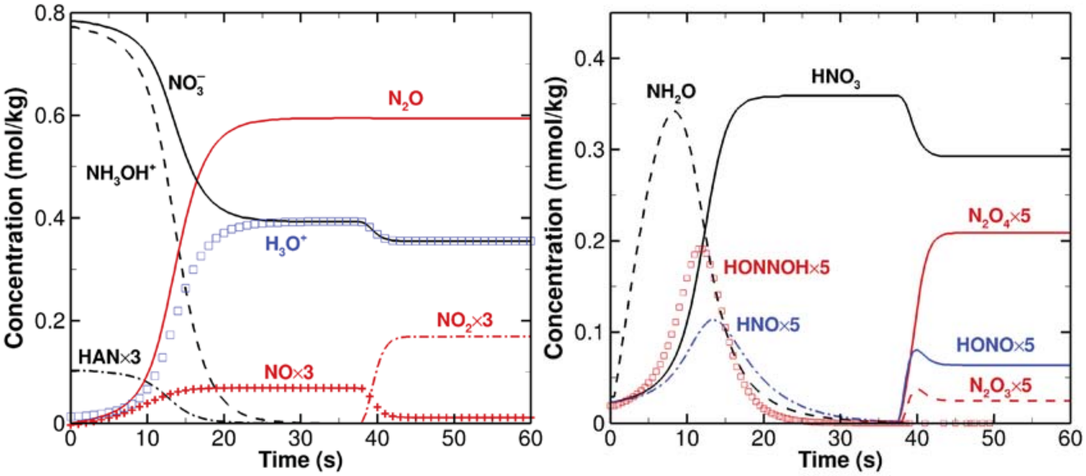

Figure 66: Predicted species' evolutions in 0.82 m HAN at 445 K.

By applying the QSSA to NO_2^+, HONO, HNO, and NO^+, the formation rate of N_2O is given by:

$$d[N_2O]/dt \approx 2K_1k_2K_{a,\,HNO_3}[NO_3^-][H^+]^2[NH_3OH^+]/[H_2O] \qquad (41)$$

The above result reveals that the autocatalysis of HAN decomposition is most likely caused by the rise of solution acidity. For example, the kinetic modeling predicts that $[H^+]$ in 0.1 m solution at 493 K only increases by roughly three times within the first half-life ($t_{1/2}$) of HAN, whereas $[H^+]$ increases by over ten times in 0.82 m solution, which leads to a much stronger autocatalytic behavior. The late emergence of HONO and NO_2 indicates that their regeneration has no significant impact on the overall decomposition rate. The following pathway is only influential in the very late stage of reaction (> $3t_{1/2}$):

$$NO_2 \xrightarrow{NO} N_2O_3 \xrightarrow{H_2O} 2HONO \xrightarrow{2H^+} 2NO^+ + 2H_2O \xrightarrow{2NO_3^-} 2ONONO_2 + 2H_2O \rightarrow 4NO_2 + 2H_2O$$

The global reaction is given by:

$$NO_2 + NO + 2HNO_3 \longrightarrow 4NO_2 + H_2O \qquad (42)$$

The above pathway is only feasible when the concentration of hydroxylamine is considerably low; otherwise, HONO or NO^+ would preferably react with hydroxylamine following the low-barrier nitrosation pathways, which leads to the formation of N_2O and NO.

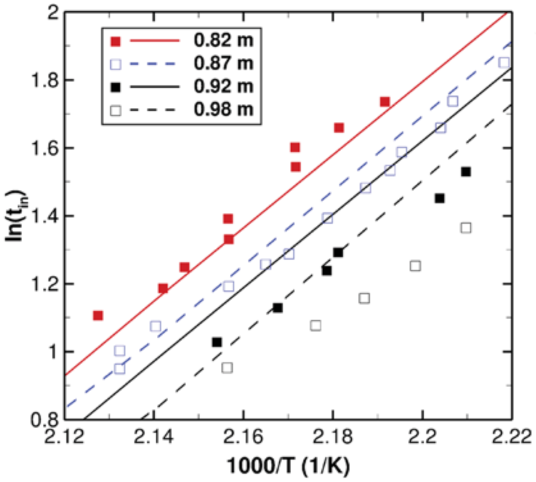

Figure 67: Temperature dependence of the induction periods of 0.82-0.98 m HAN.

The global kinetic parameters for aqueous HAN decomposition were derived based on the theory of adiabatic induction period (t_{in}). The energy equation was incorporated to account for the temperature evolution under adiabatic conditions:

$$\rho c_{\text{p}}\, dT/dt = \dot{Q} \tag{43}$$

in which the overall reaction heat release rate ($\dot{Q}$) was estimated based on the enthalpy changes of the global reaction (1c.1) (ΔH_{rxn} = -218.4 kJ/mol):

$$\dot{Q} = -(\Delta H_{\text{rxn}}/0.75)(\rho/MW_{\text{N2O}})(dy_{\text{N2O}}/dt) \tag{44}$$

t_{in} was determined based on the inflection point on the temperature profile. Figure 67 shows the predicted t_{in}'s in 0.82-0.98 m HAN at 450-470 K, which reasonably capture the trend of the experimental data obtained in the flow reactor tests, even though the t_{in}'s of 0.92-0.98 m solutions are overestimated by 5% to 15% in general. The linear relation of $\ln(t_{\text{in}})$-$1/T$ can be explained by the integral form of equation (45) using the Frank-Kamenetskii transformation and assuming a first-order rate constant in the Arrhenius form:

$$\ln(t_{\text{in}}) = \frac{E_{\text{a}}}{RT} + \ln\left(\frac{c_{\text{p}}RT^2}{-\Delta H_{\text{rxn}}\cdot AE_{\text{a}}\cdot[\text{HAN}]_0}\right) \tag{45}$$

According to equation (45), the apparent Arrhenius parameters (E_{a} and A) are related to the slopes and intercepts of the $\ln(t_{\text{in}})$-$1/T$ plots. In this work, E_{a} and $\ln(A)$ for 0.82-2.0 m HAN at 425-490 K are predicted to be 88.6±1.9 kJ/mol and 21.1±0.5, respectively.

Widely different Arrenhius parameters have been reported for HAN in various physical states and concentrations, as summarized in Figure 68 along with the predictions from this work. No clear relationships can be found between the parameter values and the physical states (or concentrations). Instead, a strong linear correlation between E_a and $\ln(A)$ can be observed among the reported values, implying a potential kinetic compensation effect (KCE):

$$\ln(A) = \alpha + E_a/(R\theta) \tag{46}$$

The fitted linear coefficients are -3.497 and 446.3 K for α and θ, respectively. A similar trend has been observed in the kinetic data of several other energetic materials, including RDX, HMX, and NTO [133]. There is still an ongoing debate about the origin of KCE, which often occurs in heterogeneous reacting systems. For HAN materials, the catalysis by the reactor surface and the dissolved metallic ions may play a major role in the variation of decomposition kinetics. KCE might be related to the reactivity of the ionic clusters under the conditions of interest. Further investigation is needed on the temperature dependence of HAN decomposition kinetics.

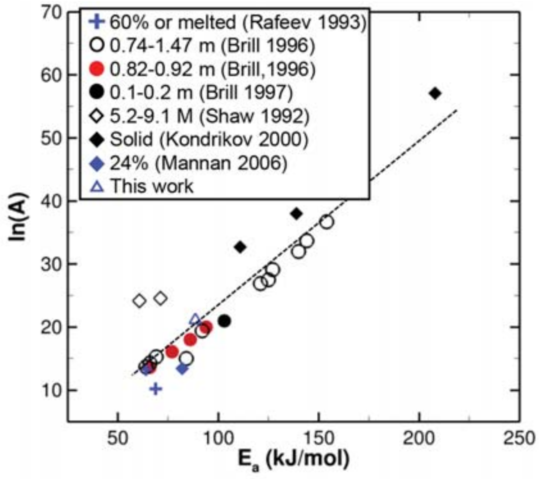

Figure 68: A summary of the Arrhenius parameters obtained from the literature.

Simulations were also performed to predict species' evolutions of highly concentrated HAN solutions under the conditions of fast thermolysis studies. The kinetic parameters describing the vaporization rates of the individual species were determined through an optimization process. Some QM-predicted thermodynamic properties were also adjusted to improve the reproduction of the experimental results. The predictions for 9 M HAN at 483 K are presented in Figure 69 in comparison with the experimental data from Ref. [119]. It is predicted that the early period is predominated by water vaporization, and fast decomposition only takes over after a clear induction period. Kinetic modeling also predicts a considerable evolution of N_2, which was not reported by the original experiments due to its IR-inactive feature. Previous studies reported that the shortest induction period takes place in around 10.7 M HAN, whereas slower reactions were observed in solutions of higher concentrations [134]. This kinetic feature has not been captured by current simulation results; instead, the induction period is predicted to consistently decrease as the concentration increases. There is still lack of a thorough understanding of the physical and chemical features of HAN at elevated temperature/pressure/concentrations conditions. Future investigation may focus on developing a database of thermophysical properties of HAN and HAN-based materials using experimental or simulation techniques.

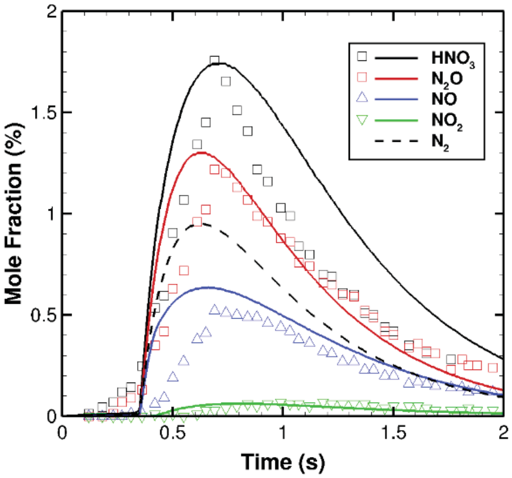

Figure 69: Evolution of gaseous species in 9 M HAN at 483 K.

Condensed-phase decomposition of ammonia borane

Boron and boron-containing compounds have been of strong interest for propulsion and its use is of strong interest to AFRL. The objective of this portion has been to elucidate and validate the decomposition of ammonia borane (AB, NH_3BH_3). Many different mechanistic steps have been proposed in the literature, but none has been validated. In this section, we summarize the results of AB decomposition in a glyme solution and the decomposition of pure AB. Our work explains the formation of species observed in various experiments, reconciling the existing conflicts regarding the initiation step, as well as the pathways of H_2 and borazine formations. The approach follows those described previously on QM calculations in a solution phase, formulation and solution to species conservation equations. Details can be found in [135].

Summary of significant results for AB decomposition in Glyme

Contrary to the previous belief that AB initiates decomposition by forming diammoniate of diborane, [DADB, $NH_3BH_2NH_3]^+[BH_4]^-$ [136-138], the results from this study suggest that the initiation step involves formation of $BH_4BH_2NH_3$ and NH_3 which react further with BH_2NH_2 to form DADB. The initiation step, however, is AB + AB, since our results from capture the second-order decomposition kinetics of AB observed in previous experiments [136,138].

QM calculations validate the common belief that DADB is a key intermediate required in the formation of hydrogen during AB decomposition. It is also concluded that in addition to DADB, another key intermediate required in the formation of H_2 is an ammonium borohydride salt, $[BH_4]^-[NH_4]^+$.

QM calculations predict that under isothermal conditions, AB in glyme releases approximately 6-6.5% of hydrogen by weight during the lower reaction temperature ranging from 323-368K, which is in close agreement with the experimental observations [138].

Reaction pathways which explain the formation of species observed in previous experiments are also provided. These pathways show that DADB, cyclodiborazane (CDB), B-(cyclodiborazanyl) aminoborohydride (BCDB), cyclotriborazane (CTB) and borazine are formed via several competing reactions involving BH_2NH_2 as the key intermediate species. The potential energy surface for two pathways of H_2 formation is provided below in Fig. 70. From Fig. 70, it can be observed that the reactions involved during the release of H_2 from AB in glyme are exothermic. The reactions listed in Fig. 70 are shown in Table 8, including free energy and enthalpy barriers in both forward and reverse directions.

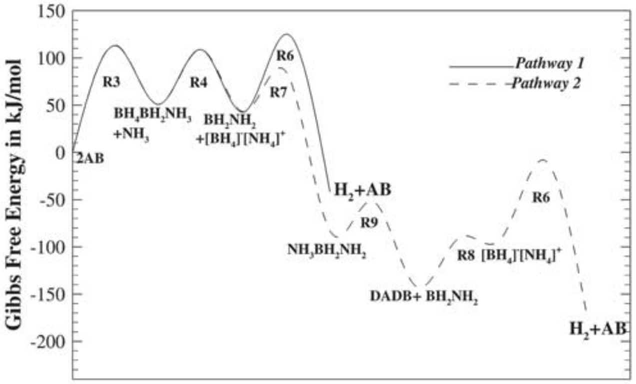

Figure 70: Potential energy surface for two pathways of H_2 formation based on QM calculations.

Table 8: Gibbs free energy barrier (Δ*G*) and enthalpy barrier (Δ*H*) in forward (*f*) and backward (*b*) direction (kJ/mol) of all the reactions involved in the developed reaction mechanism for initial decomposition of AB decomposition in glyme.

No.	Reaction	ΔG_f	ΔG_b	ΔH_f	ΔH_b
R3	$2AB \leftrightarrow BH_4BH_2NH_3 + NH_3$	143.5	62.8	113.4	30.1
R4	$BH_4BH_2NH_3 + NH_3 \leftrightarrow BH_2NH_2 + [BH_4]^-[NH_4]^+$	58.2	66.1	17.6	15.9
R5	$BH_4BH_2NH_3 + NH_3 \leftrightarrow DADB$	83.7	131.8	46.9	136.4
R6	$[BH_4]^-[NH_4]^+ \leftrightarrow AB + H_2$	82.4	166.9	101.3	164.0
R7	$BH_2NH_2 + NH_3 \leftrightarrow NH_3BH_2NH_2$	41.0	29.3	4.2	39.3
R8	$NH_3BH_2NH_2 + [BH_4]^-[NH_4]^+ \leftrightarrow DADB + NH_3$	0.0	51.0	0.0	56.5
R9	$NH_3BH_2NH_2 + BH_4BH_2NH_3 \leftrightarrow DADB + BH_2NH_2$	31.4	90.0	-14.6	39.7

Summary of significant results for pure AB decomposition

In the case of pure AB, our QM and species conservation modeling calculations suggest that initiation of AB decomposition also begins via a bimolecular reaction producing $BH_4BH_2NH_3$, which quickly undergoes unimolecular decomposition to form BH_3, which plays a catalytic role in the process of H_2 release from AB. It is also clear that the initiation step is the primary source of NH_3 evolved into the gaseous phase, which is seen experimentally [139]. Furthermore, this study also identifies critical intermediate species required for the formation of H_2, borazine and other ring-containing species during the process of AB decomposition. It is evident from this study that $[BH_4]^-[NH_4]^+$ and $BH_3NH_2BH_2NH_3$ are two important sources for the formation of H_2. However, $BH_3NH_2BH_2NH_3$ also plays a major role in the process. This study also identifies 3 pathways for formation of borazine, and it can be observed from the mechanism that BH_2NH_2, BH_2NHBH_2 and $BH_2NHBHNH_2$ formed via several competing reactions from $BH_3NH_2BH_2NH_3$ play a critical role in the process of ring formation during the second phase of AB decomposition. Based on the results shown in this work, further details have been provided on the initiation of decomposition of AB, as well as identification of intermediates and reactions responsible for the growth to borazine and larger molecular weight ring-containing compounds. Numerical simulations using a control volume analysis are performed at different heating conditions. Simulated results match very well with the experimental findings [139] which confirms the validity of the proposed mechanism.

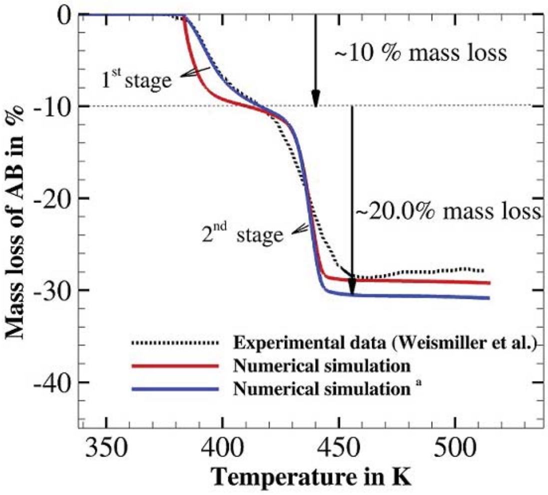

Figure 71: Comparison of predicted mass loss curve with TGA data by Weismiller et al. for heating rate of 20K/min [139].

Figure 71 shows the comparison between simulation results and thermogravimetric analysis (TGA) mass loss data of Weismiller et al. [139]. Using a sensitivity analysis, it has been observed that if the forward barrier of one of the most sensitive reactions in the mechanism (**R3** of Table 8**)** is increased by ~4.2-8.4 kJ/mol, which is relatively small amount and most likely less than the uncertainty associated with the QM calculations, a better agreement with the experimental data is obtained. With such a small change, the rate of H_2 release during the first phase of AB decomposition is reduced causing the mass to decrease less rapidly in the first step resulting to better match with the experimentally obtained TGA mass loss curve. From Fig. 71 it is evident that the proposed mechanism predicts the two-step decomposition of AB quite well. Mechanism predicts that during the first half of AB decomposition below ~415K (~140°C), only H_2 and NH_3 are released in gaseous phase. The predicted mass loss during this phase (~10.0%) closely matches the experimental data. Furthermore, it is to be noted that H_2 and NH_3 evolve into gaseous phase simultaneously, and that NH_3 cease to enter the gas phase very quickly (mass fraction of NH_3 becomes steady). The similar observation was made by Weismiller et al. [139] as well during the TOF-MS spectrometry.

Initiation of Modeling of Chemical Reactions in the Condensed Phase

It is our firm belief that a deep understanding of decomposition of energetic materials in the condensed phase must involve both a formulation of a detailed reaction mechanism and validation of the reaction mechanism using experimental data. The reaction mechanism is derived from quantum mechanics calculations using the highest possible level of theory using the experimental data as a guide. The experimental data should involve transient experiments and measurements of as many chemical species as possible. There are however, very few, if any, such previous studies in the literature. We began by examining the decomposition of ionic compounds, which are of strong interest to AFRL in their effort of developing new hypergolic bipropellants. If our studies were successful, then focus would shift on other energetic materials such as ammonium perchlorate mentioned earlier sections. Our initial effort focused on the high-nitrogen, ionic compounds guanidinium 5-amino tetrazolate (GA) [140] and guanidinium azotetrazolate (GzT) [141]. The molecular structures of these compounds are shown in Fig. 72. Here we show results from modeling of the TGA experiments in Fig. 73. The reaction mechanism has 55 species and 85 reactions. Using the compound method CBS-QB3 and a sensitivity analysis, it was required to modify one reaction with 2 kcal/mol in order to get a good agreement of the mass loss in TGA experiments. In summary, we concluded the following: a) decomposition of GA begins with chemical interaction within the ion pair Gu^+ and ATz^-, where the carbon in Gu^+ bonds to a ring nitrogen next the carbon in $5ATz^-$, forming the intermediate INT5, b) pathway in which the intermediate species INT5 is formed is the most critical, c) the first step observed in mass loss is caused by formation and evaporation of NH_3, HN_3, N_2 and NH_2CN whereas melamine evaporation results in the second step, d) decomposition at first proceeds through endothermic reactions, but is later replaced by exothermic reactions producing the N_2, NH_3, and HN_3, and finally e) proton transfer between Gu^+ and $5ATz^-$ is not predicted to occur by the quantum mechanics calculations for the liquid phase.

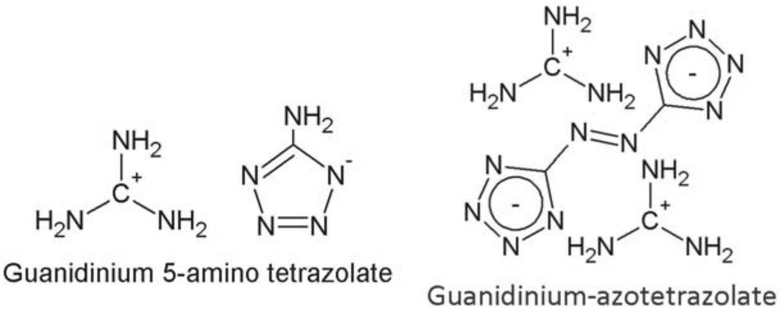
Guanidinium 5-amino tetrazolate

Guanidinium-azotetrazolate

Figure 72: Structures of the two high-nitrogen ionic compounds in our initial effort of detailed chemical kinetic modeling of condensed-phase reactions.

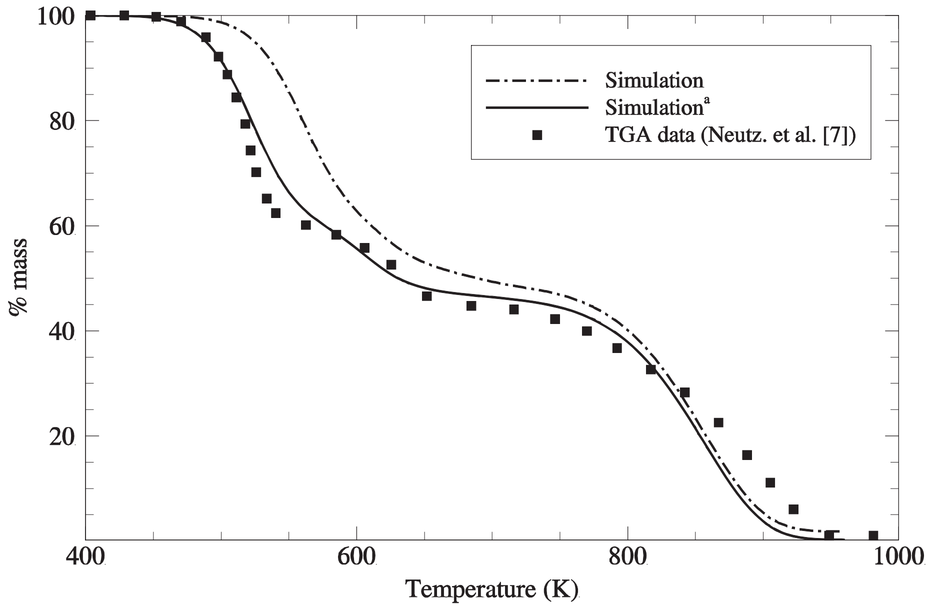

Figure 73: Variation of liquid mass with temperature (Heating rate = 10 K/min).
[a]Mass loss profile with the forward activation enthalpy of reaction R1 reduced by 2 kcal/mol. Ref. 7 in figure: J. Neutz, O. Grosshardt, S. Schäufele, H. Schuppler, W. Schweikert, Synthesis, Characterization and Thermal Behaviour of Guanidinium-5-aminotetrazolate (GA) – A New Nitrogen-Rich Compound, Propell. Explos. Pyrot., 28 (4) (2003) 181-188.

Failures that Occurred

The most challenging aspect of our work has been the slow process for installing a new FTIR spectrometer to which is attached a new TGA/DSC instrument.

The development of detailed chemical reaction mechanisms can be viewed as technology development enablers. For example, hydroxylammonium nitrate is an important ingredient in liquid propellants (AF315E) and is of great interest as a green material. The use of the liquid propellant AF315E requires a heated a catalyst bed. How such a bed should be designed for optimum performance is today achieved by trial and error. The results described in this report could serve as the basis for the development of the required modeling tools for new thruster designs. Similarly, with further work on AP decomposition, it may be possible to develop improved AP diffusion flame models, which ultimately could be integrated with and utilized combustion instability studies.

HEAT TRANSFER AND COMBUSTION OF METAL-BASED ENERGETIC MATERIALS

V. Yang, Georgia Institute of Technology

In the last 6 years of research, we studied the nanoscale heat transfer effects on flame propagation in nanoenergetic materials by using the nano-aluminum – water (nAl-H_2O) suspension as an example system. A fundamental treatment of heat transport in nanoparticles and interfaces is carried out. Firstly, *ab initio* and atomistic scale simulations were performed to investigate the nanoscopic nature of heat transport in bulk and nanosized aluminum and aluminum oxide, as well as at the interface of these materials. Atomistically informed macroscale modeling techniques were then employed to treat heat transport in mixtures of nanoparticles in liquid oxidizer to study combustion wave propagation. The key findings of this research are summarized herein.

Before delving into investigating the nuances, a simple analysis was performed on the factors contributing towards thermal conductivity. The analysis showed that size effects could be important and also that the thermal interfacial resistance (TIR) could be the limiting resistance. Therefore, as the first step, a detailed analysis of phonon transport properties in aluminum (Al) and aluminum oxide (Al_2O_3) has been performed via lattice dynamics (LD) using input from density functional theory (DFT) calculations. DFT-LD methods reproduce the transverse and longitudinal phonon branches in Al and Al_2O_3 along the edges of Brillouin zone accurately. Furthermore, temperature dependent phonon thermal conductivity (TC) of Al and Al_2O_3 are also evaluated by solving the Boltzmann transport equation (BTE) under the relaxation time approximation (RTA), and the thermal conductivity accumulation functions were also evaluated. This analysis gave insights on what phonon mean free paths were affected by the system size. Spectral distribution of TC was also analyzed to assess the possibility of engineering phonon transport properties. These studies provide a fundamental understanding of phonon frequencies and their contribution in pristine bulk Al and Al_2O_3 crystals.

Building on the understanding of thermal transport in bulk Al and Al_2O_3, the study was extended to understand heat transport across Al/Al_2O_3 interfaces. The thermal interfacial conductance (G) of the aluminum (Al)-aluminum oxide (α-Al_2O_3) interface along the crystal directions (111) Al || (0001) Al_2O_3 was accurately predicted. Two fundamentally different formalisms were used to make these predictions in the temperature range 50-1800 K: interfacial conductance modal analysis (ICMA) and the atomistic green function (AGF) method. ICMA formalism is based on the fluctuation-dissipation theorem whereas AGF is based on phonon gas model (PGM). The study reveals the right description of the interfacial heat flux, and the shortcomings of PGM in including full anharmonicity of vibrational modes.

Subsequently, we question the traditional nanofluid theory that substantiates the presence of nanolayers and Brownian motion (otherwise termed as ‘dynamic’ modes of thermal conductivity) in enhancing thermal conductivity of nanoparticle suspensions. To assess the role of dynamic mechanisms, a rigorous study based on equilibrium molecular dynamics (MD) simulations was conducted. We identify that the abnormally high thermal conductivity reported in prior studies is due to an error source originating from the artificial correlations of periodic images of atoms in the simulation system. We also devise a method to alleviate these artificial correlations and calculate thermal conductivity accurately. Hence, an alternative explanation to the unusually high thermal conductivity of nano-suspensions obtained using Green-Kubo relations is provided.

Finally, building on the knowledge of how the transport properties are affected by the nanometer length scales involved, a detailed numerical analysis of flame propagation in nano-aluminum (nAl) - water (H_2O) mixtures was performed. Considering a multi-zone framework, the nonlinear energy equation is solved iteratively using the Gauss-Seidel method. Thermal conductivity of nanoparticles is modeled using thermal conductivities of aluminum and oxide layer, as well as interfacial conductance. The effective thermal conductivity of the mixture is modeled using the Maxwell-Eucken-Bruggeman model as a function of temperature, spatial coordinate, and local mixture composition. Sensitivity of linear burning rate, r_b to changes in thermal conductivities of aluminum (k_{Al}) and aluminum oxide (k_{Al2O3}), and interface conductance (G) is also studied for various particle sizes in the nanometer range. This study illustrates how the nanoscale effects on the transport properties ultimately impact the combustion wave propagation in nanoenergetic materials, providing a solid foundation to their bottom-up rational design.

Metal based nanoenergetic materials

Energetic materials are typically defined as substances with large amounts of stored chemical energy and high rates of energy release. They can be classified based on composition as either monomolecular or composite. Metal-based energetic materials have higher volumetric energy densities than their hydrocarbon counterparts [97]. Among the metals, aluminum (Al) is particularly attractive due to its abundance in the earth's crust, low cost of extraction, and relatively safe products of combustion. Macro and micron-sized Al particles have been routinely used in combination with various oxidizers and binding agents to create solid propellants since the 1950's. Micron-sized Al particles nonetheless suffer from several drawbacks such as high ignition temperatures, agglomeration, and low reaction rates, resulting in low energy release rates [142-144]. The advent of nanotechnology and concurrent developments in synthesis and characterization techniques have offered new opportunities to realize different properties with nanomaterials and the possibility of using them as additives in energetic compositions. Nanomaterials are substances with characteristic dimensions <100 nm. They have lower melting and boiling temperatures [145], lower ignition time and temperatures, lower activation energy of oxidation [146] and enhanced chemical activity due to higher specific surface area (SSA) and surface energy [147]. In addition, due to the large SSA, nanoparticles also offer tailorable surface properties that have the potential to allow precision control of thermal transport and chemical kinetics [148, 149]. Hence, during the mid-1990's, widespread replacement of microparticles with nanoparticles created a new class of energetic materials called nanoenergetic materials.

Flame propagation in nAl mixtures: Prior studies

There have been numerous experimental studies conducted to understand the burning properties of nAl in various oxidizers. Tyagi *et al.* [150] measured the ignition probability of diesel droplets laden with aluminum nanoparticles. The diameter of particles used was 50 nm. The ignition probability increased by more than 100% due to the addition of nanoparticles, and was attributed to the increased reaction rates of nAl particles, resulting in faster and lower temperature ignition. Apart from being used as additives in conventional propellants and fuels, novel energetic materials created by dispersing nanometallic particles in liquid oxidizers have also been studied. Risha *et al.* [151] considered a green energetic material consisting of nano-aluminum particles dispersed in water and studied the effects of pressure and particle size on the burning characteristics. The burning rate was inversely proportional to the particle diameter, and the pressure exponent was in the range of 0.27-0.47, depending on the particle size. Despite the enormous potential of nAl combustion in propulsion applications, there have been very limited theoretical studies reported in the literature that describe flame propagation in these systems. Sundaram *et al.* [142] performed a companion theoretical analysis for the experiments of Risha *et al* [151] to investigate the effects of particle size and pressure on the linear burning rate, r_b of nAl-H_2O mixtures. Particle sizes ranging from 38-130 nm were considered for chamber pressures in the range 1-10 MPa. They used a mean particle burning time, τ_b, as a surrogate to the particle burning rate, given by [152]:

$$\tau_b = \frac{c\left[a_1 \exp(b_1 T) + a_2 \exp(b_2 T)\right] d_p^2}{p^m} \tag{47}$$

$$m = a_3 \exp(b_3 T) + a_4 \exp(b_4 T)$$

where the free parameters c, a_1, a_2, a_3, a_4, b_1, b_2, b_3, b_4 are free parameters that are optimized to experimentally measured burning times.

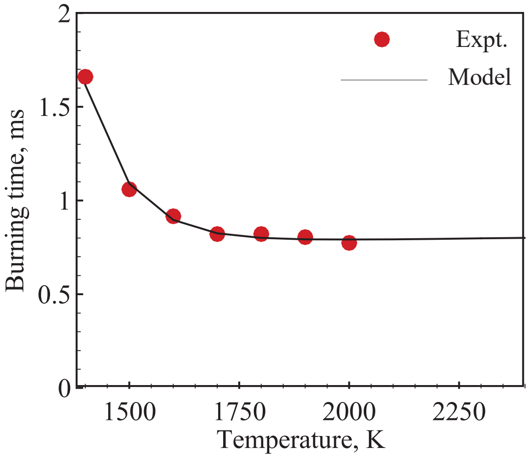

Figure 74: Comparison of nAl burning times predicted by Eq. 6.1 and experimental burning times [152] for a range of temperatures representative of the reaction zone of a flame

Figure 74 demonstrates the fidelity of the burning time model for a wide range of temperatures in the reaction zone of a nAl – water combustion system at 1 bar pressure, when compared with the experimentally obtained burning time values [152]. The burning time value at the ignition temperature (~1380 K) is > 1.5 ms, which reduces as we go to higher temperature due to the enhanced reaction rates. Sundaram *et al.* [142] combined this independently benchmarked burning time model with an effective thermal conductivity model to model flame propagation in nAl-H_2O mixtures. The thermal conductivity of Al and water were assumed to be constant throughout preheat and combustion zones. An effective thermal conductivity was calculated using an effective medium theory approach, which was originally developed for micron Al particles without accounting for the size and random distribution of particles. These methods overpredict r_b for particle sizes 80 and 130 nm for all pressures when compared with experimental results. The mean error in r_b for 130 nm particle is ~25%, whereas for the 80 nm particles, the error increases to 31%. For 38 nm particles, the predicted quantitative and qualitative trends differ substantially from the experimental results. In addition, the mean error is more than 50%, with a peak error in r_b of 104% at 3.5 MPa. Risha *et al.* attributed this error to the adsorption of water molecules to the nanoparticle surface, which prevents diffusion towards Al atoms within the core.

Note that for kinetically controlled combustion, heat conduction rates from the reaction zone to the unburnt reactants is crucial in sustaining a flame. If heat conduction rates are low, the thin reaction zone (flame) can get quenched before the reactants get preheated to the ignition temperature, or if it does not, the resulting flame will be slow-propagating. If the conduction rates are very fast, heat is conducted out to the system walls, subsequently quenching the flame. Hence, it is certain that heat conduction is as important as chemical kinetics. Heat conduction rates can be characterized by the thermal conductivity of the system. Until now, thermal conductivity has not been given the attention it perhaps deserves, and has been approximated using somewhat *ad hoc* modeling approaches.

In summary, there is a significant disparity between predicted burning properties and experimental results [142]. Since chemical reaction rates are accurately captured by the burning time model, it is reasonable to assume that the inadequate modeling of thermal conductivity could be a reason for this disparity. To ensure a high-fidelity combustion model, it is imperative that an *atomistically* informed heat conduction model be incorporated. An atomistically informed model should ideally account for how thermal conductivity changes at the nanoscale. Similar to reaction kinetics, another open question is: can higher burning rates be achieved by improving the heat conduction properties of the system? To answer such a question, it is important that we first review the physics of heat conduction in a nano-suspension.

Thermal conductivity of nanosuspensions

Thermal conductivity, *k,* is the constant of proportionality in Fourier's law of heat conduction that relates a heat flux density (Q) to the local temperature gradient (∇T), given by,

$$Q = -k\nabla T \ . \tag{48}$$

Thermal conductivity in solids is a property that consists of cumulative contributions from different types of heat carriers, namely electrons and phonons. A nano-suspension is a dispersion of nanoparticles in a fluid medium. To model effective thermal conductivity of nAl-H_2O mixtures, a fundamental understanding of the physics of heat conduction in nano-suspensions is required. The various components of the system are oxide coated nAl particles (Al core and Al_2O_3 shell) dispersed in a fluid as shown in Fig. 75.

:

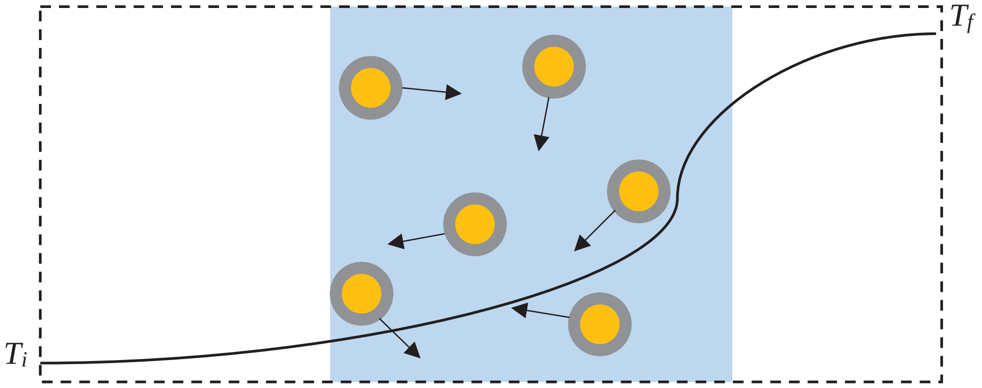

Figure 75: Schematic diagram showing nAl particles coated by an oxide layer dispersed in water. Temperature profile shows initial (T_i) and final (T_f) temperatures. Nanoparticles move around within the system in random directions, as shown by the arrows.

As can be seen from Figure 75, at any given instance, the particles undergo Brownian motion (random motion due to the collision of fluid molecules on the surface resulting in a net unbalanced force) with velocities indicated by the arrows. In theory, the effective thermal conductivity of the system has the following components: i) thermal conductivity of the core-shell nanoparticle, ii) thermal conductivity of the fluid, and iii) contributions to thermal conductivity due the *dynamic* modes of heat conduction. Thermal conductivity of the core-shell particle has contributions from thermal conductivity of the Al core, the Al_2O_3 shell, and the Al/Al_2O_3 thermal interfacial conductance (TIC). Temperature dependent thermal conductivities of bulk Al and Al_2O_3 have been experimentally studied and documented [153]. Availability of thermal interfacial conductance data is very limited (only in the temperature ranges: 50-480 K) and the temperature dependence of conductance is unknown beyond 480 K [154]. The thermal conductivity of different oxidizers has also been characterized and documented. The term *dynamic* mode is quite misleading. It was first introduced to explain the enhanced thermal conductivity in nanofluids. Nanofluids are a class of heat transfer fluids which are dilute (<1% volume fraction) suspensions of nanoparticles in a fluid medium. The dynamic modes of heat conduction in a nanofluid are associated with Brownian motion and nanolayering [155]. Brownian motion is the random thermal motion of suspended particle within the system. Nanolayering is the phenomenon by which the fluid forms a high-density crystalline layer on the surface of the nanoparticle due to its adhesive properties. The existence of these dynamic modes is highly disputed [156]. There are numerous works in the literature [156] suggesting the presence of these dynamic modes, that also propose theories to support it, though lately, these theories have been called into question [157]. The next three sections summarize our investigations and findings regarding these thermal conductivity components, and the fourth to follow summarizes their application in a flame propagation model.

Phonon transport in Al and Al_2O_3

Lattice dynamics (LD) calculations

Lattice dynamics (LD) can be used to evaluate the phonon thermal conductivity, phonon DOS, and polarization vectors of crystal structures. LD is a generalized formulation that can provide a clearer picture into the spectral characteristics of phonons. We start by evaluating the interatomic force constants (IFC) by LD calculations, which can be used to analyze phonon properties.

The major carriers of heat in solids are electrons and phonons. In metals, due to the large density of free electrons, the primary heat carriers are electrons and consequently, the phonon contributions are comparatively very low. Jain and McGaughey [143] calculated the phonon contributions to thermal conductivity of Al via solution of the phonon Boltzmann transport equation (BTE). Their results show that the phonon thermal conductivity of Al at 300 K is only 7 W/m-K, which is only a very small fraction (~3%) the total thermal conductivity of Al (237 W/m-K). Another DFT-LD calculation by Wang et al. [144] gives a phonon thermal conductivity of 4 W/m-K for Al at the same temperature. The differences in these results may be ascribed to the difference in pseudopotential used to perform the DFT calculations. Aluminum oxide, on the other hand, is an insulator. Due to the high band gap resulting in the unavailability of conduction band electrons, heat conduction in Al_2O_3 is phonon-dominated. Therefore, the dominant heat carriers in Al_2O_3 are phonons. To our knowledge, there has not been any work reported in the literature that reports the thermal conductivity of Al_2O_3 via DFT-LD calculations.

Here, we try to understand the effect of particle size on phonon thermal conductivity in Al and Al_2O_3. Here, we first employ a DFT-LD framework to study the temperature dependent phonon thermal conductivity of Al and Al_2O_3 and benchmark the framework with experimental results and/or prior theoretical studies. Secondly, the thermal conductivity accumulation as a function of phonon mean free path (MFP) is evaluated to assess the role of system sizes on thermal conductivity. Ideally, if the system size is larger than the smallest phonon MFP at which thermal conductivity accumulates, then phonons will not be affected by the system boundaries. Conversely, if system sizes are smaller, some of the large MFP phonons will have MFP restricted to the size of the system. These phonons are excessively scattering with the material's boundaries, thereby leading to a reduced thermal conductivity.

Firstly, direct displacement of relaxed lattice structure was performed to create numerous perturbed structures, which was followed by DFT calculations on each of the structure. The DFT calculations were performed by employing LDA for the exchange-correlation functional, and the norm conserving Perdew-Zunger [145] scalar relativistic pseudopotential was used to describe the core electrons. The projector-augmented wave formalism was implemented in QUANTUM ESPRESSO (QE) [146] with a plane wave energy cutoff of 750 eV. The Brillouin zone was sampled using 4x4x4 uniform (Monkhorst-Pack) k-point grids. For the self-consistent field (SCF) calculations, the electron energy convergence threshold was set 1x10^{-7} eV, and for the initial structural optimization, the force/atom convergence threshold was set to 1 x10^{-4} eV/Å. Forces on atoms obtained from DFT calculations as well as the displacement values were then used as input to LD calculations.

To perform LD calculations, the open-source ALAMODE code [147] was used, which is useful for calculating the harmonic and anharmonic force constants from DFT data and also facilitates the calculation of dispersion relations and the phonon DOS. The phonon DOS was calculated using a 4x4x4 mesh resolution, and dispersion relations were extracted using a fine 150 one-dimensional grid points along each phonon branch. The phonon BTE was solved under a relaxation time approximation (RTA) using a 30x30x30 grid, which produced converged phonon thermal conductivity values that can be compared with our results and with experimental data.

Phonon properties

Phonon dispersion relations

The phonon dispersion relations represent the phonon branches, and their frequencies as a function of wavevector, ω. The phonon group velocity, v_g can be calculated from the derivative of phonon frequency with respect to wave vector. Then v_g can be used to calculate phonon TC from the solution of BTE. In addition, dispersion relations can also be compared with experimental data to ensure that harmonic force constants are evaluated accurately.

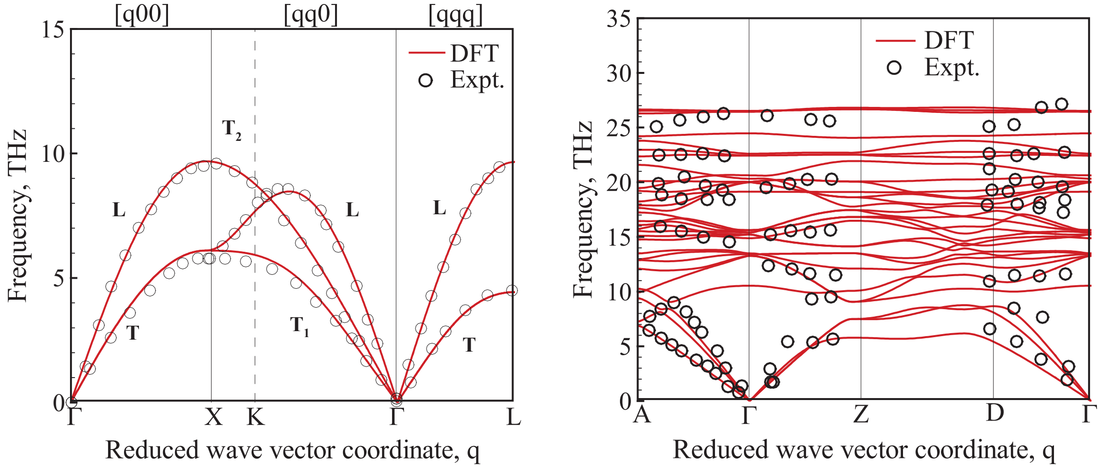

Figure 76: Phonon dispersion relations of a) Al and b) Al_2O_3 evaluated via DFT-LD method compared with experimental results [148] suggesting that the phonons are captured reasonably well by the DFT-LD framework

Figure 76 (a) and (b) show the dispersion relations of Al and Al_2O_3 respectively evaluated via LD calculations. The experimental results are also overlaid for comparison. Figure 76 (a) compares the transverse (T) and longitudinal (L) branches of phonons along the different crystal directions. Here, the relations are plotted in the Brillouin zone where the gamma point (center of the Brillouin zone), $\Gamma = 0$. The DFT-LD calculations are in accordance with the experimental results [148]. Figure 76 (b) compares the phonon branches evaluated by DFT-LD calculations with the experimental results. Note that there is very limited experimental data available on Al_2O_3 phonon branches. Nevertheless, for Al_2O_3, there is decent agreement between DFT-LD and experimental results. It is, therefore, clear from Figure 76 that phonon dispersion relations are reproduced with reasonable accuracy using DFT calculations; such accuracy suggests that the DFT calculations are correct and are useful for modeling the phonons in these materials.

Phonon density of states

In addition to the dispersion relations, the phonon DOS also gives important information about phonons present in a crystal. The DOS gives the density of phonons corresponding to different frequencies in a crystal structure. The total number of phonons (i.e. eigenmodes) is three times the number of atoms in the crystal geometry, corresponding to the three degrees of freedom available to every atom. Figure 77shows the phonon DOS for Al and Al_2O_3 crystals obtained from DFT-LD calculations. The experimental data [148] are also overlaid in the figures.

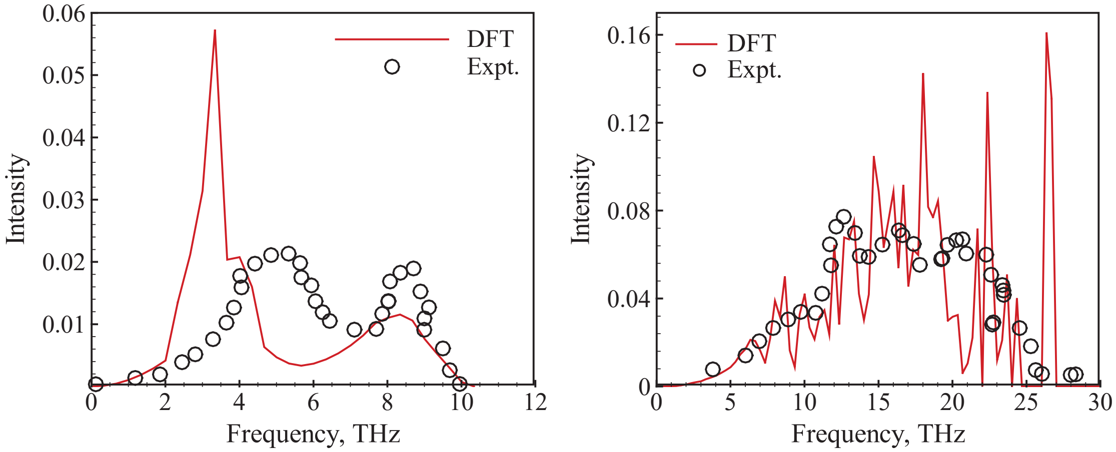

Figure 77: Phonon density of states (DOS) of a) Al and b) Al_2O_3 evaluated via DFT-LD method compared with experimental results [16] giving further validation to the fact that the phonons are captured reasonably well by the DFT-LD framework

From Figure 77 (a), it is evident that for Al, the first peak frequency predicted by DFT-LD calculations is ~ 2 THz lower than that of the experimental values, whereas the second peak frequency is correctly predicted. For Al_2O_3 as shown in Figure 77 (b), the DFT predictions match well with experimental results. By reproducing the phonon DOS, DFT framework has been further validated, and may be expected to give reasonably good predictions of phonon thermal conductivity.

Phonon thermal conductivity

The temperature dependent phonon thermal conductivity of Al and Al_2O_3 as a function of only p-p interactions are plotted in Figure 78 (a) and (b) respectively. The phonon thermal conductivity decreases with increase in temperature. The number of active phonons in a system increases proportional to k_BT where k_B is the Boltzmann constant. This increase in phonons leads in turn to an increase in p-p scattering, which results in a reduction in phonon TC.

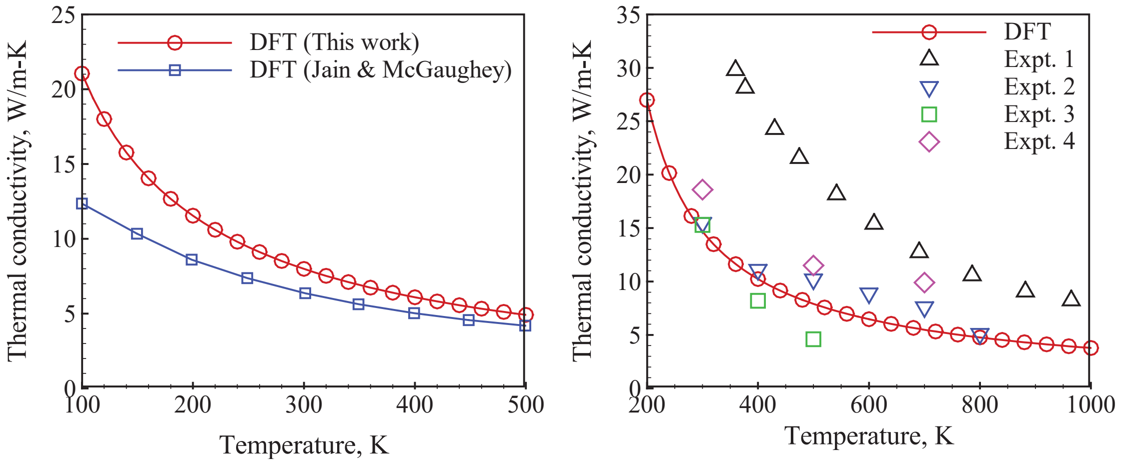

Figure 78: Phonon thermal conductivity (TC) of a) Al and b) Al_2O_3 evaluated via DFT-LD method compared with prior DFT calculations and experimental results

Experimental results for the phonon contributions to TC for Al are unavailable because no technique currently exists that can isolate the phonon thermal conductivity by itself. However, one can measure the electrical conductivity, which is intrinsically interrelated with the electronic component of the thermal conductivity. Using this approach, one can indirectly deduce the phonon contribution to the thermal conductivity by subtracting the electron contribution from the total thermal conductivity. However, this is not a very robust method, since it contains aggregated errors from the direct measurement and the subsequent deduction of the electronic thermal conductivity via the Wiedemann Franz law. Furthermore, the Wiedemann Franz law is not a rigorous law but instead a constitutive relation born out of a model for electron conduction and a relation to describe the energy carried by electrons along with their own charge. Nonetheless, deviations from this law have been frequently observed and this consequently introduces a great deal of uncertainty into the notion that one can indirectly deduce the phonon contribution to thermal conductivity from this approach. As a result, the results of prior DFT-LD calculations by Jain and McGaughey [143] are overlaid for comparison in Figure 78 (a); our predictions are comparable. To our knowledge, DFT prediction of phonon thermal conductivity of Al_2O_3 has not been reported in the literature. However, experimental results for Al_2O_3 [149] thermal conductivity from four different sources are overlaid in Figure 78 (b). As seen in Figure 78 (b), our calculations are in accordance with three out of four experimental results. This agreement suggests that the phonon thermal conductivity has been calculated accurately. Thus, the focus in the next section is on assessing the phonon MFP and size effects, which can become important at the nanometer length scales that involve in nAl combustion.

Size affected phonon thermal conductivity

Thermal conductivity accumulation function

The thermal conductivity accumulation plot as a function of phonon MFP calculated at T=300 K is shown in Figure 79. For Al, as can be seen in Figure 79 (a), phonon thermal conductivity accumulates at a MFP of only ~ 34 nm, as the contributions to thermal conductivity from larger MFP phonons are negligible. This observation suggests that if the system size is below 34 nm, phonon TC can be reduced, as larger MFP phonons become affected by the boundaries. As clearly illustrated by Jain and McGaughey [143] from the study of electron thermal conductivity as a function of MFP of electrons, it is quite evident that TC is affected for system sizes lower than 20 nm.

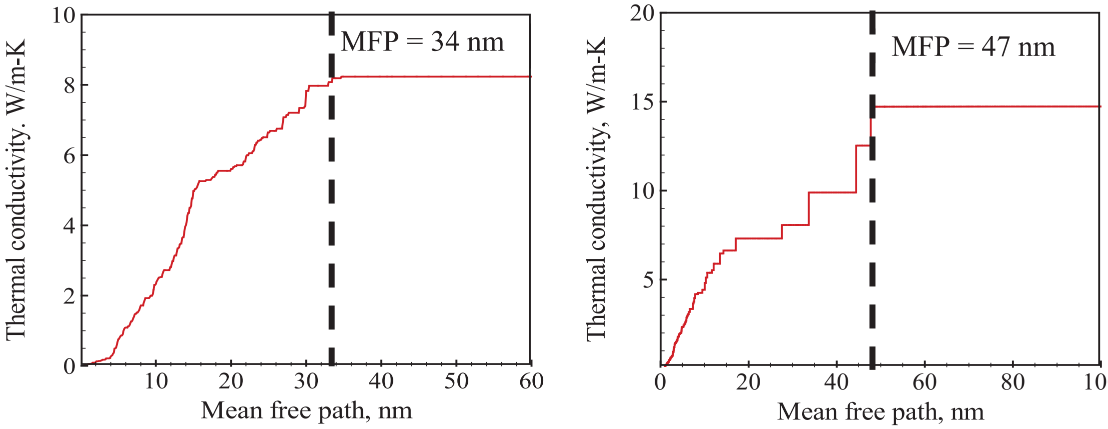

Figure 79: Phonon thermal conductivity accumulation plots of a) Al and b) Al_2O_3

For Al_2O_3, however, thermal conductivity saturates at MFP ~ 47 nm as shown in Figure 79 (b). Hence Al_2O_3 is more strongly impacted by size effects. Nonetheless, neither material is strongly affected as compared to longer MFP materials such as crystalline silicon, where the average MFP is 100 nm but almost half of the bulk TC comes from phonons with MFPs longer than 1 micron [158]. As a result, while modeling the thermal conductivity of a nanoparticle, the effect of particle size (or more conveniently, particle diameter) should be factored in, but only becomes significant for particle diameters less than about 47 nm, and we can roughly approximate the thermal conductivity, *k* as:

$$\begin{gathered} k = k_{bulk} \ \text{ for } D \geq L \\ k = \left(\frac{D}{L}\right) k_{bulk} \ \text{ for } D < L, \end{gathered} \tag{49}$$

where k_{bulk} is the bulk thermal conductivity, *D* is the system dimension, *L* is the peak mean free path at which $k \rightarrow k_{bulk}$.

Spectral thermal conductivity distribution

The phonon thermal conductivity contributions as a function of phonon frequency – termed the spectral thermal conductivity distribution – for Al and Al_2O_3 are given in Figure 80 (a) and (b) respectively. As can be seen from Figure 80 (a), for Al, a significant contribution to phonon TC is due to phonons with frequencies in the range 5-8 THz, whereas from Figure 80 (b), for Al_2O_3, significant contribution is from phonons within frequencies 4-9 THz.

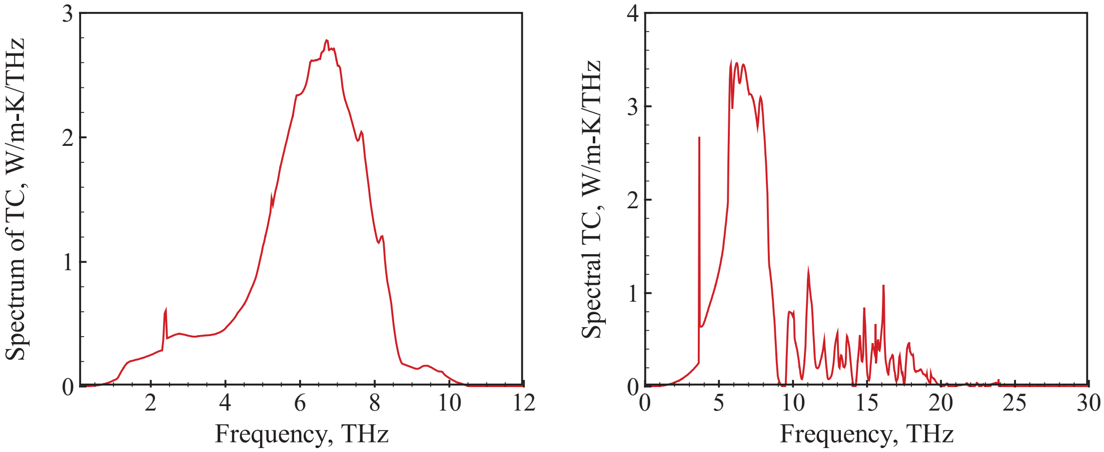

Figure 80: Spectral distribution of phonon TC of a) Al and b) Al_2O_3

Spectral thermal conductivity gives the relative importance of phonons at specific frequencies with respect to other phonons. It is assumed the relative importance of these phonon frequencies may be tied to their higher lifetimes and/or MFP's. Both phonon MFP and frequency dependent studies are very important in thinking about phonon engineered materials.

In summary, a detailed analysis of phonon transport properties in Al and Al_2O_3 has been performed via LD calculations using input from density functional theory (DFT) calculations. Firstly, the phonon dispersion relations and phonon density of states (DOS) are evaluated and compared with experimental data. The DFT-LD method reproduces the transverse and longitudinal phonon branches in Al and Al_2O_3 along the edges of Brillouin zone. Substantial agreement is found between LD predictions and available experimental data. Predictions in phonon DOS via lattice dynamics are also accurate. Two peaks in phonon density are observed in Al at ~3 and ~8.5 THz respectively. When compared with neutron scattering experimental data, the lower frequency is off by ~1 THz whereas at higher frequencies, data is reproduced more accurately. This discrepancy is due to neglecting electron-phonon scattering in Al metal. For Al_2O_3, the DFT-LD predictions of phonon DOS compare well with the neutron scattering data, confirming that the phonon properties are evaluated accurately. Furthermore, temperature dependent phonon thermal conductivity of Al and Al_2O_3 are also evaluated by solving the Boltzmann transport equation (BTE) under the relaxation time approximation (RTA). Calculated phonon TC of Al is very close to prior lattice dynamics calculations. Experimental data on phonon thermal conductivity of Al are unavailable; phonon thermal conductivity of Al_2O_3 evaluated by LD is close to three out of four experimental results reported in the literature. Furthermore, the thermal conductivity accumulation function was evaluated. Our results suggest that for Al, phonon TC accumulates at mean free path (MFP) ~ 30 nm. This finding suggests that if the system size is below 30 nm, phonon TC can be reduced due to the fact that some of the larger MFP phonons become inaccessible. For Al_2O_3, however, TC accumulates at a MFP of ~ 50 nm. Hence the system is more easily size affected than Al, but generally speaking the size effects are weaker than many other materials that have been analyzed [143]. Nonetheless, since particle diameters in the range of 10-50 nm are of interest for nAl combustion, the effect of particle size should be considered in modeling the combustion. Spectral distribution of TC was also analyzed to assess the possibility of engineering phonon transport properties. For Al, more than 80% of phonon thermal conductivity is due to phonons within frequencies between 5 and 8 THz. For Al_2O_3, more than 92% of TC was contributed by phonons with frequencies between 4 and 9 THz. The findings here provide a foundation to understand phonon transport across Al/Al_2O_3 interfaces, which can now be addressed in the next section.

Thermal conductance of Al/Al_2O_3 interface

Interfacial conductance modal analysis (ICMA)

To understand and quantify thermal interface conductance, *G*, one may seek experimental measurements, theory-based predictive models, or a combination of both. The time-domain thermo-reflectance (TDTR) method, an optical-pump probe technique, is the most widely used experimental method [154,159]. A typical TDTR experiment measures the total conductance but neither resolves the modal contributions nor elucidates the governing mechanisms. Sometimes, merely due to the low thermal conductivity of the constituent sides of the interface, the measurement is incapable of measuring *G* because of the low sensitivity to the interfacial resistance. In addition, experimental methods can be challenging and expensive especially from a standpoint of making clean and defect-free interfaces by epitaxial growth, and achieving high temperatures and/or pressures. Moreover, the results are sensitive to experimental conditions thus challenging reproducibility.

To serve the purpose, the recently reported interfacial conductance modal analysis (ICMA) formalism [160] based on the fluctuation-dissipation theorem and lattice dynamics has important features. In the ICMA formalism, the instantaneous energy transfer across an interface of material A and B can be given as:

$$Q_{A\to B} = -\sum_{i\in A}\sum_{j\in B}\left\{\frac{p_{i,\alpha}}{m_i}\left(\frac{-\partial H_j}{\partial \mathbf{r}_i}\right)+\frac{p_{j,\alpha}}{m_j}\left(\frac{\partial H_i}{\partial \mathbf{r}_j}\right)\right\}. \tag{50}$$

Here, $Q_{A\to B}$ is the instantaneous energy transfer across the interface of material *A* and *B*; *p, H,* and *m* represent the momentum, Hamiltonian, and mass of atoms *i* and *j* respectively. From this relation, the conductance can be calculated by the time integration of correlation of autocorrelation of the equilibrium fluctuations of the heat flow as:

$$G = \frac{1}{Ak_BT^2}\int_0^\infty \left\langle Q_{A\to B}(t)\cdot Q_{A\to B}(0)\right\rangle dt\,. \tag{51}$$

Since ICMA is implemented in classical molecular dynamics (MD) framework, it is capable of full inclusion of anharmonic contributions to the interfacial heat transfer by all types of vibrational modes including the localized interfacial modes. Most importantly, ICMA can resolve the modal heat flux Q_n (i.e. $Q=\sum_n Q_n$) yielding the modal contribution to conductance, G_n (i.e. $G=\sum_n G_n$) by utilizing the input eigenvector basis set given as input.

ICMA method is implemented in equilibrium molecular dynamics (EMD). A simulation cell size of ~19.2 nm in length having a cross sectional area of ~80 nm^2 with 1260 atoms containing an interface with crystal directions (111) Al ‖ (0001) Al_2O_3 representing the primary orientation in FCC metal-metal oxide [161] interfaces is used for the simulations. The system length was chosen based on an initial size-dependency calculation, which suggested that a system size larger than ~18 nm yields a size independent *G*. To model atomic interactions, the Streitz-Mintmire (SM) potential is used.

Total conductance

The total *G* values as a function of temperature obtained from various sources are summarized in Figure 81. Results of our ICMA and atomistic green function (AGF) calculations are compared with the experimental results from three different sources [154,162] as well as the diffuse mismatch model (DMM) predictions [154]. Experimental data from 50-300 K are obtained from Stoner and Maris [154b], whereas the experimental results for 300-480 K are obtained from Hopkins *et al.* [162]. Another set of experimental data and DMM calculations reported by Hopkins *et al.* [154a] are also overlaid for comparison. Experimental data above 480 K is not available.

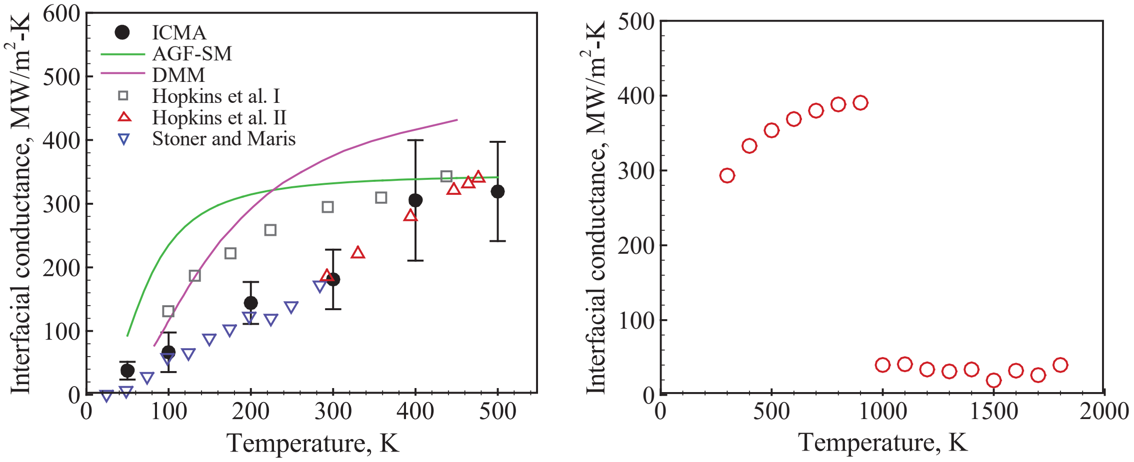

Figure 81: a) TIC predicted by ICMA and AGF methods compared with experimental results and diffused-mismatch model (DMM) prediction, and b) TIC predicted by ICMA from T = 300-1800 K

As seen in Figure 81(a), except for a slight proximity with Hopkins et al. experimental results below 150 K, DMM predictions are considerably above the experimental results. This is possibly because of the severely restrictive assumption on phonon scattering to be purely diffusive in nature. The green line represents the results of AGF calculations. It is quite evident that except for the coincidence with the experimental result of Hopkins et al. at T = 450 K, the AGF significantly over-predicts *G* from 50-450 K. The temperature trend of *G* predicted by AGF is also not in agreement with two of the experiments. AGF results steeply rise from 50-100 K and plateaus thereafter. At higher temperatures, *G* is nearly constant; no temperature dependence is observed.

We attribute the poor predictive power of AGF to two factors. Firstly, AGF does not take into account the intrinsic anharmonicity associated with the vibrational modes, which can play a vital role in heat conduction [163]. Secondly, the only mechanism that the AGF accounts for, in evaluating the temperature dependence is the quantum (Bose-Einstein) correction applied to the modal calculations. This is different from ICMA in which we calculate conductance using classical MD followed by quantum correction at every single temperature, thereby including anharmonicity and the quantum effect on specific heat. To examine these ideas, a detailed analysis of modal anharmonic energy distribution and modal contribution to *G* is discussed in the following sections.

With this high level of accuracy in predictions, ICMA can be deemed to be thoroughly benchmarked with experiments, and can be extended to higher temperatures as well. Figure 81 (b) shows the results of *G* calculated via ICMA for T = 300-1800 K, an ideal temperature regime of combustion of nano-suspensions. As can be seen from Figure 81 (b), *G* increases monotonically with temperature until the melting temperature of Al = 933 K. At the melting temperature, there is a sharp fall in TIC, which remains nearly constant thereafter. This is due to the loss of crystallinity of core Al lattice as it melts.

Modal analysis

Partial DOS of the interface structure, modal summation of TIC, and mode-mode correlations at 300 K is shown in Figure 82 (a)-(c) respectively. Figure 82 (a) shows the partial DOS calculated from the eigenvector basis set obtained by lattice dynamics calculations. From the partial DOS, we can identify four types of modes based on their participation ratio as: i) extended modes, ii) partially extended modes, iii) isolated modes, and iii) interfacial modes [160,164]. Extended modes are present at the interface, but the majority of them by contrast, are delocalized into both materials. Partially extended modes are also present at the interface, but majority of them are not present at the interface, and are localized on one side of the interface. Isolated modes exist far away from the interface while interfacial modes are localized vibrational modes which are mostly present at the interface. Figure 82(b) shows the dominance of partially extended modes in Al (< 9 THz) and Al_2O_3 (<12 THz) and the negligible presence of extended modes (< 0.6 THz). A small percentage of modes (> 9 THz) are interfacial in nature whereas the remaining modes seem to be isolated.

In Figure 82 (b) and (c), two distinguishable regions are marked as Region 1 and 2. Region 1 is below 9 THz marking the peak frequency in Al. Region 2 comprises all frequencies above 9 THz. In region 1, distinct regions of strong positive correlations are observed. Except below 0.6 THz where extended modes are present, this region is dominated by the cross-correlation (CC) of partially extended modes of Al with that of Al_2O_3 reflecting as red regions in the correlation map. Considering the large population of states of partially extended modes of Al and that of Al_2O_3, this region of high CC is the major reason for the initial high slope of TIC accumulation until ~ 9 THz. After that, within region 1, 9-12 THz marks a narrow region of interaction between interfacial and partially extended modes of Al_2O_3, which due to a combined effect of weak correlations and low density, only gives a very shallow slope in TIC accumulation.

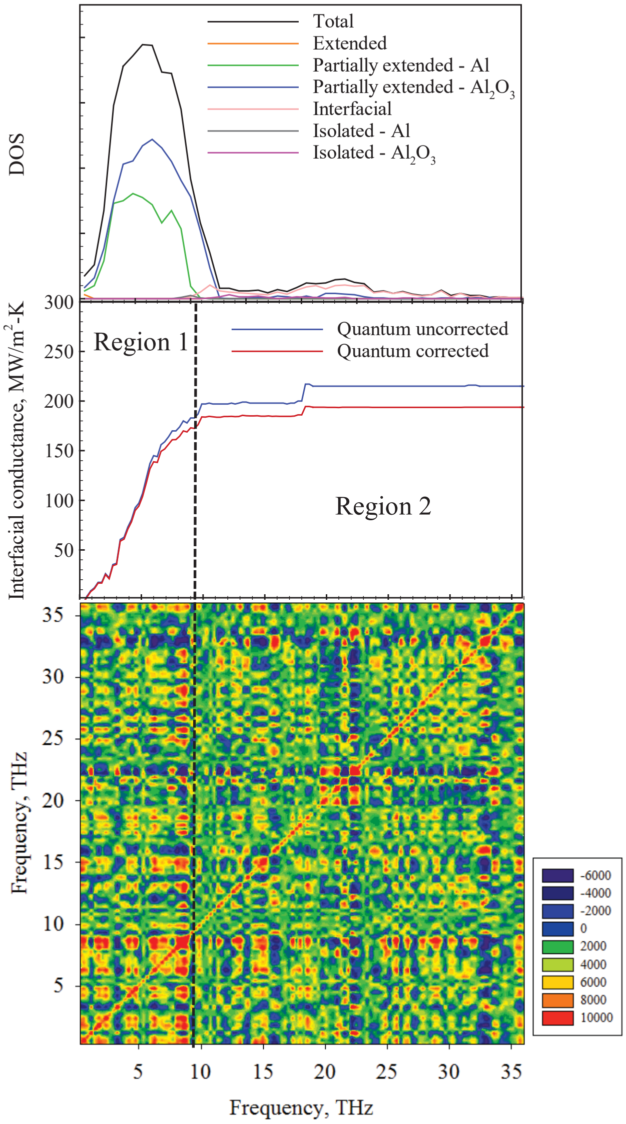

Figure 82: a) Partial DOS showing different types of modes, b) TIC accumulation (In this system, >90% of the total conductance is contributed by partially extended modes on Al and Al_2O_3, and the extended modes below 12 THz, c) mode-mode correlation map at T = 300 K showing three distinguishable regions.

From 12-15.5 THz, interfacial modes, and the isolated and partially extended modes of Al_2O_3 co-exist. The frequency ranges in region 2 also show a strong correlation. However, the very low density of these modes is clear evidence of the small increment of *G* in this region. In region 2, the modal characteristics shift drastically from strong positively to strong negatively correlated regions in effect canceling each other, maintaining a cumulative *G* constant until ~17.5 THz. From 17.5

THz to 22.5 THz, there are observable regions of strong correlation and a slight increase in the density of vibrational states. Especially around the diagonal, there is a strong observable positive correlation from the interaction between the interfacial modes. The combined effect is a jump in *G* accumulation in Figure 82 (b) at around the same frequency, i.e., 17.5 THz. In order to further gauge the role of each mode, it is important to obtain the contribution of each type of mode normalized by the *DOS,* i.e., *G/DOS*.

Table 9: Contribution of different types of modes to partial DOS and G, and the percentage relative contribution of G to DOS

Mode Type	$DOS(\%)$	$G(\%)$	G/DOS
Extended	0.18	0.31	1.72
Partially extended	89.52	91.83	1.02
Interfacial	9.31	7.80	0.84
Isolated	0.90	0.06	0.07

Table **9** shows the population of each type of mode in partial *DOS*, and their contribution towards *G*. Also given is the normalized contribution of *G*. The high density of partially extended modes in the region from frequency < 12 THz corresponding to 89.52% of DOS together constitute towards ~92% of TIC. The *G/DOS* ratio of partially extended modes ~1 suggesting that the role of partially extended modes in *G* is justified by their presence in the partial *DOS*. In the remaining 10.5% modes, 9.31% is constituted by interfacial modes and under 1% by isolated modes. The percentage of extended modes in the system is only 0.18%. Prior studies have shown that extended modes occur on regimes with high frequency overlap [164]. Therefore, it is surprising that, given the great degree of frequency overlap in this regime, the percentage of extended modes is significantly low. This suggests that whether or not the extended modes are likely to exist within a frequency regime is not purely dictated by frequency overlap, but may also require matching structural structures. Since Al and Al_2O_3 have significantly different crystal structures, it may be difficult for the modes of vibration of each material to extend throughout the interface structure while not only conserving energy (i.e., frequency) but also momentum (i.e., wavelength).

Also considering the *G/DOS* value of 1.72, it is to be understood that there is a disproportionately high contribution to *G* from the extended modes for their relatively small presence in *DOS*. Therefore, we doubt that the presence of high concentration of extended modes is the reason for the apparent high *G* of cSi-cGe [164] interfacial system reported in a prior work. We believe that for the Al/Al_2O_3 system, a major portion of *G* is contributed by partially extended modes, subsequently helping us achieve realistic predictions. In summary, ICMA has not only been able to provide an accurate theoretical prediction of interfacial conductance, but also capture the physical picture of modal interactions governing thermal transport.

The TIC of the aluminum (Al)-aluminum oxide (α-Al_2O_3) interface along the crystal directions (111) Al || (0001) Al_2O_3 has been accurately predicted. Two fundamentally different approaches: interfacial conductance modal analysis (ICMA) and atomistic green function (AGF) method in the temperature range 50-500 K. While AGF over predicts *G*, predictions of ICMA show great agreement with experimental results both quantitatively and qualitatively. The ICMA formalism seems to do a better job of explaining the experimental data than the PGM based models, which can be ascribed to its more fundamental treatment of the interfacial heat flux, its inclusion of full anharmonicity of vibrational modes, and for its ability to access to phonon mode level details. Using the benchmarked ICMA framework, the TIC of Al/Al_2O_3 interface was calculated for temperatures up to 1800 K. It was observed that TIC increases monotonously up to the melting point of Al (= 933 K) and drops sharply by an order of magnitude thereafter. Experimental measurement of TIC at higher temperatures is challenging, hence ICMA provides a promising way to achieve this. In a real combustion system, elevated temperatures exist, and in the ignition and combustion zone, Al exists in molten state. In this regime, the significantly low TIC value could be a major resistance to overall heat conduction in the nanosuspension. In summary, we quantified TIC across a wide range of temperatures, which can now be fitted to a mathematical model.

Insignificant contribution from dynamic modes

Molecular dynamics of heterogeneous systems

EMD simulations are conducted for a system consisting of a single alumina (Al_2O_3) nanoparticle and water molecules. GK relations are used to calculate thermal conductivity at a temperature of 300 K. Partial enthalpy correction is applied. The volume fraction is in the range 1-10%. Particle sizes of 1 and 3 nm are considered. Note that when the particle size is changed, simulation cell size is readjusted to obtain the target volume fraction. Atomic interactions within Al_2O_3 are modeled using the potential function developed by Vashishta et al. [165]. Interactions in water are captured using the Extended Simple Point Charge [166]. (SPC/E) model, with bonds constrained by the SHAKE algorithm [167]. Long-range electrostatic interactions are treated by particle-particle-particle-mesh (pppm) summation [166]. The alumina-water cross-interaction is modeled using Lorentz-Berthelot mixing rules [168]:

$$\sigma_{ij} = \frac{\sigma_{ii} + \sigma_{jj}}{2} \qquad (52)$$
$$\varepsilon_{ij} = \sqrt{\varepsilon_{ii}\varepsilon_{jj}}$$

where $\varepsilon_{Al\text{-}Al} = 1.4383 \times 10^{-8}$ eV, $\sigma_{Al\text{-}Al} = 5.3814$ Å, $\varepsilon_{O\text{-}O} = 1.6847 \times 10^{-3}$ eV, and $\sigma_{O\text{-}O} = 3.9883$ Å [169].

The nanoparticle and water systems are independently equilibrated at the target temperature. For the water system, isobaric-isothermal (NPT) ensemble is used and PBC are imposed in all three directions. Temperature and pressure were controlled by Nose-Hoover thermostat and barostat, respectively. For the nanoparticles, the microcanonical (NVE) ensemble is used, and free boundary conditions are imposed on all directions. A Berendsen thermostat [170] is used to maintain the temperature of the nanoparticle at 300 K. The suspension is created by creating a spherical cavity at the center of the water domain and inserting the equilibrated nanoparticle in the cavity. Care was taken to make sure that there is no overlap of atomic positions. The box dimensions were chosen based on the volume fraction, while ensuring that densities of both materials match the experimental counterparts. After the particle and water systems are independently equilibrated, they are combined. The resulting system is equilibrated at 300 K and 1 bar in Nose-Hoover isobaric-isothermal (NPT) ensemble for 100 ps using a time step of 0.1 fs. The thermal conductivity calculation is then carried out for a time period of 5 ns; heat current correlation times are in the range 2.5-10 ps. All simulations are conducted using the LAMMPS [171] MD code; the Verlet Algorithm is used for time-integration.

Thermal conductivity of water and nano-suspensions

Figure 83 shows thermal conductivity of water as a function of temperature calculated from GK relations using different interatomic potentials. Experimental results are also overlaid for comparison. As can be seen from Figure 83, the thermal conductivity of water increases from 0.72 to 0.81 W/m-K, when the temperature increases from 300 to 370 K. Predictions differ from experimental values marginally, suggesting the model is valid and SPC/E potential is effective for calculating the thermal properties of water.

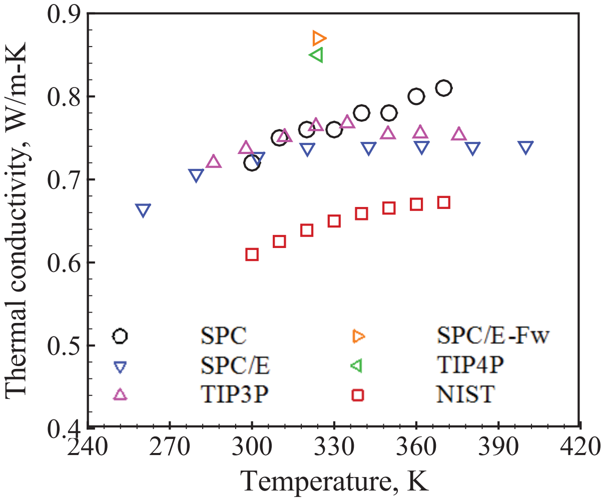

Figure 83: Thermal conductivity of water as a function of temperature evaluated by MD simulations using different potential functions, compared with experimental results

Figure 85 shows the variation of effective thermal conductivity (k_e/k_f) of the mixture with volume fraction (ϕ). Results suggest a near-linear variation of k_e/k_f with ϕ, aligning well with the behavior of nanofluids [178]. For a particle size of 3 nm and $\phi \sim 9$ %, k_e/k_f is ~200%, substantially greater than the predictions of the nanofluid thermal conductivity models [163]. As particle size is reduced to 1 nm, the enhancement increases to 235% at $\phi \sim 9$%. This is similar to the observations of other researchers [156]. In the absence of aggregation or Brownian motion, enhancements may be credited to possible nanolayer effects, but that hypothesis can be tested. In essence, the nanolayer thickness, *h*, may be estimated using a radial density profile, as shown in Figure 84 (b), evaluated using 0.5-1 Å thick spherical shells around the particle. The nanolayer can be approximately taken as the region between the particle surface and the shell in which the density reduces to the bulk density of water. For the cases in Figure 85, the estimated nanolayer thickness is ~ 6.5-9 Å or 2-3 atomic layers, and it is independent of the particle size. This is in agreement with the physisorption theory [174] as well as with *ab initio* findings [175]. As a result, smaller particles may be expected to have a higher relative nanolayer thickness, *h/D*, resulting in a higher thermal conductivity, producing a seemingly convincing validation of the nanolayer hypothesis.

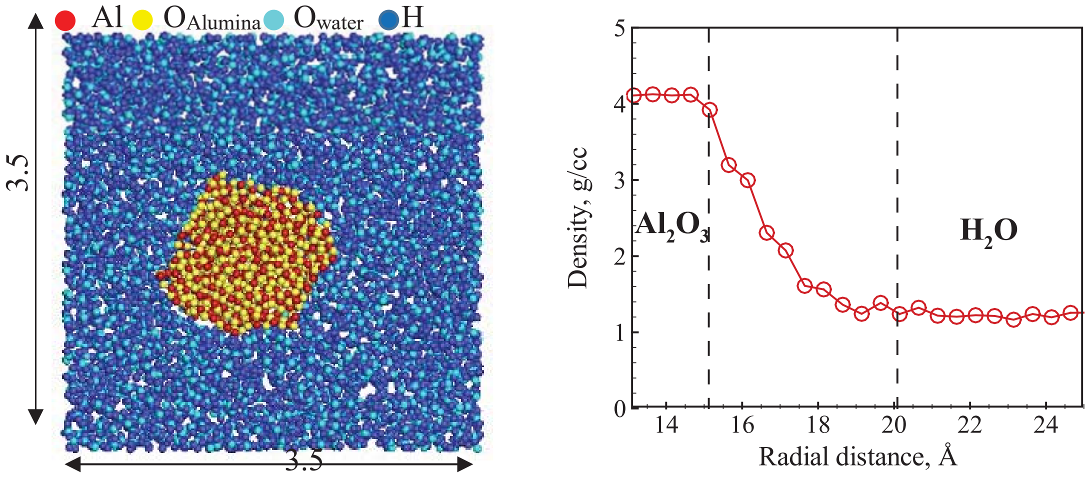

Figure 84: (a). Cross-section of single nanoparticle simulation system, and (b) radial density profile for 1 nm particle suspension at $\phi \sim 1\%$

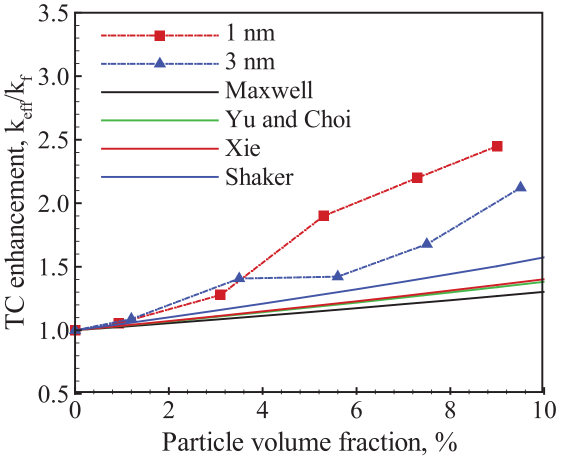

Figure 85: Enhancement in effective thermal conductivity (TC) as a function of particle volume fraction compared with various thermal conductivity models

This hypothesis, however, has several issues. Firstly, as seen in Figure 84 (a), the nanoparticle is not a perfect sphere. Surface roughness, with a characteristic dimension of a few angstroms, could contribute to an increase in mass density near the surface. Furthermore, water layering occurs mainly by hydrogen bonding, which does not cause significant density changes [176], as reported in other works [156]. In addition, the NEMD analysis of Liang et al. [177] suggests that the nanolayer thermal conductivity is only ~1.6 times that of the liquid, suggesting its insignificant role in interfacial conduction.

Figure 86 below shows thermal conductivity enhancement as a function of particle thermal conductivity. As shown in Figure 85, at lower volume fractions, 3 nm particle suspensions have a higher thermal conductivity than 1 nm particle suspensions, probably because the system sizes are so large that the effect of artificial correlations are not very strong. However, as the volume fraction increases (or system shrinks), these effects intensify, and we observe a shift in the trend.

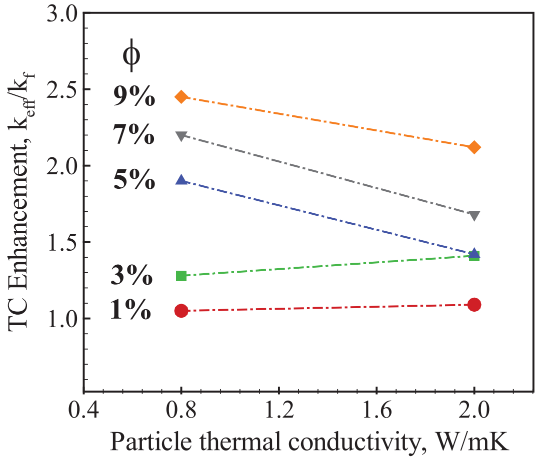

Figure 86: Enhancement in effective thermal conductivity (TC) calculated from single particle simulations as a function of particle thermal conductivity for various volume fractions

Artificial correlations

The size effect on thermal conductivity poses concerns. Figure 87 shows the effect of particle size on thermal conductivity, k_p, of alumina nanoparticles. For a 1 nm particle, k_p is only about one-fifteenth of the bulk value. This is expected, as the phonon MFP decreases with decreasing particle size due to boundary scattering [178] and accessible phonon modes are limited due to size-restricted phonon wavelengths. This suggests that the effective thermal conductivity of nanofluids may decrease with decreasing particle size, contrary to the trend shown in Figure 85.

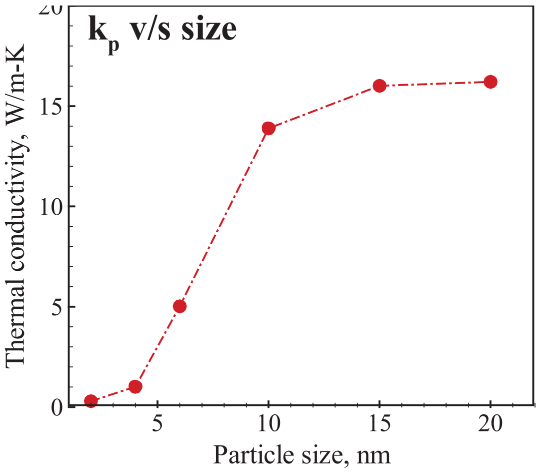

Figure 87: Thermal conductivity of alumina nanoparticle as a function of particle size

This contradiction highlights two factors governing the calculated thermal conductivity, namely the magnitude of the HCACF, and the time required for the fluctuations to lose correlation. If the correlations are large and/or remain intact for a long time, greater thermal conductivity may be expected. As periodic boundary conditions are imposed, it is possible that an atom will experience perturbations from its own periodic image. In particular, an atom can thus experience an artificial enhancement in the self-correlated heat current, as its motion perturbs the surrounding atoms, which can then be transmitted through the entire supercell back to itself. The returning and initial perturbations are likely to be well-correlated, as they originate from the same atom. This is unrealistic because every atom is unique, and perturbations to its surrounding environment can never possess a circular resonance with its own motion, in reality. The observed thermal conductivity enhancement could thus simply be a numerical artefact arising from the periodic boundary conditions.

Disparities in vibrational frequencies may also play an important role in exacerbating this problem. Comparison of the vibration spectra of alumina and water [165,179], as shown in Figure 88, reveals that the frequencies associated with water are 3-4 times higher than that of alumina. Consequently, water would experience vibrations of alumina atoms as low frequency waves. As lower frequency waves can be transmitted farther through a medium, since they experience less attenuation [180], alumina vibrations have a greater propensity to establish a circular resonance from the PBC. These perturbations can thus form a feedback loop if they are not sufficiently damped by the surrounding water molecules. Furthermore, this effect would be more pronounced in smaller simulation domains and/or systems with long-range forces, such as those in ionic suspensions.

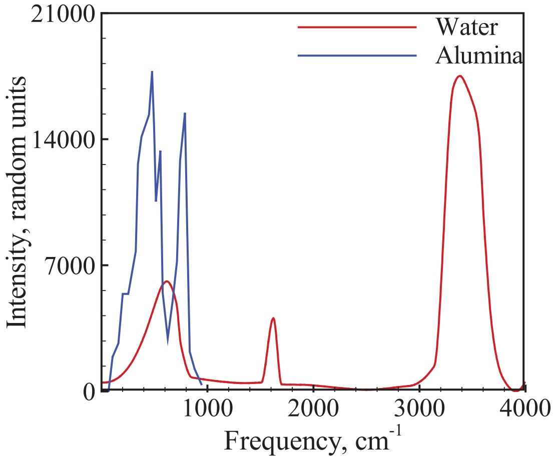

Figure 88: Comparison of the vibrational spectra of water and alumina

For the alumina-water system, the electrostatic part of the SPC/E force-field is truncated at 10 Å, whereas the Vashishta et al. [165] potential is truncated at 6 Å. For a 1 nm particle suspension, however, the minimum distance between an alumina atom and its nearest image is only ~4 Å. Therefore, in such a small supercell, an atom can experience self-interactions, which are intrinsically correlated, and consequently lead to a component in the HCACF associated with fictitious self-correlations. As the particle size and volume fraction decreases, the system gets larger and self-interactions and artificial correlations are suppressed. This is an intrinsic problem associated with PBC and small system sizes, but the problem can be mitigated by choosing a system size large enough to minimize artificial correlations. This, however, imposes constraints on the maximum attainable volume fraction with single-nanoparticle, although only volume fractions as high as 20-30% are of concern for many practical propulsion and energy-conversion systems. Alternatively, we may use multiple nanoparticles in the system, as illustrated in Figure 89 (inset).

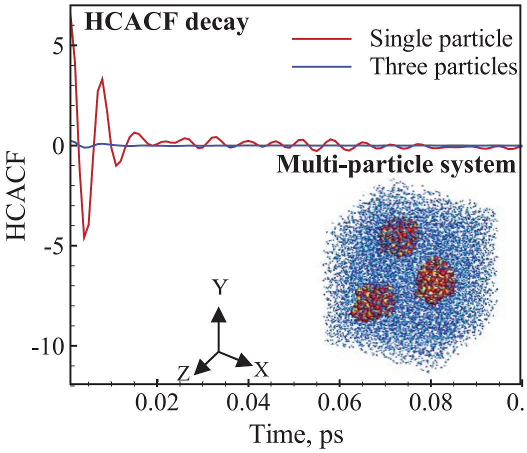

Figure 89: Time decay of heat current autocorrelation function 1 nm particle, ϕ = 10%; *Inset*: multi-particle simulation system

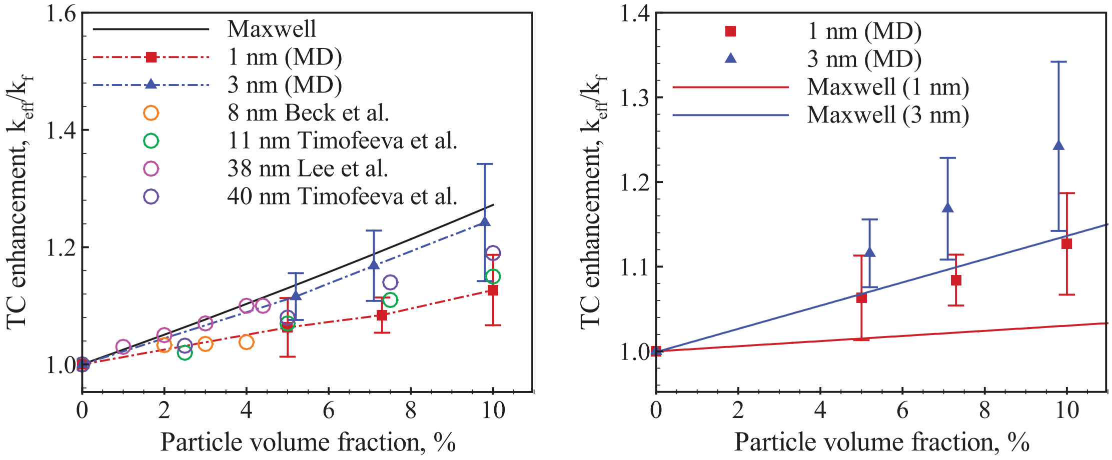

Figure 90: Enhancement in effective thermal conductivity (TC) calculated from multi-particle simulations as a function of particle volume fraction compared with (a) Maxwell model [173] with bulk thermal conductivity of alumina and experimental results [181](b) Maxwell model with thermal conductivity of alumina particles from Fig. 78.

It is logical to expect that the addition of more nanoparticles is likely to hamper the development of artificial self-correlations due to the presence of unrelated perturbations from other nanoparticles, thereby breaking the symmetry that a single particle tries to establish with its own image. This hypothesis was then tested by comparing the time decay of HCACF for single and three-particle systems, as shown in Figure 89. For single-particle systems, HCACF oscillates substantially before decaying to zero. These fluctuations are, however, damped in three-particle systems, resulting in a quicker and smoother decay. Prior studies attributed these oscillations to back-scattering of phonons at the particle-fluid interface [155] or to the relative motion of dissimilar atoms [182]. However, the results of the present study, suggest that the oscillations are merely associated with artificial correlations.

The thermal conductivity was then recalculated for multi-particle supercells. By gradually increasing the particle count and testing for convergence, it was found that a minimum of three alumina particles are required to diminish the artificial correlations. Multiple initial configurations were used to remove any directional dependencies, and an average of twelve independent runs were used to calculate thermal conductivity. Figure 90 (a) shows the resulting variation of k_{eff}/k_f

with ϕ for different particle sizes and the MD predictions are compared with experimental results [181] and the Maxwell model. In Figure 90 (a), bulk thermal conductivity is used, while in Figure 90 (b), nanoparticle thermal conductivity (from Figure 87) is used. Experimental data correspond to nanofluids with negligible aggregation. The results do not suggest any anomalous enhancement beyond the Maxwell model. In fact, MD predictions are slightly lower than the Maxwell model, and agree well with the experimental data. Furthermore, the effective thermal conductivity also increases with increasing particle size, which is consistent with the size dependent thermal conductivity behavior of nanoparticles. Figure 90 (b) shows that MD predictions are marginally greater than Maxwell model predictions, when the nanoparticle thermal conductivity values are used instead of the bulk values. This may be because the Vashishta potential underestimates the thermal conductivity of alumina, as explained earlier.

To conclude, an alternative explanation to the unusually high thermal conductivity of nanosuspensions obtained using Green-Kubo relations has been investigated. While prior studies credit them to dynamic heat transport mechanisms, our results suggest that these high values are merely an outcome of artificial correlations, arising from single nanoparticle systems and PBC, thereby introducing artificial contributions to the heat current autocorrelation function (HCACF). This problem is expected to be prominent for systems in which vibration frequencies of the constituents are disparate. In such cases, low frequency perturbations are transmitted through the surrounding high frequency medium and return to the originating particle due to PBC. The resulting circular resonance contaminates the HCACF, which is more pronounced for smaller particles and/or higher volume fractions. In an effort to alleviate this artifact, multi-particle systems were considered. The presence of additional particles impedes the development of artificial self-correlations by breaking the particle-image symmetry. Thermal conductivity predicted from the rectified HCACF is in good agreement with experimental data and the Maxwell model predictions. It is to be noted that the required minimum number of particles depends on the simulation system, which can be determined by devising an appropriate convergence test. In summary, Brownian motion and nanolayering have negligible roles on enhancing the effective thermal conductivity of a nanosuspension and they need not be explicitly included in the effective thermal conductivity model.

Numerical modeling of flame propagation in nanosuspensions

Thermal conductivity modeling

The inputs of an effective thermal conductivity model are the particle thermal conductivity (k_p), fluid thermal conductivity (k_f) and the particle volume fraction, Φ. In order to evaluate k_p, let us first consider a series circuit model representing the interface of Al and Al_2O_3 as shown in Fig. 91.

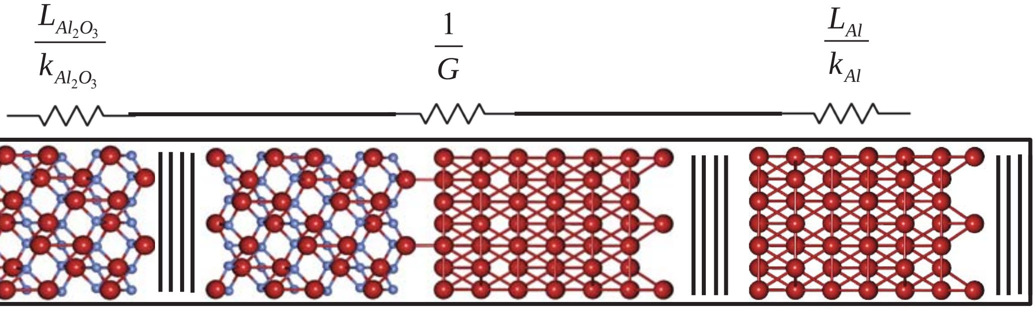

Figure 91: Series circuit framework to evaluate thermal conductivity of nanoparticle

This circuit is a partial representation of the nano-aluminum particle with oxide coating. It consists of three main components: bulk Al whose thermal conductivity is denoted by k_{Al}, bulk Al_2O_3 whose thermal conductivity is denoted by k_{Al2O3}, and the interfacial device whose conductance is denoted by G. As shown in Fig. 91, the thermal resistance from Al_2O_3, Al, and the interface are given as: $\frac{L_{Al_2O_3}}{k_{Al_2O_3}}, \frac{L_{Al}}{k_{Al}}$, and $\frac{1}{G}$ respectively. L denotes the length of each device. The net thermal conductivity of the interfacial system, k_{int} shown in Fig. 91 can be obtained as:

$$k_{\text{int}} = \frac{L}{\left(\frac{L_{Al_2O_3}}{k_{Al_2O_3}} + \frac{L_{Al}}{k_{Al}} + \frac{1}{G}\right)} \tag{53}$$

This concept can be extended to estimate the thermal conductivity of a passivated nAl particle of total diameter D_p, and can be given as:

$$k_p = \frac{D_p}{\left(2.\frac{L_{Al_2O_3}}{k_{Al_2O_3}} + \frac{D_p}{k_{Al}} + \frac{2}{G}\right)}. \tag{54}$$

Now that we obtained k_p, the next step is to model the effective thermal conductivity of the mixture, k_m. There are several effective thermal conductivity models for nanoparticle suspensions[173,183] Some of them are based on *dynamic* heat conduction mechanisms [155] in nanofluids, namely base-fluid nanolayering and Brownian motion. In a recent study on thermal conductivity of nano-suspensions, Muraleedharan et al. [184] conducted molecular dynamics simulations in combination with fluctuation-dissipation theorem to rigorously show that nanolayering and Brownian motion have negligible contribution towards effective thermal conductivity of mixture. Therefore, in this work, we have neglected these effects. Two other important factors to be considered in modeling k_m of a dense suspension are the random particle distribution and the viscous interaction between nanoparticles. Maxwell-Eucken [173,185] effective medium theory properly accounts for the random distribution of particles, and can be given as:

$$k_m = \frac{\phi_f k_f + \phi_p k_p \left(\frac{3k_f}{2k_f + k_p}\right)}{\phi_f + \phi_p \left(\frac{3k_f}{2k_f + k_p}\right)} \tag{55}$$

Interaction between particles is also important in capturing the viscous effects in the system, and can be taken care of by using the Bruggeman effective medium theory [186], given by:

$$\phi_p \left(\frac{k_p - k_m}{k_p + 2k_m}\right) + \phi_f \left(\frac{k_f - k_m}{k_f + 2k_m}\right) = 0 \tag{56}$$

Therefore, in order to include both these effects, it is desirable to unify the Maxwell-Eucken and Bruggeman theories into a Maxwell-Eucken-Bruggeman (MEB) model, yielding effective thermal conductivity of the mixture, k_m as:

$$k_m = \frac{D + \sqrt{D^2 + 2k_p k_f}}{2}, \tag{57}$$

where,

$$D = (2k_p - k_f)\Phi_p(1-\alpha_p) + (2k_f - k_p)\Phi_f\left(\frac{2\Phi_f + 2\Phi_p\alpha_p - 1}{2\Phi_f}\right). \tag{58}$$

Here α_p is the volume fraction of particle in a mixture with a Maxwell-Eucken structure. The value of α_p is chosen to be 0.5 so as to conform to the condition that for $\Phi_p \to 1, k_m \to k_p$.

Flame modeling

A one-dimensional, isobaric flame propagating vertically downward through a stoichiometric mixture of nAl particles and liquid water is considered. This model represents the real physical system on which combustion experiments were performed, and the results are available for validation [187]. A multi-zone framework representing the flame and preheat zones is shown in Figure 92.

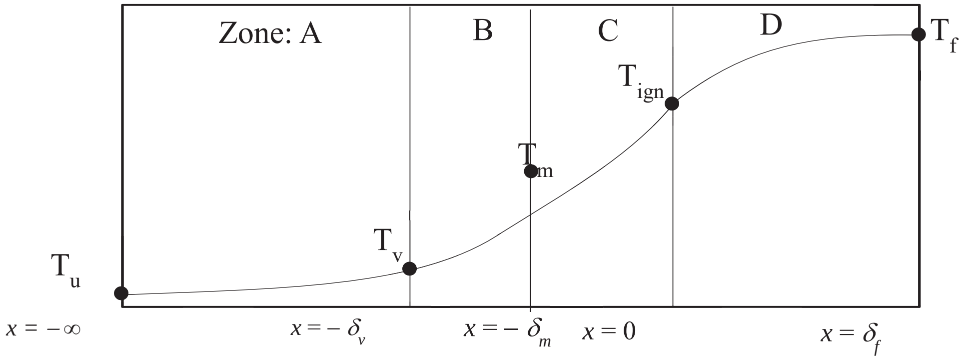

Figure 92: Theoretical multizone framework used to represent reaction and preheat zones. Zone A-C represent preheat zones and zone D represents the reaction zone.

As can be seen from Figure 92, several distinct zones can be identified within the framework. Zone A represents the nAl-H_2O (l) reactant mixture, which constitutes the propellant pellet originally synthesized for experimental study. The initial temperature of the unburnt propellant, T_u may be assumed to be equal to the ambient temperature i.e. $T_u = 298$ K. In Zone A, the major physical process is preheating of the system from T_u to the vaporization temperature of water, T_v and there are no notable chemical reactions in this zone due to the presence of a stable capping oxide layer. Once the water vaporizes at T_v, resulting vapor acts as an oxidizer in the following zones. The end of Zone B is marked by the melting of the aluminum core at a temperature T_m. The melting of the aluminum core causes a volume expansion which cracks the oxide layer. Molecules diffuse through these cracks and react with the water vapor. Near the end of Zone B and throughout Zone C, ignition reactions occur. Marking the end of Zone C, at temperature $T_{ign} = 1360$ K, an overall ignition of the system is obtained. Zone D represents the flame zone leading to a flame temperature $T_f = 1800$ K.

The temperature profile, *T(x)* and zone thicknesses, δ can be obtained by solving the energy equation in each zone and matching the physical conditions at the boundaries. The general equation of the energy balance can be given as:

$$\frac{\partial}{\partial t}\left(\rho C_p T\right) = \frac{\partial}{\partial x}\left(k\frac{\partial T}{\partial x}\right) + \dot{Q}, \tag{59}$$

where, ρ is the density, C_p is the specific heat, T is the temperature, k is the effective thermal conductivity of the mixture, and $\dot{Q}$ is the heat release rate. Note that ρ, C_p, and k are functions of temperature and local mixture composition. In a flame coordinate system, assuming constant r_b, the partial time derivative, $\frac{\partial}{\partial t}$ can be written as $r_b \frac{d}{dx}$ and Eq. 59 can be rewritten as:

$$r_b \frac{d}{dx}\left(\rho C_p T\right) = \frac{d}{dx}\left(k \frac{dT}{dx}\right) + \dot{Q} \tag{60}$$

The linear burning rate, r_b needs to be evaluated via the shooting method [188]. Therefore, the first step is to assume an initial solution for r_b. Neglecting the source term and expanding the right-hand side of the Eq. (60), the energy equation can be written as:

$$r_b \frac{d}{dx}\left(\rho C_p T\right) = \frac{dk}{dx} \cdot \frac{dT}{dx} + k \frac{d^2 T}{dx^2}. \tag{61}$$

Eq. (61) can be discretized by the one-dimensional finite difference method as:

$$r_b \frac{\left(\rho C_p T\right)_{i+1} - \left(\rho C_p T\right)_{i-1}}{2\Delta x} = \frac{k_{i+1} - k_{i-1}}{2\Delta x} . \frac{T_{i+1} - T_{i-1}}{2\Delta x} + k_i \frac{T_{i+1} - 2T_i + T_{i-1}}{\left(\Delta x\right)^2}, \tag{62}$$

and solved using Gauss-Seidel iteration:

$$T_i^{n+1} = \frac{\left(\Delta x\right)^2}{2k_i} \left[\frac{k_{i+1}^n - k_{i-1}^n}{2\Delta x} . \frac{T_{i+1}^n - T_{i-1}^n}{2\Delta x} + k_i \frac{T_{i+1}^n + T_{i-1}^n}{\left(\Delta x\right)^2} - r_b \frac{\left(\rho C_p T\right)_{i+1}^n - \left(\rho C_p T\right)_{i-1}^n}{2\Delta x} \right]. \tag{63}$$

Here i is the grid point index in the one-dimensional stencil consisting of r grid points, and n denotes the iteration. Note that the number of grid points should be chosen so as to include at the minimum a full nanoparticle and the surrounding fluid medium, so that the model is representative of the average mixture properties of the zone. If the grid size is smaller, then the effective thermal conductivity model fails for the control volume, leading to the failure of convergence of the iterative scheme. With the finite difference grid set up, the next step is to consider energy equations, identify boundary conditions, and perform the same numerical treatment for each zone present in the framework.

Thermal transport

Muraleedharan et al. [189] have implemented ICMA calculations in equilibrium molecular dynamics (EMD) framework for Al/Al_2O_3 system to evaluate TIR, and have achieved conclusive experimental validation for temperatures ranging from 50-500 K. They considered a (111) Al || (0001) Al_2O_3 crystal direction representing the primary orientation in FCC metal-metal oxide interface for both Al- and O-terminated Al_2O_3 surfaces. Here, the same ICMA framework is extended to temperatures up to 1800 K to evaluate TIR. Following ICMA calculations, a temperature dependent TIR model was also fitted to the data points using least squares algorithm.

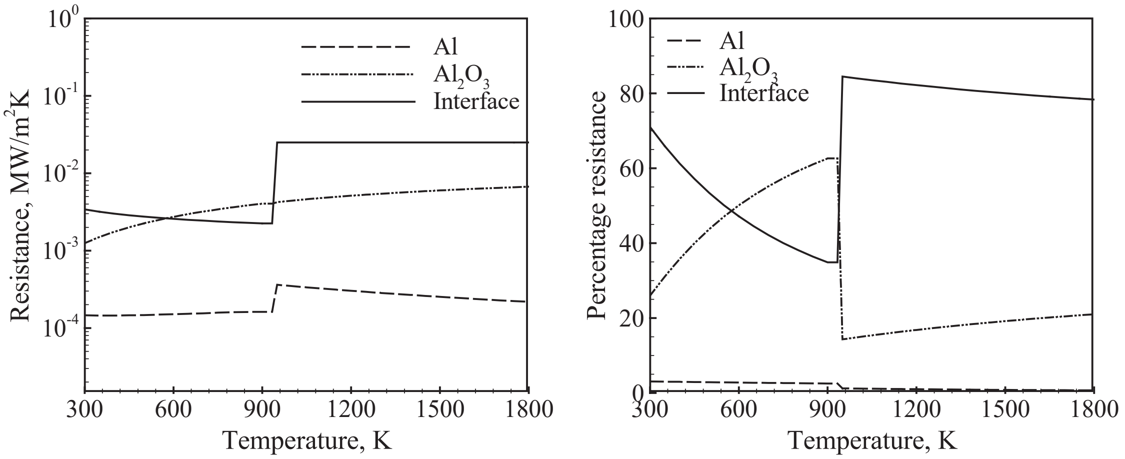

Figure 93: (a) Thermal resistance of Al, Al_2O_3, and interface (b) Percentage contribution by each resistance component to the total thermal resistance of the nanoparticle

Figure 93 shows the thermal resistance offered by Al, Al_2O_3, and the interface and Fig. 93 (b) shows the percentage contribution of each of the thermal resistance to total thermal resistance of the particle for temperatures ranging from 300-1800 K. Results correspond to a nanoparticle of diameter 38 nm coated by an oxide layer of initial thickness 2.7 nm which increases as the reaction proceeds. As can be seen from Fig. 93 (a), TIR decreases monotonically with temperature until the melting temperature of Al = 933 K. At the melting temperature, there is a sharp rise in TIR, which remains nearly constant thereafter. This is due to the loss of crystallinity of core Al lattice as it melts. Thermal resistance of Al_2O_3, on the other hand, shows a monotonically increasing trend as it remains in solid state throughout the temperature range considered. Its increase is a combined result of the decrease in thermal conductivity and the increase in oxide layer thickness. Also note that, for most temperatures, TIR is higher than Al_2O_3 resistance, indicating that TIR is crucial in modeling the net thermal resistance of nanoparticle. Moreover, from Fig. 93 (a), it is quite evident that the contribution to total resistance is the lowest from Al. Thermal resistance of Al is two orders of magnitude lower than that of Al_2O_3 and interface. In other words, Al offers the highest conductive pathway for energy released at reaction zone to traverse through unburnt mixture. Had the oxide layer been absent on the Al surface, the medium would have offered much lower resistance to heat conduction, and would have resulted in a much higher burning rate. In liquid state, similar to the interface, Al also offers significantly higher resistance due to lack of crystallinity. Furthermore, from Fig. 93 (b), comparing the percentage contribution of each of the components, it is evident that TIR and oxide layer resistance together contributes towards > 95% of thermal resistance. Now the same approach can be extended to various particle sizes and used in conjunction with MEB model to predict thermal conductivity of the mixture.

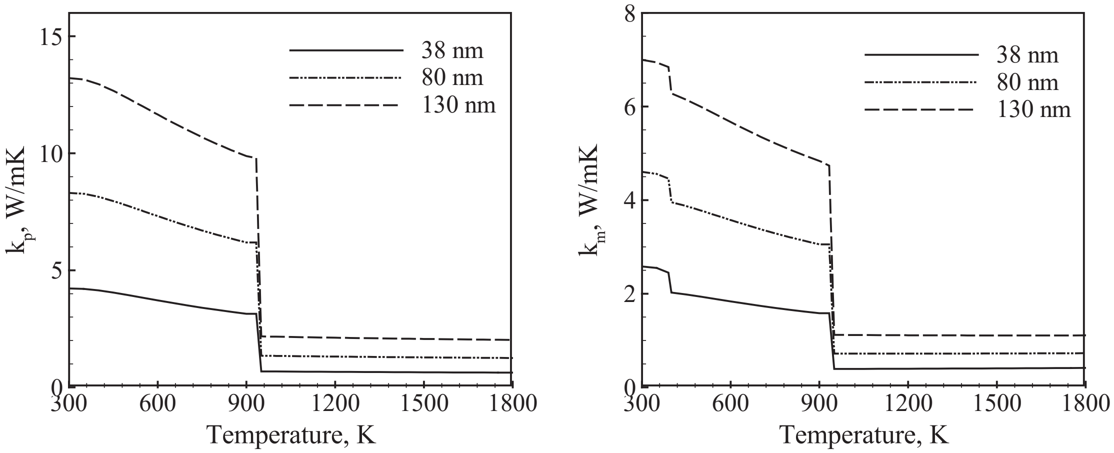

Figure 94: (a) Thermal conductivity of nanoparticles of diameters D_p = 38 nm, 80 nm, and 138 nm, and (b) Effective thermal conductivity of nAl-H_2O mixture for different particle sizes, as a function of temperature

Utilizing the temperature dependent thermal resistance values depicted in Fig. 93 (a), particle thermal conductivity, k_p is evaluated for three different particle diameters D_p: 38 nm, 80 nm, and 138 nm. Figure 94(a) shows k_p as a function of temperature. As can be seen from Fig. 94 (a), k_p decreases steadily with temperature, drops sharply at the melting temperature of Al, and remains nearly constant thereafter. Using the particle and fluid thermal conductivities, effective thermal conductivity of the mixture, k_m can be evaluated using the MEB model. Results of the temperature dependent k_m for different particle sizes are shown in Fig. 94 (b). In addition to the decreasing trend in k_m, two sharp drops are also observed corresponding to the vaporization temperature of water at 373 K and the melting point of Al respectively. More importantly, k_m increases with an increase in particle size because the thermal resistance of core Al decreases. Results shown in Fig. 94 are obtained straightforward, and need to be validated against experimental measurements by applying in the numerical framework to predict burning properties.

Flame propagation

A numerical solution of the flame problem yields the temperature profile across the reaction and preheat zones, as shown in Fig. 95. Figure 95 represents zones A-D in the multizone framework corresponding to a baseline case of 38 nm particle suspension at pressure, P = 1 bar. Results of r_b and thicknesses of various zones are given in Table 10. r_b predicted for the baseline case is 1.79 cm/s, and the two distinct experimental measurements [187] give a value of ~1.61 cm/s and ~1.40 cm/s respectively. Error in r_b predictions is < 10%, demonstrating the fidelity of the numerical framework. Prior theoretical studies [142] severely overpredict r_b to be 4.4 cm/s because they do not account for interface resistance and spatial variation of thermal transport properties. In addition, thicknesses of zones B, C, and D are also obtained as 4.7 µm, 1.01 µm, and 1.49 µm respectively. Zone thicknesses elucidate finer details of the flame structure that are difficult to measure experimentally. Also note that the slope of temperature profile increases while crossing A-B interface accounting for the enthalpy of vaporization of water. A similar increase in slope is observed at B-C to account for enthalpy of fusion of Al. The end of zone D is marked by a zero-slope corresponding to constant flame temperature, T_f as there is no heat transfer between reaction zone and products.

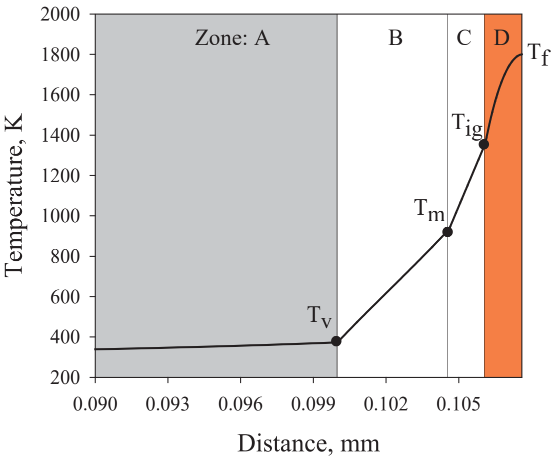

Figure 95: Detailed flame structure obtained via numerical solution of the 1D flame propagation problem clearly showing the different zones and their thicknesses

Table 10: Summary of results obtained from numerical solution of flame structure and burning properties for baseline case (P = 1 bar; D_p = 38 nm) compared with experimental results [190] and prior theoretical model [142]

Linear burning rate, r_b	Zone B	Zone C	Zone D
This work = 1.79 cm/s Expt 1.: 1.61 cm/s [47] Expt 2. :1.40 cm/s [47] Prior work: 4.4 cm/s [4]	4.7 µm	1.01 µm	1.49 µm

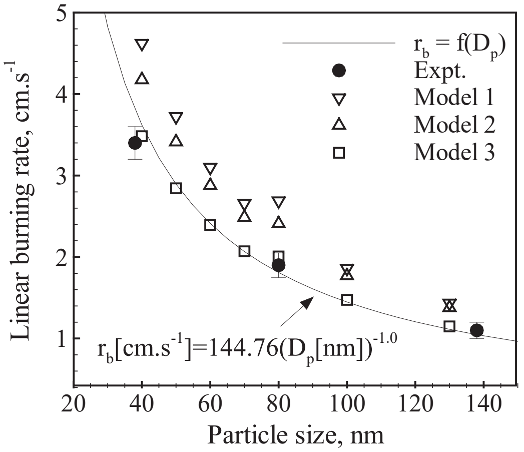

Figure 96: Linear burning rate as a function of particle diameter illustrating how increasing levels of complexity in modeling particle thermal conductivity gives better prediction of particle size dependent burning rates

Having the numerical framework benchmarked with baseline experimental results, a detailed analysis of r_b as a function of k_p modeled with increasing levels of complexity is studied. Figure 96 compares r_b predicted using 3 different k_p models at P =10 bar. Model 1 includes only the thermal conductivity of Al, k_{Al} to represent k_p. This model neglects the presence of oxide layer and, therefore, chooses the highest thermal conduction pathway. In model 2, Al core and the oxide layer are considered but TIR is neglected. Model 3 has the highest complexity wherein TIR is also used to model k_p. Experimentally measured r_b values are also overlaid for comparison [187]. As can be clearly seen, predictions of model 3 are closer to the experimental values. Models 1 and 2 over-predict r_b because they intrinsically model a higher thermal conductivity for the mixture. The mean error in model 1 is ~20% whereas in model 2, it reduces to ~18%. The mean error in model 3 is < 5% and the maximum error in prediction is ~12% for $D_p = 38$ nm. A model fit on r_b v/s D_p predicted from model 3 obtained from least squares algorithm gives a relation: $r_b\left[\mathrm{cm.s^{-1}}\right]=144.76\left(D_p\left[\mathrm{nm}\right]\right)^{-1.0}$. Hence r_b is inversely proportional to D_p, which is also in accordance with the experimental measurements.

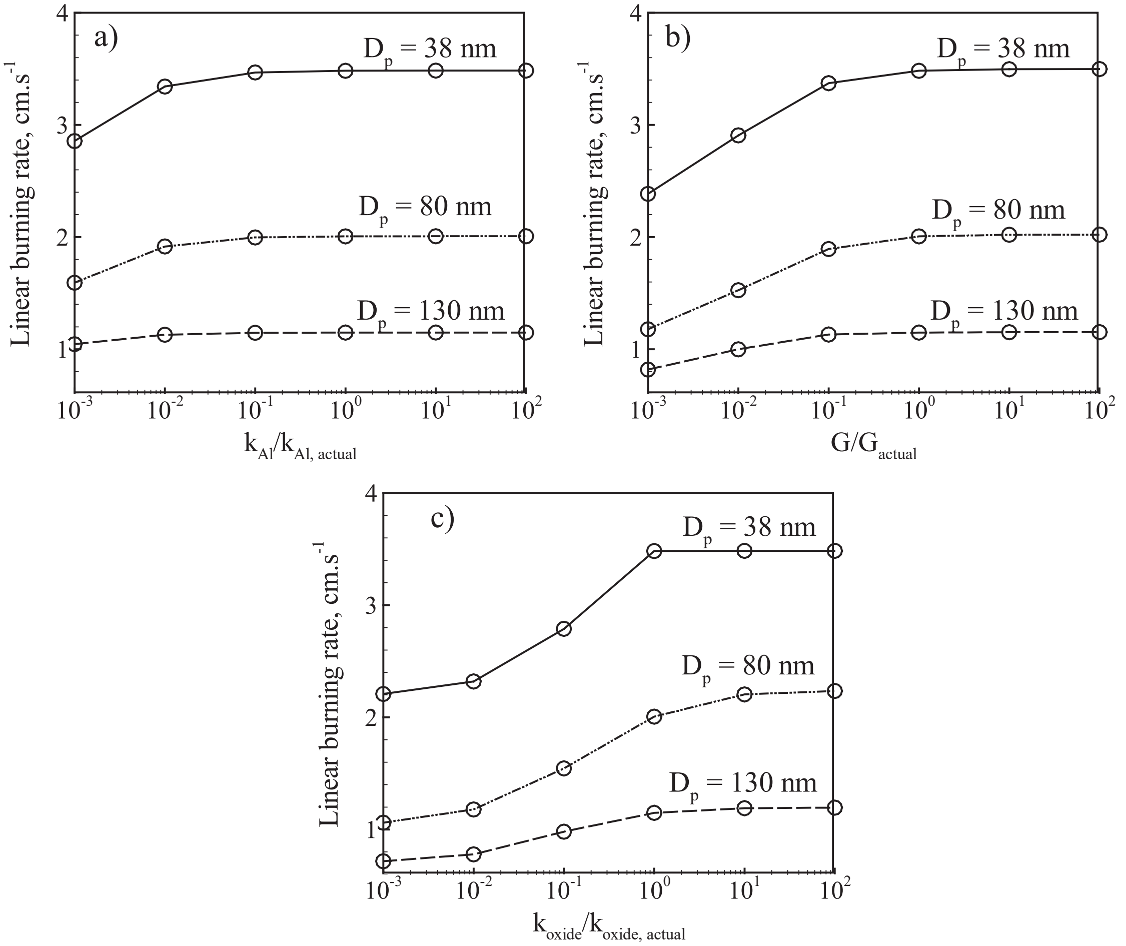

Figure 97: Sensitivity of linear burning rate to changes in thermal conductivity of a) Al and b) Al_2O_3, and c) thermal interfacial conductance, *G* for three different particle sizes

Finally, we study the sensitivity of r_b to changes in thermal conductivity of Al and Al_2O_3, and *G* at P = 10 bar. This study is motivated by recent advances in nanotechnology whereby thermal conductivity can be tuned by rational design of materials i.e. by engineering features to target certain group of vibrational modes to either inhibit or enhance their role in heat conduction [191]. Tuning thermal conductivity provides means to precisely control burning rates of energetic materials in propulsive missions. Here, the individual thermal conductivity components k_{Al}, *G*, and k_{Al2O3} are arbitrarily varied with respect to their actual values and the effects on r_b is analyzed. Figure 97 (a)-(c) present the sensitivity of r_b to changes in k_{Al}, *G*, and k_{Al2O3} respectively.

From Fig. 97(a)-(c), it is evident that in general, r_b sensitivity is highest for 38 nm particle suspensions. From Fig. 97 (a), it can be seen that for D_p = 38 nm, for two orders of magnitude reduction in k_{Al}, reduction in r_b is only ~15%. Whereas, Fig. 97 (b) indicates that for the same reduction in G, reduction in r_b is nearly ~30%. On the other hand, Fig. 97 (c) clearly shows that r_b drops by ~34% when k_{Al2O3} is dropped by two orders of magnitude. It is, therefore, quite evident that thermal conductivity of oxide layer and interface conductance dictate r_b sensitivity. While k_{Al2O3} seems to have the highest influence on r_b, it is also important to note that oxide layer forms on particle surface *in situ* during the combustion process, and its thermal conductivity is practically uncontrollable. TIC, on the other hand, can be tuned to user requirements if certain vibrational modes in Al core are preferentially altered by means of nanoengineered defects, doping, and/or alloying. In other words, precise tuning of burning rate in nanoenergetic materials is achievable by careful consideration of interfacial conductance. Nonetheless, as particles becomes larger, sensitivity of r_b to changes in k seems to diminish. Note also that for all particle sizes, even with several-fold enhancement in k and G, the effect on r_b is feeble. Therefore, to increase burning rates in nanoenergetic materials, one has to adopt conventional strategies like high pressure combustion, active metal coating, or catalysis that improve reaction rates.

In summary, a detailed numerical analysis of flame propagation in nano-aluminum (nAl) - water (H_2O) mixtures was performed. Considering a multi-zone framework, the nonlinear energy equation was solved iteratively using Gauss-Seidel method. Thermal conductivity of nanoparticle was modeled using thermal conductivities of aluminum and oxide layer, as well as the thermal interface resistance. Effective thermal conductivity of mixture was modeled using Maxwell-Eucken-Bruggeman model as a function of temperature, spatial coordinate, and local mixture composition. Results indicated that the oxide layer and the interface together contributed towards 95% of the net thermal resistance of the nanoparticle. The effect of complexity in modeling particle thermal conductivity, k_p was studied by predicting the particle size dependent linear burning rate, r_b. Error in r_b prediction was the least (< 5%) when interface resistance was taken into account in modeling k_p. When interface resistance was neglected, error in r_b prediction increases to 20%. Furthermore, r_b varied as the inverse of particle diameter, as observed in experimental measurements. Sensitivity of r_b to changes in thermal conductivities of aluminum (k_{Al}) and aluminum oxide (k_{Al2O3}), and interface conductance (G) was also studied for three particle sizes: 38 nm, 80 nm, and 138 nm. r_b sensitivity was the highest for 38 nm particle, and it decreased with increase in particle size. r_b drops by 15%, 30%, and 34% for two orders of magnitude reduction in k_{Al}, G, and k_{Al2O3} respectively. No notable enhancement in r_b was achieved by an enhancement in thermal conductivity or interface conductance.

SENSITIZATION OF ALUMINUM-FLUOROPOLYMER COMPOSITES

L. Groven, SDSMT and S.F. Son, Purdue University

Research was also conducted on nanoscale aluminum (nAl)/fluoropolymer composites for the piezoelectric nature of the fluoropolymers, as a means to sensitize the composite. This work demonstrated that such mixtures can be sensitized with the application of a DC voltage to have drop weight sensitivities on par with powdered secondary explosives. Phase determination with XRD and FTIR indicated that the materials do not need to be poled or stretched during fabrication in order to contain the electroactive crystalline phase, which appears to be necessary for the piezoelectric effect and the ability to observe sensitization. Details of this effort can be found in Ref. [192]

SUMMARY

One of the major goals of this program was to develop new macroscale (micron-sized or larger) energetic materials with nanoscale features that would provide alternative ways of introducing nanoscale energetic materials into solid and liquid propellants. It was desirable that these new materials would lead to improved performance and ease of processing and handling, managed energy release, reduced sensitivity, and the potential for internal/external control and actuation. In the present program, new macroscale materials with nanostructured features were developed to address this goal. These materials included Al mesoscopic aggregates, nanoscale inclusion materials, encapsulated nanocatalysts in energetic oxidizers, and multi-layered functionalized graphene sheet (FGS)-tetrazine compounds. In many applications, these macroscale materials exhibited improved handling and performance characteristics over the separate nanomaterials, indicating the importance of the assembly of nanomaterials towards achieving their full potential when included in propellant formulations. Theoretical models were also developed for the effective thermal conductivity of energetic nanomaterials and the thermal decomposition of hydroxylammonium nitrate and ammonia borane, which has provided improved understanding of the properties and combustion characteristics of nanomaterials and the surrounding chemical kinetics of liquid and solid propellant ingredients. Future details of the research presented in this report may be found in the published papers and student theses listed in the Metric section of this report.

CITED LITERATURE

1. Li, Y.; Alain-Rizzo, V.; Galmiche, L.; Audebert, P.; Miomandre, F.; Louarn, G.; Bozlar, M.; Pope, M. A.; Dabbs, D. M.; Aksay, I. A., Functionalization of Graphene Oxide by Tetrazine Derivatives: A Versatile Approach toward Covalent Bridges between Graphene Sheets. *Chem. Mater.* **2015,** *27*, 4298-4310.
2. Sabourin, J. L.; Dabbs, D. M.; Yetter, R. A.; Dryer, F. L.; Aksay, I. A., Functionalized Graphene Sheet Colloids for Enhanced Fuel/Propellant Combustion. *ACS Nano* **2009,** *3*, 3945-3954.
3. Sabourin, J. L.; Dabbs, D. M.; Yetter, R. A.; Dryer, F. L.; Aksay, I. A., The Role of Graphene Sheet Functionalization on the Combustion of Nitromethane. PennState and Princeton Universities: 2013.
4. Liu, L.-M.; Car, R.; Selloni, A.; Dabbs, D. M.; Aksay, I. A.; Yetter, R. A., Enhanced Thermal Decomposition of Nitromethane on Functionalized Graphene Sheets: ab initio Molecular Dynamics Simulations. *J. Am. Chem. Soc.* **2012,** *134*, 19011-19016.
5. McAllister, M. J.; Li, J. L.; Adamson, D. H.; Schniepp, H. C.; Abdala, A. A.; Liu, J.; Herrera-Alonso, M.; Milius, D. L.; Car, R.; Prud'homme, R. K., et al., Single sheet functionalized graphene by oxidation and thermal expansion of graphite. *Chemistry of Materials* **2007,** *19*, 4396-4404.
6. Aksay, I. A.; Pope, M. A.; Roy-Mayhew, J. Nano-graphene and Nano-graphene oxide. March 20, 2014, 2014.
7. Clavier, G.; Audebert, P., s-Tetrazines as Building Blocks for New Functional Molecules and Molecular Materials. *Chem. Rev.* **2010,** *110*, 3299-3314.

8. Fischer, N.; Klapotke, T. M.; Stierstorfer, J., New Nitriminotetrazoles - Synthesis, Structures and Characterization. *Zeitschrift Fur Anorganische Und Allgemeine Chemie* **2009,** *635*, 271-281.
9. Oxley, J. C.; Smith, J. L.; Zhang, J., Decomposition pathways of some 3,6-substituted s-tetrazines. *Journal of Physical Chemistry A* **2000,** *104*, 6764-6777.
10. Audebert, P.; Miomandre, F.; Clavier, G.; Vernieres, M. C.; Badre, S.; Meallet-Renault, R., Synthesis and properties of new tetrazines substituted by heteroatoms: Towards the world's smallest organic fluorophores. *Chemistry-a European Journal* **2005,** *11*, 5667-5673.
11. Sarkar, B.; Laye, R. H.; Mondal, B.; Chakraborty, S.; Paul, R. L.; Jeffery, J. C.; Puranik, V. G.; Ward, M. D.; Lahiri, G. K., Synthesis, structure and spectroelectrochemical properties of a dinuclear ruthenium complex exhibiting a strong electronic interaction across a 1,2,4,5-tetrazine bridging ligand. *Journal of the Chemical Society-Dalton Transactions* **2002**, 2097-2101.
12. Marcano, D. C.; Kosynkin, D. V.; Berlin, J. M.; Sinitskii, A.; Sun, Z. Z.; Slesarev, A.; Alemany, L. B.; Lu, W.; Tour, J. M., Improved Synthesis of Graphene Oxide. *Acs Nano* **2010,** *4*, 4806-4814.
13. Pope, M. A.; Korkut, S.; Punckt, C.; Aksay, I. A., Supercapacitor Electrodes Produced through Evaporative Consolidation of Graphene Oxide-Water-Ionic Liquid Gels. *Journal of the Electrochemical Society* **2013,** *160*, A1653-A1660.
14. Zhu, Y.; Stoller, M. D.; Cai, W.; Velamakanni, A.; Piner, R. D.; Chen, D.; Ruoff, R. S., Exfoliation of Graphite Oxide in Propylene Carbonate and Thermal Reduction of the Resulting Graphene Oxide Platelets. *Acs Nano* **2010,** *4*, 1227-1233.
15. Briggs, D.; Beamson, G., *High Resolution XPS of Organic Polymers*. John Wiley & Sons Inc.: 1992.
16. Bai, H.; Xu, Y.; Zhao, L.; Li, C.; Shi, G., Non-covalent functionalization of graphene sheets by sulfonated polyaniline. *Chem. Commun.* **2009**, 1667.
17. Jin, M.; Jeong, H. K.; Kim, T. H.; So, K. P.; Cui, Y.; Yu, W. J.; Ra, E. J.; Lee, Y. H., Synthesis and systematic characterization of functionalized graphene sheets generated by thermal exfoliation at low temperature. *J. Phys. D, Appl. Phys.* **2010**, 275402.
18. Varughese, B.; Chellamma, S.; Lieberman, M., XPS Study of Self-Assembly of Ruthenium Dimers [((acac)2Ru)2bptz]0,+ on Hydrophobic and Hydrophilic SAMs. *Langmuir* **2002,** *18*, 7964-7970.
19. Zhou, L.; Piekiel, N.; Chowdhury, S.; Zachariah, M. R., T-Jump/time-of-flight mass spectrometry for time-resolved analysis of energetic materials. *Rapid Communications in Mass Spectrometry* **2009,** *23*, 194-202.
20. Mallik, B. S.; Siepmann, J. I., Thermodynamic, Structural and Transport Properties of Tetramethyl Ammonium Fluoride: First Principles Molecular Dynamics Simulations of an Unusual Ionic Liquid. *J. Phys. Chem. B* **2010,** *114*, 12577-12584.
21. Hoover, W. G., Canonical dynamics: Equilibrium phase-space distributions. *Phys. Rev. A* **1985,** *31*, 1695-1697.
22. Zhang, C.; Dabbs, D. M.; Liu, L.-M.; Aksay, I. A.; Car, R.; Selloni, A., Combined Effects of Functional Groups, Lattice Defects, and Edges in the Infrared Spectra of Graphene Oxide. *J. Phys. Chem. C* **2015,** *119*, 18167-18176.
23. Miners, S. A.; Rance, G. A.; Khlobystov, A. N., Chemical reactions confined within carbon nanotubes. *Chemical Society Reviews* **2016,** *45*, 4727-4746.

24. Petrosko, S. H.; Johnson, R.; White, H.; Mirkin, C. A., Nanoreactors: Small Spaces, Big Implications in Chemistry. *Journal of the American Chemical Society* **2016,** *138*, 7443-7445.
25. Britz, D. A.; Khlobystov, A. N.; Porfyrakis, K.; Ardavan, A.; Briggs, G. A. D., Chemical reactions inside single-walled carbon nano test-tubes. *Chemical Communications* **2005**, 37-39.
26. Botos, A.; Biskupek, J.; Chamberlain, T. W.; Rance, G. A.; Stoppiello, C. T.; Sloan, J.; Liu, Z.; Suenaga, K.; Kaiser, U.; Khlobystov, A. N., Carbon Nanotubes as Electrically Active Nanoreactors for Multi-Step Inorganic Synthesis: Sequential Transformations of Molecules to Nanoclusters and Nanoclusters to Nanoribbons. *Journal of the American Chemical Society* **2016,** *138*, 8175-8183.
27. Abou-Rachid, H.; Hu, A.; Timoshevskii, V.; Song, Y.; Lussier, L.-S., Nanoscale High Energetic Materials: A Polymeric Nitrogen Chain N(8) Confined inside a Carbon Nanotube. *Physical Review Letters* **2008,** *100*, 196401.
28. Ji, W.; Timoshevskii, V.; Guo, H.; Abou-Rachid, H.; Lussier, L.-S., Thermal stability and formation barrier of a high-energetic material N8 polymer nitrogen encapsulated in (5,5) carbon nanotube. *Applied Physics Letters* **2009,** *95*, 021904.
29. Sharma, H.; Garg, I.; Dharamvir, K.; Jindal, V. K., Structure of Polynitrogen Clusters Encapsulated in C60: A Density Functional Study. *The Journal of Physical Chemistry C* **2010,** *114*, 9153-9160.
30. Smeu, M.; Zahid, F.; Ji, W.; Guo, H.; Jaidann, M.; Abou-Rachid, H., Energetic Molecules Encapsulated Inside Carbon Nanotubes and between Graphene Layers: DFT Calculations. *J. Phys. Chem. C* **2011,** *115*, 10985-10989.
31. Liu, Y.; Yu, T.; Lai, W.; Kang, Y.; Ge, Z., Ordered and layered structure of liquid nitromethane within a graphene bilayer: toward stabilization of energetic materials through nanoscale confinement. *Journal of Molecular Modeling* **2015,** *21*, 1-5.
32. Cai, H.; Tian, L.; Huang, B.; Yang, G.; Guan, D.; Huang, H., 1,1-Diamino-2,2-dinitroethene (FOX-7) nanocrystals embedded in mesoporous carbon FDU-15. *Microporous and Mesoporous Materials* **2013,** *170*, 20-25.
33. Bozym, D. J.; Korkut, S.; Pope, M. A.; Aksay, I. A., Dehydrated Sucrose Nanoparticles as Spacers for Graphene–Ionic Liquid Supercapacitor Electrodes. *ACS Sustainable Chemistry & Engineering* **2016**, ASAP.
34. Torrisi, F.; Hasan, T.; Wu, W. P.; Sun, Z. P.; Lombardo, A.; Kulmala, T. S.; Hsieh, G. W.; Jung, S. J.; Bonaccorso, F.; Paul, P. J., et al., Inkjet-Printed Graphene Electronics. *Acs Nano* **2012,** *6*, 2992-3006.
35. Hernandez, Y.; Nicolosi, V.; Lotya, M.; Blighe, F. M.; Sun, Z. Y.; De, S.; McGovern, I. T.; Holland, B.; Byrne, M.; Gun'ko, Y. K., et al., High-yield production of graphene by liquid-phase exfoliation of graphite. *Nature Nanotechnology* **2008,** *3*, 563-568.
36. Parviz, D.; Das, S.; Ahmed, H. S. T.; Irin, F.; Bhattacharia, S.; Green, M. J., Dispersions of Non-Covalently Functionalized Graphene with Minimal Stabilizer. *ACS Nano* **2012,** *6*, 8857-8867.
37. Meakin, P., Formation of Fractal Clusters and Networks by Irreversible Diffusion-Limited Aggregation. *Phys. Rev. Lett.* **1983,** *51*, 1119-1122.
38. Kolb, M.; Botet, R.; Jullien, R., Scaling of Kinetically Growing Clusters. *Phys. Rev. Lett.* **1983,** *51*, 1123-1126.
39. Meakin, P., Diffusion-controlled flocculation: The effects of attractive and repulsive interactions. J. Chem. Phys. 1983, 79, 2426-2429.

40. Chaturvedi, S. and Dave, P. N. (2012). Nano-Metal Oxide: Potential Catalyst on Thermal Decomposition of Ammonium Perchlorate. J. Exp. Nanosci. 7(2), 205–231.
41. Ma, Z., Li, F. and Bai, H. (2006). Effect of Fe2O3 in Fe2O3/AP Composite Particles on Thermal Decomposition of AP and on Burning Rate of the Composite Propellant. Propellants, Explosives, Pyrotechnics 31, 447–451.
42. Reese, D. A., Son, S. F., and Groven, L. J. (2014). Composite Propellant Based on a New Nitrate Ester. Propellants, Explosives, Pyrotechnics 39(5), 684-688.
43. Isert, S., Groven, L. J., Lucht, R. P., and Son, S. F. (2015). The Effect of Encapsulated Nanosized Catalysts on the Combustion of Composite Solid Propellants. Combustion and Flame 162(5), 1821–1828.
44. Hedman, T. D., Cho, K. Y., Satija, A., Groven, L. J., Lucht, R. P., and Son, S. F. (2012). Experimental Observation of the Flame Structure of a Bimodal Ammonium Perchlorate Composite Propellant Using 5 kHz PLIF. Combust. Flame 159(1), 427-437.
45. Hedman, T. D., Reese, D. A., Cho, K. Y., Groven, L. J., Lucht, R. P. and Son, S. F. (2012). An Experimental Study of the Effect of Catalysts on an Ammonium Perchlorate Based Composite Propellant. Combust. Flame 159(4), 1748–1758.
46. Hedman, T. D., Groven, L. J., Lucht, R. P. and Son, S. F. (2013). The Effect of Polymeric Binder on Composite Propellant Flame Structure Investigated with 5 kHz OH PLIF. Combustion and Flame 160(8), 1531–1540.
47. Hedman, T. D., Cho, K. Y., Groven, L. J., Lucht, R. P. and Son, S. F. (2013). The Diffusion Flame Structure of an Ammonium Perchlorate Based Composite Propellant at Elevated Pressures," Proceedings of the Combustion Institute 34(1), 649–656.
48. Sabourin, J. L., Dabbs, D. M., Yetter, R. A., Dryer, F. L. and I. Aksay, A. (2009). Functionalized Graphene Sheet Colloids for Enhanced Fuel/Propellant Combustion. ACS Nano 3(12), 3945-3954.
49. R. A. Yetter, G. A. Risha, and Son, S. F. (2009). Metal Particle Combustion and Nanotechnology. Proceedings of the Combustion Institute 32(2), 1819-1838.
50. Sippel, T. R., Son, S. F. and Groven, L. J. (2013). Altering Reactivity of Aluminum with Selective Inclusion of Polytetrafluoroethylene through Mechanical Activation. Propellants, Explosives, Pyrotechnics 38(2), 286-295.
51. Sippel, T. R., Son, S. F. and Groven, L. J. (2013). Modifying Aluminum Reactivity with Poly (Carbon Monofluoride) via Mechanical Activation. Propellants, Explosives, Pyrotechnics 38(3), 321-326.
52. Sippel, T. R., Son, S. F., and Groven, L. J. (2014). Aluminum Agglomeration Reduction in a Composite Propellant Using Tailored Al/PTFE Particles. Combustion and Flame 161(1), 311-321.
53. Sippel, T. R., Son, S. F., Groven, L. J., Zhang, S., and Dreizin, E. L. (2015). Exploring Mechanisms for Agglomerate Reduction in Composite Solid Propellants with Polyethylene Inclusion Modified Aluminum. Combustion and Flame 162(3), pp. 846-854.
54. Law, C. K. (2006). "Combustion Physics," Cambridge University Press, New York.
55. Ivanov, V. M. and Nefedov, P. I. (1965). Experimental Investigation of the Combustion Process in Nature and Emulsified Fuels. NASA Scientific and Technical Publications from Trudy Instituta Goryacikh Ishkopayemykh 19, 25-45.
56. Blander, M. and Katz, J. L. (1975). Bubble Nucleation in Liquids. AIChE J. 21(5), 1547-5905.

57. K. Y. Cho, Pourpoint, T. L., Son, S. F., and Lucht, R. P. (2013). Microexplosion Investigation of Monomethylhydrazine Gelled Droplet with OH Planar Laser-Induced Fluorescence. Journal of Propulsion and Power 29(6), 1303-1310.
58. Cheung, H. and Cohen, N. S. (1965). Performance of solid propellants containing metal additives. AIAA Journal 3(2) 250-257.
59. Sutton, G. P. and Biblarz, O. (2011). "Rocket Propulsion Elements," 8th ed, Wiley.
60. Timnat, Y. M. (1987). "Advanced Chemical Rocket Propulsion," Academic Press, Orlando, FL.
61. Wang, H., Jian, G.,Yan, S., DeLisio, J. B., Huang, C. and Zachariah, M. R. (2013). Electrospray Formation of Gelled Nano-Aluminum Microspheres with Superior Reactivity. ACS Appl. Mater. Interfaces 5(15), 6797–6801.
62. Young, G., Wang, H., and Zachariah, M . R. (2015). Application of Nano-Aluminum/Nitrocellulose Mesoparticles in Composite Solid Rocket Propellants. Propellants, Explosives, Pyrotechnics, Online Version, DOI: 10.1002/prep.201500020.
63. Geisler, R. L. (2002). A Global View of the Use of Aluminum Fuel in Solid Rocket Motors. AIAA 2002-3748, 38th Joint Propulsion Conference, 7-10 July, Indianapolis, Indiana.
64. Edwards, T. Cracking and deposition behavior of supercritical hydrocarbon aviation fuels. Combust. Sci. Technol. 178, 307-334 (2006).
65. Lander, H. & Nixon, A. C. Endothermic fuels for hypersonic vehicles. J. Aircr. 8, 200-207 (1971).
66. Wickham, D. T., Engel, J. R., Rooney, S. & Hitch, B. D. Additives to improve fuel heat sink capacity in air/fuel heat exchangers. J. Propuls. POWER 24, 55-63 (2008).
67. Edwards, T. USAF supercritical hydrocarbon fuels interests. AIAA Pap. 93, (1993).
68. Maurice, L. Q., Lander, H., Edwards, T. & Harrison, W. E. Advanced aviation fuels: a look ahead via a historical perspective. Fuel 80, 747-756 (2001).
69. Daniau, E. et al. Contribution to Scramjet active cooling analysis using n-dodecane decomposition model as a generic endothermic fuel. AIAA Pap. 6920, 2003 (2003).
70. Huang, H., Sobel, D. R. & Spadaccini, L. J. Endothermic heat-sink of hydrocarbon fuels for scramjet cooling. AIAA Pap. 3871, 1985 (2002).
71. Stewart, J. F. Supercritical pyrolysis of the endothermic fuels methylcyclohexane, decalin, and tetralin. (PhD dissertation, Princeton University, 1999).
72. Edwards, T. Cracking and deposition behavior of supercritical hydrocarbon aviation fuels. Combust. Sci. Technol. 178, 307-334 (2006).
73. Meng, F., Liu, G., Zhang, X. & Wang, L. Pd-Pt/HZSM-5 Coating Catalyst for Supercritical Cracking and dehydrogenation of Endothermic Fuel. 45th AIAA/ASME/SAE/ASEE Jt. Propuls. Conf. Exhib. - 5 August 2009, Denver, Color. (2009).
74. Colket, M. B. & Spadaccini, L. J. Scramjet fuels autoignition study. J. Propuls. POWER 17, 315-323 (2001).
75. Cooper, M. & Shepherd, J. Experiments studying thermal cracking, catalytic cracking, and pre-mixed partial oxidation of JP-10. Aiaa 4687, 20-23 (2003).
76. Wickham, D. T., Cook, R., De Voss, S., Engel, J. R. & Nabity, J. Soluble nano-catalysts for high performance fuels. J. Russ. Laser Res. 27, 552-561 (2006).
77. Nabity, J., Wickham, D. T., Hitch, B. D., Engel, J. R. & Rooney, S. Additives to increase fuel heat sink capacity. (DTIC Document, 2005).

78. H.S. Sim, Understanding the role of multifunctional nanoengineered particulate additives on supercritical pyrolysis and combustion of hydrocarbon fuels/propellants, PhD dissertation, Pennsylvania State University, 2016.
79. Akimov, A. V; Prezhdo, O. V. Large-Scale Computations in Chemistry: A Bird's Eye View of a Vibrant Field. Chem. Rev. 2015, 115, 5797–5890.
80. Senftle, T. P.; Hong, S.; Islam, M. M.; Kylasa, S. B.; Zheng, Y.; Shin, Y. K.; Junkermeier, C.; Engel-Herbert, R.; Janik, M. J.; Aktulga, H. M. The ReaxFF Reactive Force-Field: Development, Applications and Future Directions. npj Comput. Mater. 2016, 2, 15011.
81. Yu, J.; Eser, S. Thermal Decomposition of C10-C14 Normal Alkanes in near-Critical and Supercritical Regions: Product Distributions and Reaction Mechanisms. Ind. Eng. Chem. Res. 1997, 36, 574–584.
82. Jiang, R.; Liu, G.; He, X.; Yang, C.; Wang, L.; Zhang, X.; Mi, Z. Supercritical Thermal Decompositions of Normal- and Iso-Dodecane in Tubular Reactor. J. Anal. Appl. Pyrolysis 2011, 92, 292–306.
83. Liu, G.; Han, Y.; Wang, L.; Zhang, X.; Mi, Z. Supercritical Thermal Cracking of N-Dodecane in Presence of Several Initiative Additives: Products Distribution and Kinetics. Energy & Fuels 2008, 22, 3960–3969.
84. Sobel, D. R.; Spadaccini, L. J. Hydrocarbon Fuel Cooling Technologies for Advanced Propulsion. J. Eng. Gas Turbines Power 1997, 119, 344–351.
85. Richards, G. A.; Sojka, P. E.; Lefebvre, A. H. Flame Speeds in Fuel Sprays with Hydrogen Addition. J. Eng. Gas Turbines Power 1989, 111, 84–89.
86. Usman, M.; Cresswell, D.; Garforth, A. Detailed Reaction Kinetics for the Dehydrogenation of Methylcyclohexane over Pt Catalyst. Ind. Eng. Chem. Res. 2011, 51, 158–170.
87. Wang, Y.; Shah, N.; Huffman, G. P. Pure Hydrogen Production by Partial Dehydrogenation of Cyclohexane and Methylcyclohexane over Nanotube-Supported Pt and Pd Catalysts. Energy & Fuels 2004, 18, 1429–1433.
88. Kariya, N.; Fukuoka, A.; Ichikawa, M. Efficient Evolution of Hydrogen from Liquid Cycloalkanes over Pt-Containing Catalysts Supported on Active Carbons under "wet–dry Multiphase Conditions." Appl. Catal. A Gen. 2002, 233, 91–102.
89. Chenoweth, K.; van Duin, A. C. T.; Goddard III, W. A. ReaxFF Reactive Force Field for Molecular Dynamics Simulations of Hydrocarbon Oxidation. J. Phys. Chem. A 2008, 112, 1040–1053.
90. Psofogiannakis, G. M.; Froudakis, G. E. DFT Study of the Hydrogen Spillover Mechanism on Pt-Doped Graphite. J. Phys. Chem. C 2009, 113, 14908–14915.
91. Psofogiannakis, G. M.; Froudakis, G. E. DFT Study of Hydrogen Storage by Spillover on Graphite with Oxygen Surface Groups. J. Am. Chem. Soc. 2009, 131, 15133–15135.
92. B. Chehroudi, D. Talley, W. Mayer, R. Branam, J.J. Smith, Understanding injection into high pressure supercritical environments, Fifth Int. Symp. Liq. Sp. Propuls. 313 (2003).
93. G. Lacaze, A. Misdariis, A. Ruiz, J.C. Oefelein, Analysis of high-pressure Diesel fuel injection processes using LES with real-fluid thermodynamics and transport, Proc. Combust. Inst. (2014).
94. D.M. a. Karwat, S.W. Wagnon, J.Y.W. Lai, M.S. Wooldridge, C.K. Westbrook, An Experimental and Computational Investigation of n-Dodecane Ignition and Chemical Kinetics, AIAA Aerosp. Sci. Meet. (2011) 1–16.
95. Sabourin, J. L.; Dabbs, D. M.; Yetter, R. A.; Dryer, F. L.; Aksay, I. A., Functionalized Graphene Sheet Colloids for Enhanced Fuel/Propellant Combustion. ACS Nano 2009, 3,

3945-3954.

96. Liu, L.-M.; Car, R.; Selloni, A.; Dabbs, D. M.; Aksay, I. A.; Yetter, R. A., Enhanced Thermal Decomposition of Nitromethane on Functionalized Graphene Sheets: ab initio Molecular Dynamics Simulations. J. Am. Chem. Soc. 2012, 134, 19011-19016.
97. E.L. Dreizin, Metal-based reactive nanomaterials, Prog. Energy Combust. Sci. 35 (2009) 141–167. doi:10.1016/j.pecs.2008.09.001.
98. Epshteyn, A., Yonke, B.L., Miller, J.B., Rivera-Diaz, J.L., and Purdy, A.P., "Sonochemically generated air-stable bimetallic nanopowders of Group 4 transition metals with aluminum," Chemistry of Materials, Vol. 25, 2013, pp. 818-824. doi:10.1021/cm3001943
99. Epshteyn, A., Weismiller, M.R., Huba, Z.J., Maling, E.L., and Chaimowitz, A.S., "Optimization of a High Energy Ti-Al-B Nanopowder Fuel", Energy and Fuels, Vol. 31, No. 2, 2017, pp.1811-1819. doi:10.1021/acs.energyfuels.6b02321
100. Weismiller, M.R., Huba, Z.J., Tuttle, S.G., Epshteyn, A., and Fisher, B.T., "Combustion characteristics of high energy Ti-Al-B nanopowders in a decane spray flame," Combustion and Flame, Vol. 176, 2017, pp. 361-369. dx.doi.org/10.1016/j.combustflame.2016.10.025
101. Epshteyn, A.; Miller, J. B.; Pettigrew, K. A.; Stroud, R. M.; Purdy, A. P. "Surface Passivated Air And Moisture Stable Mixed Zirconium Aluminum Metal-Hydride Nanoparticles" Mater. Res. Soc. Symp. Proc., 2007, 1056, 1056-HH03-16 doi:10.1557/PROC-1056-HH03-16
102. Huba, Z.J.; Donakowski, M.D.; Epshteyn, A.; "Gram-Scale, Low Temperature, Sonochemical Synthesis of Stable Amorphous Ti-B Powders Containing Hydrogen" Chemistry of Materials, Vol. 29, No.4, 2017, 1467-1471 doi:10.1021/acs.chemmater.7b00431
103. Connell, T.L., Santi, A., Risha, G.A., Muller, B.A., Batzel, T.D., "Experiment and semi-empirical modeling of lab-scale hybrid rocket performance," Paper # 2009-5086, 45th AIAA/ASME/SAE/ASEE Joint Propulsion Conference and Exhibit, Denver, CO, 2009.
104. Weismiller, M.R., Connell, T.L., Risha, G.A., Yetter, R.A., "Characterization of Ammonia Borane (NH3BH3) Enhancement to a Paraffin Fueled Hybrid Rocket System," Paper # 2010-6639, 46th AIAA/ASME/SAE/ASEE Joint Propulsion Conference and Exhibit, Nashville, TN, 2010.
105. L. O. Cisneros, W. J. Rogers, and, M. S. Mannan, X. Li and H. Koseki, “Effect of Iron Ion in the Thermal Decomposition of 50 mass % Hydroxylamine/Water Solutions,” Journal of Chemical & Engineering Data, 2003 48 (5), 1164-1169. DOI: 10.1021/je030121p
106. M. Gross and M. W. Beckstead, “Diffusion Flame Calculations for Composite Propellants Using a Vorticity-Velocity Formulation,” Journal of Propulsion and Power, Vol. 25, No. 1, 2009, pp. 74–82. https://doi:10.2514/1.36360
107. C.-C. Chen and M. J. McQuaid, “Modeling the deflagration of ammonium perchlorate at pressures from 300 to 30,000 psia. Part I: Gas-phase, finite rate, chemical kinetics mechanism development,” 2014 JANNAF Combustion Subcommittee Meeting.
108. M. J. McQuaid and C.-C. Chen, “Modeling the deflagration of ammonium perchlorate at pressures from 300 to 30,000 psia. Part II: Considerations besides the gas-phase, finite-rate, chemical kinetics mechanism,” 2014 JANNAF Combustion Subcommittee Meeting.
109. http://chemistry.emory.edu/faculty/lin/database.htm
110. https://comp.chem.umn.edu/polyrate/
111. R. Zhu and M. C. Lin, “Kinetics and Mechanism of AP Combustion Initiation: A Complete Quantum Chemical Prediction for Reactions in Three Phases,” Trans. JSASS Aerospace Tech. Japan, Vol. 10, No. ists28, pp. Pa_77-Pa_84, 2012.

112. M. Tanaka and M. W. Beckstead, "A three-phase combustion model of ammonium perchlorate," AIAA, ASME, SAE, and ASEE, Joint Propulsion Conference and Exhibit, 32nd, Lake Buena Vista, FL, July 1-3, 1996, AIAA Paper 96-2888.
113. R. Jankovsky, "HAN-Based Monopropellant Assessment for Spacecraft," 32nd AIAA/ASME/SAE/ASEE Joint Propulsion Conference and Exhibit, Lake Buena Vista, FL, July 1996, AIAA 96-2893.
114. R. Amrousse, T. Katsumi, T. Sulaiman, B.R. Das, H. Kumagai, K. Maeda and K. Hori, "Hydroxylammonium Nitrate as Green Propellant: Decomposition And Stability," 11 (2012) 241-257.
115. A. S. Gohardani, J. Stanojev, A. Demairé, K. Anflo, M. Persson, N. Wingborg and C. Nilsson, "Green Space Propulsion: Opportunities and Prospects," Progress in Aerospace Sciences 71 (2014) 128-149.
116. C. Wei, W. J. Rogers and M. S. Mannan, "Detection of Autocatalytic Decomposition Behavior of Energetic Materials Using APTAC," Journal of Thermal Analysis and Calorimetry 83 (2006) 125-130.
117. L. Liu, C. Wei, Y. Guo, W. J. Rogers, M. S. Mannan, "Hydroxylamine Nitrate Self-Catalytic Kinetics Study with Adiabatic Calorimetry," Journal of Hazardous Materials 162 (2009) 1217-1222.
118. E. S. Kim, H. S. Lee, C. F. Mallery and S. T. Thynell, "Thermal Decomposition Studies of En-ergetic Materials Using Confined Rapid Thermolysis / FTIR Spectroscopy," Combustion and Flame 110 (1997) 239-255.
119. H. Lee, T. A. Litzinger, "Chemical Kinetic Study of HAN Decomposition," Combustion and Flame 135 (2003) 151-169.
120. S. R. Vosen, "Hydroxylammonium Nitrate-Based Liquid Propellant Combustion-Interpretation of Strand Burner Data and the Laminar Burning Velocity," Combustion and Flame 82 (1990) 376-388.
121. S. R. Vosen, "Concentration and Pressure Effects on the Decomposition Rate of Aqueous Hydroxylammonium Nitrate Solutions," Combustion Science and Technology 68 (1989) 85-99.
122. J.-D. Chai and M. Head-Gordon, "Long-Range Corrected Hybrid Density Functionals with Damped Atom-Atom Dispersion Corrections," Physical Chemistry Chemical Physics 10 (2008) 6615-6620.
123. A. V. Marenich, C.J. Cramer and D.G. Truhlar, "Universal Solvation Model Based on Solute Electron Density and on a Continuum Model of the Solvent Defined by the Bulk Dielectric Constant and Atomic Surface Tensions," J Phys Chem B 113 (2009) 6378-6396.
124. M. N. Hughes and G. Stedman, "525. Kinetics and Mechanism of the Reaction between Nitrous Acid and Hydroxylamine. Part I," Journal of the Chemical Society (Resumed) 1 (1963) 2824-2830.
125. J. R. Pembridge and G. Stedman, "Kinetics, Mechanism, and Stoichiometry of the Oxidation of Hydroxylamine by Nitric Acid," Journal of the Chemical Society, Dalton Transactions 11 (1979) 1657-1663.
126. S. V. Lymar and V. Shafirovich, "Photoinduced Release of Nitroxyl and Nitric Oxide from Diazeniumdiolates," Journal of Physical Chemistry B 111 (2007) 6861-6867.
127. V. Shafirovich and S. V. Lymar, "Nitroxyl and Its Anion in Aqueous Solutions: Spin States, Protic Equilibria, and Reactivities toward Oxygen and Nitric Oxide," PNAS 99 (2002) 7340-7345.

128. M. Bringas, J. Semelak, A. Zeida and D. A. Estrin, "Theoretical Investigation of the Mechanism of Nitroxyl Decomposition in Aqueous Solution," Journal of Inorganic Biochemistry 162 (2016) 102-108.
129. K. Zhang and S. T. Thynell, "Examination of the Mechanism of the Yield of N2O from Nitroxyl (HNO) in the Solution Phase by Theoretical Calculations," Journal of Physical Chemistry A 121 (2017) 4505-4516.
130. M. N. Hughes and G. Stedman, "231. Kinetics and Mechanism of the Decomposition of Hyponitrous Acid," Journal of the Chemical Society (Resumed) 1 (1963) 1239-1243.
131. J. W. Schoppelrei, M. L. Kieke, and T. B. Brill, "Spectroscopy of Hydrothermal Reactions. 2. Reactions and Kinetic Parameters of [NH3OH]NO3 and Equilibria of (NH4)2CO3 Determined with a Flow Cell and FT Raman Spectroscopy," Journal of Physical Chemistry 100 (1996) 7463-7470.
132. J. W. Schoppelrei and T. B. Brill, "Spectroscopy of Hydrothermal Reactions. 7. Kinetics of Aqueous [NH3OH]NO3 at 463−523 K and 27.5 MPa by Infrared Spectroscopy," Journal of Physical Chemistry A 101 (1997) 8593-8596.
133. T. B. Brill, P. E. Gongwer, and G. K. Williams, "Thermal Decomposition of Energetic Materials. 66. Kinetic Compensation Effects in HMX, RDX, and NTO," Journal of Physical Chemistry 98 (1994) 12242-12247.
134. H. Lee, and S. T. Thynell, "Confined Rapid Thermolysis/FTIR Spectroscopy of Hydroxylammonium Nitrate," 33rd AIAA/ASME/SAE/ASEE Joint Propulsion Conference and Exhib-it, Seattle, WA, July 1997, AIAA 97-3232.
135. T. Chatterjee and S. T. Thynell, "Quantum mechanics investigation on initial decomposition of ammonia borane in glyme," International Journal of Chemical Kinetics, 2018, 50:568–581. DOI: 10.1002/kin.21183
136. A. Al-Kukhun, H. T. Hwang, and A. Varma, "Mechanistic studies of ammonia borane dehydrogenation," Int. J. Hydrogen Energy, vol. 38, no. 1, pp. 169–179, 2013.
137. M. Bowden, and T. Autrey, "Characterization and mechanistic studies of the dehydrogenation of NHxBHx materials," Curr. Opin. Solid State Mater. Sci., vol. 15, no. 2, pp. 73–79, 2011.
138. W. J. Shaw, J. C. Linehan, N. K. Szymczak, D. J. Heldebrant, C. Yonker, D. M. Camaioni, R. T. Baker, and T. Autrey, "In situ multinuclear NMR spectroscopic studies of the thermal decomposition of ammonia borane in solution," Angew. Chemie - Int. Ed., vol. 47, no. 39, pp. 7493–7496, 2008.
139. M.R. Weismiller, S.Q. Wang, A. Chowdhury, S.T. Thynell, and R.A. Yetter, "Confined rapid thermolysis studies of ammonia borane," Thermochim. Acta, vol. 551, pp. 110–117, 2013.
140. N. Kumbhakarna, S.T. Thynell, "Development of a reaction mechanism for liquid-phase decomposition of guanidinium 5-amino tetrazolate," Thermochimica Acta, Vol. 582, 2014, pp. 25-34, DOI: 10.1016/j.tca.2014.02.014
141. N. R. Kumbhakarna, K. J. Shah, A. Chowdhury, S.T. Thynell, "Identification of liquid-phase decomposition species and reactions for guanidinium azotetrazolate," Thermochimica Acta, Vol. 590, 2014, pp. 51-65, DOI: 10.1016/j.tca.2014.06.005
142. Sundaram, D. S.; Yang, V.; Huang, Y.; Risha, G. A.; Yetter, R. A. Effects of particle size and pressure on combustion of nano-aluminum particles and liquid water. Combustion and Flame 2013, 160 (10), 2251-2259.
143. Jain, A.; McGaughey, A. J. Thermal transport by phonons and electrons in aluminum, silver, and gold from first principles. Physical Review B 2016, 93 (8), 081206.

144. Wang, Y.; Lu, Z.; Ruan, X. First principles calculation of lattice thermal conductivity of metals considering phonon-phonon and phonon-electron scattering. Journal of Applied Physics 2016, 119 (22), 225109.
145. Perdew, J. P.; Zunger, A. Self-interaction correction to density-functional approximations for many-electron systems. Physical Review B 1981, 23 (10), 5048.
146. Giannozzi, P.; Baroni, S.; Bonini, N.; Calandra, M.; Car, R.; Cavazzoni, C.; Ceresoli, D.; Chiarotti, G. L.; Cococcioni, M.; Dabo, I. QUANTUM ESPRESSO: a modular and open-source software project for quantum simulations of materials. Journal of physics: Condensed matter 2009, 21 (39), 395502.
147. Tadano, T.; Gohda, Y.; Tsuneyuki, S. Anharmonic force constants extracted from first-principles molecular dynamics: applications to heat transfer simulations. Journal of Physics: Condensed Matter 2014, 26 (22), 225402.
148. (a) Stedman, R. t.; Nilsson, G. Dispersion relations for phonons in aluminum at 80 and 300 K. Physical Review 1966, 145 (2), 492; (b) Schober, H.; Strauch, D.; Dorner, B. Lattice dynamics of sapphire (Al 2 O 3). Zeitschrift für Physik B Condensed Matter 1993, 92 (3), 273-283.
149. (a) Powell, R.; Ho, C. Y.; Liley, P. E. Thermal conductivity of selected materials; DTIC Document: 1966; (b) Ramires, M. L.; de Castro, C. A. N.; Nagasaka, Y.; Nagashima, A.; Assael, M. J.; Wakeham, W. A. Standard reference data for the thermal conductivity of water. Journal of Physical and Chemical Reference Data 1995, 24 (3), 1377-1381; (c) Nemoto, T.; Sasaki, S.; Hakuraku, Y. Thermal conductivity of alumina and silicon carbide ceramics at low temperatures. Cryogenics 1985, 25 (9), 531-532.
150. Tyagi, H.; Phelan, P. E.; Prasher, R.; Peck, R.; Lee, T.; Pacheco, J. R.; Arentzen, P. Increased hot-plate ignition probability for nanoparticle-laden diesel fuel. Nano letters 2008, 8 (5), 1410-1416.
151. Risha, G. A.; Son, S. F.; Yetter, R.; Yang, V.; Tappan, B. Combustion of nano-aluminum and liquid water. Proceedings of the Combustion Institute 2007, 31 (2), 2029-2036.
152. Bazyn, T.; Krier, H.; Glumac, N. Combustion of nanoaluminum at elevated pressure and temperature behind reflected shock waves. Combustion and Flame 2006, 145 (4), 703-713.
153. (a) Gale, W.; Totemeier, T. Smithells Metals Reference Book" eight edition, Amsterdam, Boston, Heidelberg, London, New York. Oxford, Paris, San Diego, San Francisco, Singapore, Sydney, Tokyo: 2004; (b) Buyco, E. H.; Davis, F. E. Specific heat of aluminum from zero to its melting temperature and beyond. Equation for representation of the specific heat of solids. Journal of Chemical and engineering data 1970, 15 (4), 518-523; (c) MUNRO, M. Evaluated Material Properties for a Sintered alpha-Alumina. Journal of the American Ceramic Society 1997, 80 (8), 1919-1928.
154. (a) Hopkins, P. E.; Beechem, T.; Duda, J. C.; Hattar, K.; Ihlefeld, J. F.; Rodriguez, M. A.; Piekos, E. S. Influence of anisotropy on thermal boundary conductance at solid interfaces. Physical Review B 2011, 84 (12), 125408; (b) Stoner, R.; Maris, H. Kapitza conductance and heat flow between solids at temperatures from 50 to 300 K. Physical Review B 1993, 48 (22), 16373.
155. Keblinski, P.; Phillpot, S.; Choi, S.; Eastman, J. Mechanisms of heat flow in suspensions of nano-sized particles (nanofluids). International journal of heat and mass transfer 2002, 45 (4), 855-863.
156. Lee, S.; Saidur, R.; Sabri, M.; Min, T. Molecular dynamic simulation: Studying the effects of Brownian motion and induced micro-convection in nanofluids. Numerical Heat Transfer, Part

A: Applications 2016, 69 (6), 643-658; (b) Li, L.; Zhang, Y.; Ma, H.; Yang, M. Molecular dynamics simulation of effect of liquid layering around the nanoparticle on the enhanced thermal conductivity of nanofluids. Journal of nanoparticle research 2010, 12 (3), 811-821; (c) Özerinç, S.; Kakaç, S.; Yazıcıoğlu, A. G. Enhanced thermal conductivity of nanofluids: a state-of-the-art review. Microfluidics and Nanofluidics 2010, 8 (2), 145-170; (d) Sachdeva, P.; Kumar, R. Effect of hydration layer and surface wettability in enhancing thermal conductivity of nanofluids. Applied Physics Letters 2009, 95 (22), 223105; (e) Das, S. K.; Putra, N.; Thiesen, P.; Roetzel, W. Temperature dependence of thermal conductivity enhancement for nanofluids. Journal of Heat Transfer 2003, 125 (4), 567-574.

157. (a) Babaei, H.; Keblinski, P.; Khodadadi, J. A proof for insignificant effect of Brownian motion-induced micro-convection on thermal conductivity of nanofluids by utilizing molecular dynamics simulations. Journal of Applied Physics 2013, 113 (8), 084302; (b) Babaei, H.; Keblinski, P.; Khodadadi, J. M. Equilibrium molecular dynamics determination of thermal conductivity for multi-component systems. Journal of Applied Physics 2012, 112 (5), 054310; (c) Keblinski, P.; Prasher, R.; Eapen, J. Thermal conductance of nanofluids: is the controversy over? Journal of Nanoparticle research 2008, 10 (7), 1089-1097.
158. Ju, Y.; Goodson, K. Phonon scattering in silicon films with thickness of order 100 nm. Applied Physics Letters 1999, 74 (20), 3005-3007.
159. (a) Hohensee, G. T.; Wilson, R.; Cahill, D. G. Thermal conductance of metal–diamond interfaces at high pressure. Nature communications 2015, 6, 6578; (b) Lyeo, H.-K.; Cahill, D. G. Thermal conductance of interfaces between highly dissimilar materials. Physical Review B 2006, 73 (14), 144301; (c) Cahill, D. G.; Watanabe, F.; Rockett, A.; Vining, C. B. Thermal conductivity of epitaxial layers of dilute SiGe alloys. Physical Review B 2005, 71 (23), 235202.
160. Gordiz, K.; Henry, A. A formalism for calculating the modal contributions to thermal interface conductance. New Journal of Physics 2015, 17 (10), 103002.
161. (a) Siegel, D. J.; Hector Jr, L. G.; Adams, J. B. Adhesion, atomic structure, and bonding at the Al (111)/α− Al 2 O 3 (0001) interface: a first principles study. Physical Review B 2002, 65 (8), 085415; (b) Pilania, G.; Thijsse, B. J.; Hoagland, R. G.; Lazić, I.; Valone, S. M.; Liu, X.-Y. Revisiting the Al/Al 2 O 3 interface: coherent interfaces and misfit accommodation. Scientific reports 2014, 4, 4485.
162. Hopkins, P. E.; Salaway, R.; Stevens, R.; Norris, P. Temperature-Dependent Thermal Boundary Conductance at Al/Al 2 O 3 and Pt/Al 2 O 3 Interfaces. International Journal of Thermophysics 2007, 28 (3), 947-957.
163. Mingo, N.; Yang, L. Phonon transport in nanowires coated with an amorphous material: An atomistic Green's function approach. Physical Review B 2003, 68 (24), 245406.
164. (a) Gordiz, K.; Henry, A. Phonon transport at interfaces: Determining the correct modes of vibration. Journal of Applied Physics 2016, 119 (1), 015101; (b) Gordiz, K.; Henry, A. Phonon transport at crystalline Si/Ge interfaces: the role of interfacial modes of vibration. Scientific reports 2016, 6, 23139.
165. Vashishta, P.; Kalia, R. K.; Nakano, A.; Rino, J. P. Interaction potentials for alumina and molecular dynamics simulations of amorphous and liquid alumina. Journal of Applied Physics 2008, 103 (8), 083504.
166. Mark, P.; Nilsson, L. Structure and dynamics of the TIP3P, SPC, and SPC/E water models at 298 K. The Journal of Physical Chemistry A 2001, 105 (43), 9954-9960.

167. Miyamoto, S.; Kollman, P. A. SETTLE: an analytical version of the SHAKE and RATTLE algorithm for rigid water models. Journal of computational chemistry 1992, 13 (8), 952-962.
168. Allen, M. P.; Tildesley, D. J. Computer simulation of liquids. Oxford university press: 1989.
169. Cygan, R. T.; Liang, J.-J.; Kalinichev, A. G. Molecular models of hydroxide, oxyhydroxide, and clay phases and the development of a general force field. The Journal of Physical Chemistry B 2004, 108 (4), 1255-1266.
170. Hünenberger, P. H. Thermostat algorithms for molecular dynamics simulations. In Advanced computer simulation, Springer: 2005; pp 105-149.
171. Plimpton, S. Fast parallel algorithms for short-range molecular dynamics. Journal of computational physics 1995, 117 (1), 1-19.
172. Das, S. K.; Choi, S. U.; Yu, W.; Pradeep, T. Nanofluids: science and technology. John Wiley & Sons: 2007.
173. (a) Shaker, M.; Birgersson, E.; Mujumdar, A. Extended Maxwell model for the thermal conductivity of nanofluids that accounts for nonlocal heat transfer. International Journal of Thermal Sciences 2014, 84, 260-266; (b) Yu, W.; Choi, S. The role of interfacial layers in the enhanced thermal conductivity of nanofluids: a renovated Maxwell model. Journal of Nanoparticle Research 2003, 5 (1-2), 167-171; (c) Maxwell, J. C. A treatise on electricity and magnetism. Clarendon press: 1881; Vol. 1; (d) Xie, H.; Wang, J.; Xi, T.; Liu, Y.; Ai, F.; Wu, Q. Thermal conductivity enhancement of suspensions containing nanosized alumina particles. Journal of Applied Physics 2002, 91 (7), 4568-4572.
174. Ross, S.; Winkler, W. On physical adsorption: IX. Sub-critical and subpracritical adsorption isotherms for krypton monolayers on graphitized carbon black. Journal of Colloid Science 1955, 10 (4), 330-337.
175. Shapovalov, V.; Truong, T. N. Ab initio study of water adsorption on α-Al2O3 (0001) crystal surface. The Journal of Physical Chemistry B 2000, 104 (42), 9859-9863.
176. Argyris, D.; Ho, T.; Cole, D. R.; Striolo, A. Molecular dynamics studies of interfacial water at the alumina surface. The Journal of Physical Chemistry C 2011, 115 (5), 2038-2046.
177. Liang, Z.; Tsai, H.-L. Thermal conductivity of interfacial layers in nanofluids. Phys Rev E 2011, 83, 41602.
178. Zhang, Z. M. Nano/microscale heat transfer. McGraw-Hill New York: 2007.
179. Bernath, P. F. The spectroscopy of water vapour: experiment, theory and applications. Physical Chemistry Chemical Physics 2002, 4 (9), 1501-1509.
180. Rayleigh, J. W. S. B. The theory of sound. Macmillan: 1896; Vol. 2.
181. (a) Beck, M. P.; Yuan, Y.; Warrier, P.; Teja, A. S. The effect of particle size on the thermal conductivity of alumina nanofluids. Journal of Nanoparticle Research 2009, 11 (5), 1129-1136; (b) Timofeeva, E. V.; Gavrilov, A. N.; McCloskey, J. M.; Tolmachev, Y. V.; Sprunt, S.; Lopatina, L. M.; Selinger, J. V. Thermal conductivity and particle agglomeration in alumina nanofluids: experiment and theory. Physical Review E 2007, 76 (6), 061203.
182. McGaughey, A.; Kaviany, M. Thermal conductivity decomposition and analysis using molecular dynamics simulations: Part II. Complex silica structures. International Journal of Heat and Mass Transfer 2004, 47 (8), 1799-1816.
183. (a) Zhou, X. F.; Gao, L. Effective thermal conductivity in nanofluids of nonspherical particles with interfacial thermal resistance: differential effective medium theory. Journal of applied physics 2006, 100 (2), 024913; (b) Nan, C.-W.; Birringer, R.; Clarke, D. R.; Gleiter, H. Effective thermal conductivity of particulate composites with interfacial thermal resistance. Journal of Applied Physics 1997, 81 (10), 6692-6699.

184. Muraleedharan, M. G.; Sundaram, D. S.; Henry, A.; Yang, V. Thermal conductivity calculation of nano-suspensions using Green–Kubo relations with reduced artificial correlations. Journal of Physics: Condensed Matter 2017, 29 (15), 155302.
185. (a) Wang, J.; Carson, J. K.; North, M. F.; Cleland, D. J. A new approach to modelling the effective thermal conductivity of heterogeneous materials. International journal of heat and mass transfer 2006, 49 (17-18), 3075-3083; (b) Eucken, A. Allgemeine gesetzmäßigkeiten für das wärmeleitvermögen verschiedener stoffarten und aggregatzustände. Forschung auf dem Gebiet des Ingenieurwesens A 1940, 11 (1), 6-20.
186. Bruggeman, V. D. Berechnung verschiedener physikalischer Konstanten von heterogenen Substanzen. I. Dielektrizitätskonstanten und Leitfähigkeiten der Mischkörper aus isotropen Substanzen. Annalen der physik 1935, 416 (8), 665-679.
187. Risha, G. A.; Sabourin, J. L.; Yang, V.; Yetter, R. A.; Son, S. F.; Tappan, B. C. Combustion and conversion efficiency of nanoaluminum-water mixtures. Combustion Science and Technology 2008, 180 (12), 2127-2142.
188. Keller, H. B. Numerical methods for two-point boundary-value problems. Courier Dover Publications: 2018.
189. Muraleedharan, M. G.; Gordiz, K.; Ju, S.; Shiomi, J.; Yang, V.; Henry, A. Thermal interface conductance between aluminum and aluminum oxide: A rigorous test of atomistic level theories. arXiv preprint arXiv:1807.06631 2018.
190. Risha, G. A.; Connell Jr, T. L.; Yetter, R. A.; Sundaram, D. S.; Yang, V. Combustion of frozen nanoaluminum and water mixtures. Journal of Propulsion and Power 2013, 30 (1), 133-142.
191. (a) Kodama, T.; Ohnishi, M.; Park, W.; Shiga, T.; Park, J.; Shimada, T.; Shinohara, H.; Shiomi, J.; Goodson, K. E. Modulation of thermal and thermoelectric transport in individual carbon nanotubes by fullerene encapsulation. Nature materials 2017, 16 (9), 892; (b) Feng, L.; Shiga, T.; Han, H.; Ju, S.; Kosevich, Y. A.; Shiomi, J. Phonon-interference resonance effects by nanoparticles embedded in a matrix. Physical Review B 2017, 96 (22), 220301; (c) Ju, S.; Shiga, T.; Feng, L.; Hou, Z.; Tsuda, K.; Shiomi, J. Designing nanostructures for phonon transport via Bayesian optimization. Physical Review X 2017, 7 (2), 021024.
192. Row, S.L. and Groven, L.J., Smart Energetics: Sensitization of the Aluminum-Fluoropolymer Reactive System, Adv. Eng. Mater. 2018, 20, 1700409.